

Università di Roma Sapienza  
Dottorato in Scienza dei Materiali  
XXIV Ciclo  
A.A. 2010-2011

“Raman Spectroscopy of Insulin  
under Ambient and Extreme Conditions”

Dottoranda

Sara Mangialardo

Coordinatore Dottorato

Prof. Ruggero Caminiti

Tutor

Prof. Paolo Postorino



*Ai miei amici a 4 zampe Zorro e Pablo,  
per aver studiato con me disteso su libri e pc (il primo)  
e per avermi regalato momenti di pura gioia quando lo stress era forte (il secondo)  
Dopo la laurea abbiamo preso insieme anche il dottorato!*





# *Table of Contents*

<b>Table of Contents</b> .....	i
<b>Introduction</b> .....	iii
<b>Chapter 1 – Protein Structure and Stability</b> .....	1
1.1 Protein Structure	
1.1.1 Bovine Pancreatic Insulin	
1.1.2 Hen Egg White Lysozyme	
1.2 Protein Folding/Unfolding	
1.2.1 Pressure Mechanism of Denaturation	
1.3 Protein Fibrillation	
1.3.1 Insulin and Lysozyme Mechanism of Fibrillation	
<b>Chapter 2 - Experimental Methods and Materials</b> .....	29
2.1 Infrared and Raman Spectroscopy	
2.1.1 History and Survive	
2.1.2 Application of Raman and Infrared Spectroscopy on Proteins	
2.1.3 Experimental Set-up	
2.2 High Pressure Spectroscopy: the Diamond Anvil Cell	
2.2.1 Ruby Fluorescence for Pressure Determination	
2.2.2 Raman and Infrared Measurements at High Pressure: Experimental Procedures	
2.3 Drop Coating Deposition Method	
2.4 Band Fitting: Adopted Method and Errors	
2.5 Materials	
2.6 Fibrillation Protocols	
<b>Chapter 3 – Bovine Pancreatic Insulin &amp; Hen Egg White Lysozyme</b> .....	53
3.1 Bovine Pancreatic Insulin	
3.1.1 Insulin: State of the Art	
3.1.2 The Raman Spectra of Insulin in Native and Fibrillar Conformations	
3.1.3 Insulin Solutions: Infrared Characterization	

3.2 Hen Egg White Lysozyme	
3.2.1 Lysozyme State of the Art	
3.2.2 The Raman Spectra of Lysozyme in Native and Fibrillar Conformations	
<b>Chapter 4 – Raman and Infrared Measurements on Insulin Solutions Under Pressure</b>	<b>73</b>
4.1 High Pressure Behavior of Insulin 2mM Solution at Neutral pH	
4.1.1 Raman Measurements	
4.1.2 Infrared Measurements	
4.2 High Pressure Behavior of Insulin 20mM Solution at Neutral pH	
4.3 Appendix: 2D Correlation Plot	
<b>Chapter 5 – Raman Measurements on Insulin Powder Under Pressure</b>	<b>87</b>
5.1 Determination of the Maximum Pressure for the Elastic Response: Pressurizing/Depressurizing Cycle	
5.2 The Pressure Dependence of the Raman Spectrum: the Plastic Transition at 4.2 GPa	
5.2.1 Pressure Treated Insulin Vs Thermo-Chemical Treated Insulin	
<b>Chapter 6 – Proteins Renaturation by Ionic Liquids</b>	<b>103</b>
6.1 Ionic Liquids	
6.1.1 The Raman Spectra of Ammonium Based Ionic Liquids	
6.2 Insulin Fibrils in Ionic Liquids	
6.3 Lysozyme Fibrils in Ionic Liquids	
<b>Conclusion and Outlook</b>	<b>116</b>
<b>Appendix – Application of Raman Spectroscopy on Samples of Biological Interest</b>	<b>125</b>
A Biological Apatites from Cardiac Valves	
B Eumelanin Films	
<b>Acknowledgments</b>	<b>143</b>
<b>List of Publications</b>	<b>145</b>

# *Introduction*

Proteins are essential for all biological activities and the health of the cells. Their basic structure (*primary structure*) is a long chain of amino acids. The protein folding is the process by which these chains of amino acids reach their peculiar tri-dimensional stable structure. The problem of protein folding is fundamental in biology, as the protein correct structure is intimately tied to the protein function. The pathway by which a protein attains a specific three dimensional conformation is not yet completely understood. The problem lies mostly in the astronomically large numbers of different conformations a protein may undertake, even a small protein of 100 residues would require more time than the universe to explore all possible conformations and choose the *native* one, it would also arguably make computational prediction of protein structures under the same basis unfeasible if not impossible.

Failure to fold into native structure produces inactive proteins, usually toxic. To this respect several diseases have been already related to the *misfolding* of proteins, i.e. a protein not correctly folded. These illnesses (called neurodegenerative diseases) include: Alzheimer, Bovine Spongiform Encephalopathy (BSE or Mad Cow disease), Amyotrophic Lateral Sclerosis (ALS or Lou Gehrig's disease), Creutzfeldt-Jakob disease, and Parkinson. All protein misfolded states characteristic of these diseases show common features and in particular they all possess a similar structural morphology since proteins involved are mainly organized in highly ordered structures named fibrils (amyloidogenic diseases). The study of the mechanisms driving the protein folding is thus necessary to better understand what sometimes can go wrong and in particular the native-unfolded-fibrillar pathway needs to be more investigated.

The exploration of the space of the possible conformation of a protein through the folding funnel allows finding the local energy minima in which the protein structure can be found after applying an external perturbation. We can move through the possible conformational states of a protein by varying the environment. Most of the papers present in literature deal with high temperature, mostly associated with no neutral pH, and the use of particular solvents like alcohol, urea and other denaturants.

In this thesis a comparative analysis of the conformational changes induced by the well-established thermo-chemical protocols and those induced by the application of high hydrostatic pressure has been carried out. The effects of pressure on the protein conformations are still poorly

investigated and not yet completely understood. In particular the relationship between the structure and thermodynamic stability of proteins needs to be elucidated. Since denatured protein usually occupies a volume smaller than native protein, pressure is expected to induce denaturation. Moreover, in recent years, experimental and theoretical studies have suggested the penetration of water into the hydrophobic core as the mechanism of pressure denaturation. The latter is a particularly interesting point since the pressure induced denaturation mechanism appears to be completely different to that expected for thermo-chemical denaturation. Finally also the pressure-induced contraction of protein internal cavities is thought to play a relevant role in the volume change associated with denaturation. One of the aims of this thesis is to provide further insight into the mechanism of protein pressure denaturation.

In this work the conformational changes of the protein structure were studied by means of Raman spectroscopy. Recent researches have demonstrated that this technique is a powerful tool for protein conformational analysis as it allows studying samples in different states (liquid, powder and crystal) in very small quantities and it provides both qualitative and quantitative information on different levels of the protein structure. Moreover this technique can be easily coupled to the high pressure technique that is the principal denaturing method used in this work.

Indeed this work of thesis is thus mainly focused on the conformational changes induced by high pressure on bovine pancreatic insulin. The aim is to find new possible conformations in the folding/unfolding pathway of this protein. Insulin is a well studied protein that is involved in conformational diseases and it is able to fibrillate also *in vitro* making fibrils identical to those of the previously mentioned neurodegenerative diseases. This makes insulin an important model protein for studies on conformational changes.

Focusing on insulin under pressure, it is important to note that its pressure behavior is only partially studied in literature, although it is well known that it is a *pressure resistant* protein. Despite most of the proteins show a pressure-induced plastic modifications under a pressure not higher than 0.6-0.7 GPa, it is well known that in insulin no plastic changes (i.e. irreversible modifications) occur up to pressures of the order of 1.2 GPa.

In this work we studied first the pressure behavior of insulin in water solution at two different concentrations (2mM and 20mM) at neutral pH. Our results show that no plastic structural transitions occur in both the low- and the high-concentration solutions. The only difference between the two series of Raman spectra was the presence in the high-concentration solution of aggregates that were partially dissolved by high hydrostatic pressure. The quest for a plastic structural deformation of insulin drives our investigation from insulin solutions towards insulin powder. High pressure induced ice formation at a pressure around 1.2 GPa can indeed strongly bias the protein response to volume compression. We would like to mention that even though proteins are usually studied in solutions and within a very narrow pressure range (usually 0-1.5 GPa) the use of powder for studying amino acids in the very high pressure regime is going to become a common practice in the last years. High pressures (up to 20 GPa) were applied on amino acids to study the effect of pressure on polymorphism, to characterize the hydrogen bonds, to make a sort of “crash test” and to improve the knowledge of transformation of amino acids under interstellar or interplanetary conditions. On the other hand the results of high pressure spectroscopic studies can provide relevant information for a deeper insight into the lattice dynamics and the structural properties of amino-acids.

In this PhD work insulin powder was pressurized up to a maximum pressure of 8.1 GPa and around 4.2 GPa a structural plastic transition was finally observed, indeed largely extending the pressure range in which insulin shows an elastic response. The careful analysis of the new insulin conformation obtained after the high pressure cycle represents the core of the research work reported in this thesis. To reach a deeper understanding on this new structural state, the Raman spectra of the pressure treated sample was also compared with those of known conformations: the native insulin and the *in vitro* fibrillar sample obtained after thermo chemical treatment. In agreement with most of the previous literature, the present results show that applying moderate pressure induces the dissociation of protein oligomers as well as low-pH solution but in a completely clean manner.

Going further in the attempt of extending the knowledge on the possible insulin conformations we investigated the possibility of renaturation of protein fibrils by means of protic ionic liquids. For this study a second protein, hen egg white lysozyme, was also investigated. Lysozyme has been chosen for its biological relevance and because preliminary results about the renaturation process were already available in literature. In this respect we used lysozyme as a reference protein. The obtained results although partial are quite encouraging and some indication of chemically induced renaturation has been found in lysozyme and perhaps in insulin. We are presently trying to repeat the same renaturation experiments on the pressure treated samples.

This PhD thesis is organized as follows:

- In **Chapter 1** a general introduction on protein structure is reported. The structure of Bovine Pancreatic Insulin and Hen Egg White Lysozyme is presented. It follows a brief discussion about the folding/unfolding problem, with a particular accent on the pressure induced denaturation. Finally the fibrillation mechanisms will be reviewed.
- In **Chapter 2** the experimental techniques are briefly presented and discussed. Sample preparation methods are also reported.
- In **Chapter 3** the Raman and Infrared measurements on the native and fibrillar conformations are shown and analyzed. The spectroscopic markers that characterize the two different conformations are highlighted.
- In **Chapter 4** the pressure behavior of two different concentrated solutions of insulin are analyzed by Raman and Infrared spectroscopy.
- In **Chapter 5** the high pressure behavior of the insulin powder is discussed in the elastic and in the plastic regime. Particular attention is made on the plastic transition that give rise to a new stable conformation of the protein. The Raman spectra obtained from the new conformations are compared with those collected from the native and the fibrillar protein.
- In **Chapter 6** the results of renaturation experiments carried out on fibrillar insulin and lysozyme are reported and discussed. In particular we report on the renaturation efficiency of several protic ionic liquids.
- In the **Conclusion** the results obtained in the previous Chapters are compared and discussed and several general conclusions are drawn.
- In the **Appendices A and B** there are two examples of the successful application of the Raman spectroscopy on biological materials. In particular in appendix A is reported the characterization (by means of Raman and Infrared spectroscopy) of bio-apatite found in human heart valves; while in appendix B is reported the Raman characterization (that is part of a more general work focused onto the optical properties) of eumelanin films deposited onto suitable substrate by means of electro-spray deposition.

# *Chapter 1*

## *Protein Structure and Stability*

After a brief general summary on protein structure, the general properties of the two proteins subject of this thesis, namely bovine pancreatic insulin and hen egg white lysozyme are presented and briefly discussed.

The second part of the Chapter is dedicated to the discussion of the folding/unfolding mechanisms, with particular attention to the pressure-induced unfolding.

Finally the question of proteins fibrillation is introduced together with the specific mechanisms of fibrillation of insulin and lysozyme.

## 1.1 Protein structure

Proteins, term originated from the Greek πρώτα (“prota”) “of primary importance”, were first described and named by Jöns Jakob Berzelius in 1838. They are multi purposed molecules in living organisms, participating in all biological process. As structural molecules they take part to the cytoskeletal cell wall; as enzymes, they act as catalysts for many different biological reactions; they give motion to cellular structures. Moreover they control and stabilize the activity of DNA and RNA and provide to the identification of cell membranes. Although proteins play so many different functions, they are all similar in structure. Proteins are made up of amino acids, the building blocks. Usually proteins contain 50-100 amino acids, but there are also proteins that possess a number of amino acids among 3 and 10 or more than 50'000. A pair of amino acids can bind through a condensation reaction (removal of a water molecule) between the carboxyl group of an amino acid and the amine group of the other, to form a dipeptide (see Figure 1.1). The peptide bond is evidenced by the square in Figure 1.2 (A and B).

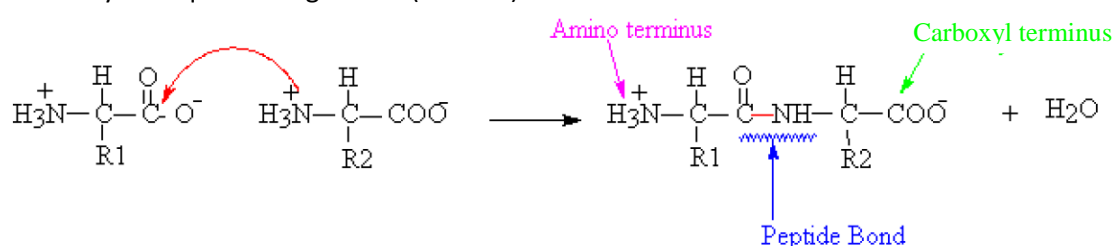


**Figure 1.1** – The peptide bond is an amide bond, such as the one that is formed between a carboxylic acid and a primary amine.

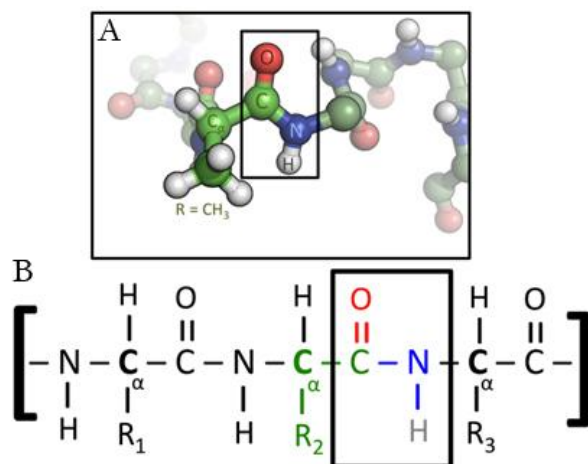


**Figure 1.2** – The peptide bond, evidenced by a square both in A and in B. (<http://en.wikipedia.org/wiki/File:Peptide-Figure-Revised.png>)

X-rays diffraction studies have shown that the C-N bond length in the peptide bond is shorter than the usual C-N bond and that the C=O is a little bit longer than the usual C=O double bond. In Table 1.1 are reported some important bond length involved in the peptide bond.

Peptide bond	Average length	Single bond	Average length	Hydrogen bond	Average ( $\pm 30$ )
C $_{\alpha}$ -C	153 pm	C-C	154 pm	O-H ... O-H	280 pm
C-N	133 pm	C-N	148 pm	N-H ... O=C	290 pm
N-C $_{\alpha}$	146 pm	C-O	143 pm	O-H ... O=C	280 pm

**Table 1.1** – Important bond length involved in the protein backbone.

([http://en.wikipedia.org/wiki/Protein\\_structure](http://en.wikipedia.org/wiki/Protein_structure))



The differences in the bond lengths reflect the C-N partial double bond features (over 40%), while the C=O double bond behaves in part (40%) as a single bond.<sup>1</sup> All this is justified by the resonance structures of the peptide between two limit structures:

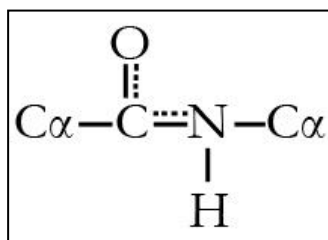


**Figure 1.3** – Schematic explanation for the bond lengths found by X-ray (see text for more details).

The characteristics of partial double bond prevents the free rotation around the peptide bond, C-N, which thus constitutes a point of rigidity of the polypeptide chain. The energy barrier preventing the free rotation is of about 20 kcal/mole.

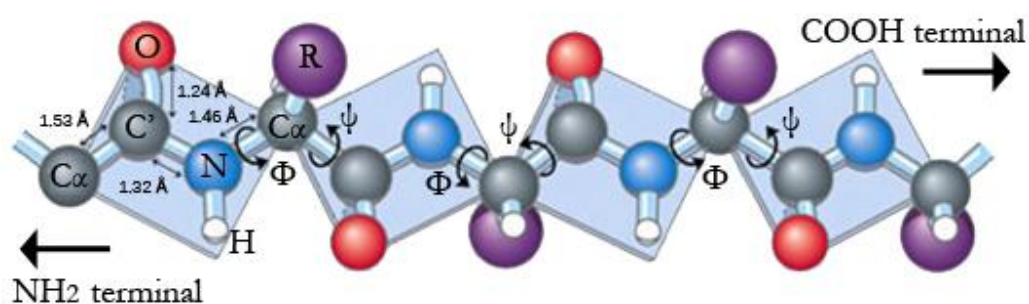


**Figure 1.4** – Polypeptide chain and definition of the dihedral angles between side peptides.

A further consequence of the resonance that affects the peptide bond is that the atoms in the peptide group (the C and N atoms, and the 4 atoms linked to them, i.e. O, H and the two C $\alpha$ ) lie on the same plane. The preferred configuration of the peptide is the one in which the two C $\alpha$  position are trans, so that the consecutive groups R show less steric hindrance. Despite the rigidity imposed by the peptide bond, the successive plans that contain the peptide groups are free to rotate around the C $\alpha$ , which represent a sort of "joint". In this way, each plan of the peptide unit has two possible rotations: one around the C $\alpha$ -C bond (angle of rotation:  $\psi$ ), and one around the N-C $\alpha$  bond (angle of rotation:  $\phi$ ) (see Figure 1.4).

For reasons of mutual steric hindrance of the large side groups R and of optimize stabilization of the peptide through the formation of intra-chain H bonds, the angles  $\psi$  and  $\phi$  can only assume certain values that define the conformation of the polypeptide chain. Plotting  $\psi$  as a function of  $\phi$ , we obtain the Ramachandran plot by the Indian biophysicist who made the calculations on the allowed values of the pairs of angles of rotation, which identifies well-defined regions corresponding to 3 pairs of allowed values. The regions are shown in Figure 1.5 and correspond to the structures of left handed  $\alpha$  helices, right handed  $\alpha$  helices and  $\beta$  strands. The red regions correspond to zones where atoms (treated as hard spheres with dimensions corresponding to their Van der Waals radii) of different side chains cannot collide, the green regions are those in the limit of possible collisions, while the white areas correspond to conformations where atoms in the polypeptide come closer than the sum of their van der Waals radii (i.e. they collide). An exception to this rule is provided by glycine that does not stand inside these restrictions as it has a hydrogen as side chain and consequently a limited steric hindrance, so it can take angles not allowed to other amino acids.

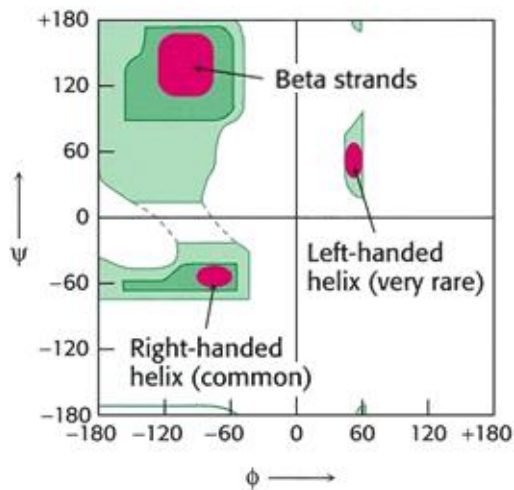


**Figure 1.5** –Ramachandran plot for amino acids side chains. Red zones: no collision, green zones: limiting regions to the collision, and white zones: collision between atoms of different side chains.

The biological function of a protein is intimately connected to the three-dimensional structure that the polypeptide chain assumes. This particular organization is defined native conformation. The three dimensional structure of a protein is organized, by means of a hierarchical policy, into four structures as is shown in Figure 1.6.

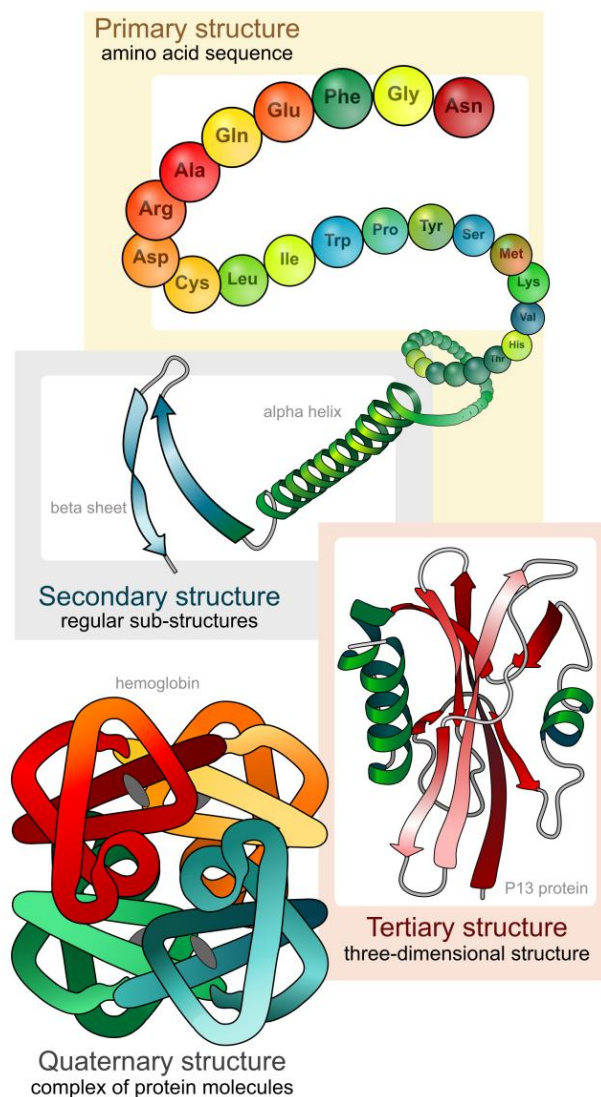


**Figure 1.6** – Proteins structures: from primary to quaternary. (Figure from [http://en.wikipedia.org/wiki/File:Main\\_protein\\_structure\\_levels\\_en.svg](http://en.wikipedia.org/wiki/File:Main_protein_structure_levels_en.svg))

The primary structure of a protein is the sequence of amino acids in the protein. The secondary structure of a protein occurs when the sequence of amino acids are linked together by the hydrogen bonds, folding into helices or  $\beta$  sheet. The value of the Ramachandran angles ( $\phi$ ,  $\psi$ ) for the most important conformations are:  $(-57^\circ, -47^\circ)$  for the  $\alpha$  helices,  $(-139, 135)$  for the anti-parallel  $\beta$  sheets and  $(-119^\circ, 113^\circ)$  for the parallel  $\beta$  sheets. The tertiary structure refers to a higher level of folding in which helices and sheets of the secondary structure fold upon themselves. This higher level folding arises for several reasons. First, different regions of the amino acid chain are hydrophilic or hydrophobic and arrange themselves accordingly in water. Second, different regions of the chain bond with each other via hydrogen bonding or disulfide linkages. Many proteins are made up of a single, continuous polypeptide chain and are thus called monomeric. Other proteins are composed of two or more polypeptide chains called subunits. The quaternary structure describes the arrangement and position of each of the subunits in a multiunit protein. The stabilizing forces that hold the polypeptide subunits together are the same forces that are responsible for tertiary structure stabilization. Indeed the major force stabilizing the quaternary structure is the hydrophobic interaction among nonpolar side chains at the contact regions of the subunits. Additional stabilizing forces include interactions between side chains of the subunits, as electrostatic interactions between ionic groups of opposite charge, hydrogen bonds between polar groups, and disulfide bonds. An example of a protein with quaternary structure is hemoglobin.<sup>2</sup> Hemoglobin, an oxygen transport protein, is a tetrameric (four unit) protein consisting of two  $\alpha$  and two  $\beta$  subunits (see Figure 1.7).

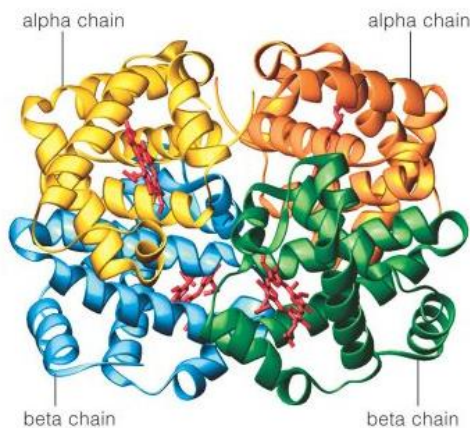


**Figure 1.7** – *Quaternary structure of hemoglobin.*

### 1.1.1 Bovine Pancreatic Insulin

Insulin was the first hormone identified in late 1920s. For its discovery Banting and Best won the Nobel Prize. Like many hormones insulin is a protein. It is secreted by groups of cells within the pancreas called islet cells and it is fundamental for human body as it allows the entrance of glucose into cells and its use as an energy source. Alteration of its function and/or of its concentration in human cells may cause many diseases, among which diabetes is the most known one.

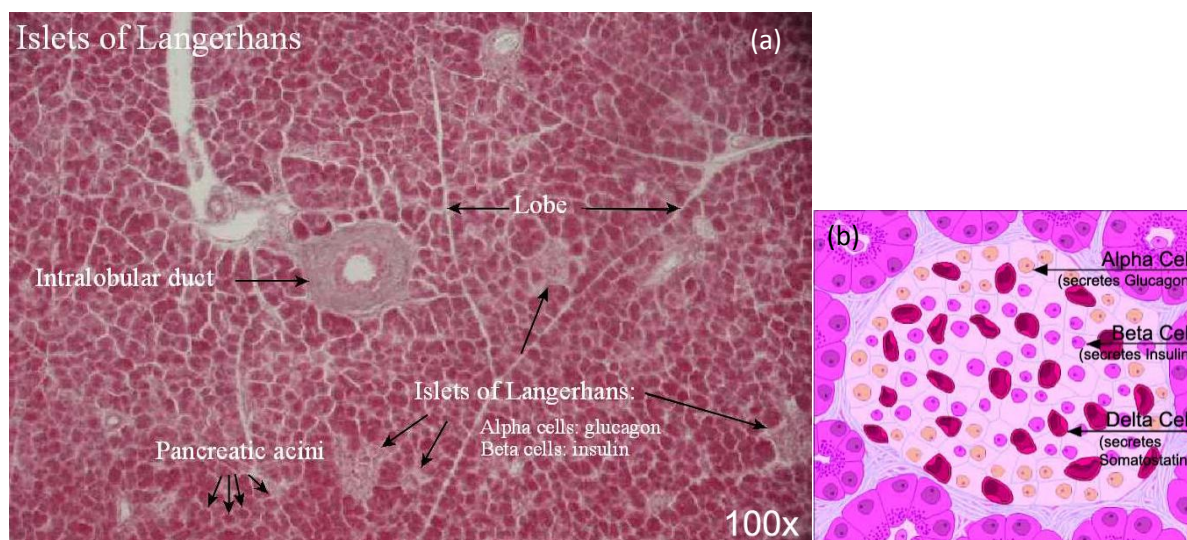


**Figure 1.8** – (a) Photo of a region of the pancreas, where the islets of Langerhans are. (b) Cartoon of the islet of Langerhans, the region of the pancreas that contains its endocrine (i.e., hormone-producing) cells. The beta cells are those secreting insulin.

To have an idea of the importance of diabetes, without attempting to enter the pathology, it is worth to notice that type I diabetes (juvenile form) affects 16 out of 100'000 people each year, while type II diabetes (adult form) affects 1 out of 4 people over 55 years old. The most common treatment for diabetes consists of subcutaneous injections of insulin. Behind all the contraindications, sometimes injection leads insulin into fibrous aggregates, losing its efficacy as a therapy.<sup>3,4</sup> Histological studies show the amazing similarity of insulin fibrous aggregates with amyloid fibrils involved in neurodegenerative diseases as Alzheimer, Parkinson, Bovine Spongiform Encephalopathies (BSE), and Huntington, among other well-known diseases.<sup>5,6</sup> Insulin is capable of produce such aggregates in vitro. This has ascribed a great importance to this hormone, that in the last decade has been object of many studies.<sup>7,8,9</sup>

#### Primary Structure

Insulin is a small polypeptide hormone, its molecular weight (MW) is 5.7 kDa. Its primary structure is known since 1953 by Sanger<sup>10,11</sup> and its crystal structure was first shown by Hodgkin in 1972. Insulin is composed of 2 chains (see Figure 1.9): A (21 residues) and B (30 residues) linked by two disulfide inter-chain bridges between Cys7 and Cys7 and between Cys 20 and Cys19, while a third intra-chain bridge binds Cys residues 6 and 11 of the A chain (Cys = cysteine).<sup>12</sup>

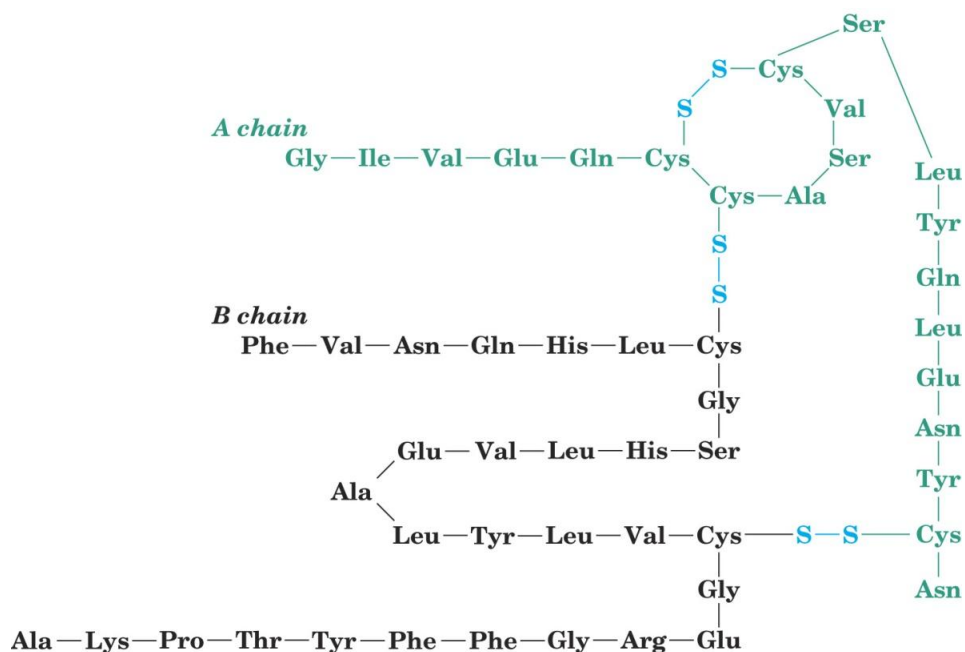


**Figure 1.9 – Primary structure of Bovine Pancreatic Insulin.**

The primary chain is very similar in human, bovine and porcine insulin. In particular porcine and human insulin differs in one amino acid at residue B30, and bovine differs from human insulin for three amino acids sited at A8, A10 and B30 (see Table 1.2). Despite the differences in their primary sequence the upper structure are all the same.

Residue	Bovine	Human	Porcine
A8	Ala	Thr	Thr
A10	Val	Ile	Ile
B30	Ala	Thr	Ala

**Table 1.2 – Differences in the amino acid in Bovine, Human and Porcine Insulin.**

### **Secondary and Tertiary Structure**

The two main chains that form insulin are shown in Figure 1.10: in blue the A chain and in red the B chain. The former contains one  $\alpha$  helix in the N terminal (between the residues A1-A8), and a second one in the C terminal (A12-A19), the rest of the A chain is composed predominantly of  $\beta$  turns. The B chain possess an extended region of  $\beta$  strand in the N terminal (B1-B5), a region of  $\beta$  turns (B6-B9), a  $\alpha$  helix (B9-B19) a second series of  $\beta$  turns (B20-B23) and finally a region of  $\beta$  strand in the C terminal (B24-B28).<sup>13</sup> The N terminal of the B chain is in contact with a non polar region of the A chain (A10 Ile and A13 Leu), while the C terminal of B chain shows the objection of elements of the  $\alpha$  helix of the B chain (B12 Val, B15 Leu, B16 Tyr and B19 Cys) to those of the  $\alpha$  helix of the N terminal of the A chain (A2 Ile and A3 Val).



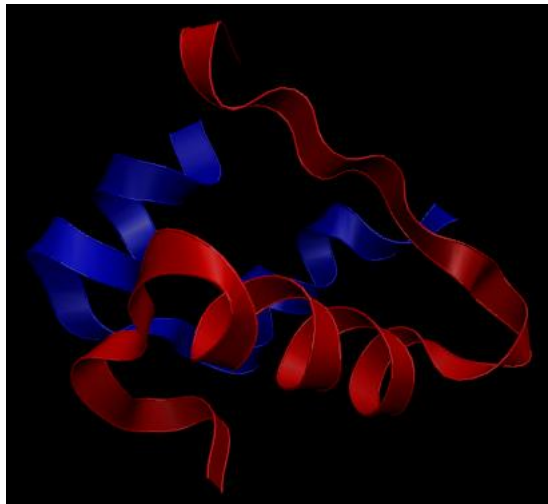


**Figure 1.10** – Secondary structure of Bovine Pancreatic Insulin. A chain is in blue, while B chain is in red.

In the tertiary structure of insulin we can see that its tridimensional structure is further stabilized by disulphide bridges. These are made by thiol groups (-SH) of Cys residues. Insulin has six Cys residues and so three disulphide bridges can be made, as it has been said before two of the disulphide bridges are interchain, while one is intrachain inside the A chain. The molecule is arranged to expose only polar groups, while the non polar ones are buried in the inside.

**Quaternary Structure**

Insulin exists as a monomer only at low concentration ( $< 0.1 \mu\text{M}$ ) or at higher concentration but at acid pH ( $\text{pH} < 3$ ). Otherwise insulin has a strong tendency to aggregate into both dimer and hexamer (see Figure 1.11). The former are due to the occurrence of H-bonds between the residues of the C terminal of B chain, while the latter are formed in presence of Zn ion at pH 4-8 or in absence of the metal at neutral pH and at concentration around 2mM.

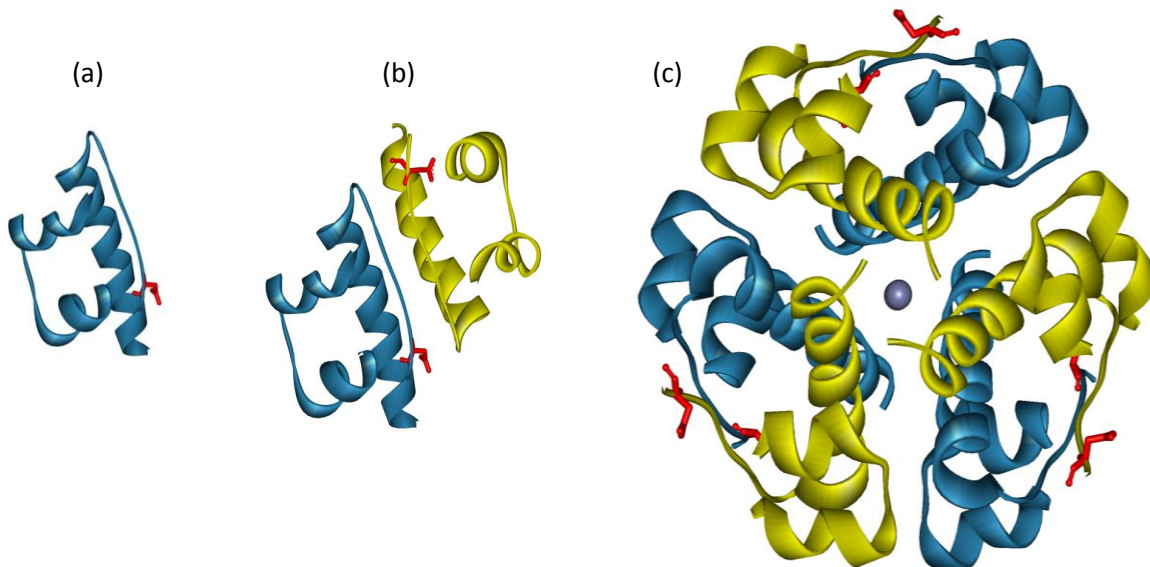


**Figure 1.11** – Quaternary structure of Bovine Pancreatic Insulin. (a) monomer; (b) dimer; (c) hexamer.

The hexamer is almost spherical with around 50 Å of diameter and 35 Å height. Zinc ions are situated inside the polar channel and are coordinated with Histidine (His) residue B10. Hexamers possess a little tendency to move in the bloodstream, while monomers and dimers diffuse quickly in it. The monomers are the active form of insulin. Medical preparations for diabetes show huge percentage of hexamers, diminishing their efficacy.

### 1.1.2 Hen Egg White Lysozyme

Lysozyme is an enzyme found in the secretions (tears) of the lacrimal glands of animals and in nasal mucus, gastric secretions, and egg white. In 1922 Fleming while working in his laboratory accidentally added a few drops of nasal mucus to a bacterial culture. To his surprise something in the mucus killed the bacteria. He realized that this was largely due to the action of a protein within the mucus that caused the bacterial cells to lyse or break apart. Hence, he named the protein lysozyme.<sup>14</sup> Alternative name for lysozyme are 1,4-N-acetylmuramidase, L-7001, N,O-diacetylmuramidase, PR1-Lysozyme, Globulin G1, Globulin G, Lysozyme g, Mucoprotein N-acetylmuramoylhydrolase, Mucoprotein glucohydrolase and Muramidase. In 1965 the structure of lysozyme was solved by X-Ray analysis with 2Å resolution by David Chilton Phillips.<sup>15</sup> The structure was publicly presented at a Royal Institution lecture in 1965.<sup>16</sup> Lysozyme was the second protein structure and the first enzyme structure to be solved via X-ray diffraction methods, and it was also the first enzyme to be fully sequenced that contains all twenty common amino acids.<sup>17</sup> As a result of Phillips' elucidation of the structure of lysozyme, it was also the first enzyme to have a detailed, specific mechanism suggested for its method of catalytic action.<sup>18</sup> For many years Lysozyme was the best object for X-Ray analysis due to many unique properties of this enzyme. First of all it is easy to purify from egg-white (Hen Egg White Lysozyme, HEWL), secondly this protein is very easy to crystallize (see Figure 1.12), which is not the case for most of the other proteins. Finally the structure of HEWL is also the best resolved by the X-ray diffraction technique, indeed it has currently the highest resolution structure in Protein Data Bank (0.94 Å).

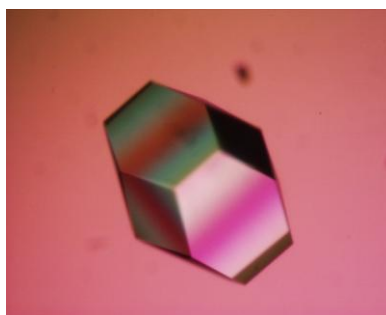


**Figure 1.12** – *Single Protein crystals of HEWL (photographed by Mathias Klode).*

Lysozyme is the most prominent member of the very large class of glycosidases or glycohydrolases, enzymes that catalyze the transfer of a glycosyl group to water.<sup>19</sup> In vivo HEWL is an enzyme that plays an important role in the prevention of bacterial infections. It does this by attacking a specific component of certain bacterial cell walls, peptidoglycan. Peptidoglycan is composed of the repeating amino sugars, N-acetylglucosamine (NAG) and N-acetylmuramic acid (NAM), crosslinked by peptide bridges. Lysozyme acts by hydrolyzing the bond between NAG and NAM, increasing the bacteria's permeability and causing the bacteria to burst.

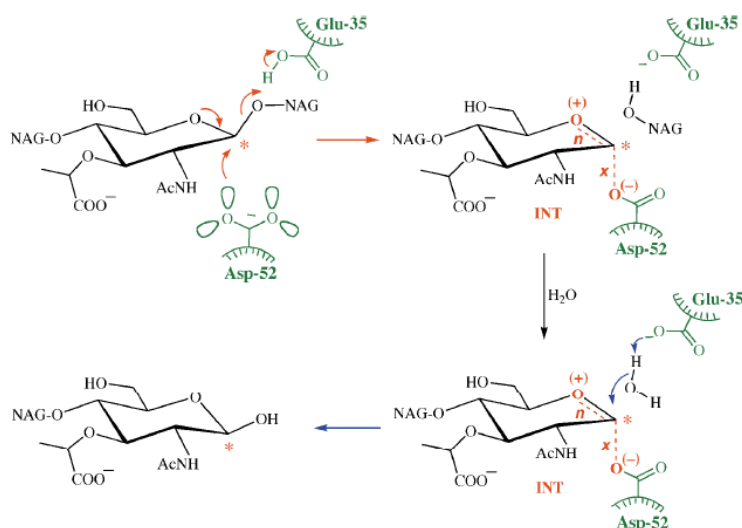


**Figure 1.13** –Scheme of the reaction catalyzed by HEWL. The substrate is bound so that the leaving group oxygen, the 4-OH group of an N-acetylglucosamine (NAG) residue, is protonated as it leaves by the COOH group of Glu 35. Groups on the enzyme are colored green, electron movements and the key developing bonds and charges in red. Figure from ref. 19.

In physiological conditions, HEWL is folded into a compact, globular structure with a long cleft in the protein surface. This cleft is the active site involved in binding to the bacterial carbohydrate chain and subsequently cleaving it.

### Primary Structure

Molecular weight of HEWL is 14.8 kDa. The primary structure of HEWL is a single polypeptide containing 129 amino acids (see Figure 1.14).

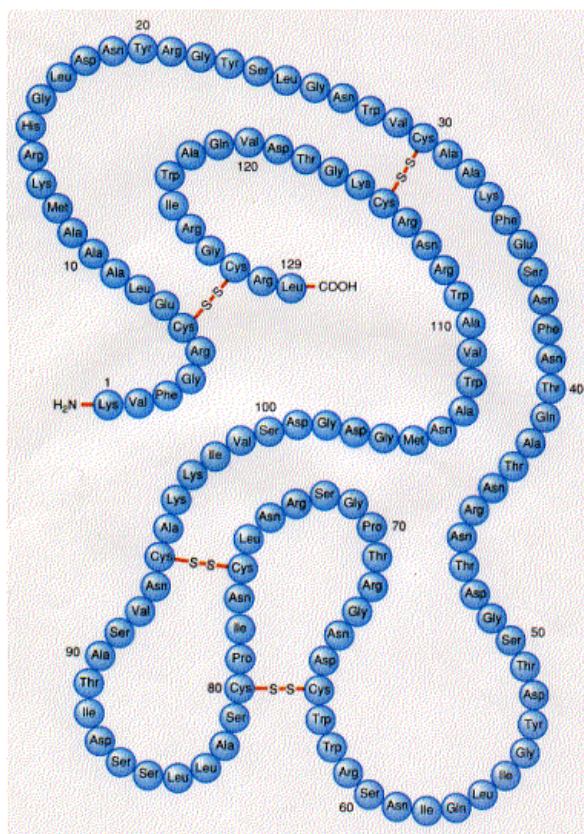


**Figure 1.14** – Primary structure of HEWL.



There are four pairs of Cysteine that form disulfide bridges between positions: 6 and 127, 30 and 115, 64 and 80, 76 and 94 (counting from the N terminal of the protein).

### **Secondary and Tertiary Structure**

Lysozyme structure consists of two domains, a helical domain known as the  $\alpha$ -domain, and a sheet/coil domain known as the  $\beta$ -domain. The  $\alpha$ -domain is constituted by three  $\alpha$  helices: helix A (residues 5-14), helix B (residues 25-36), helix C (residues 90-100), one  $\alpha$  helix that is close to a pi helix: helix D (residues 109-115), and by a helix that shows an intermediate structure between an  $\alpha$  helix and a  $3_{10}$  helix (residues 120-124).<sup>20</sup>  $\beta$ -domain is composed of five regions of beta sheet and a large amount of random coil and beta turns, and it also possess a small helix intermediate between an  $\alpha$  and a  $3_{10}$  helix (residues 80-84).<sup>21</sup> The interface between the two domains forms a cleft in which the substrate binds. In Figure 1.15 it is impossible to identify the cleft because of the openness of the structure.

Lysozyme is a small protein which folds in a highly cooperative manner.<sup>22</sup> There is little evidence for the independent unfolding and refolding of each domain<sup>23,24</sup> while there is good evidence that the C-domain refolds first and then stabilizes the folding of the N-terminal domain.<sup>25,26</sup>

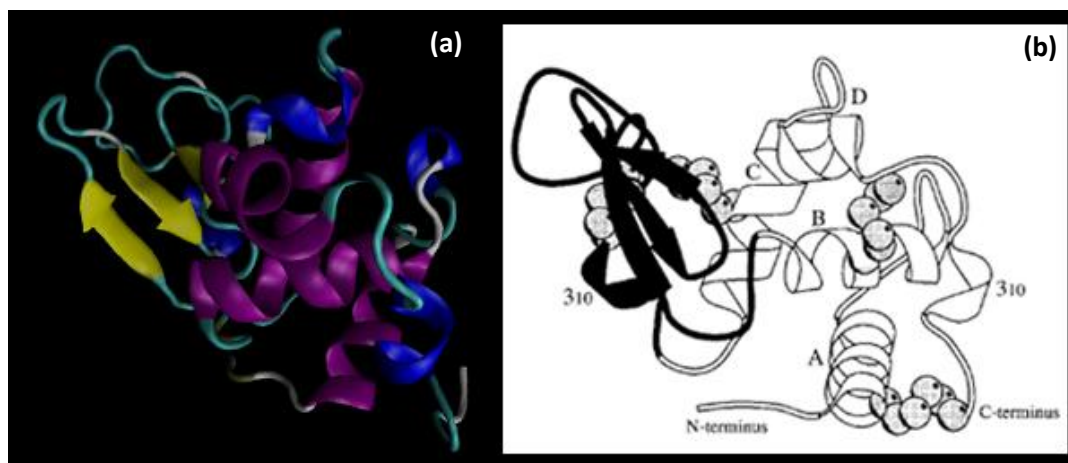


**Figure 1.15** – Secondary structure of HEWL. (a) Helix are in violet and blue, loop in light blue and beta sheet in yellow. (b) Schematic diagram showing the crystal structure of HEWL. The  $\alpha$ -domain (residues 1 to 35; 85 to 129) is shown in white and the  $\beta$ -domain (residues 36 to 84) in black. The helices and N and C termini of the protein are labeled. The positions of disulphide bridges are also indicated. The Figure is taken from ref. 24.

As in the insulin molecule, the tertiary structure of lysozyme is further stabilized by four disulfide bridges between the Cysteine residues (as shown in Figure 1.15b).

## 1.2 Protein Folding/Unfolding

One of the great unsolved problems of science is the prediction of the three dimensional structure of a protein from its amino acid sequence: the “folding problem”. Its understanding would lead to immeasurable benefits: engineering proteins to have a specific shape and function would go a long way toward controlling cancer, viral infections, and aging effects. Several ailments are already related to the misfolding of proteins, where a particular protein simply does not fold correctly so that metabolic pathways or disease resistance methods are halted.

When a protein is in the folded state it is in its functional state and its conformation is called the native state of the protein (**N**). When a protein is denatured (**D**), does not works properly as it is intended. An everyday example of denaturation is the protein lysozyme contained in chicken eggs. As the egg is cooked, the heat destroys the weaker bonds contributing to the three-dimensional structure of the protein, but does not disrupt the strong covalent bonds of the primary structure. This is what gives cooked eggs its texture and white foamy appearance. Most of the time when a protein is denatured, it cannot fold back to its original state: there is no way to un-cook an egg.

The pathway a protein takes to its native state is a hotly debated subject, with several plausible explanations available. The most important pathways that were hypothesized in literature<sup>27</sup> are reported in Figure 1.16. Since it is not the place to deeply discussed the folding problem, only a brief explanation of these folding pathways is reported.<sup>28</sup>

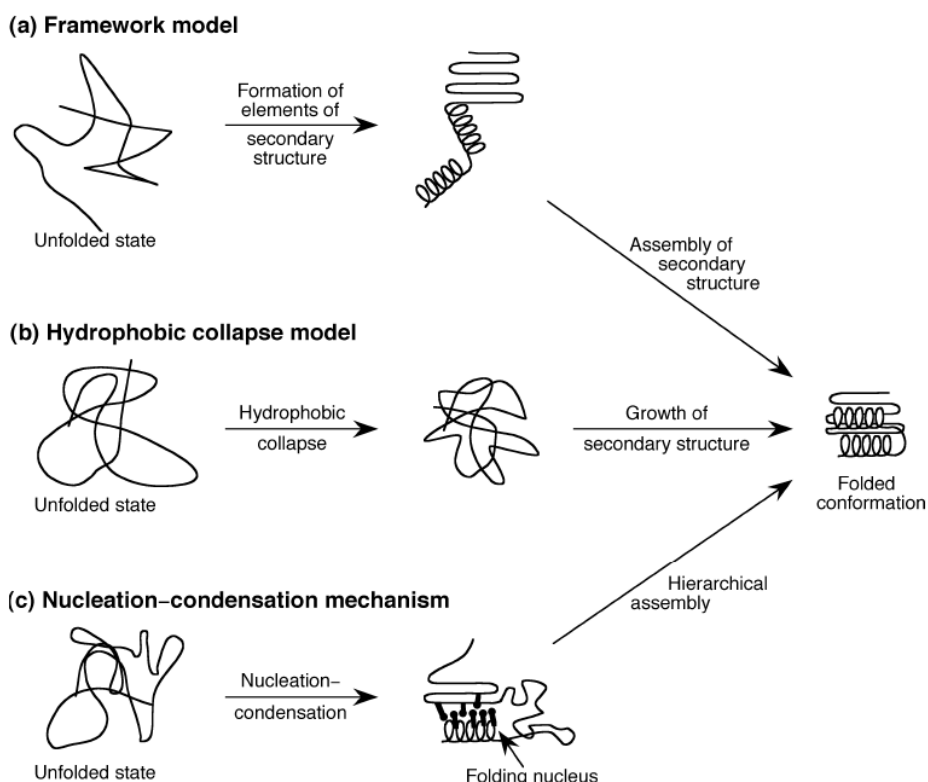


**Figure 1.16** – Models for protein folding. See text for details. Figure is from ref. 27.

In the framework model<sup>29,30,31</sup> (a) the protein folding is thought to start with the formation of elements of secondary structure. These elements form independently of tertiary structure, or at least before tertiary structure is locked in place. The elements then assemble into the tightly packed native tertiary structure either by diffusion and collision<sup>32</sup> or by propagation of structure in a stepwise manner.<sup>33</sup> In the hydrophobic collapse model (b) for folding<sup>34,35</sup> the initial event of the folding reaction is thought to be a relatively uniform collapse of the protein molecule, mainly driven

by the hydrophobic effect,<sup>36</sup> i.e. the tendency of non-polar groups dissolved in water to cluster together. Stable secondary structure elements can only form in the resulting collapsed state. In the nucleation-condensation mechanism<sup>37,38,39</sup> (c) the early formation of a folding nucleus catalyzes further folding. The nucleus is diffuse, but comprises secondary structure interactions and approximately correct tertiary structure interactions.

The latter mechanism is consistent with the funnel model<sup>40</sup> (see Figure 1.17) which focuses on the rapid decrease of the conformational scattering in the course of the reaction.

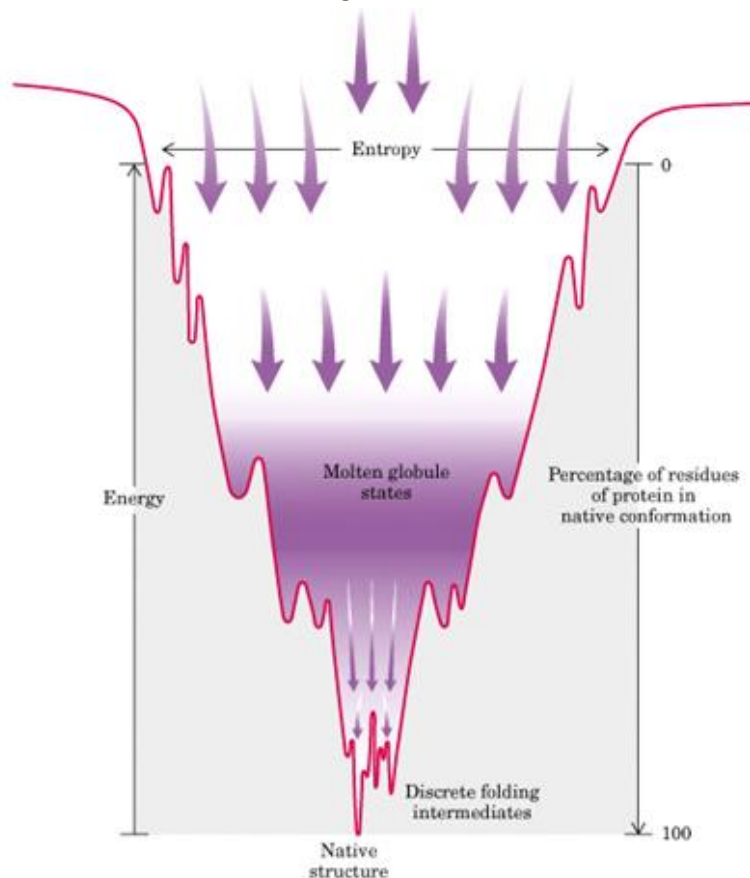


**Figure 1.17** – Folding funnel, two dimensional scheme.

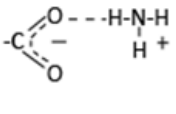
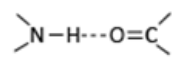
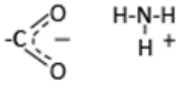
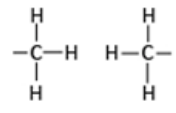
The folding funnel diagram, introduced by Wolynes, Onuchic and Thirumalai (see ref. 40), is intended to provide a pictorial representation of how the Levinthal paradox,<sup>41</sup> which had dominated discussion of protein folding for many years, is resolved. It is possible to understand the Levinthal paradox through the golf course analogy: if a golfer was blindfolded, stood at the edge of a very large golf course, and was told to hit the ball in a random direction, then the chances of sinking the ball in a single hole are infinitesimally small. This is analogous to a protein existing in a large number of non-native states of equal energy and having just one native state of much lower energy. There is no driving force to push the protein in the direction of folding; this is the Levinthal paradox. Suppose, instead, that the golf course sloped down from all directions to the hole. Then the gravity would funnel the ball to the hole, and the golfer would always score a hole-in-one.<sup>42</sup>

The funnel is a conceptual mechanism for understanding the self-organization of a protein that is based on the physics concept of minimizing free energy. At the top of the funnel, the unfolded protein (**U**) exists in a large number of random states that have relatively high enthalpy and high entropy. The high entropy corresponds to a large number of possible conformational states. The high free energy means that the molecule is unstable, and flops easily between the different conformational states. As the protein starts to fold, the free energy drops and the number of

available conformational states (denoted by the width of the funnel) decreases. There are local minima along the way that can trap the protein in a metastable state for some time, slowing its progress towards the free energy minimum. At the bottom of the funnel, the free energy is at a minimum. This is its native state, and is the ground state of the system. It is possible that the native state is not unique, it can be that there are several states with approximately equal free energy at the bottom of the funnel. The funnel is thus a progressive collection of geometrically similar collapsed structures, one of which is more thermodynamically favorable than the rest.

The interactions affecting protein folding and stability are listed in Table 1.3. The two most important interactions are the Van der Waals forces and the hydrogen bonds and are briefly discussed in the following.

- **Van der Waals** interactions occur whenever the fluctuating electronic clouds on an atom or group of bonded atoms induce an opposite fluctuating dipole on a non-bonded neighbor, resulting in a very weak electrostatic interaction. The effect is greater with those groups that are most polarizable; in proteins these are usually the methyl groups and methylene group of hydrophobic side chains such as leucine and valine. Van der Waals interactions diminish rapidly as the interacting species get farther apart, so only atoms that are already close together (about 5 Å apart or less) have a chance to participate in such interactions. A given Van der Waals interaction is extremely weak, but in proteins they sum up to a substantial energetic contribution.
- **Hydrogen bonds** are formed when a hydrogen atom has a significant partial positive charge by virtue of being covalently bound to a more electronegative atom, such as oxygen, and is attracted to a neighboring atom that have significant partial negative charge. This electrostatic interaction draws the two non-hydrogen atoms closer together than the sum of their radii would normally allow. So, if two polar non-hydrogen atoms in a protein, one of which has a hydrogen attached, are found to be less than 3.5 Å apart, a hydrogen bond is assumed to exist between them. If the donor, the acceptor or both are fully charged, the hydrogen bond is stronger than when both are uncharged. When both the donor and acceptor are fully charged, the bonding energy is significantly higher and the hydrogen bonded ions pair is called salt bridge.

Interaction	Example	Distance dependence	Typical distance	Free Energy (bond dissociation enthalpies for the covalent bonds)
Covalent bond	$-C_{\alpha}-C-$	-	1.5 Å	356 kJ/mol (610 kJ/mol for a C=C bond)
Disulfide bond	$-Cys-S-S-Cys-$	-	2.2 Å	167 kJ/mol
Salt bridge		Donor (here H) and acceptor (here O) atoms < 3.5 Å.	2.8 Å	12.5-17 kJ/mol; may be as high as 30 kJ/mol for fully or partial buried salt bridges, less if the salt bridge is external
Hydrogen bond		Donor (here H) and acceptor (here O) atoms < 3.5 Å.	3.0 Å	2-6 kJ/mol in water; 12.5-21 kJ/mol if either donor or acceptor is charged
Long-range electrostatic interaction		Depends on dielectric constant of medium. Screened by water. $1/r$ dependence.	Variable	Depends on distance and environment. Can be very strong in non polar region but very weak in water
Van der Waals interaction		Short range. Falls off rapidly beyond 4Å separation. $1/r^6$ dependence.	3.5 Å	4 kJ/mol (4-17 in protein interior) depending on the size of the group (for comparison, the average thermal energy of molecules at room temperature is 2.5 kJ/mol)

**Table 1.3** –Table of the typical chemical interactions stabilizing polypeptides. Values for the interatomic distances and free energies are approximate average values as any specific number is highly dependent on the context in which the interaction is found.

A protein has very specific pH, temperature, and pressure ranges where it is folded.<sup>43</sup> When these values are varied slightly, the weaker bonds in the higher levels of structure are the first to break. In this way, the process by which a protein reaches its native state can be studied by watching the way bonds break. The pressure-temperature phase diagram of biomolecules is reported in Figure 1.18.

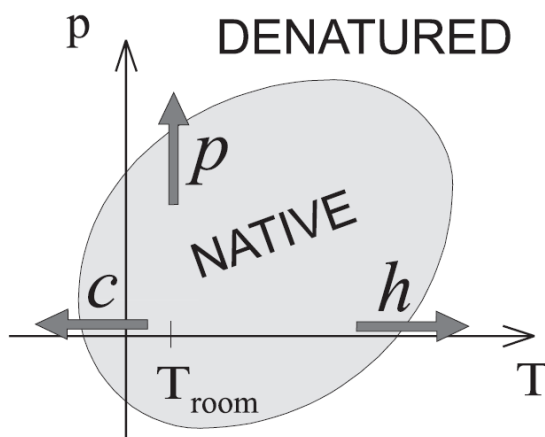


**Figure 1.18** – Schematic representation of the elliptical phase diagram of proteins. The arrows marked by the letters *p*, *h*, *c* show the specific denaturation ways known as pressure, heat and cold denaturation. Figure from ref. 43.

On discussing about the previous Figure it is important to recall that the picture which emerges more consistently from experimental facts<sup>44,45</sup> assumes a stable native state of the protein in a closed range of the *p*-*T* plane. Crossing the boundary of that region, the native conformation loses

its stability, and the protein unfolds. The consistent thermodynamic description of the phase boundary of protein unfolding was developed by Hawley.<sup>46</sup> He started from the assumption that there are only two distinct states of the protein (**N** and **D**) and that the transition between **N** and **D** is a two-state process. The Gibbs free energy difference between these states is defined as:

$$(1.1) \quad \Delta G = G_D - G_N$$

$$(1.2) \quad d\Delta G = -\Delta S dT + \Delta V dp$$

where G is the Gibbs free energy, S is the entropy, V is the volume, T is the absolute temperature and p is the pressure. Upon integration of this equation from an arbitrarily chosen reference point  $T_0, p_0$  to T, p one obtains:

$$(1.3) \quad \Delta G = \frac{\Delta\beta}{2}(p - p_0)^2 + \Delta\alpha(p - p_0)(T - T_0) - \Delta C_p \left[ T \left( \ln \frac{T}{T_0} - 1 \right) + T_0 \right] + \Delta V_0(p - p_0) - \Delta S_0(T - T_0) + \Delta G_0$$

where  $\Delta$  always means the change of the corresponding parameter during denaturation (i.e. the value in the denatured state minus that in the native state).  $\alpha$  is the thermal expansion factor  $\alpha = (\partial V / \partial T)_p = -(\partial S / \partial p)_T$ ,  $\beta$  is the compressibility factor:  $\beta = (\partial V / \partial p)_T$ , and  $C_p$  is the heat capacity  $C_p = T(\partial S / \partial T)_p$ .

In the vicinity of the reference point one can use the following second order approximation:

$$(1.4) \quad T \left( \ln \frac{T}{T_0} - 1 \right) + T_0 = \frac{(T - T_0)^2}{2T_0}$$

Substituting eq. 1.4 into eq. 1.3 one gets:

$$(1.5) \quad \Delta G = \frac{\Delta\beta}{2}(p - p_0)^2 + \Delta\alpha(p - p_0)(T - T_0) - \Delta C_p \frac{(T - T_0)^2}{2T_0} + \Delta V_0(p - p_0) - \Delta S_0(T - T_0) + \Delta G_0$$

The transition line, where the protein denatures (or refolds depending on the direction of the crossing), is defined by  $\Delta G=0$ . Substituting this into eq. 1.5 one gets the equation of a second order curve in the T-p plane. Mathematically this is a general equation for a conic section, which can be either a hyperbola or an ellipse, but actually it was found to be always elliptic for proteins. The mathematical constraint ensuring the elliptic shape is:

$$(1.6) \quad \Delta\alpha^2 > \Delta C_p \frac{\Delta\beta}{T_0}$$

which is satisfied by the different signs of  $\Delta C_p$  and  $\Delta\beta$ .<sup>46</sup>

The region where the protein is more stable in the native phase ( $\Delta G > 0$ ) is shown in grey in Figure 1.18. The grey ellipse shows the conditions for the native state. Curves with similar elliptic shape, but different actual values of thermodynamic parameters have been determined for several proteins.<sup>47,48,49,50</sup>

The actual shape, size, and orientation of the elliptic boundary are defined by six thermodynamic parameters:  $\Delta\beta$ ,  $\Delta\alpha$ ,  $\Delta C_p$ ,  $\Delta V_0$ ,  $\Delta S_0$  and  $\Delta G_0$ . The lines at which T and p reach their maximum value (corresponding to  $\Delta V=0$  and  $\Delta S=0$  respectively) for a general case of the ellipse are shown in Figure 1.19. Below these lines the entropy or volume changes associated to the unfolding are positive. Below the  $\Delta S = 0$  line the order decreases during denaturation. Above the  $\Delta V=0$  line, the contribution of decreasing volume to the  $\Delta G$  promotes unfolding.

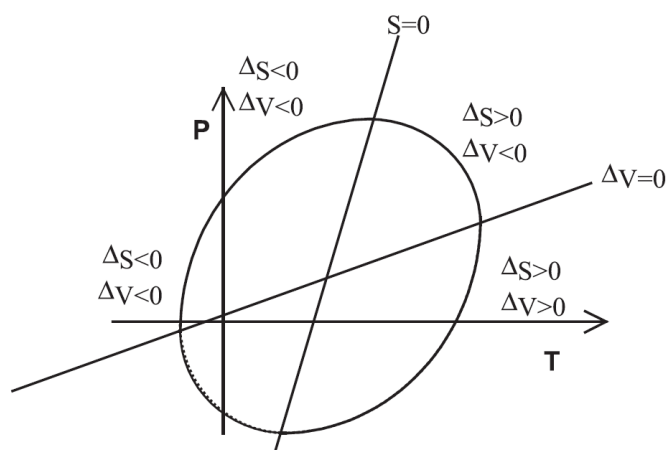


**Figure 1.19** – Relative position of the  $\Delta S = 0$  and  $\Delta V = 0$  lines compared to the ellipse. From ref. 43.

Finally observing the  $\Delta V = 0$  and  $\Delta S = 0$  lines in Figure 1.19, one can see that the temperature denaturation is entropy driven, while the other two are mainly volume change driven. Therefore both the pressure and cold denatured phases are expected to be more compact than the heat unfolded one.

The protein denaturation mechanism mostly investigated in this thesis is the pressure denaturation and it will be discussed in more detail in the following paragraph.

### 1.2.1 Pressure Mechanism of Denaturation

In general, protein conformational states differ in their degree of organization and thus solvation, a feature that can be exploited by the use of high hydrostatic pressure. In fact, the effect of pressure on protein structure is to favor states that exhibit a smaller specific volume, because the pressure derivative of the Gibbs free energy change between two states is equal to their difference in volume (from Eq. 1.2):

$$(1.7) \quad \frac{d\Delta G}{dp} = \Delta V$$

Therefore, the application of pressure can lead to a population of conformers of proteins, including low-lying excited states and partially or completely unfolded conformations, as all these states exhibit a lower degree of order, and hence are more solvated, than the native state.<sup>51</sup>

The volume of a protein comprises contributions from three terms:<sup>52</sup>

$$(1.8) \quad V_{protein} = V_{atoms} + V_{voids} + \Delta V_{hydration}$$

where  $V_{atoms}$  is the sum of the volumes of the constituent atoms of the protein,  $V_{voids}$  is the volume of void space within the protein, and  $\Delta V_{hydration}$  is a system volume change that results from protein-solvent interactions.  $V_{atoms}$  is a fixed quantity for a given protein. Thus, determination of  $\Delta V$  for an equilibrium transition, provides information on how the protein structure and solvent interactions change during that transition.<sup>53</sup> The specificity and stability of each individual structure reside in the packing characteristics of each protein.<sup>51,54</sup>

The decrease in specific volume of proteins observed upon partial or complete unfolding of the native structure is caused by a combination of several effects: disruption of salt bridges, followed by hydration and a corresponding decrease in volume because of electrostriction;<sup>55</sup> hydration of newly exposed nonpolar and polar residues; and the loss of free volume arising from packing defects in

the completely folded structure. The magnitude of the volume decrease upon unfolding is small, ~0.5–1.0% of the total specific volume of the protein, and the volume changes for the population of intermediate states tend to be even smaller. Nonetheless, given the marginal stability of most proteins, volume changes of this magnitude usually lead to complete unfolding below 800 Mpa (1.0 atmosphere = 1.0 bar = 0.1 Mpa).<sup>56</sup>

The pressure-induced elimination of internal cavities in proteins is thought to be a significant contribution to the volume change associated with pressure denaturation.<sup>57,58,59</sup> Moreover, in recent years, studies have implicated the penetration of water into the hydrophobic core as the mechanism of pressure denaturation, a mechanism that is distinct from that of thermal denaturation.<sup>60</sup>

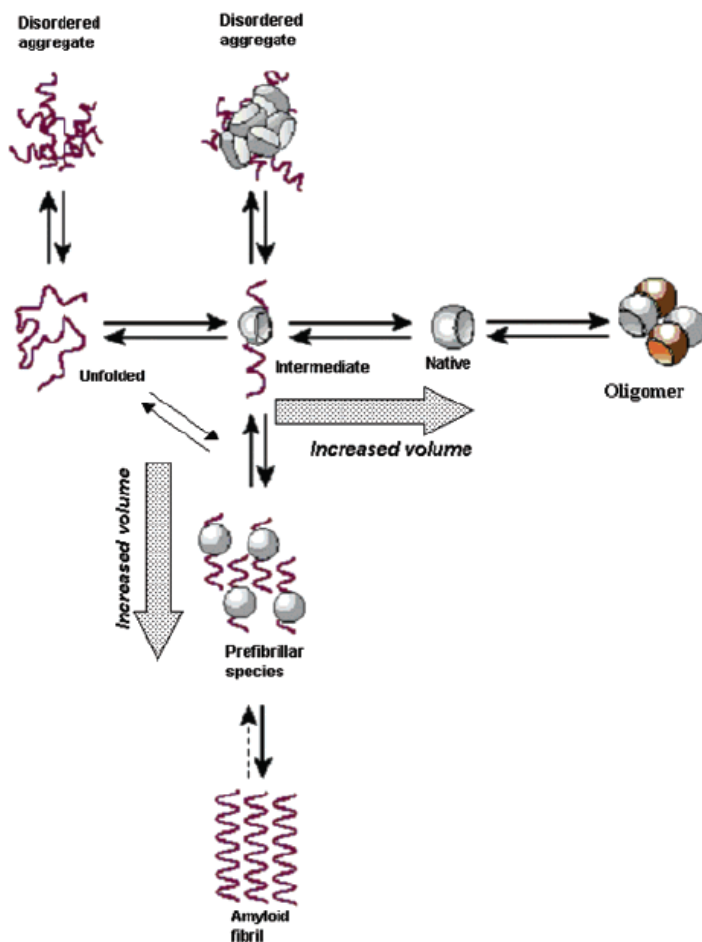


**Figure 1.20** – Protein folding and misfolding pathways. The diagram shows how amyloid fibrils and other aggregates can be formed from totally or partially unfolded intermediates. As pointed out by Dobson,<sup>61</sup> other assemblies such as oligomers, containing natively folded molecules, are usually the most favorable species. As indicated by the large arrows, the native states and aggregates share the property of having water excluded cavities, having larger volumes, which makes their structures highly susceptible to pressure.

According to Figure 1.20, both folded and aggregated states would exhibit larger specific volumes because of the formation of water-excluded cavities. Therefore, pressure would dissociate aggregates very easily. According to this, protofibrils may be more easily dissociated by pressure than the mature fibrils. On the other hand, pressure may promote the formation of intermediates that are prone to aggregation.



The interest for protein aggregates is due to the the study of proteins that aggregate in vivo in amyloidic disease states,<sup>62,63,64</sup> in which several soluble cellular proteins undergo fibrillogenesis under special conditions, and the accumulation of fibrils in specific organs and tissues can ultimately lead to death. Understanding the mechanism that leads to the formation of these aggregates could be important in view of a larger effort towards the understanding and, subsequently, towards a possible cure of neurodegenerative pathologies.

### 1.3 Protein Fibrillation

Abnormalities in protein folding and assembly may be important mechanism of diseases (conformational diseases).

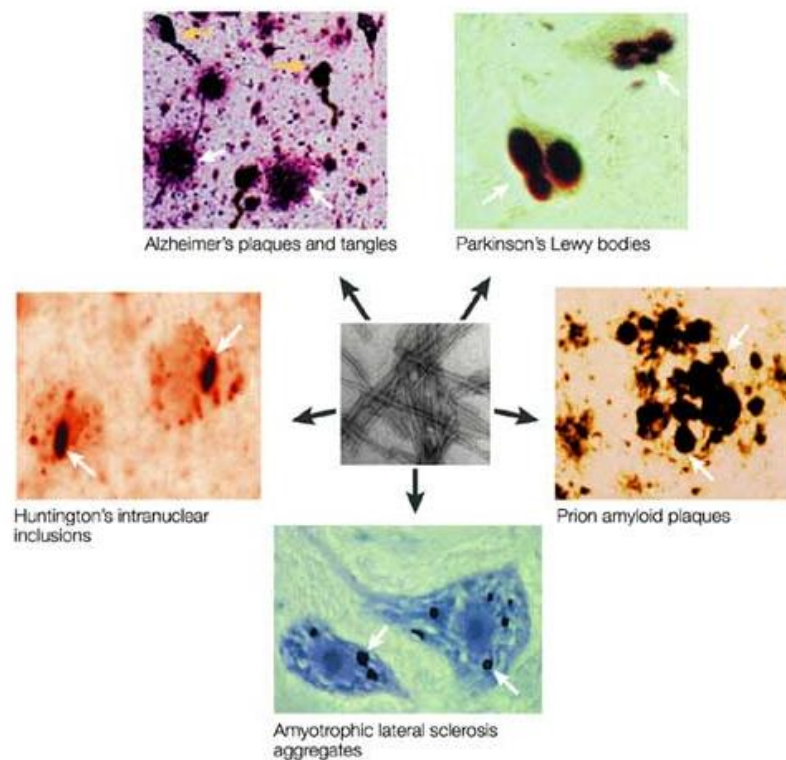


**Figure 1.21** – Extracellular amyloid plaques (white arrows) are the pathological signature of Alzheimer's disease. The structure of these deposits seems to be similar and composed mainly of a network of fibrillar polymers (centre). Image from ref. 64.

Over 25 diseases, often fatal, have a common hallmark in the aggregation and the extracellular deposition of normally soluble proteins in certain tissues in the form of insoluble aggregates known as amyloid fibrils or amyloid plaques.<sup>65</sup> These includes neurodegenerative diseases, a group of late-onset progressive brain disorders with different symptoms such as dementia and disordered movements. Examples of neurodegenerative disorders characterized neuropathologically by the presence of intracellular and/or extracellular protein deposits are listed in Table 1.4.<sup>66</sup>

Amyloid was discovered in 1854 by German physician R. Virchow, who named it in the belief that the iodine-staining component was starch-like and he gave it the name of amyloid, derived from the Latin *amylum* and the Greek *amylon*.<sup>67</sup>

<b>Disease</b>	<b>Aggregating polypeptide</b>	<b>Structure of polypeptide</b>
<b>Neurodegenerative diseases</b>		
Alzheimer's disease	Amyloid $\beta$ peptide	Natively unfolded
Spongiform encephalopathies	Prion protein or fragments	Natively unfolded (residues 1–120) and $\alpha$ -helical (residues 121–230)
Parkinson's disease	$\alpha$ -Synuclein	Natively unfolded
Dementia with Lewy bodies	$\alpha$ -Synuclein	Natively unfolded
Amyotrophic lateral sclerosis	Superoxide dismutase-1	All- $\beta$ , Ig like
Huntington's disease	Huntingtin with polyQ expansion	Largely natively unfolded
Spinocerebellar ataxia 17	TATA box-binding protein with polyQ expansion	$\alpha$ + $\beta$ , TBP like (residues 159–339); unknown (residues 1–158)
<b>Nonneuropathic systemic amyloidoses</b>		
AL amyloidosis	Immunoglobulin light chains or fragments	All- $\beta$ , Ig like
AA amyloidosis	Fragments of serum amyloid A protein	All- $\alpha$ , unknown fold
Senile systemic amyloidosis	Wild-type transthyretin	All- $\beta$ , prealbumin like
<b>Disease</b>	<b>Aggregating polypeptide</b>	<b>Structure of polypeptide</b>
Familial amyloidotic polyneuropathy	Mutants of transthyretin	All- $\beta$ , prealbumin like
Hemodialysis-related amyloidosis	$\beta$ 2-microglobulin	All- $\beta$ , Ig like
Apo amyloidosis	N-terminal fragments of apolipoproteins	Natively unfolded
Lysozyme amyloidosis	Mutants of lysozyme	$\alpha$ + $\beta$ , lysozyme fold
Fibrinogen amyloidosis	Variants of fibrinogen $\alpha$ -chain	Unknown
<b>Nonneuropathic localized diseases</b>		
Type II diabetes	Amylin, also called islet amyloid polypeptide (IAPP)	Natively unfolded
Injection-localized amyloidosis	Insulin	All- $\alpha$
Corneal amyloidosis associated with trichiasis	Lactoferrin	$\alpha$ + $\beta$
Cataract	$\gamma$ -Crystallins	All- $\beta$

**Table 1.4** – Human amyloid diseases and associated proteins (from ref. 66).

The amyloids are composed of fibrillar proteins with a cross- $\beta$  structure as revealed by X-ray diffraction<sup>68,69,70,71</sup> and electron<sup>72</sup> and atomic force microscopy.<sup>73</sup> These experimental techniques have revealed that amyloids exhibit distinct fibrillar morphological properties as shown in Figure 1.22 and 1.23. The fibrils range in width are from 60 to 130 Å (average 75 to 100 Å), in length are up to microns and are composed typically of 2–6 protofilaments.

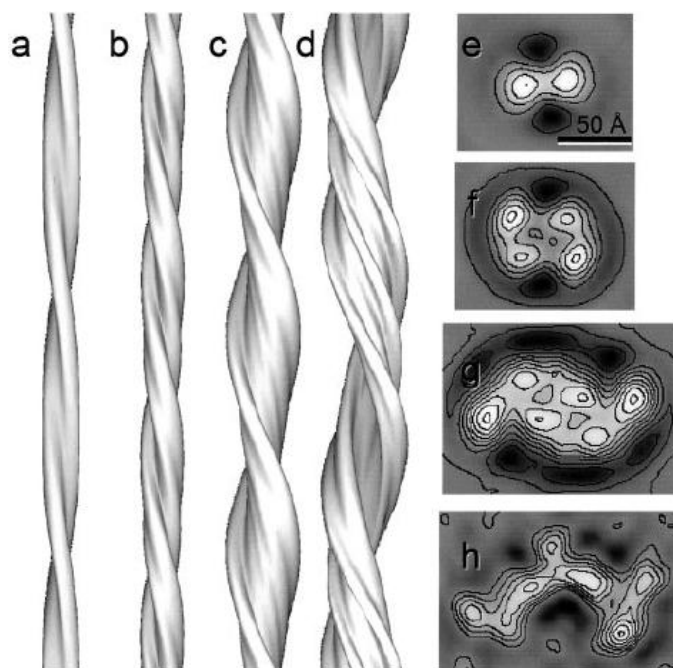


**Figure 1.22** – Surface representation of 3D maps and contoured density cross sections of four insulin fibril structures (from ref. 72): (a and e) structure of the fibril with a pair of protofilaments twisting around each other; (b and f) the four-protofilament fibril; (c and g) the six-protofilament fibril; (d and h) the twisted ribbon. The protofilaments are well resolved in the first three structures, but are less clear in the twisted ribbon. (e–h, bar = 50 Å.)

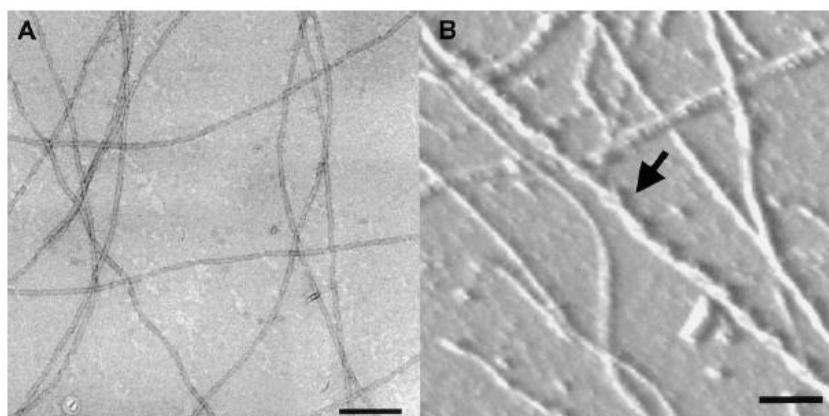


**Figure 1.23** – The structure of fibrils assembled from human lysozyme from ref. 72. Transmission electron microscopy (A); Atomic force microscopy (B).

Although different amyloid protofilaments appear similar in size, the protein sequence can influence the sheet packing into protofilaments, for example because of the constraints of preexisting disulfide bonds. Finally, a common protofilament unit may assemble into fibrils (see Figure 1.24) with extremely variable packing, but particular protofilament interactions can be approximately maintained along the length of a given fibril. This finding suggests that the protofilaments adopt a series of inter-chain interactions during their assembly process that can be propagated during fibrillar growth.

During the last decade, a number of proteins not associated with diseases have been found to convert into amyloid fibrils *in vitro*, showing the physicochemical characteristics of those related to diseases (e.g. myoglobin<sup>74</sup>,  $\alpha$  lactalbumin<sup>75</sup>, and hen egg white lysozyme<sup>76</sup>). The similarity in dimensions and morphology, as well as in tinctorial properties between *ex-vivo* and *in vitro* protein

fibrils has been observed and, based on the accumulated data, it has been suggested that the ability to form amyloid fibrils is an inherent property of polypeptide chains and most if not all polypeptides have ability to form amyloids, though their propensity to amyloid self-assembly can be different.<sup>77</sup>

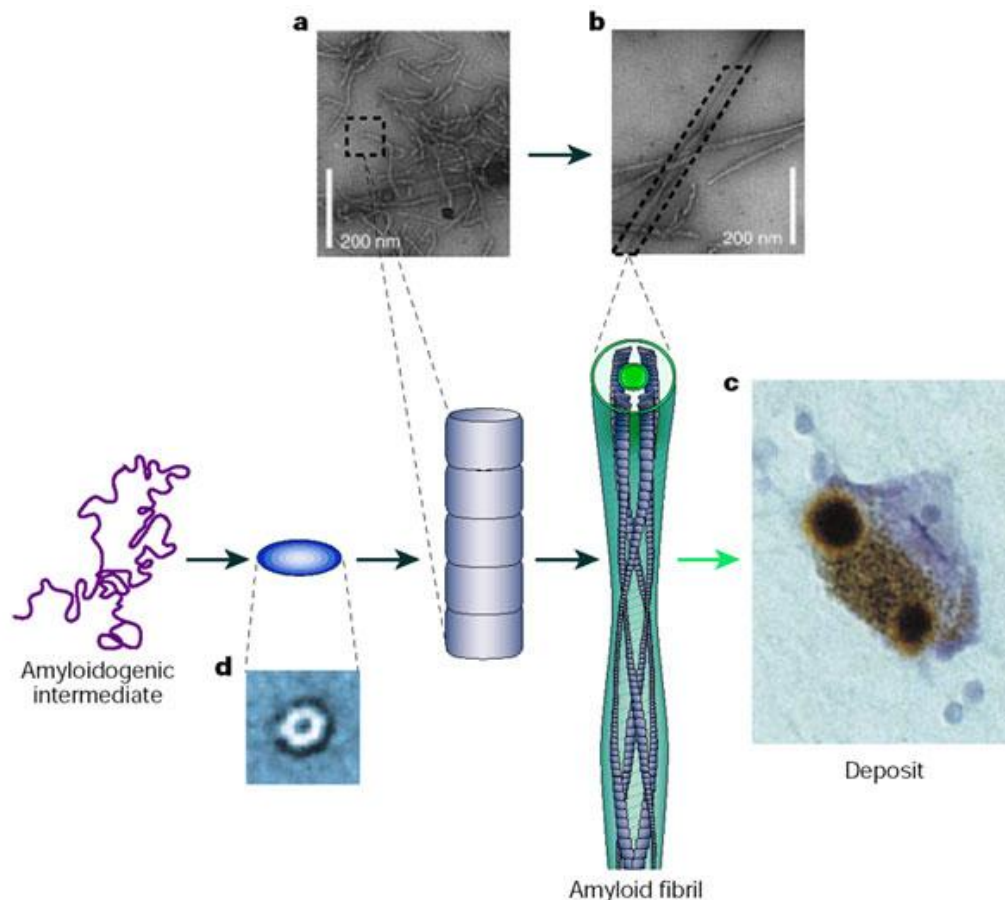


**Figure 1.24** – Unfolded or partially unfolded proteins associate with each other to form small, soluble aggregates that undergo further assembly into protofibrils or protofilaments (a) and then mature fibrils (b), as seen in these electron microscope images. The fibrils often accumulate in plaques or other structures, such as the Lewy bodies associated with Parkinson's disease (c; electron microscope image on the right). Some of the early aggregates seem to be amorphous or micellar in nature, although others form ring-shaped species with diameters of approximately 10 nanometers (d; electron microscope image). From ref. 61.

The typical sequence of steps for protein fibrillation is presented in Figure 1.25.<sup>78</sup> Partially unfolded protein initially undergoes acid hydrolysis, yielding peptides, which then aggregate to form amyloid fibrils held together by inter-molecular  $\beta$  sheets. The constituting peptides of these fibrils can differ from the building blocks of the original protein.<sup>79</sup> The temporal evolution of this rearrangement can be attributed to the modified solvent conditions and consequently the changed total free energy of the system: the system is forced to evolve structurally towards equilibrium to minimize the total free energy.

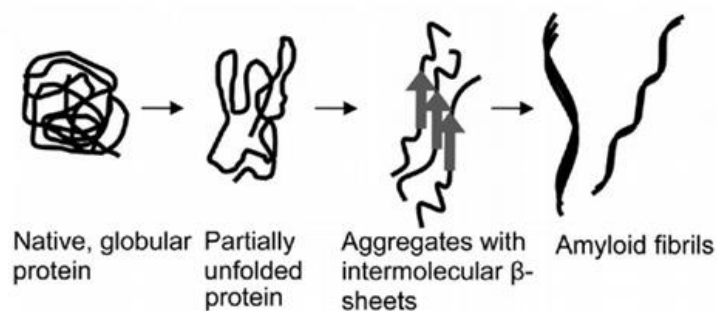


**Figure 1.25** – Schematic representation of the formation of amyloid fibrils from a globular protein during heat denaturation and hydrolysis under acidic conditions. Figure modified from ref. 78.

The partial unfolding of proteins seems to facilitate specific inter-molecular interactions, such as hydrophobic and electrostatic interactions, which are required to drive the polymerization of protein molecules into amyloid fibrils. It has been shown for many proteins that the propensity to fibrillate is determined by, and is related inversely to, the stability of the protein.<sup>80,81,82,83</sup> Consequently, factors destabilizing the native fold of a protein tend to increase the propensity of the protein to fibrillate.

Nucleation-dependent fibrillation is the prevalent model for assessing the self-assembly process, wherein the reaction appears to commence from oligomeric nuclei, which grow by the sequential addition of monomeric intermediates.<sup>84,85,86</sup> In many proteins spherical oligomers and/or protofibrils are seen to form rapidly, and, in many cases, mature fibrils appear upon extended incubation.<sup>87,88,89</sup>

In the following paragraphs the mechanism of insulin and lysozyme (paragraphs 1.3.1) will be discussed in more detail.

### **1.3.1 Insulin and Lysozyme Mechanism of Fibrillation**

Under certain conditions (low pH, high temperature, in presence of strong denaturants) insulin<sup>90,91,92</sup> and lysozyme<sup>93,94,95</sup> are known to convert its native structure into fibrils that remind very close those found in neurodegenerative diseases.<sup>96</sup>

The two proteins seem to have the same fibrillation mechanism based onto the nucleation dependent mechanism proposed by Dobson et al. in 1997<sup>97</sup> and previously introduced.

The scheme for step-by-step insulin fibrillation proposed by Q. Wua and M. Weiss in ref. 13 is shown in Figure 1.26, while the scheme for step-by-step Lysozyme fibrillation proposed by Shashilov et al.<sup>98</sup> is shown in Figure 1.27.

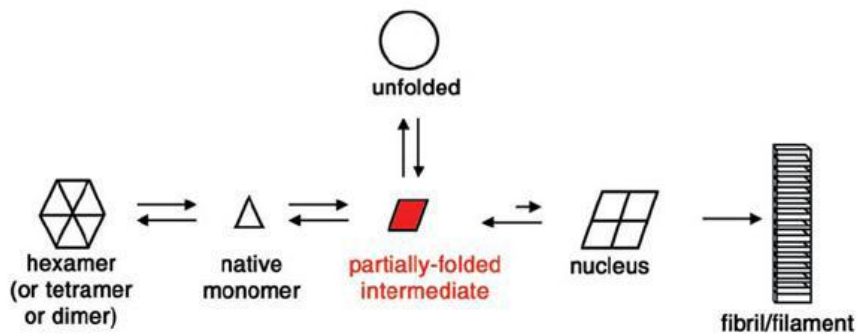


**Figure 1.26** – Scheme of mechanism of fibrillation of Insulin, from ref. 13.

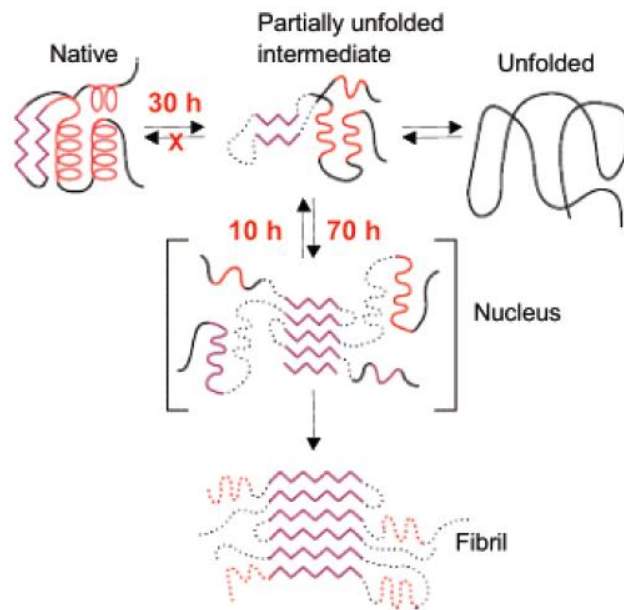


**Figure 1.27** – Mechanism of HEWL fibrils formation from ref. 98. Blue is  $\beta$  sheet, red is helical structure, dotted line is undefined structure.

By comparing the two mechanisms of fibrillation shown in Figure 1.20 and 1.21 it is possible to see that the  $\beta$  sheet develops from a partially unfolded intermediate. During the two processes there is a situation of coexistence between different secondary structures ( $\alpha$  helix,  $\beta$  sheet, and unordered) that may turn into a predominantly unordered structure in the complete unfolded molecule (the circle in Figure 1.26 and the unfolded in Figure 1.27) or into a mainly  $\beta$  structure in fibrils.

For insulin the process is complicated by the hexameric quaternary structure (see section 1.1.1). The break of this condition leads to the onset of a state of equilibrium between the native (triangle in Figure 1.26) and the partially unfolded (red trapezium in Figure 1.27) monomers.

## *Bibliography of Chapter 1*

- 
- <sup>1</sup> A.S. Edison, *Nature Structural Biology*, 2001, 8, 3, 201.
- <sup>2</sup> M. F. Perutz, *Scientific American*, 1978, 239: 92–93.
- <sup>3</sup> Storkel, Sheneider et al. Iatrogenic, Insulin-Dependent, Local Amyloidosis Brief Communication, 1983, 48(1) 108.
- <sup>4</sup> Stewart, Oadiah et al., *Diabetes Res. Clin. Pract.*, 2007, 75, 374-376.
- <sup>5</sup> Horwich, A., *J. Clin. Invest.*, 2002, 110, 1221-1232.
- <sup>6</sup> Caughey, B., and Lansbury, P. T., *Annu. Rev. Neurosci.*, 2003, 26, 267-298.
- <sup>7</sup> R. Jansen, W. Dzwolak, and R. Winter, *Biophys. J.*, 2005, 88, 1344–1353.
- <sup>8</sup> R. Khurana, C. Ionescu-Zanetti, M. Pope, J. Li, L. Nielson, M. Ramirez-Alvarado, L. Regan, A.L. Fink, and S.A. Cartery, *Biophys. J.*, 2003, 85, 1135–1144.
- <sup>9</sup> C.M. Gryniewicz, J.F. Kauffman, *J. Pharmaceut. Sci.*, 2008, 97, 3727.
- <sup>10</sup> Sanger, F., *Adv. Protein Chem.*, 1952, 7, 1–66.
- <sup>11</sup> Antony O. W. Stretton, *Genetics*, 2002, 162, 527–532.
- <sup>12</sup> J. Brange, L. Langkjoer, *Pharmacol. Biotechnol.* 1993, 5, 315–350.
- <sup>13</sup> Q. Hua and M. Weiss, *J. Biol. Chem.*, 2004, 279, 21449-21460.
- <sup>14</sup> Fleming A., *Proc Roy Soc Ser B*, 1922, 93, 306-317.
- <sup>15</sup> C.C.F. Blake, D.F. Koenig, G.A. Mair, A.C.T. North, D.C. Phillips & V.R. Sarma, *Nature*, 1965, 206, 757-761.
- <sup>16</sup> Johnson L.N., *Nat. Struct. Mol. Biol.*, 1998, 5(11), 942–944.
- <sup>17</sup> Canfield R.E., *J. Biol. Chem.*, 1963, 238(8), 2698–2707.
- <sup>18</sup> *Proc. R. Soc. Lond. B Bio.*, 1967, 167(1009), 389–401.
- <sup>19</sup> Anthony J. Kirby, *Nature Structural Biology*, 2001, 8.
- <sup>20</sup> C. Redfield and C. M. Dobson, *Biochemistry*, 1990, 29, 31.
- <sup>21</sup> S.J. Demarest, S.-Q. Zhou, J. Robblee, R. Fairman, B. Chu, and D.P. Raleigh, *Biochemistry*, 2001, 40, 2138-2147.
- <sup>22</sup> L.V. Najbar, D.J. Craik, J.D. Wade, and M.J. McLeish, *Biochemistry*, 2000, 39, 19.
- <sup>23</sup> Desmadril, M., and Yon, J. M., *Biochemistry*, 1984, 23, 11-19.
- <sup>24</sup> L.J. Smith, A.E. Mark, C.M. Dobson and W.F. van Gunsteren, *J. Mol. Biol.*, 1998, 280, 703-719.
- <sup>25</sup> Llinas, M., and Marqusee, S., *Protein Sci.*, 1998, 7, 96-104.
- <sup>26</sup> Gassner, N. C., Baase, W. A., Lindstrom, J. D., Lu, J., Dahlquist, F. W., and Matt, *Biochemistry*, 1999, 38, 14451-14460.
- <sup>27</sup> Nölting B, Andert K, *Proteins: Struct. Funct. Genetics*, 2000, 41, 288–298.
- <sup>28</sup> Nölting B., *Protein Folding Kinetics, Biophysical methods 2<sup>nd</sup> edition*, Springer, 2006.
- <sup>29</sup> Ptitsyn OB, Rashin AA, *Biophys. Chem.*, 1975, 3, 1–20.
- <sup>30</sup> Udgaonkar JB, Baldwin RL, *Nature*, 1988, 335, 694–699.
- <sup>31</sup> Kim PS, Baldwin RL, *Annu. Rev. Biochem.*, 1990, 59, 631–660.
- <sup>32</sup> Karplus M, Weaver DL, *Protein Science*, 1994, 3, 650–668.
- <sup>33</sup> Wetlaufer DB, *Proc. Natl. Acad. Sci. USA*, 1973, 70, 697–701.
- <sup>34</sup> Rackovsky S, Scheraga HA, *Proc. Natl. Acad. Sci. USA*, 1977, 74, 5248–5251.

- 
- <sup>35</sup> Dill K.A., *Biochemistry*, 1985, 24, 1501–1509.
- <sup>36</sup> Dill K.A., *Science*, 1990, 250, 297-298.
- <sup>37</sup> Fersht A.R., *Proc. Natl. Acad. Sci. USA*, 1995, 92, 10869–10873.
- <sup>38</sup> Itzhaki L.S., Otzen D.E., Fersht A.R., *J. Mol. Biol.*, 1995, 254, 260–288.
- <sup>39</sup> Shakhnovich E.I., Abkevich V., Ptitsyn O., *Nature*, 1996, 379, 96–98.
- <sup>40</sup> Wolynes, P.G., Onuchic, J.N. & Thirumalai, D., *Science*, 1995, 267, 1619–1620.
- <sup>41</sup> Levinthal, C., *Proceedings of a Meeting held at Allerton House, Monticello, Illinois* (Debrunner, P., Tsibris, J.C.M. & Münck, E., eds.) 22 (University of Illinois Press, Urbana, 1969).
- <sup>42</sup> A. Fersht, *Structure and Mechanism in Protein Science*, W. H. Freeman and Company, New York, 1999, 598.
- <sup>43</sup> L. Smeller, *Biochim. Biophys. Acta*, 2002, 1595, 11-29.
- <sup>44</sup> K. Heremans, L. Smeller, *Biochim. Biophys. Acta*, 1998, 1368, 353-370.
- <sup>45</sup> J.F. Brandts, in: S.N. Timashej, G.D. Fasman (Eds.), *Structure and Stability of Biological Macromolecules*, Vol. 2, Marcel Dekker, New York, 1969, 213.
- <sup>46</sup> S.A. Hawley, *Biochemistry* 1971, 10, 2436-2442.
- <sup>47</sup> J. Zhang, X. Peng, A. Jonas, J. Jonas, *Biochemistry*, 1995, 34, 8361-8641.
- <sup>48</sup> G. Panick, G.J.A. Vidugiris, R. Malessa, G. Rapp, R. Winter, C. Royer, *Biochemistry*, 1999, 38, 4157-4164.
- <sup>49</sup> N. Takeda, M. Kato, Y. Taniguchi, *Biochemistry*, 1995, 34, 5980-5987.
- <sup>50</sup> G. Panick, R. Malessa, R. Winter, *Biochemistry*, 1999, 38, 6512-6519.
- <sup>51</sup> J.L. Silva, D. Foguel and C.A. Royer, *TRENDS Biochem. Sci.*, 2001, 26, 612.
- <sup>52</sup> W. Kauzmann, *Adv. Protein Chem.*, 1959, 14, 1-63.
- <sup>53</sup> T.W. Randolph, M. Seefeldt, J.F. Carpenter, *Biochim. Biophys. Acta*, 2002, 1595, 224-234.
- <sup>54</sup> Chalikian, T. V., *Annu. Rev. Biophys. Biomol. Struct.*, 2003, 32, 207-235.
- <sup>55</sup> V.V. Mozhaev, K. Heremans, J. Frank, P. Masson, C. Balny, *Proteins*, 1996, 24, 81-91.
- <sup>56</sup> L. Smeller, *Biochim. et Biophys. Acta*, 2002, 1595, 11.
- <sup>57</sup> K. J. Frye and C. A. Royer, *Protein .Sci.*, 1998, 7, 2217–2222.
- <sup>58</sup> A. Paliwal, D. Asthagiri, D. P. Bossev, and M. E. Paulaitis, *Biophys. J.*, 2004, 87, 3479–3492.
- <sup>59</sup> C. A. Royer, *Biochim. Biophys. Acta*, 2002, 1595, 201–209.
- <sup>60</sup> G. Hummer, S. Garde, A. E. Garcia, M. E. Paulaitis, and L. R Pratt. *Proc. Natl. Acad. Sci. USA*, 1998, 95, 1552–1555.
- <sup>61</sup> Dobson, C. M. *Nature*, 2003, 426, 884-890.
- <sup>62</sup> Horwich, A., *J. Clin. Invest.*, 2002, 110, 1221-1232.
- <sup>63</sup> Kelly, J. W., *Curr. Opin. Struct. Biol.*, 1998, 8, 101-106.
- <sup>64</sup> C. Soto, *Nature Review Neuroscience*, 2003, 4, 49-60.
- <sup>65</sup> J. P. Taylor, J. Hardy, and K. H. Fischbeck, *Science*, 2002, 296, 1991-1995.
- <sup>66</sup> B. Caughey, and P. T. Lansbury, *Annu. Rev. Neurosci.* 2003, 26, 267-298.
- <sup>67</sup> Cohen A.S. & Jones L.A., *Amyloidosis. Curr. Opin. Rheumatol.*, 1991, 3, 125–138.
- <sup>68</sup> Sunde, M. and Blake, C., *Adv. Protein Chem.*, 1997, Vol 50. 50, 123-159.
- <sup>69</sup> Sunde, M., Serpell, L. C., Bartlam, M., Fraser, P. E., Pepys, M. B. and Blake, C. C. F., *J. Mol. Biol.*, 1997, 273, 729-739.
- <sup>70</sup> Serpell, L. C., Fraser, P. E. and Sunde, M., *Methods Enzymol*, 1999, 309, 526-36.



- 
- <sup>71</sup> Sipe, J. D. and Cohen, A. S., *J. Struct. Biol.*, 2000, 130, 88-98.
- <sup>72</sup> J.L. Jimenez, E.J. Nettleton, M. Bouchard, C.V. Robinson, C.M. Dobson, and H.R. Saibil, *Proc. Natl. Acad. Sci. USA*, 2002, 99, 9196-9201.
- <sup>73</sup> Chamberlain A.K., MacPhee C.E., Zurdo J., Morozova-Roche L.A., Hill H.A., Dobson C.M., Davis JJ., *Biophys. J.*, 2000, 79, 3282-3293.
- <sup>74</sup> Fandrich M., Fletcher M.A., Dobson C.M., *Nature*, 2001, 410, 165-166.
- <sup>75</sup> Goers J., Permyakov S.E., Permyakov E.A., Uversky V.N., Fink A.L., *Biochemistry*, 2002, 41, 12546-12551.
- <sup>76</sup> Goda S., Takano K., Yamagata Y., Nagata R., Akutsu H., Maki S., Namba K., Yutani K., *Protein Sci.*, 2000, 9, 369-375.
- <sup>77</sup> Dobson C.M., *Philos. Trans. R. Soc. Lond. B., Biol. Sci.*, 2001, 356, 133-145.
- <sup>78</sup> Jordens et al., *Biomacromolecules*, 2011, 12(1), 187-193.
- <sup>79</sup> Calamai, M.; Chiti, F.; Dobson, C. M. *Biophys. J.* 2005, 89, 4201-4210.
- <sup>80</sup> Hurle, M. R., Helms, L. R., Li, L., Chan, W. and Wetzel, R., *Proc. Natl. Acad. Sci. USA*, 1994, 91, 5446-5450.
- <sup>81</sup> Chiti, F., Taddei, N., Bucciantini, M., White, P., Ramponi, G. and Dobson, C. M., *EMBO J.*, 2000, 19, 1441-1449.
- <sup>82</sup> Ramirez-Alvarado, M., Merkel, J. S. and Regan, L., *Proc. Natl. Acad. Sci. USA*, 2000, 97, 8979-8984.
- <sup>83</sup> Ahmad, A., Millett, I. S., Doniach, S., Uversky, V. N. and Fink, A. L., *Biochemistry*, 2003, 42, 11404-11416.
- <sup>84</sup> Hamada, D. and Dobson, C. M., *Protein Sci.*, 2002, 11, 2417-2426.
- <sup>85</sup> Wood, S. J., Wypych, J., Steavenson, S., Louis, J. C., Citron, M. and Biere, A. L., *J. Biol. Chem.*, 1999, 274, 19509-19512.
- <sup>86</sup> Smith, A. M., Jahn, T. R., Ashcroft, A. E. and Radford, S. E., *J. Mol. Biol.*, 2006, 364, 9-19.
- <sup>87</sup> Apetri, M. M., Maiti, N. C., Zagorski, M. G., Carey, P. R. and Anderson, V. E., *J. Mol. Biol.*, 2006, 355, 63-71.
- <sup>88</sup> Kumar, S. and Udgaonkar, J. B., *J. Mol. Biol.*, 2009, 385, 1266-1276.
- <sup>89</sup> Librizzi, F. and Rischel, C., *Protein Sci.*, 2005, 14, 3129-3134.
- <sup>90</sup> W. Dzwolak, R. Ravindra, J. Lendermann, and R. Winter, *Biochemistry*, 2003, 42, 11347-11355.
- <sup>91</sup> Nettleton, E. J., Tito, P., Sunde, M. et al., *Biophys. J.*, 2000, 79, 1053-1065.
- <sup>92</sup> C. Ortiz, D. Zhang, A.E. Ribbe, Y. Xie, Dor Ben-Amotz, *Biophys. Chem.*, 2007, 128, 150-155.
- <sup>93</sup> L. N. Arnaudov and R. de Vries, *Biophys. J.*, 2005, 88, 515-526.
- <sup>94</sup> M. Xu, V.V. Ermolenkov, V.N. Uversky, and I.K. Lednev, *J. Biophoton.* 2008, 1, 215-229.
- <sup>95</sup> S. Goda, K. Takano, Y. Yamagata, R. Nagata, H. Akutsu, S. Maki, K. Namba, and K. Yutani, *Protein Sci.*, 2000, 9:369-375.
- <sup>96</sup> Dische, Wernstedt et al., *Diabetologia*, 1988, 31: 158-161.
- <sup>97</sup> Booth, D. R.; Sunde, M.; Bellotti, V.; Robinson, C. V.; Hutchinson, W.L.; Fraser, P. E.; Hawkins, P. N.; Dobson, C. M.; Radford, S. E.; Blake, C. C. F.; Pepys, M. B. *Nature*, 1997, 385, 787-793.
- <sup>98</sup> V. Shashilov, M. Xu, V.V. Ermolenkov, L. Fredriksen, and I.K. Lednev, *J. Am. Chem. Soc.*, 2007, 129, 6972-6973.



# *Chapter 2*

## *Experimental Methods and Materials*

In this Chapter a brief introduction to the experimental techniques (Raman and IR spectroscopy) used in the present work is made. The high pressure set-up and the drop coating deposition method (DCDR) are also described. Finally some information on the fibrillation protocol, the fitting procedure and some technical data on the materials used in this thesis are reported.

## 2.1 – Infrared and Raman Spectroscopy

Infrared and Raman spectroscopy can provide important information about the structure, the function and the reactivity of biological molecules.<sup>1,2</sup> Edsall<sup>3</sup> was a pioneer in studying the ionization of aqueous amino acids as a function of pH using Raman spectroscopy in 1936. In the 1940s and 1950s Darmon and Sutherland<sup>4</sup> studied the IR spectra of amides and peptides, Elliott and Ambrose<sup>5</sup> used polarized IR spectra to study the structures of oriented proteins, and Jones et al. made comprehensive studies of steroids.<sup>6</sup> From the 1960s Lord's group studied the spectra of nucleotides and nucleic acids,<sup>7</sup> and D. Chapman investigated phase changes in lipids and bio-membranes.<sup>8</sup>

Basic principles of Infrared and Raman spectroscopy will be briefly introduced in section 2.1.1. The application of these spectroscopic methods to the study of biological samples and in particular of proteins will be described in section 2.1.2.

### 2.1.1 – History and Survey

Before introducing infrared and Raman spectroscopy, it is convenient to give a basic description of a simple molecule on the basis of quantum mechanics. It must be stressed that only the possible vibrations of the molecule shall be considered, and then how the electromagnetic (EM) field can exchange energy with the vibrational degrees of freedom. Therefore, the rotational degrees of freedom, i.e. the possibility that the EM field exchange energy with rotations shall not be considered. Also the possibility that a high energy EM field exchange energy with electrons shall not be considered. In practice, the molecule is (and remains) in the electronic ground state, its possible rotations are ignored, and only its vibrations are considered.

Considering a simple diatomic molecule, from a classical viewpoint the system can then be simply described by two masses linked by an ideal spring characterized by a constant  $k$ . This harmonic approximation implies that, when a mass is displaced from its equilibrium position by  $\Delta x$ , a restoration force  $F = -k\Delta x$  appears (Hooke's law). According to this, the vibrational frequency  $\nu$  of the system is given by

$$(2.1) \quad \nu = \frac{1}{2\pi} \left( \frac{k}{m} \right)^{1/2}$$

where  $m$  is the reduced mass and  $\nu$  is the frequency of vibration. Note that the vibrational frequency is higher when the force constant is higher, i.e., when the bonding between the two atoms is stronger. Conversely, the heavier are the vibrating masses, the lower is the vibrational frequency. The energy of the harmonic oscillator, given by  $E = (1/2)kx^2$ , is illustrated in Figure 2.1 A.

In the quantum mechanical approach, the vibrational energy is given by:

$$(2.2) \quad E_{vib} = h\nu \left( n + \frac{1}{2} \right) = \frac{h}{2\pi} \sqrt{\frac{k}{m}} \left( n + \frac{1}{2} \right)$$

where  $n = 0, 1, 2, 3, \dots$  is the vibrational quantum number that characterizes the eigenstates of the harmonic oscillator. Note that the energy of the ground state ( $n = 0$ ), the so-called zero point energy, is given by:

$$(2.3) \quad E_{vib,0} = \frac{1}{2} h\nu_0$$

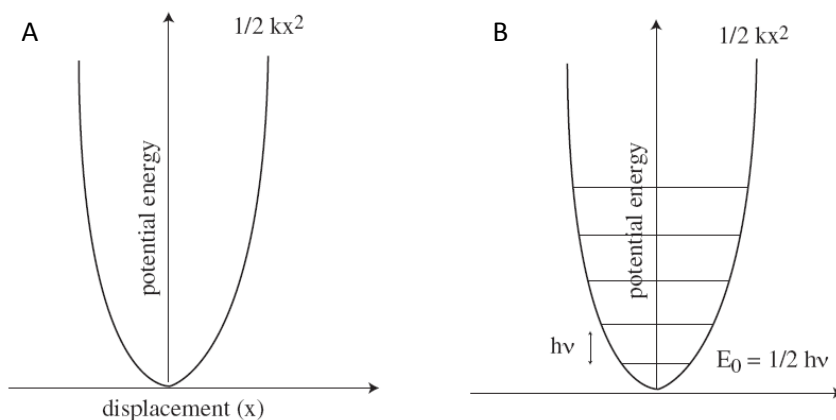


**Figure 2.1** – Energy curve for a vibrating spring in the classical (A) and quantum mechanical model (B).

In this brief overview, it has been assumed a simple harmonic model. This assumption made the mathematics easier, but it is not realistic for a vibrating molecule since anharmonic terms cannot be neglected. Therefore a simple parabolic behavior for the energy is not correct (on increasing  $x$ , the molecule tends to dissociate), and the spacing between energy level is not constant but decreases on increasing  $n$  (see Figure 2.2).<sup>9</sup>

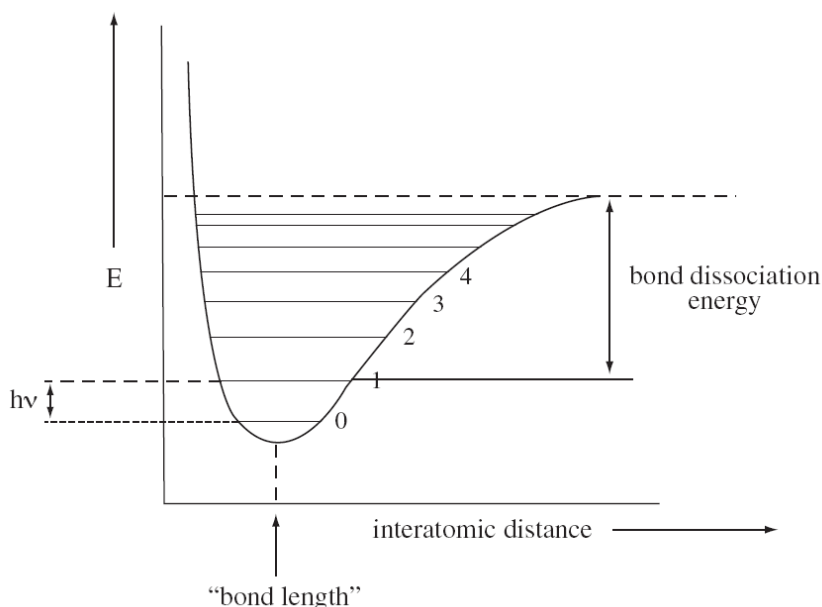


**Figure 2.2** – The anharmonic potential. Unlike the energy levels of the harmonic oscillator potential, which are evenly spaced by  $h\nu$ , the anharmonic potential level spacing decreases as the energy approaches the dissociation energy.

In the case of a polyatomic molecule, the problem becomes more complex because pair interactions can be considered as harmonic (in a first approximation), but the molecule must be considered as a system of coupled anharmonic oscillators. If there are  $N$  atomic nuclei in the molecule, there will be a total of  $3N$  degrees of freedom for all the nuclear masses in the molecule. Since 3 degrees of freedom describe the translational motions and 3 the rotational motions, the remaining  $3N-6$  degrees of freedom define the vibrational motions of the molecule. To simply deal with the problem, it is convenient to introduce the normal coordinates, which allow to describe the molecular vibrations in terms of  $3N-6$  independent harmonic modes: each normal coordinate  $Q_i$

mode describes a vibration of the entire molecule (not of a single atom), the energy of each normal mode  $Q_i$  is given by  $E_i = h\nu_i(n + 1/2)$ . As an example, the three normal modes of a water-like molecule are described in Figure 2.3.

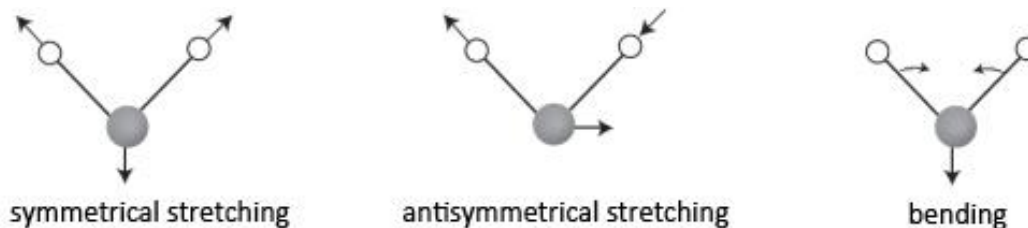


**Figure 2.3** –Stretching and bending of vibrational modes for  $H_2O$ .

Note that, given a polyatomic molecule with a well defined geometrical configuration, it is possible to determine number, symmetry and frequency of the possible normal modes, but a detailed treatment of this problem is well beyond the scope of this discussion.

On the above basis, the vibrations on any molecule composed by  $N$  atoms can be described by considering  $3N-6$  harmonic oscillators, each one characterized by the vibrational frequency  $\nu_i$ , and thus (from a quantum-mechanical viewpoint) by a energy level scheme in which the first excited vibrational level ( $n=1$ ) is  $h\nu_i$  above the ground ( $n=0$ ) level.

After this brief introduction on the vibrational energy levels, it is possible to consider a quantum system characterized by a simple energy level scheme ( $n=0, 1, 2, \dots$ ) at fixed distance  $E_0 = h\nu_0$  interacting with electromagnetic (EM) radiation. Although this thesis mainly deals with Raman measurements, it is convenient to first consider the simplest effect, i.e. the absorption process. We briefly recall that Fermi's golden rule allows the calculation of probability of transition per unit time (transition rate) from the *initial* ( $n=0$ , ground state) to the *final* excited state ( $n>1$ ).

$$(2.4) \quad T_{i \rightarrow f} = \frac{2\pi}{h} |\langle f | H' | i \rangle|^2 \delta(\nu - \nu_0)$$

The transition  $i \rightarrow f$  is due to the coupling between the EM field  $E = E_0 \sin(\nu t)$  and the system. In the dipole approximation, the coupling described by the perturbing Hamiltonian  $H' \propto \vec{\mu} \cdot \vec{E}$  is given by the interaction between EM field and a dipole moment  $\vec{\mu}$  oscillating at frequency  $\nu_0$ . In this treatment (first-order perturbation theory) absorption occurs if  $\nu = \nu_0$  (energy conservation, first fundamental condition) and, in considering vibrational energy levels, if the vibration modulates a dipole moment at frequency  $\nu_0$ . In other words, a normal mode  $Q$  can be classified as IR active if it produces a dipole moment  $\mu$  which varies in time with the vibrational frequency  $\nu_0$ :

$$(2.5) \quad \frac{\partial \mu}{\partial Q} \neq 0$$

We finally recall that, because of the characteristics of the harmonic oscillator wavefunctions, the selection rule  $\Delta n = 1$  does hold. Therefore, if the  $n=0$  ground state is populated, only transitions to the  $n=1$  state are possible. Furthermore, if the  $n=1$  state is populated, the  $n=1 \rightarrow 2$  transition will occur at the same frequency since the distance among vibrational levels is always the same in the harmonic approximation. However, when anharmonic effects are important, the  $n=0 \rightarrow 1$  and  $n=1 \rightarrow 2$  transitions will occur at different frequencies (see Fig. 2.2); furthermore overtones ( $\Delta n = +2, +3, \text{etc}$ ) and (in the case of polyatomic molecules) combination bands (sum or subtraction of two vibrational frequencies) can appear in the absorption spectrum.

Going to the Raman spectroscopy, it is important to first remark that the Raman effect is based on a physical process, i.e. scattering, which is completely different from the absorption process described above. Always considering a quantum system characterized by the simplest energy level scheme ( $n=0, 1$  at distance  $E_0 = h\nu_0$ ), the first condition for the absorption process is that a component at  $\nu = \nu_0$  is present in the incident radiation. In the scattering process, a monochromatic incident radiation at a frequency  $\nu$  different from  $\nu_0$  is considered (therefore no absorption can take place), and radiation is diffused (scattered) in different directions at the frequency  $\nu_0$  (elastic scattering, Rayleigh scattering) and at frequencies  $\nu - \nu_0$  and  $\nu + \nu_0$  (inelastic scattering) (see Fig. 2.4). The inelastic components (Raman) have intensity much lower than that of the Rayleigh component, and the component at  $\nu_0 - \nu_s$  (Stokes component) is much more intense of the  $\nu_0 + \nu_s$  component (anti-Stokes).

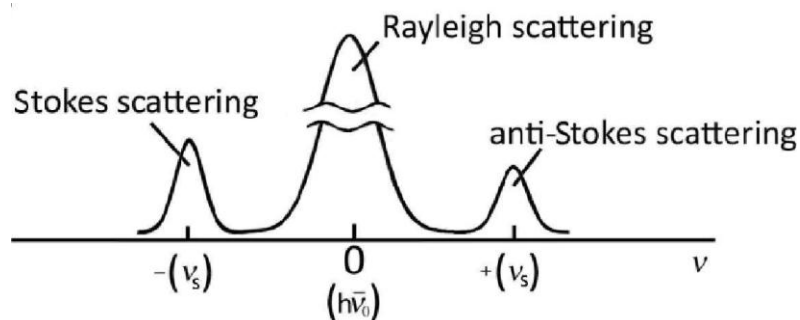


**Figure 2.4** – Scattered light: elastic contribution (Rayleigh) and Raman inelastic contribution (Stokes and Anti-Stokes scattering).

Raman effect was discovered in 1928 by Raman and Krishnan studying light diffusion through liquids. Raman received the Nobel prize for "for his work on the scattering of light and for the discovery of the effect named after him" in 1930 (see Figure 2.5).

A first explanation of the Raman effect can be done using a classical theory.<sup>10</sup> The monochromatic electromagnetic field  $\vec{E} = \vec{E}_0 \cos(2\pi\nu_0 t)$  induces a dipole moment  $\vec{P}$ :

$$(2.6) \quad \vec{P} = \alpha \vec{E}$$

Note that, since  $\nu_0$  is usually in the visible range, only the electronic polarizability is involved, which depends on how the electronic cloud is deformed (i.e., polarized) by the electric field. The time-dependent induced dipole moment is then given by:

$$(2.7) \quad \vec{P}(t) = \alpha \vec{E}_0 \cos(2\pi\nu_0 t)$$

Considering the normal mode  $Q$  of a diatomic molecule (or one of the normal modes of a polyatomic molecule) given by

$$(2.8) \quad Q(t) = Q_0 \cos(2\pi\nu_s t)$$

the molecular polarizability  $\alpha$  can slightly vary in time with frequency  $\nu_s$ . Since for a typical diatomic molecule (e.g.  $N_2$ ) the maximum displacement is much lower than the bond length (a few percent), the polarizability may be approximated by a series expansion, namely:

$$(2.9) \quad \alpha = \alpha_0 + \frac{\partial \alpha}{\partial Q} dQ$$

where  $\alpha_0$  is the polarizability of the molecular mode at equilibrium position.

SIR CHANDRASEKHARA V. RAMAN

## The molecular scattering of light

*Nobel Lecture, December 11, 1930*

*The colour of the sea*



In the history of science, we often find that the study of some natural phenomenon has been the starting-point in the development of a new branch of knowledge. We have an instance of this in the colour of skylight, which has inspired numerous optical investigations, and the explanation of which, proposed by the late Lord Rayleigh, and subsequently verified by observation, forms the beginning of our knowledge of the subject of this lecture. Even more striking, though not so familiar to all, is the colour exhibited by oceanic waters. A voyage to Europe in the summer of 1921 gave me the first opportunity of observing the wonderful blue opalescence of the Mediterranean Sea. It seemed not unlikely that the phenomenon owed its origin to the scattering of sunlight by the molecules of the water. To test this explanation, it appeared desirable to ascertain the laws governing the diffusion of light in liquids, and experiments with this object were started immediately on my return to Calcutta in September, 1921. It soon became evident, however, that the subject possessed a significance extending far beyond the special purpose for which the work was undertaken, and that it offered unlimited scope for research. It seemed indeed that the study of light-scattering might carry one into the deepest problems of physics and chemistry, and it was this belief which led to the subject becoming the main theme of our activities at Calcutta from that time onwards.

**Figure 2.5** – Extract of the Nobel lecture of Sir C. Raman, 1930.

The induced dipole moment is then given as:

$$(2.10) \quad P(t) = \alpha_0 E_0 \cos(2\pi\nu_0 t) + \frac{\partial\alpha}{\partial Q} Q_0 E_0 \cos(2\pi\nu_0 t) \cos(2\pi\nu_s t)$$

Using a trigonometric identity, the above relation may be recast as:

$$(2.11) \quad P(t) = \alpha_0 E_0 \cos(2\pi\nu_0 t) + \left(\frac{\partial\alpha}{\partial Q} \frac{Q_0 E_0}{2}\right) \{\cos[2\pi(\nu_0 - \nu_s)t] + \cos[2\pi(\nu_0 + \nu_s)t]\}$$

Therefore, the dipole moment oscillates with three frequencies, namely  $\nu_0$ ,  $\nu_0 - \nu_s$ ,  $\nu_0 + \nu_s$ . The three components resulting from the scattering process are then explained since it is well known that a dipole moment oscillating at a frequency  $\nu$  emits EM radiation with intensity  $I$  given by :

$$(2.12) \quad I \propto \left| \frac{\partial^2 P}{\partial t^2} \right|^2 \propto \nu^4 \alpha^2 |\vec{E}|^2$$

Therefore, the intensity of the Raman emission increases with the fourth power of the frequency and with the second power of the molecular polarizability.

It is important to remark that the observation of Raman vibrational lines is possible whenever a vibration leads to a change in the polarizability of the molecule.<sup>11</sup> In other words, a normal mode  $Q$  at a frequency  $\nu_0$  can be classified as Raman active if it gives a polarizability  $\alpha$  which varies in times with the vibrational frequency  $\nu_0$ .

In conclusion, a normal mode  $Q$  is IR active if  $\partial\mu/\partial Q \neq 0$ , while it is Raman active if:

$$(2.13) \quad \frac{\partial\alpha}{\partial Q} \neq 0$$



The above treatment provides a classical framework for the understanding of Raman scattering. However, on the basis of eq. 2.12, the Stokes line at  $\nu_0 - \nu_s$  should be less intense than the anti Stokes line at  $\nu_0 + \nu_s$ . On the contrary, the Stokes line is much more intense than the corresponding anti Stokes one.

A correct explanation of the Raman effect can be only obtained through a proper quantum mechanical treatment, but this is well beyond the scope of this work. However a simple explanation can be obtained by considering the scheme in Figure 2.6.

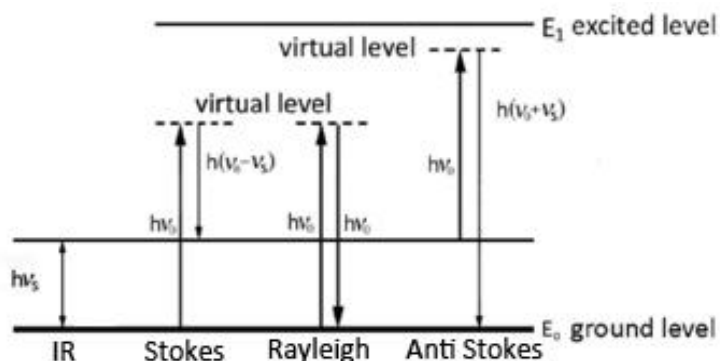


**Figure 2.6** – Quantum scheme of the IR absorbance, Rayleigh scattering and Raman (Stokes and Anti-Stokes) scattering.

On discussing the Figure 2.6 it is important to underline that the IR absorbance is a first-order process (the molecule is excited onto a possible level), while the Raman scattering is a second-order process. Following the quantum scheme in Figure 2.6, the photon  $h\nu_0$  first determines a transition (from the ground state or from the first excited state at  $h\nu_s$ ) to a virtual state (this is not an absorption process since the transition to the virtual state is not allowed), and then the molecule decays to a state at lower energy (to the excited state at  $h\nu_s$  in the Stokes case, to the ground state in the anti-Stokes case). Since the intensity of a line is determined by the population of the starting level, the Stokes line is more intense than the anti-Stokes because the ratio between the population of the two possible starting levels (ground state  $n=0$  and excited state  $n=1$ ) is given by the Boltzmann factor:

$$(2.14) \quad \frac{P_1}{P_g} = e^{-\frac{\Delta E}{kT}}$$

where  $\Delta E = E(n = 1) - E(n = 0)$ .

For a simple molecule like CO,  $\Delta E \approx 2000 \text{ cm}^{-1}$ . Since at  $T = 300K$ ,  $kT = \text{circa } 200 \text{ cm}^{-1}$ , it follows that:

$$(2.15) \quad \frac{I_{\text{Anti-Stokes}}}{I_{\text{Stokes}}} = \frac{P_1}{P_g} \approx e^{-10}$$

This result clearly shows that the intensity of the anti-Stokes line can be completely negligible.

In practice, Raman measurements are made by using a laser, i.e. a monochromatic, intense, collimated light source. In general, the Raman signal intensity is orders of magnitude weaker than the elastic scattering intensity. For example, diatomic nitrogen ( $N_2$ ) at the wavelength 488 nm has an elastic scattering cross-section (i.e. Rayleigh scattering) of  $8.9 \cdot 10^{-28} \text{ cm}^2/\text{sr}$ , and a Raman scattering cross-section of  $5.5 \cdot 10^{-31} \text{ cm}^2/\text{sr}$ . The Raman scattering signal is more than  $10^3$  times weaker than the Rayleigh signal. The elastically scattered light can dominate the Raman signal.

Therefore, notch filters or edge filters (sharp cut-off high pass filters) are used to reject the elastically scattered light prior to entering the spectrometer. Another important problem is the selection of the laser frequency. Selecting a high laser frequency can increase the Raman intensity (see Eq. 2.12). However, at high laser frequency (in particular, in the UV range), fluorescence can strongly increase and mask the Raman signals (in the fluorescence process, incident photons are absorbed and then re-emitted at lower frequency after some non-radiative decay process). Therefore, the choice of a laser in the IR region can be convenient since fluorescence can be minimized.

As a final remark, it must be noted that in all the above treatment only isolated molecules (and their normal vibrational modes) have been considered. In general, and in particular in this thesis, the EM radiation interacts with complex liquids and solids, not with single molecules. It is thus important to briefly discuss how above treatments can be extended to complex systems.

The simplest solid is the ideal crystal, that is defined as an infinite lattice with a component (atom, molecule or molecular complex) in each site. By considering the center of mass of each component, it is possible to define the normal modes of vibration of the crystal lattice, that can origin spectral contributions (phonons) in the far IR region of the absorption spectrum, and at low frequency (i.e. at frequencies close to the laser frequency) in the Raman spectrum. Besides these contributions, each component (molecule or molecular complex) keeps its own identity even when it is in the crystal lattice, since intra-molecular bonds are much stronger than inter-molecular ones. As a consequence, if the isolated component vibrates at a given frequency, this vibrational frequency in the solid will be only slightly modified because the inter-molecular bonds can only slightly perturb the intra-molecular vibration.

In an amorphous system (i.e. a solid without a well defined crystal structure) or in a liquid the collective vibrational modes are not possible and thus phonons cannot be observed in the IR or Raman spectrum. However, as discussed above, the vibrational frequencies that characterize the different components are not strongly affected by inter-molecular interactions. Therefore both Raman and IR vibrational spectroscopy can provide information on the vibrational frequencies in the system, and thus on the nature of the different components and on the interactions among them.

### **2.1.2 – Application of Raman and IR spectroscopy on proteins**

It is a fundamental belief in structural biology that protein function or dysfunction is related to its structure or change in structure. Both IR and Raman vibrational spectroscopy provide information on the secondary structure of proteins, ligand interactions and folding.

As an example of the sensitivity of vibrational spectroscopy on protein conformation, Figure 2.7 shows the mid-infrared spectra and the Raman spectra of two proteins with very different conformations: albumin, whose structure is almost all helical, and concanavalin A, a  $\beta$ -sheet rich protein (no helix and ~40% sheet).<sup>12</sup>

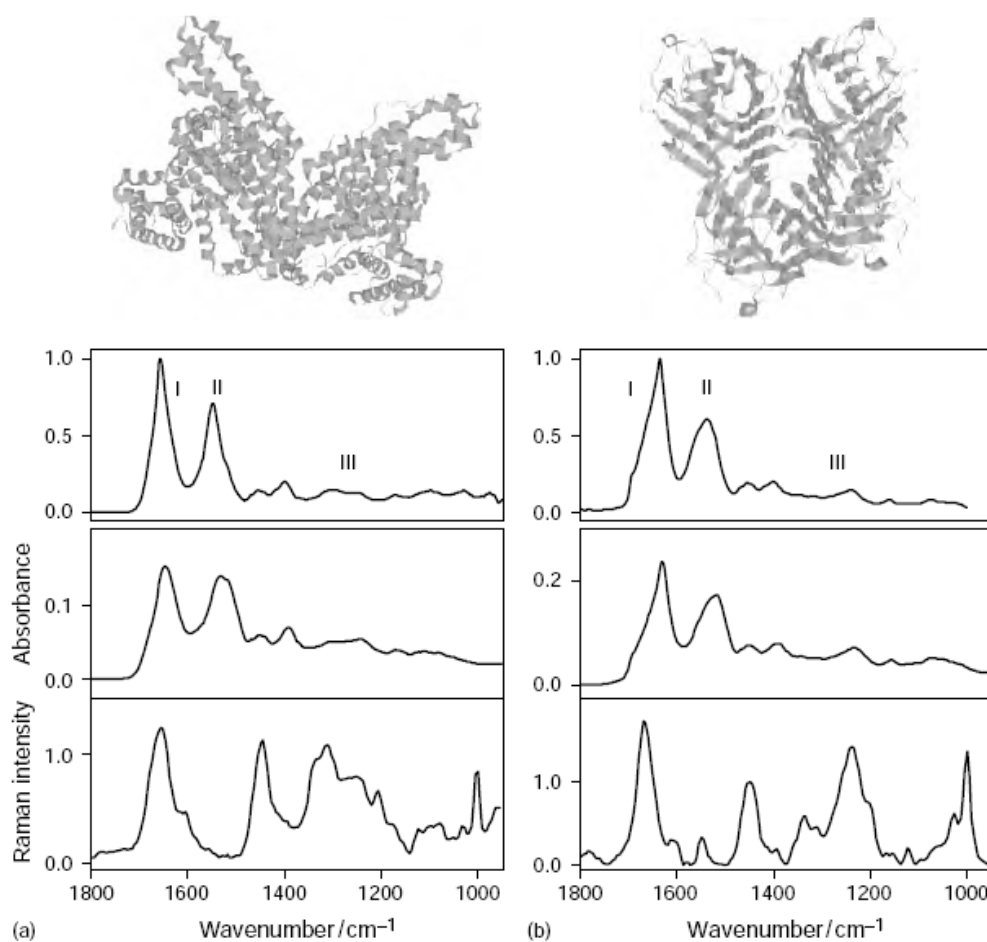


**Figure 2.7** – IR spectra in solution (top), solid (middle) and Raman spectra in solution (bottom) of: (a) albumin; (b) concavalin A. For solution spectra, proteins were measured in buffered water at concentration of ~2% for IR measurements and in 0.1M phosphate buffer at concentration of ~5% for Raman measurements. Amide I, II and III modes are marked as such on the spectra. Taken from ref. 12.

In the vibrational spectra, the amide bonds of proteins form so-called chromophores that give rise to nine strong characteristic bands that are named: Amide A, Amide B and Amides I–VII (see Table 2.1).<sup>13,14</sup>

Designation	Approximate frequency (cm <sup>-1</sup> )	Description
Amide A	3300	NH stretching
Amide B	3100	NH stretching
Amide I	1600–1690	C=O stretching
Amide II	1480–1575	CN stretching, NH bending
Amide III	1229–1301	CN stretching, NH bending
Amide IV	625–767	OCN bending
Amide V	640–800	Out-of-plane NH bending
Amide VI	537–606	Out-of-plane C=O bending
Amide VII	200	Skeletal torsion

**Table 2.1** –Characteristic vibrational bands of the peptide linkage (from ref. 14)

Among these bands, Amide I, which is due mostly to the C=O stretching vibrations of the peptide backbone, is by far the best characterized. It gives rise to a Raman and IR band in the 1600–1700  $\text{cm}^{-1}$  region and has been used the most for structural studies due to its high sensitivity to small changes in molecular geometry and hydrogen bonding of the peptide group. The amide II band, due largely to a coupling of C-N stretching and in-plane bending of the N-H group, is extremely weak in the Raman spectrum and fairly strong in the IR giving rise to a band in the 1480–1575  $\text{cm}^{-1}$  region. Although that the amide II band is not often used for structural studies in the IR analysis because it is less sensitive than Amide I band to the conformational changes of the poly-peptide backbone and it is subject to interference from absorption bands of amino acid side chain vibrations.<sup>15</sup> The amide III band, arising from coupling of C-N stretching and N-H bending, and giving rise to bands in the 1230–1300  $\text{cm}^{-1}$  region, is fairly weak in the IR but strong in the Raman spectra. Like Amide II, also this band can be mixed with the vibrational peaks from the side-chains.

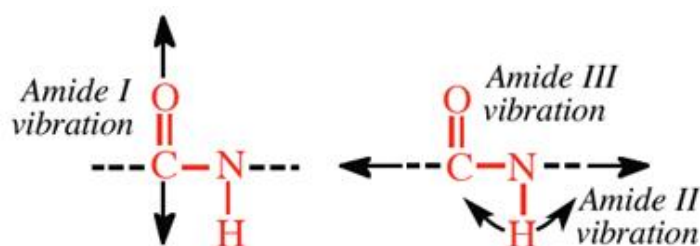


**Figure 2.8**– Stretching and bending modes that constitutes the Amide I,II and III bands.

In addition to secondary structure information, Raman can provide insight on dihedral angles of C-S-S-C bonds and C-C-S-S bonds and their related conformers; it can also determine how tyrosine are hydrogen-bonded and whether tryptophan residues are in a hydrophobic or hydrophilic environment.

Vibrational spectroscopic studies carried out in combination with the technique of the hydrogen isotope exchange can provide relevant information on the protein folding/unfolding process.<sup>16</sup> When a polypeptide folds to form the well-defined three dimensional structure of a protein, many of the amide hydrogen become buried in the interior of the protein and no longer come into direct contact with the solvent heavy water. While the unfolding of a protein is taking place the buried part of the protein becomes accessible and the H exchanges with the solvent D. As the process goes on the relative intensities of the Amide II and Amide II' changes (see Figure 2.9), providing a clear indication of the unfolding.<sup>17</sup>

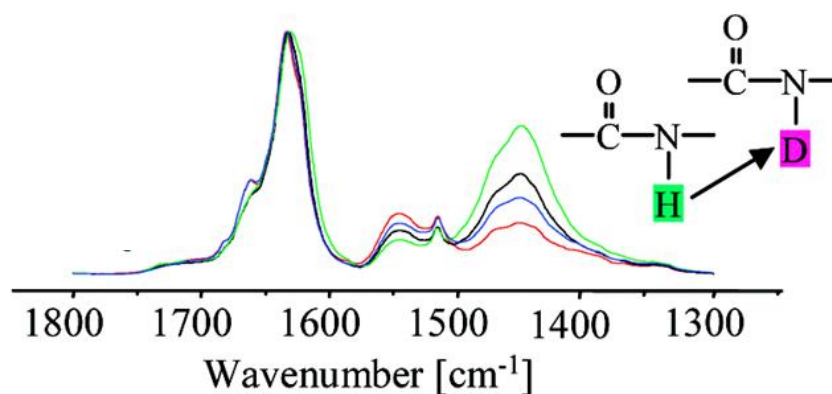


**Figure 2.9** – Example of H substitution with D (from red to green spectra) induced by high temperature on insulin solution. The FTIR spectra is taken by ref. 17.

The proteins “big” dimensions (up to hundreds of kilo Dalton) render the vibrational spectra of these samples quite complex and it is common to have superimposition of many vibrations into one broad features that is analyzed by means of resolution-enhancement technique.<sup>18</sup>

Vibrational spectroscopy does not compete with other methods of structural analysis because it has different objectives, but its full power can be exploited if a three-dimensional structure is available. Although X-ray crystallography provides the most detailed information concerning positions of individual atoms in the protein structure, it is not, however, possible for all proteins to form a quality crystal for such analysis. In addition, the crystallographic data of a protein cannot be easily extrapolated to the dynamic properties of the proteins in solutions. Vibrational spectroscopy can then be used to prove or refute models, to improve models, and to suggest other mechanisms. The advantage of these methods of spectroscopy is their extreme sensitivity to changes in molecular interaction and structure. Moreover, these spectroscopic techniques are direct, nondestructive or noninvasive, and require small sample quantities. Raman spectroscopy offers structural information about secondary and tertiary protein structure, and infrared spectroscopy provides information particularly on protein secondary structure.

### 2.1.3 – Experimental Set-up

#### Raman Set-up

Raman measurements were performed at the HPS (High Pressure Spectroscopy) laboratory at the Physics Department of Sapienza University in Rome. The Raman instrument used is a LABRAM Infinity micro-Raman by Jobin-Yvon and its optical scheme is shown in Figure 2.10.

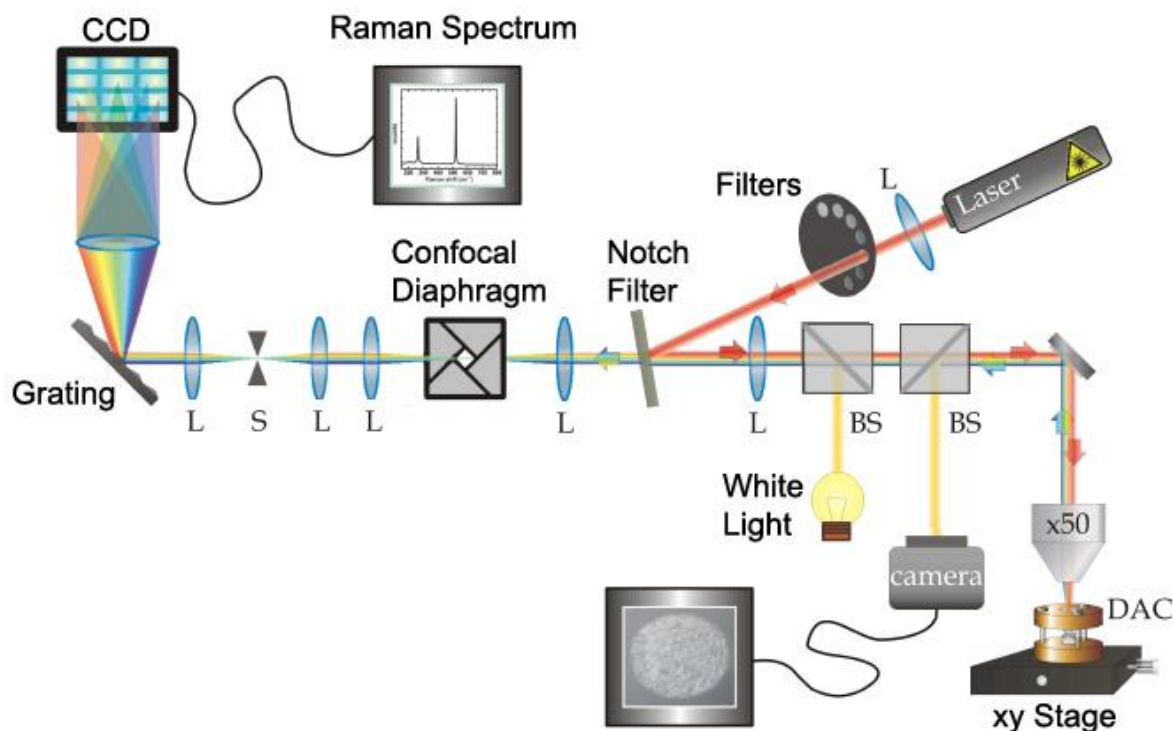


**Figure 2.10** – Optical scheme of the Micro-Raman spectrometer employed in the present work.

The laser is a 20mW He-Ne (632.81 nm wavelength) and its light could be attenuated, if needed, by filters with an attenuation factor from 1 to  $10^{-4}$ . The laser beam, reflected by a notch filter, passes

into the microscope equipped with objectives with 4x, 10x, 20x, 50x and 100x magnifications. The microscope focuses the laser light onto the sample and collects the backscattered light sending it again on the notch-filter. In the backscattering configuration the notch filter is used to reject the elastic contribution, which prevents the collection of spectra close to the excitation line (above  $150\text{ cm}^{-1}$ ). Before entering in the monochromator, the light is focused into an adjustable pinhole, which gives the chance to select along the optical axis the region of the sample from which the scattered light is collected and analyzed (confocal effect). The instrument is equipped with two monochromators (with 600 or 1800 lines/mm which give a spectral resolution of about  $9\text{ cm}^{-1}$  and less than  $3\text{ cm}^{-1}$  respectively) in order to select the spectral range. The detector is a charge coupled device (CCD), which works at a temperature of  $-70^\circ\text{C}$  to minimize background noise. An absolute frequency calibration of each spectral range was obtained by using the well known emission lines of a neon lamp.

## IR Set-Up

The infrared measurements have been carried out at the SISSI beamline of the Elettra Synchrotron in Trieste.<sup>19</sup>

The infrared beamline SISSI (Source for Imaging and Spectroscopic Studies in the Infrared) extracts the IR and visible components of synchrotron emission for applications of spectroscopy, microspectroscopy and imaging. Hereafter the major technical specifications were reported.

The radiation is collected from bending magnet over acceptance angles of 70 mrad (horizontal) and 25 mrad (vertical) and comprises both edge and constant field emission. A set of ellipsoid and plane mirrors delivers the light to the instrumentations (Figure 2.11), consisting in a Michelson interferometer and a confocal infrared microscope.

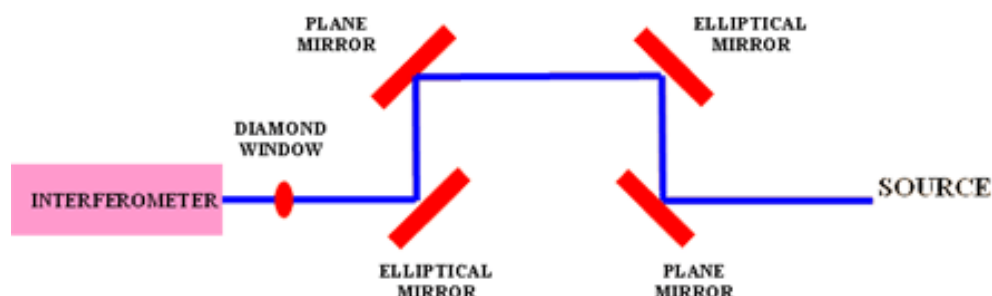


Figure 2.11 – Optical scheme of the beamline.

For the IR measurements included in this thesis a Bruker IFS66v interferometer (designed to work either in N purging or under vacuum (3 mbar)) and a Hyperion 2000 infrared microscope were used. The interferometer can be operated both in rapid scan and step scan, allowing the study of rapidly evolving systems, with a time resolution in the range from nanoseconds to milliseconds. The combination of beamsplitters (KBr) and detectors covers the spectral range from  $3\text{ cm}^{-1}$  up to  $25000\text{ cm}^{-1}$ .

The microscope operates under diffraction limited conditions when used in conjunction with synchrotron light emission and allows spatial resolution of details in the  $\mu\text{m}$  range. The brightness of the synchrotron emission provides mid-IR spectra from  $\nu = 6000\text{ cm}^{-1}$  ( $\lambda = 1.6\text{ }\mu\text{m}$ ) to  $\nu = 800\text{ cm}^{-1}$  ( $\lambda = 12\text{ }\mu\text{m}$ ) of objects with a size of  $4 \times 4\text{ }\mu\text{m}$ .

<b>Energy Range</b>	10-25,000 $\text{cm}^{-1}$ (1 meV-3eV)
<b>Space Resolution</b>	Diffraction limited
<b>Energy Resolution</b>	0.2 $\text{cm}^{-1}$
<b>Time Resolution</b>	$\sim 1$ ns (step-scan mode) and $\sim 1$ msec (slow-scan mode)
<b>Configuration</b>	Transmission, Reflection, ATR
<b>Additional Features</b>	Fluorescence Imaging Experiments in High Magnetic Fields

**Table 2.2** – *Beamline features.*

## 2.2 – High Pressure Spectroscopy: the Diamond Anvil Cell

The Diamond Anvil Cell (DAC)<sup>20</sup> is really a powerful tool to study matter under extreme pressure. The principle of operation is rather simple and is outlined in Figure 2.12(a). The diamond anvil cell is a small mechanical press that forces the small, flat faces (the culets) of two flawless, brilliant-cut diamonds together with a metallic plate with a small hole in the center (to host the sample). It uses diamonds because, in addition to being recognized as the hardest and least compressible material, has the important property of being transparent to most of the spectrum of electromagnetic radiation, including  $\gamma$ -ray, X-ray, portions of ultraviolet, visible, and most of the infrared region.

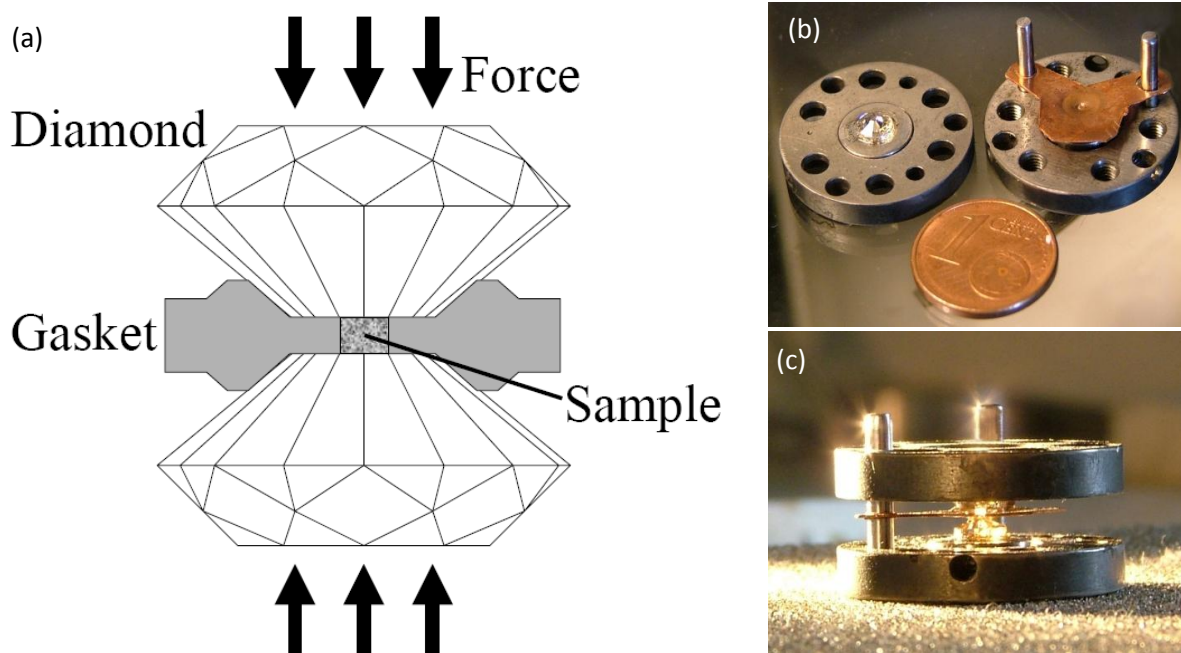


**Figure 2.12** – *Schematic representation of the working mechanism of a DAC (a); photos of one of the two DAC used in this thesis.*

The diamonds are in an opposed anvil configuration and mounted on a pair of carbur tungsten plates. Aperture in the plates permits light and other kind of radiation to enter through the diamond anvils and, because of the transparency of diamond, the sample may be examined in situ (while at elevated pressure) by optical microscope, spectroscopy (Raman, Infrared, Brillouin), and diffraction techniques. The large ratio between the surface of the external and internal anvil faces strongly amplifies the effect of the external force leading to very large pressure inside the hole. Pressure is exerted on the outside culet of the diamonds by means of different devices. They can be



either mechanical (screws) or pneumatic. The latter consists on a flowing gas (He) at a moderate pressure (0-200 bar) inside a metallic membrane able to expand against the piston. This system allows fine regulation of the pressure and a very homogeneous pressure on the gasket. The maximum pressure attainable depends on several factors: the quality of the diamonds, the dimension of the culet and the hole and the material of the gasket. The range of static pressure attainable today extends to the estimated pressures at the Earth's center (~ 360 GPa).

The quality of the diamonds depends on the number of impurities and vacancies in the crystal. For Raman measurements type IIa (low fluorescence) can be employed. The inner culet is a 16-side polygon with a 200-800  $\mu\text{m}$  typical diameter. The external face diameter is 2-4 mm large and each diamond is typically 1-3 mm thick. The gasket material can be any metal with a high mechanical hardness such as molybdenum and stainless steel (0-30 GPa), or rhenium for very high pressure measurements (0-50 GPa). The gasket has the double function: it is the sample holder and moreover it exerts a force which compensate to the internal pressure. The hole in the gasket must be not larger than 1/2 of the diameter of the inner culet. The sample chamber is thus always very small. Gaskets are prepared by indenting a 200-250  $\mu\text{m}$  thick metal foil between the diamonds until the final thickness (between 20  $\mu\text{m}$  and 100  $\mu\text{m}$ ) is reached. The indented-gasket has a characteristic crater-like shape which perfectly allocates the diamonds and ensures massive support all around. In the end, in the center of the indented gasket the hole is made by means of spark eroding machine equipped with an optical microscope. In the case in which the sample is not hydrostatic itself, a proper hydrostatic medium should be placed in the hole together with the sample. The best performances as hydrostatic medium are obtained using noble gases (Ar, Xe or Ne) but they require a cryogenic or a high-pressure loading device. For Raman measurements performed at pressure up to 20 GPa cubic salts or a 4:1 ethanol-methanol mixture can be employed.

### 2.2.1 – Ruby Fluorescence for Pressure Determination

One of the biggest problem encountered in making the DAC operational was the in situ pressure measurement. In 1971 it was suggested to try with fluorescence spectroscopy. Among the multitude of materials that were tested, such as ruby ( $\text{Al}_2\text{O}_3$ ),  $\text{YAlO}_3$ , YAG, MgO, and a few others, ruby was the most promising one.

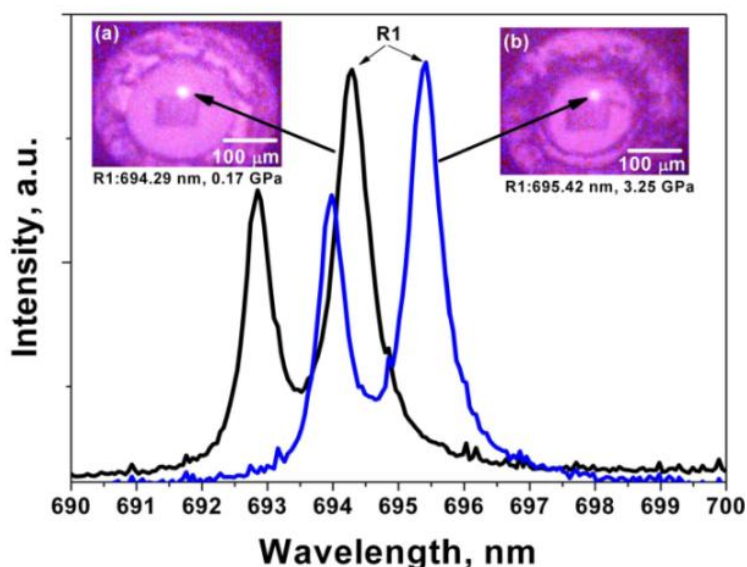


Figure 2.13 – Ruby spectrum fluorescence at 0.17 GPa (black curve) and 3.25 GPa (blue curve)



Ruby's main fluorescence lines (the R-line doublet lines) were intense and sharp and the lines shifted towards the red end of the spectrum with increasing pressure (see Figure 2.13). Significantly, pressure could be detected in situ using only a very small amount of ruby nanosphere ( $\sim 10 \mu\text{m}$  diameter) as the internal pressure sensor. Furthermore, because it is inert, ruby could be present in the sample chamber without interfering with the sample itself.

It was important to calibrate the R-line shift against reliable pressure values. This calibration was carried out using a x-ray powder diffraction method to measure the compression of NaCl (utilizing a well established equation of state) and relating this to the measured shift in the wavelength of the ruby R1-line.<sup>21</sup> The most widely used ruby calibration scale is shown in Figure 2.14.<sup>22</sup> From this calibration pressure can be calculated as:

$$(2.16) \quad P(\Delta\lambda) = \frac{A}{B} \left[ \left( 1 + \frac{\Delta\lambda}{\lambda_0} \right)^B - 1 \right]$$

where:  $A = 1904 \text{ GPa}$  and  $B = 7.665$  are constants from ref. 22 and  $\lambda_0 = 649.2 \text{ nm}$  is the R1-line peak wavelength at ambient pressure. It was found that up to 29 GPa ruby red shift is linear with pressure (see Figure 2.15) and so eq. 2.16 can be approximated with a linear dependence<sup>23</sup>:

$$(2.17) \quad P = \alpha\Delta\lambda \quad \text{with: } \alpha = 2.74 \text{ GPa/nm.}$$

Ruby fluorescence lines depends also on the temperature, so a correction to eq. 2.16 and eq. 2.17 is needed. The temperature-induced shift of R1 wavelength was measured at ambient pressure and fitted by a cubic law:

$$(2.18) \quad \Delta\lambda(T) = C_1(T - T_0) + C_2(T - T_0)^2 + C_3(T - T_0)^3$$

where:  $C_1 = 0.00696 \text{ nm/K}$ ,  $C_2 = 7.76671 \cdot 10^{-6} \text{ nm/K}^2$ ,  $C_3 = -1.697 \cdot 10^{-8} \text{ nm/K}^3$ , and  $T_0 = 298 \text{ K}$ .<sup>24</sup> On the assumption that the temperature-induced shift is pressure independent, eq. 2.16 (or eq. 2.17) can be simply corrected by subtracting from  $\Delta\lambda$  the thermal contribution given by eq. 2.18.

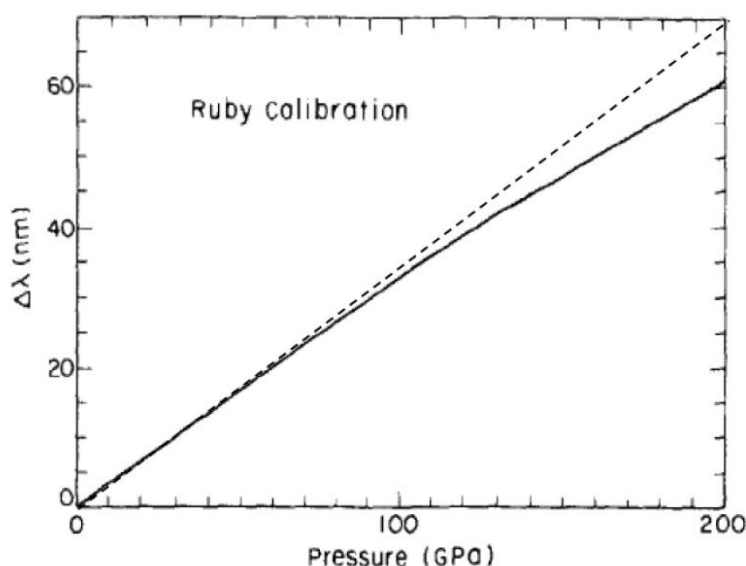


**Figure 2.14** – Pressure dependence of the wavelength shift of the R2 ruby fluorescence line (solid line, from ref.23) and linear approximation in the low pressure regime (dashed line, from ref. 22).

The ruby fluorescence technique ensure an uncertainty in the pressure determination of about  $\pm 0.1 \text{ GPa}$  in the 0-10 GPa range,  $\pm 0.5 \text{ GPa}$  for pressure up to 30 GPa, and  $\pm 1 \text{ GPa}$  or more at higher pressure. This successful calibration established ruby as a standard for measuring pressure in DAC.

## 2.2.2 –Raman and Infrared Measurements at High Pressure: Experimental Procedures

### Raman Measurements

For high pressure Raman measurements a 50x objective with 10 mm focal length was used and the confocal pinhole was adjusted typically to a diameter of 150  $\mu\text{m}$  to collect light from a region of a few microns along the optical axis thus reducing the amount of signal from the diamonds. In this configuration the laser spot on the sample was around 3  $\mu\text{m}$ . The 1800 lines/mm grating was chosen to have a resolution better than 3  $\text{cm}^{-1}$ .

A gas membrane DAC was used with type IIA low fluorescence diamonds, 400  $\mu\text{m}$  culet diameter. The gaskets were made of Molybdenum and were 50-85  $\mu\text{m}$  thick under working conditions. They had all a 150  $\mu\text{m}$  diameter hole. The powder sample were loaded without hydrostatic media, because they were considered as quasi-hydrostatic themselves, while in the case of the protein in water solution the hydrostatic medium was the water itself. A small ruby nanosphere for in situ pressure calibration was loaded in the sample chamber together with each sample and its fluorescence was measured directly by means of the Raman spectrometer. An image of the Molybdenum gasket loaded with insulin powder and with the small ruby nanosphere is shown in Figure 2.15.

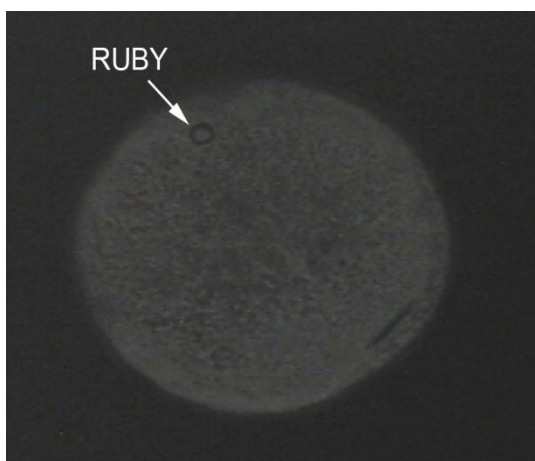


**Figure 2.15** – Photo of the insulin powder sample loaded in the DAC after a pressure cycle up to 3 GPa, the sample is inside the hole of the molybdenum gasket (black part of the photo). The arrow indicates

### Infrared Measurements

For high pressure IR measurements on the insulin water solutions a Bruker IFS-66v interferometer was used (the detector was cooled by means of dry ice and the resolution was around 4  $\text{cm}^{-1}$ ). The DAC was put onto the xy motorized stage of an IR microscope with a 15x objective (under vacuum to avoid atmospheric interferences). The gaskets were made of Copper and were 45-65  $\mu\text{m}$  thick under working conditions with a diameter of 250  $\mu\text{m}$ . The choice of a non-hard material as copper was motivated by the rather low maximum pressure of the measurements carried out on water solutions ( $P_{\text{max}}= 2\text{GPa}$ ). Pressure was applied by means of a screw clamped DAC. The diamonds have a culet of 800  $\mu\text{m}$  diameter. A small ruby nanosphere for in situ pressure calibration was loaded in the sample chamber together with the water protein solution. The optical path of the fluorescence set-up is shown in Figure 2.16. The ruby fluorescence was excited by means of a green laser (doubled Nd:YAG 532 nm). The light is directed onto the sample by means of a dichroic mirror. The light scattered or re-emitted by the sample was collected along the same direction of the incoming beam (backscattering configuration) and, using the dichroic mirror, the

fluorescence signal is selected. Using an optical fiber, this is finally directed to the monochromator for the spectral analysis.

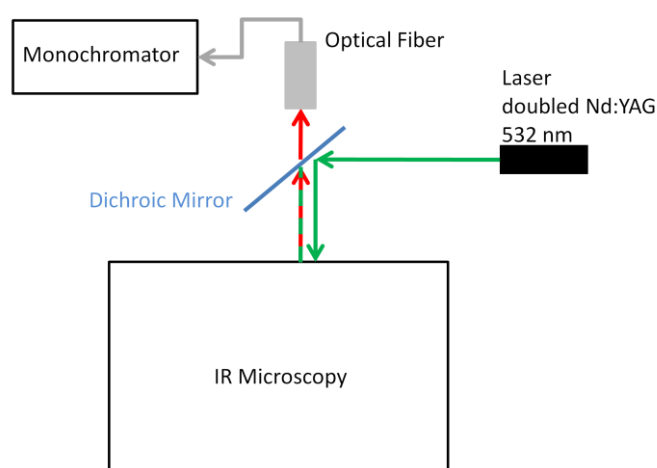


**Figure 2.16** – Experimental apparatus to excite and measure the ruby fluorescence at the Sissi beamline.

### 2.3 – Drop Coating Deposition Method

*“When a spilled drop of coffee dries on a solid surface, it leaves a dense, ring-like deposit along the perimeter.*

*The coffee—initially dispersed over the entire drop—becomes concentrated into a tiny fraction of it. Such ring deposits are common wherever drops containing dispersed solids evaporate on a surface, and they influence processes such as printing, washing and coating.*

*Ring deposits also provide a potential means to write or deposit a fine pattern onto a surface.”*

(R.D. Deegan et al., NATURE |Vol. 389 | 23 October 1997)

With this simple, daily observation R.D. Deegan et al. gave birth to the drop coating deposition method. Recently there has been a lot of interest in methods of enhancing the sensitivity of Raman spectroscopy.<sup>25</sup> The most common method is the so called surface-enhanced Raman spectroscopy (SERS) and is achieved by having the analyte in close proximity to a roughened noble metal surface. SERS permits the detection of molecules in concentrations as low as parts per billion, but its effectiveness is very dependent on the active surface and can suffer from poor reliability and reproducibility,<sup>26</sup> even if nowadays the use of photonic crystal substrates is improving this area.<sup>27</sup>

Another method that is gaining increasing consensus for its highly reproducibility and sensitivity, consists of increasing the Raman signal from an analyte by pre-concentration by using the coffee-ring drying pattern<sup>28</sup>: the so called Drop Coating Deposition Raman (DCDR) technique.<sup>29</sup> The coffee ring pattern arises from a capillary flow (see Figure 2.17) in which pinning of the contact line of the drying drop ensures that liquid evaporating from the edge is replenished by liquid from the interior. The resulting outward flow carries the dispersed material to the edge. When a liquid micro-drop is applied to the substrate, it beads up and dries to a smaller diameter, thus concentrating the analyte deposit. Thus DCDR may be used to obtain high quality normal Raman spectra from volumes (down to sub-nL) of dilute protein solutions (down to sub  $\mu\text{M}$  concentrations). It can be easily reached a 1000 fold increase in the sensitivity of Raman for the analysis of protein solutions, relative to the best normal Raman results obtained prior to DCDR.<sup>29</sup>

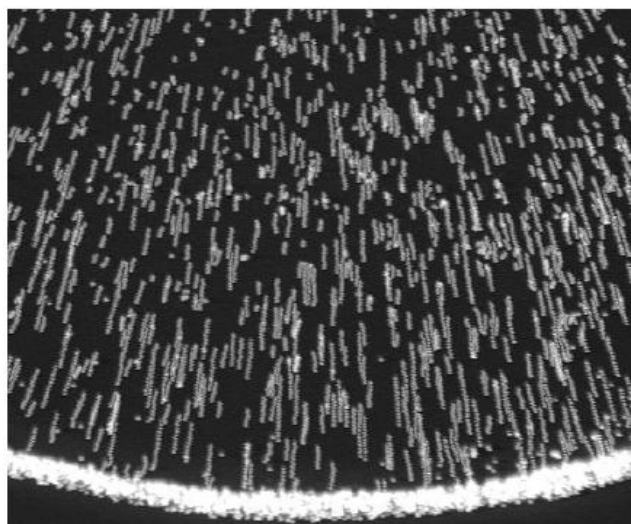


**Figure 2.17** – Image from ref. 28. Spheres in water during evaporation. Image is obtained by superimposition of multiple exposures to indicate the motion of the microspheres.

Since the intensity of a normal Raman spectrum is proportional to the surface density of the analyte on the substrate (for a given laser power), it is desirable to confine the deposited sample to the smallest possible area to maximize the Raman signal-to-noise ratio (see Figure 2.18).

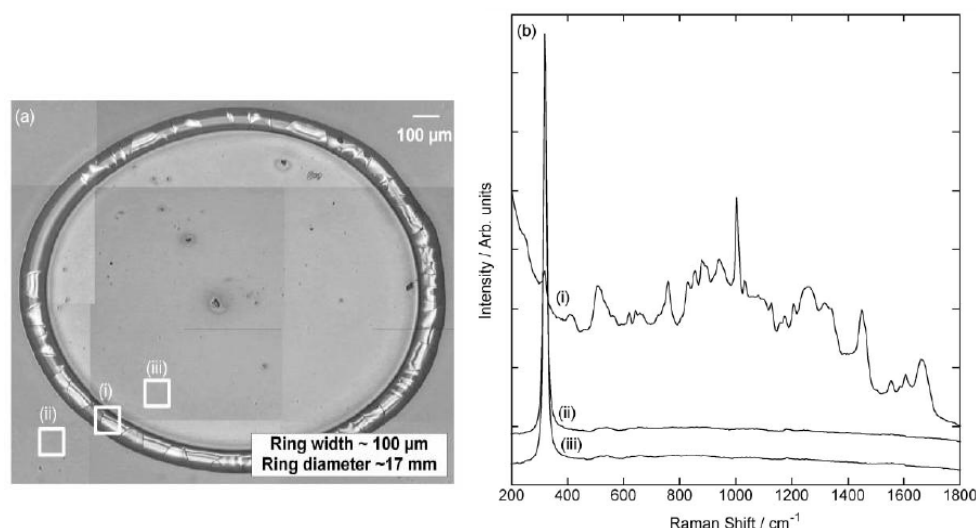


**Figure 2.18** – Image from ref. 25. (a) Ring pattern produced by drying a 3 mg/ml lactoferrin solution on  $\text{CaF}_2$ ; (b) spectra obtained at positions (i), (ii) and (iii).

To achieve these results it is critically important to optimize the properties of the substrate. In particular, an ideal DCDR substrate should have: low optical absorbance and high optical reflectance, little or no interfering background signals, and most importantly a non-wetting interaction with the analyte solution (i.e., low solvent affinity). In fact when sample solutions of the same volume are deposited on different substrates, the diameter of the droplet on the surface depends on the degree of affinity (wetting) between the solution and the substrate, and obviously it is desirable to confine the sample within the smallest possible area. Typical Raman substrates are: quartz, glass covered by a foil of gold, stainless steel, Teflon, SpectRIM™ Slide (Tienta Sciences, Inc)<sup>29,30</sup>. It has been shown that the DCDR method is most sensitive to low-protein concentrations when depositions are performed on hydrophobic substrates (such as SpectRIM slides).<sup>31</sup> The importance of substrates and wetting interaction has been discussed in a recent paper based on the

careful analysis of the shape of the deposits after the desiccation process.<sup>32</sup> The main parameter to play with is the initial contact angle ( $\theta_0$ ). Depending on that, different time evolutions of the shape have been observed (see Figure 2.19). For low contact angle (Figure 2.19(a),  $\theta_0 < \theta_{0c} \cong 30^\circ$ ) the drop progressively flattens following solvent evaporation. In this case the evaporation is faster than the formation of the glassy skin that protects proteins from desiccation. For all higher contact angles (Figure 2.19(b) and (c),  $\theta_{0c} < \theta_0$ ) a surface instability takes place and, following  $\theta_0$ , this instability results in different drop shapes. In particular for intermediate contact angles such as:  $\theta_{0c} < \theta_0 < \theta_0^* \cong 60^\circ$ , the final shape is a Mexican hat (Figure 2.19(b)), while for higher contact angles:  $\theta_0^* \cong 60^\circ < \theta_0$ , the final shape is crater-like. In both these cases the formation of the glassy skin surrounding the drop is faster than total evaporation, ensuring protein hydration. Protein-water interactions play a critical role in protein folding and stability.<sup>33</sup> Although the DCDR pre-concentration (solvent evaporation) process produces protein deposits that are in a solid-like state, they appear to remain well hydrated. It has been shown recently that proteins remain substantially hydrated in the DCDR deposits and that the secondary structure of proteins is largely preserved in DCDR deposits.<sup>31</sup> This is particularly true for small proteins like insulin and lysozyme.<sup>34,35,36,30</sup>

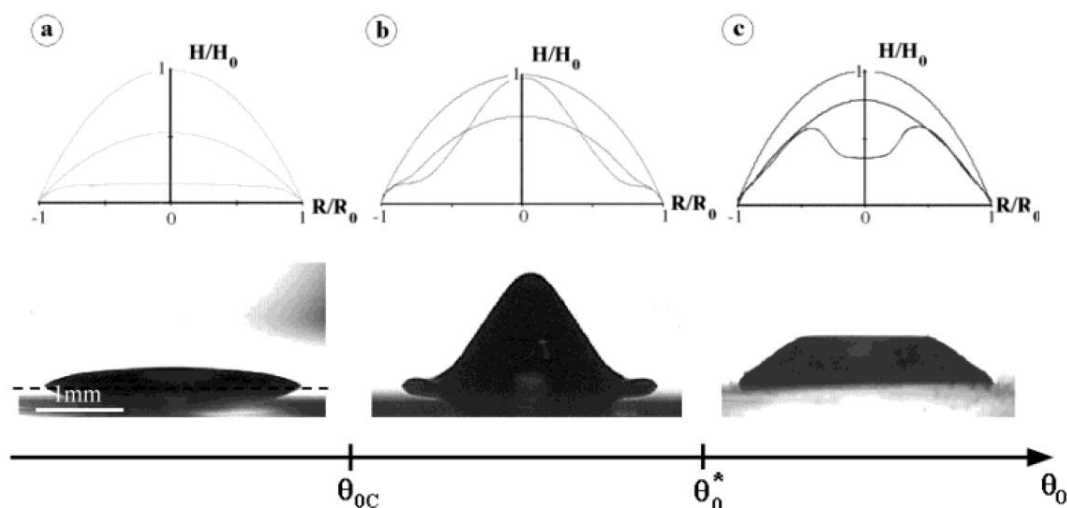


**Figure 2.19** – Figure from ref. 32. (top) Superimposition of dimensionless profiles of drops of dextran solutions recorded at different time during desiccation. the initial concentration is the same in all three cases, while initial contact angle ( $\vartheta_0$ ) increases from case (a) to (c).  $H_0$  and  $R_0$  are the initial height and radius of the drop, respectively. (below) Corresponding digitalized side views of the drops taken 1h after the beginning of the experiment.

Another advantage in using the DCDR method with respect to the standard Raman technique is the possibility of an accurate determination of the amide I band shape ( $1640\text{--}1780\text{ cm}^{-1}$ ). The Raman shift of the O–H bending of water is around  $1650\text{ cm}^{-1}$  and overlaps with the protein amide I band. Because of the large difference between the Raman cross section of the protein Amide I band and the OH bending of water, water interference in the fingerprint region of DCDR spectra is actually insignificant.

## 2.4 – Band Fitting: Adopted Method and Errors

The fitting procedure used to analyze all the sample in this thesis (both Raman and IR) is basically the same. It is a procedure of minimization of the  $\chi^2$  based on the Levenberg-Marquardt

Algorithm (LMA).<sup>37,38</sup> This procedure was joined by the second derivative method that is a well established technique to determine the number and the frequency of the components to the fit.<sup>39</sup> Each component was fitted by means of a convolution of Lorentzian and Gaussian functions (despite this the out of the fit was almost always a Gaussian function, that is reasonable for these complicated systems). Most of the times the two above mentioned method were sufficient in obtaining a reproducible and reliable result also in the analysis of the Amide bands. But in the case of the fitting procedure of the strongly overlapped Amide I bands in the Raman spectra (see section 4.2) or for the Amide I band of the IR spectra (usually less structured than the Raman Amide I band), it was necessary to use a resolution-enhancement technique: the Fourier-self deconvolution (FSD).<sup>17,40</sup> The FSD is a well established narrowing methodology that helps researcher in their fitting routine. To control the goodness of the deconvolving parameters that each times have to be chosen (full width half maximum, FWHM, and noise reduction, NR) it is common practice to compare the outfit of the FSD with that of the second derivative technique (see Figure 2.20).

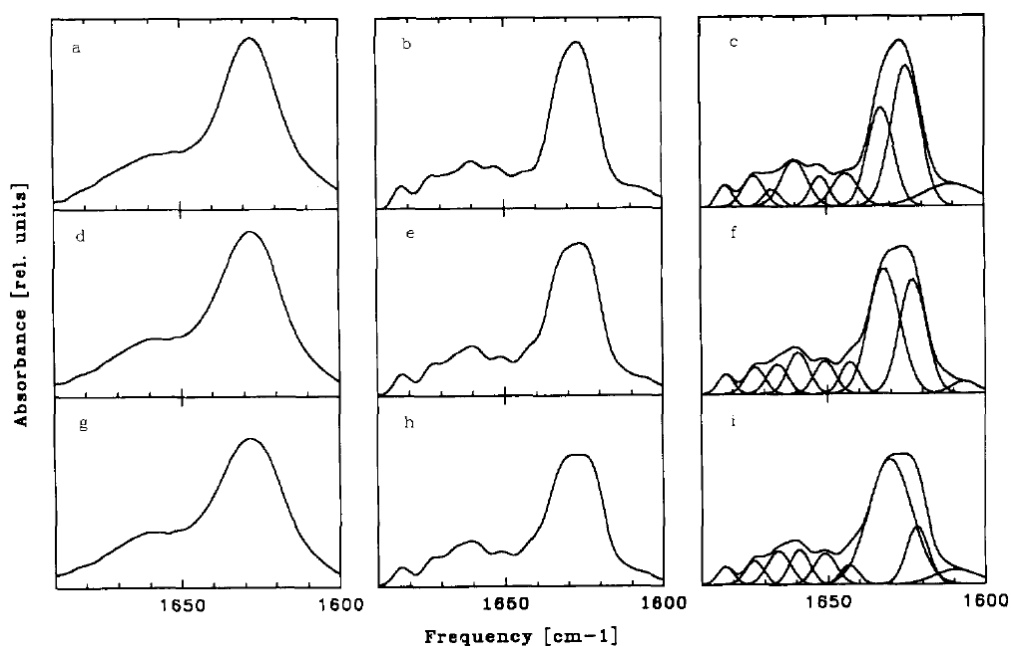


**Figure 2.20** – (a, d, g) The experimental spectra, (b, e, h) the deconvolved and (c, f, i) the deconvolved and fitted infrared spectra of gramicidin in dioleoylphosphatidylcholine (DOPC). Pressure: upper row (a, b, c): 0.044 GPa; middle row (d, e, f): 0.91 GPa; bottom row (g, h, i): 1.35 GPa. From ref.40.

On analyzing the Amide bands (mainly the Amide I band) it is possible to make a quantitative estimation of the secondary structure of a protein by studying the area of a single component of the fit (ascribed to a secondary structure of the protein) respect to the total area of the Amide band (see how the fitting results provide useful information in the following chapters).

Errors associated with estimated percentages of the secondary structure are those typical for the fitting procedure used.<sup>41,42</sup> In particular we repeated every fitting procedure for at least three times varying every time the set of initial parameters. Amide I band estimates were significantly better than amide III band estimates. This reflects the greater intensity and sharpness of the amide I band as well as reduced interference from adjacent non-structure peaks. The error found for the estimated structures from Amide I band is less than 5% for  $\alpha$  helix, around 8% for  $\beta$  sheet. Estimates for disordered structures (turn and random coil) were least accurate,<sup>13</sup> reflecting perhaps the multiple individual and variable peaks that represent these motifs. Every time that a series of

Raman and IR spectra were acquired as a function of an external perturbation (like high pressure) or as a function of time, the following spectrum of the series was fitted starting from the output of the previous one.<sup>40</sup> To demonstrate the robustness of the estimation technique adopted here, estimate accuracies for proteins within and outside the reference set were found to be similar.

## **2.5 – Materials**

### ***Bovine Pancreatic Insulin***

For this PhD work Bovine Pancreatic Insulin was purchased from Sigma Aldrich: I6634 (used for powder measurements) and I5500 (used for solution measurements). Both the samples contain a percentage of Zinc equal to 0.8% while the loss on drying was different: 10% for the I6634 and 5% for I5500.

### ***Hen Egg White Lysozyme***

For this PhD work Hen Egg White Lysozyme was purchased from Fluka: 62970. In this case the protein is lyophilized (i.e. completely dehydrated).

## **2.6 – Fibrillation Protocols**

Among the different protocols that can be used to fibrillate proteins,<sup>43,44,45</sup> in this thesis a thermo-chemical process was adopted both for Insulin and Lysozyme.

### ***Insulin***

Two sets of Insulin fibrils were prepared. The initial preparation was common to both of them: a 2mM solution was firstly prepared in distilled, purified water at a low pH (pH=2 by adding HCl). The solution was gently mixed to ensure the homogeneity but at the same time to avoid possible aggregation of the protein.<sup>46</sup> The temperature of the solution was then gradually increased with a rate of 10°C / h up to 80°C. The difference between the two sets of fibrils is simply the time (maturation time) at which the two solutions were kept at the maximum temperature: 4 and 22 hours. The two samples allowed for an analysis of the fibrillation process since different maturation times means different extent and quality of the protein aggregation<sup>47</sup> (see Chapter 3 for more details). The two samples will be thus denoted as fibrillar-4h and fibrillar-22h in the following Chapters.

### ***Lysozyme***

A rather similar procedure was adopted for preparing Lysozyme fibrils. In this case 14 mg of Lysozyme were dissolved in 1 ml of distilled, purified water. The pH of the solution was lowered by adding HCl (pH=2) and the temperature was gradually increased with a rate of 10 °C / 1h up to 72°C.<sup>48</sup> The maturation time in this case was very long since the solution was left at high temperature for 6 days.

## *Bibliography of Chapter 2*

- 
- <sup>1</sup> Elliott A, Ambrose E.J., *Nature*, 1950, 165, 921–922.
- <sup>2</sup> Krimm S, Bandekar J., *Adv. Protein Chem.*, 1986, 38, 181–364.
- <sup>3</sup> J.T. Edsall, *J. Chem. Phys.*, 1936, 4, 1.
- <sup>4</sup> S. Darmon and G.B.B.M. Sutherland, *J. Am. Chem. Soc.*, 1947, 69, 2047.
- <sup>5</sup> A. Elliott and E.J. Ambrose, *Discuss. Faraday Soc.*, 1950, 9, 246.
- <sup>6</sup> K. Dobriner, E.R. Katzenellenbogen and R.N. Jones, 'Infrared Absorption Spectra of Steroids', Interscience, New York, 1953.
- <sup>7</sup> R.C. Lord, G.J.Jr, *Spectrochim. Acta*, 1967, 23A, 2551-2593.
- <sup>8</sup> Chapman D. *Q Rev Biophys.*, 1975, 8(2), 185–235.
- <sup>9</sup> Bransden and Joachain, *Physics of Atoms and Molecules*, Prentice Hall, 2<sup>nd</sup> edition.
- <sup>10</sup> David W. Hahn, report: "The Raman Scattering Theory", February 2007 and reference therein.
- <sup>11</sup> Raman C.V., Krishnan K.S., *Nature*, 1928, 121, 501.
- <sup>12</sup> Rina K. Dukor, "Handbook of Vibrational Spectroscopy, Vol. I", Biomedical Applications, editors J.M. Chalmers and P.R. Griffiths, Wiley, 2002.
- <sup>13</sup> John T. Pelton and Larry R. McLean, *Analyt. Biochem.*, 2000, 277, 167–176.
- <sup>14</sup> Jilie KONG and Shaoning YU, *Acta Biochimica et Biophysica Sinica* 2007, 39(8), 549–559
- <sup>15</sup> Krimm S, Bandekar J. *Adv Protein Chem* 1986, 38, 181–364.
- <sup>16</sup> Kunihiro, K., Kim, P. and Baldwin, R.L. *Biopolymers*, 1984, 22, 59-67
- <sup>17</sup> W. Dzwolak et. al., *Biochemistry* (2006) 45: 8143-8151 .
- <sup>18</sup> D.M.Byler and H.Susi, *Journal of Industrial Microbiology*, 1988, 3, 73-88.
- <sup>19</sup> <http://www.elettra.trieste.it/beamlines/SISSI/>
- <sup>20</sup> A. Jayaraman, *Rev. Sci. Instrum.*, 1986, 57, 1013.
- <sup>21</sup> G. J. Piermarini, S. Block, J. D. Barnett, and R. A. Forman, *J. Appl. Phys.* 1975, 46, 2774-2780.
- <sup>22</sup> H.K. Mao, J. Xu, and P.M. Bell, *J. Geophys. Res.* 1986, 91, 4673.
- <sup>23</sup> G.J. Piermarini and S. Block, *Rev. Sci. Instrum.* 1975, 46, 973.
- <sup>24</sup> D.R. Ragan, R. Gustacsen, and D. Schieferl, *J. Appl. Phys.* 1992, 72, 5539.
- <sup>25</sup> Jacob Filik and Nicholas Stone, *Analyst*, 2007, 132, 544–550.
- <sup>26</sup> L. A. Lyon, C. D. Keating, A. P. Fox, B. E. Baker, L. He, S. R. Nicewarner, S. P. Mulvaney and M. J. Natan, *Anal. Chem.*, 1998, 70, 341R.
- <sup>27</sup> N.M.B. Perney, J. J. Baumberg, M.E. Zoorob, M.D.B. Charlton, S. Mahnkopf and C.M. Netti, *Opt. Express*, 2006, 14, 847.
- <sup>28</sup> R.D. Deegan et al., *NATURE*, 1997, 389.
- <sup>29</sup> D. Zhang, Y. Xie, M. F. Mrozek, C. Ortiz, V. J. Davisson and D. Ben-Amotz, *Anal. Chem.*, 2003, 75, 5703.
- <sup>30</sup> C. Ortiz et al., *Anal. Biochem.*, 2006, 353, 157–166.
- <sup>31</sup> C. Ortiz et al., *Analytical Biochemistry*, 2004, 332, 245–252.
- <sup>32</sup> Y. Gorand et al., *Langmuir*, 2004, 20, 12.
- <sup>33</sup> G.I. Makhatadze, G.M. Clore, A.M. Gornenborn, *Nat. Struct. Biol.* 1995, 218, 852–855.



- 
- <sup>34</sup> Yu, N.-T.; Liu, C. S. *J. Am. Chem. Soc.* 1972, 94, 3250-3251. Yu, N.-T.; Liu, C. S.; O'Shea, D. C. *J. Mol. Biol.* 1972, 70, 117-132.
- <sup>35</sup> Pelletier, M. J.; Altkorn, R. *Anal. Chem.* 2001, 73, 1393-1397.
- <sup>36</sup> Dong, J.; Dinakarandian, D.; Carey, P. R. *Appl. Spectrosc.* 1998, 52, 1117-1122.
- <sup>37</sup> D.W. Marquardt. *SIAM Journal of Applied Mathematics*, 1963, 11(2):431-441.
- <sup>38</sup> K. Levenberg. A Method for the Solution of Certain Non-linear Problems in Least Squares. *Quarterly of Applied Mathematics*, 1944, 2(2):164-168.
- <sup>39</sup> Byler, D. M., and Susi, H., *Biopolymers*, 1986, 25, 469-487.
- <sup>40</sup> L. Smeller, K. Goossens, K. Heremans, *Vibrational Spectroscopy*, 1995, 8, 199-203.
- <sup>41</sup> J. Grdadolnik, *Bulletin of the Chemists and Technologists of Macedonia*, 2002, 21, 1, 23-34.
- <sup>42</sup> G. Vedantham, H.G. Sparks, S.U. Sane, S. Tzannis, and T.M. Przybycien, *Analytical Biochemistry*, 2000, 285, 33-49.
- <sup>43</sup> Ahmad, A., Millett, I. S., Doniach, S., Uversky, V. N., and Fink, A. L., *J. Biol. Chem.*, 2004, 279, 14999-15013.
- <sup>44</sup> Nielsen, L., Frokjaer, S., Brange, J., Uversky, V. N., and Fink, A. L., *Biochemistry*, 2001, 40, 8397-8409.
- <sup>45</sup> C. Ortiz, D. Zhang, A. E. Ribbe, Y. Xie, D. Ben-Amotz, *Biophysical Chemistry*, 2007, 128, 150-155.
- <sup>46</sup> S. Grudzielanek, V. Smirnovas and R. Winter, *J. Mol. Biol.*, 2006, 356, 497-509.
- <sup>47</sup> F. Librizzi and C. Rischel, *Protein Science*, 2005, 14, 3129-3134.
- <sup>48</sup> M. Xu, V.V. Ermolenkov, V.N. Uversky, and I.K. Lednev, *J. Biophoton.* 2008, 1(3), 215-229.



# *Chapter 3*

## *Bovine Pancreatic Insulin & Hen Egg White Lysozyme*

In this Chapter, a brief summary of the state of the art about vibrational spectroscopy studies carried out on Insulin and Lysozyme is reported and discussed. Raman spectra collected on both proteins in their native and fibrillar state are presented and analyzed on the light of the current knowledge.

The infrared spectrum, collected on the insulin in solution, is also discussed in the final paragraph of this Chapter.

### 3.1 Bovine Pancreatic Insulin

Raman measurements were performed on native Bovine Pancreatic Insulin (BPI) both in powder and in solutions. The aim was characterizing the Raman spectra of the protein and comparing the results obtained with those present in literature (see next paragraph). The Raman spectra of fibrillar samples were also collected and analyzed to have reference spectra for renaturation experiments (see Chapter 6) and to compare the denaturing effects of temperature and pressure (see Chapter 5).

#### 3.1.1 Insulin: State of the Art

In 1972 Yu, Liu and O'Shea published on the Journal of Molecular Biology the paper entitled "Laser Raman Spectroscopy and the Conformation of Insulin and Proinsulin".<sup>1</sup> This fundamental article put the basis for every following spectroscopic work on Insulin. From the comparison between the native and thermo chemical denatured BPI in the solid state (see Figure 3.1) Yu et al. confirmed that fibrillar insulin exists in a  $\beta$  conformation, as it was predicted by Ambrose and Elliott in 1951,<sup>2</sup> and they were able to assign for the first time the Raman marker of denaturation.

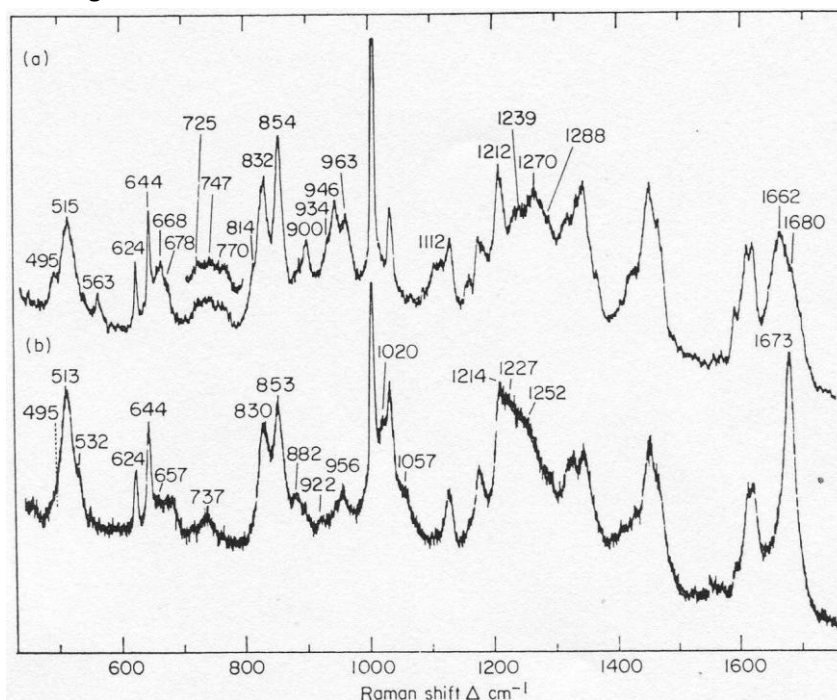


**Figure 3.1** – Raman spectra of native and denatured insulin (bovine) in the solid state taken from ref. 1. (a) Native zinc-insulin crystalline powder, resolution  $4\text{ cm}^{-1}$ . (b) Denatured insulin (heat precipitated = fibrils), resolution  $5\text{ cm}^{-1}$ . The solution from which the sample was prepared had a concentration of  $10\text{ mg/ml}$  at  $\text{pH } 2.4$ . The laser power for both samples was  $200\text{ mW}$  at  $514.5\text{ nm}$ .

The largest change in the Raman spectra of native and denatured insulin shown in Figure 3.1 concerns the Amide I band that shifts from around  $1660\text{ cm}^{-1}$  (with a shoulder near  $1685\text{ cm}^{-1}$ ) to  $1673\text{ cm}^{-1}$  and sharpened considerably upon denaturation. The frequency shift was interpreted as due to the weakening of the hydrogen bonding, and the sharpening as a reflection of the greater uniformity in the hydrogen bonding. But they also pointed out that strong coupling between adjacent peptide units (both intra- and inter-chain coupling) should equally play an important role in determining the frequency of the Amide I vibration.

Frequencies in $\text{cm}^{-1}$		Tentative assignments
Native (crystals)	Denatured (solid)	
	265 (0.9)	} Skeletal bending
333 (0.9)	325 (0.8)	
410 (0.8)	420 (0.5)	
467 (0.8)	460 (0.4)	
495 (1.2)	480 (0.3)	
515 (3.2)	513 (4.4)	$\nu(\text{S}-\text{S})$
	532 (1.5sh)	Skeletal bending
563 (1.0)		
624 (2.0S)	624 (2.0S)	Phe
644 (3.6S)	644 (3.6S)	Tyr
668 (2.0)	657 (1.1)	} $\nu(\text{C}-\text{S})$ of the $\text{C}-\text{S}-\text{S}-\text{C}$ group
678 (1.0sh)	680 (1.3)	
725 (0.8T)		} Skeletal bending
747 (0.8T)	737 (0.9B)	
770 (0.8T)		
814 (1.4sh)		
832 (4.4D)	830 (3.9D)	} Tyr
854 (5.5D)	853 (4.5D)	
900 (2.0)	882 (1.5)	} $\nu(\text{C}-\text{C})$
934 (2.0sh)	922 (0.8)	
946 (3.2D)		
963 (2.9D)	956 (1.6B)	
1004 (10.0S)	1004 (10.0S)	Phe
	1020 (2.5)	$\nu(\text{C}-\text{N})$
1032 (3.3S)	1032 (3.3S)	Phe
	1057 (1.3sh)	} $\nu(\text{C}-\text{N})$
1112 (1.5sh)		
1128 (1.8)	1127 (1.7)	
1162 (0.9)	1161 (0.5sh)	
1177 (2.4)	1175 (2.4)	Tyr
1212 (4.6S)	1214 (4.9)	Tyr & Phe
	1227 (4.3)	} Amide III ( $\beta$ -structure)
	1252 (4.0sh)	
1239 (5.0sh)		Amide III (random-coil)
1270 (5.3)		Amide III ( $\alpha$ -helical)
1288 (4.7sh)		Amide III ( $\alpha$ -helical)
1322 (2.0sh)	1327 (2.0D)	} CH deformation
1344 (4.0)	1343 (3.1D)	
1367 (1.6sh)		
	1407 (0.4sh)	} Symmetrical $\text{CO}_2^-$ stretching
1425 (2.5sh)	1422 (1.1sh)	
1450 (5.0)	1450 (3.8)	} $\text{CH}_2$ deformation
1462 (4.6sh)	1462 (3.1sh)	
1587 (1.3)	1587 (1.0sh)	Phe
1607 (3.6D)	1607 (3.5D)	Phe & Tyr
1615 (3.6D)	1615 (3.5D)	Tyr
1662 (4.6)		Amide I ( $\alpha$ -helical structure)
	1673 (8.6S)	Amide I ( $\beta$ -structure)
1685 (4.0sh)		Amide I (random-coil)
	1735 (0.4B)	-COOH

**Table 3.1** – Raman spectra of insulin (bovine) (200-1800  $\text{cm}^{-1}$ ) taken from ref. 1.

Other spectral changes on denaturation in the Raman spectrum were observed in the following spectral regions: the disulphide bonds (S-S) and the C-S stretching (around 515  $\text{cm}^{-1}$  and 670  $\text{cm}^{-1}$  respectively), the skeletal bending (around 400-500, 550 and 750  $\text{cm}^{-1}$ ) and the skeletal stretching (900-1000 and 1050-1150  $\text{cm}^{-1}$ ). All these changes were both in frequencies and in shapes and are still now considered Raman markers of insulin denaturation. In Table 3.1 the complete assignments made by Yu et al. is reported.

A comparison between the spectra collected from a 100 mg/ml solution of BPI in doubly distilled and purified water at pH 2.4 and from solid BPI obtained from air drying the same solution was also made. They observed that on going from solid to solution BPI there was a relaxation of the backbone side chain and side groups resulting in a slight increase in the random coil structure. Slight changes in line shape also occurs around  $950\text{ cm}^{-1}$  in the region of the C-C stretching modes. Except for these small differences, the rest of the spectra show very good agreement. Similar results were obtained comparing solid and liquid phase of a solution at pH 8.3.

In more recent time literature has focused on understanding the mechanism of insulin fibrillation. Nielsen et al.<sup>3</sup> investigated the rate of fibrillation of insulin varying the protocol of thermo-chemical denaturation. They used FTIR (Fourier Transform Infrared) spectroscopy to study the secondary structure of BPI samples and TEM (Transmission Electron Microscopy) to determine the 3D structure of fibrils. Moreover the percentage of fibrils in every sample was determined by UV absorption (276 nm) of the supernatant obtained through centrifugation (3000 RPM) of the gel in which the sample was after the denaturing process.

He found that the rate of fibrillation and the fibrils morphology depend both on the medium that was used to lower the pH of the solution and from the temperature used in denaturing (see Figure 3.2).

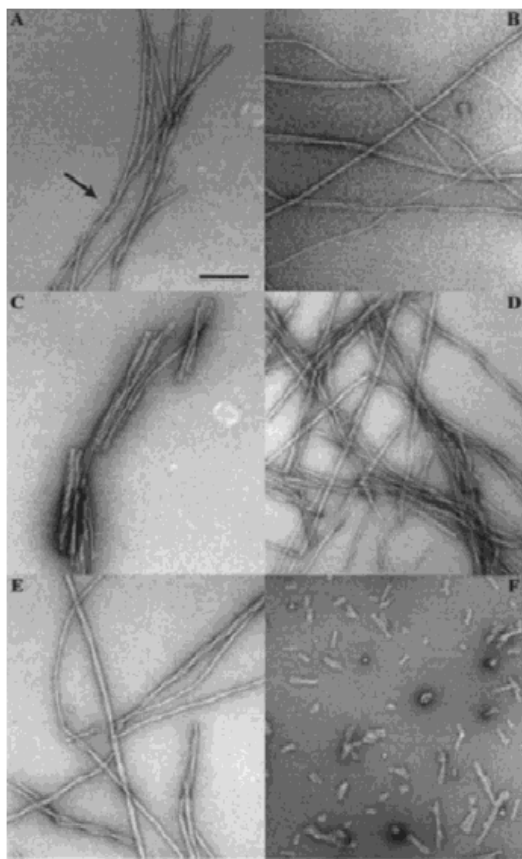


**Figure 3.2** – Image from ref. 3. Negative staining TEM of BPI fibrils prepared at pH 1.6 in(A) 0.1 M HCl heated at 60 °C, (B) 8.3 M acetic acid heated at 60 °C, (C) 8.3 M acetic acid, 0.1 M NaCl heated at 60 °C,(D) 0.1 M HCl rotated at 37 °C, (E) 0.1 M HCl heated at 80 °C, and (F) 0.1 M HCl heated at 80 °C and freeze–thawed six times. The scale bar represents 100 nm.

The same type of study was conducted by Dzwolak that in a series of papers studied the effect of ethanol on insulin fibrillation.<sup>4,5</sup> He found that the use of ethanol as cosolvent profoundly diversified the effect on the amyloidoigenic self assembly of insulin, yielding spectroscopically and morphologically distinguishable forms of fibrils. In particular, increasing the concentration of the cosolvent promotes curved, amorphous, and finally donut-shaped forms (see Figure 3.3).

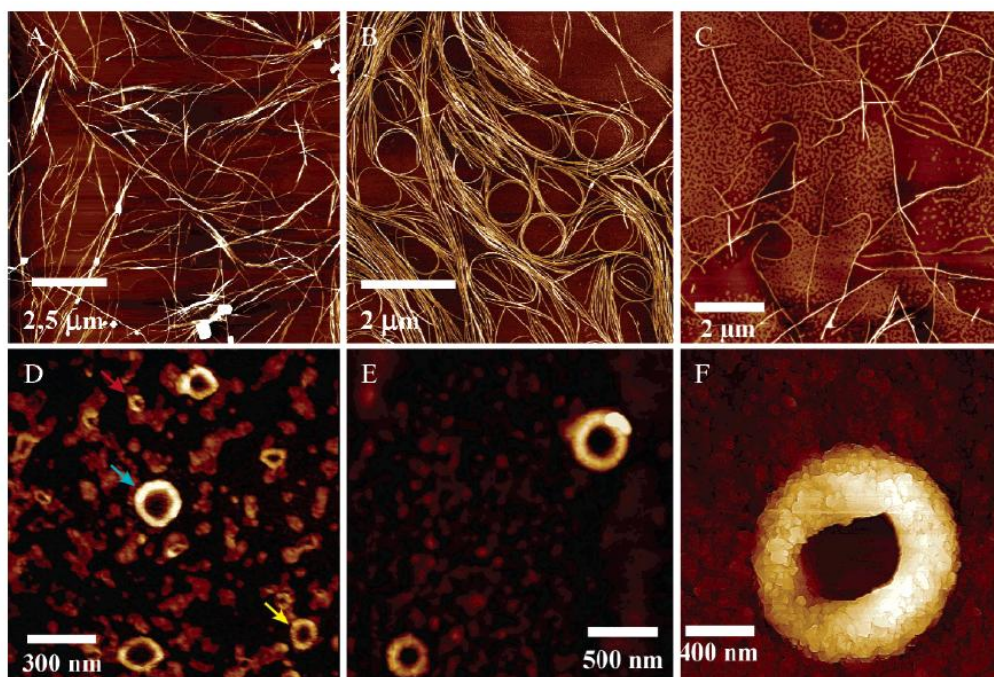


**Figure 3.3** – Image from ref. 4. AFM height images of insulin aggregates obtained through a 24 h incubation of 0.1 wt % native protein at pH 1.9 and 60 °C in the presence of increasing concentrations of ethanol: 0 (A), 5 (B), 20 (C), 40 (D), and 70 wt % (E and F).

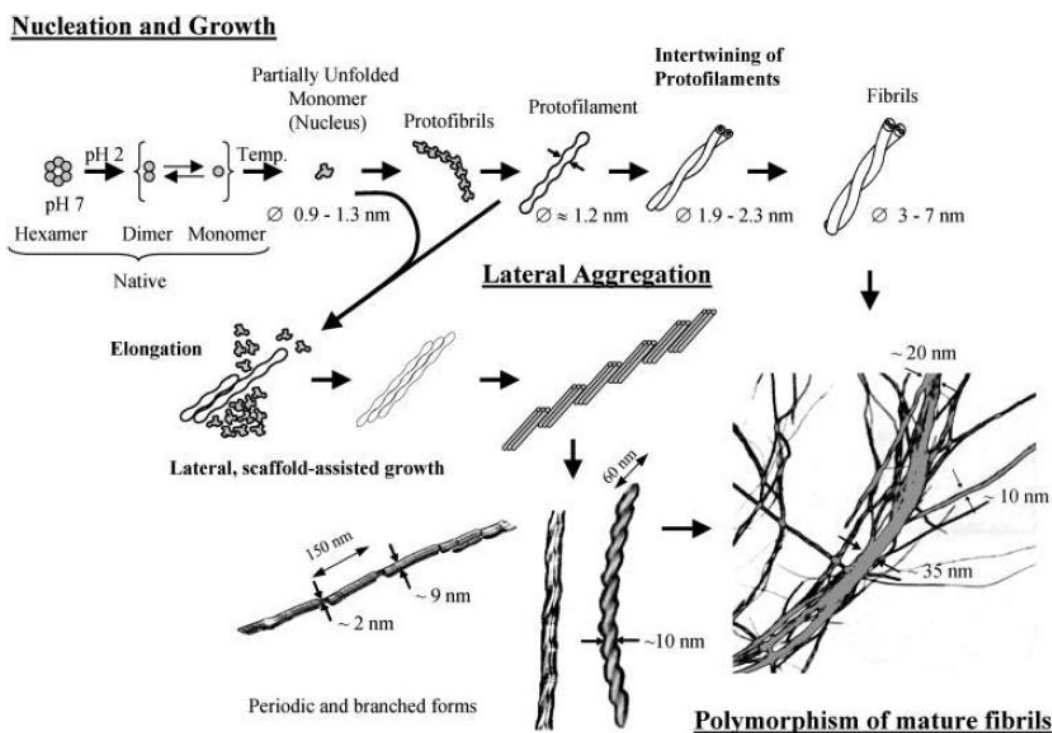


**Figure 3.4** – Image from ref. 6. General scheme of the multi-pathway fibrillation of insulin. The lateral interaction of early, prefibrillar forms with protofibrils and protofilaments, followed by the lateral association of protofilaments, is a self assembly route alternative to the hierarchical intertwining of protofilaments. The observed polymorphism of mature amyloid samples suggests that, under the given conditions, insulin fibrillation proceeds from both pathways.

The influence of ethanol on insulin aggregation shows a non-monotonic character, that was explained by Dzwolak with a preferential exclusion at low concentration of ethanol and direct



alcohol-protein interactions at higher concentrations. He concluded that the perturbed hydration of aggregation nuclei appears to be a decisive factor in selection of a dominant mode of  $\beta$  strand alignment in the fibrils. Thanks to all these efforts the pathways of insulin fibrillation were finally achieved (see Figure 3.4).<sup>6</sup>

The challenge is nowadays mostly directed to isolate the pre-fibrillar states in the insulin fibrillation process (see Figure 3.4). In this scenario high pressure finds its natural place, as it acts in a very clean and controlled way, allowing the access to the intermediate state of denaturation and fibrillation processes (see section 1.2.1 for more details on pressure and proteins).

Insulin shows a peculiar huge resistance to high pressure. While most of the proteins denature at pressure lower than 1 GPa, it is known that no plastic (irreversible) structural modifications occur on insulin at least up to pressures of the order of 1.2 GPa.<sup>7</sup> Dirix et al. (see ref. 7) performed a FTIR study on a 20 mg/ml solution of insulin at pH 2. They found that at the maximum pressure reached (1.2 GPa) the secondary structure of insulin varies only of a small percentage in the  $\beta$  structure that decrease in favor of the  $\alpha$  structure and that it was a completely reversible process. Moreover they found that the pressure treated sample was less prone to aggregate at high temperature. Their conclusion was that the elastic effect of pressure on going from 0 to 1.2 GPa involves bond length, hydration and protein cavity, but that it was not accompanied by any conformational change. The reason for such a huge structural resistance to high pressure is still basically lacking. To this respect, it is worth to notice that the investigation of insulin-water solution at pressure higher than that can be strongly biased by pressure-induced ice-forming.

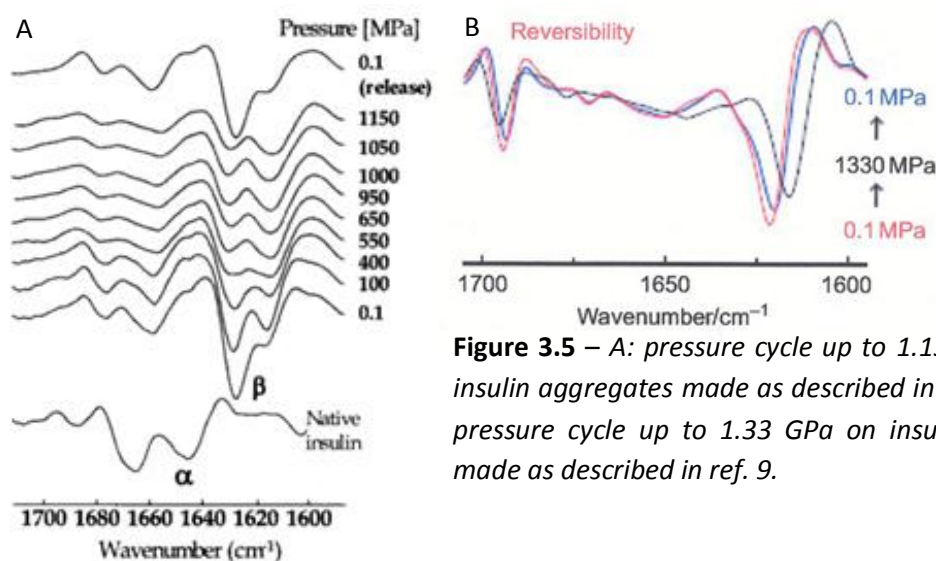


**Figure 3.5** – A: pressure cycle up to 1.15 GPa on insulin aggregates made as described in ref. 8. B: pressure cycle up to 1.33 GPa on insulin fibrils made as described in ref. 9.

Pressure was used also to study the behavior of aggregates induced by thermo processes<sup>8</sup> and of fibrils.<sup>9</sup> The use of pressure as a co-variable in denaturation and fibrillation process is reported in the paper of Grudzielanek of 2006.<sup>10</sup> The same author recently published an important work on the role of pressure on the nucleation rate of insulin under fibril-forming conditions.<sup>11</sup> He used classical nucleation theory with a new pressure-volume term to better understand and quantify the influence of pressure on protein aggregation/fibrillation reactions. He found that the application of pressure should have a drastic accelerating effect on the nucleation and growth process of insulin fibrils and showed that this effect arises from a volume decrease upon nucleus formation, as a less hydrated and more compact transition state is reached. This is an important point and, to our opinion can have a deep impact on the studies of proteins under pressure.



### 3.1.2 The Raman Spectra of Insulin in Native and Fibrillar Conformations

The Raman spectra of BPI in native and fibrillar conformations that are shown in Figure 3.6 and 3.7 respectively were collected using the experimental apparatus shown in Figure 2.12. Preliminary measurements on powder samples placed onto a quartz slide were performed using available filters and objectives to find the best experimental conditions. Moreover the sample homogeneity and the absence of polarization effects have been proved by repeating measurements on different sample regions.

The spectrum of native powder BPI is shown in Figure 3.6 with some labels highlighting the spectral features that mostly characterize the protein conformation and that will be analyzed throughout this thesis. In section 2.1.2 a brief introduction to the Raman spectrum of proteins has been reported, here it is possible to see how rich in information the Raman spectrum is.

Besides the side chains Phenylalanine and Tyrosine that display a quite intense Raman signal (Phe and Tyr respectively in Figure 3.6) and the well known Amide I and III bands, the Raman spectrum of BPI makes it possible to follow the tertiary conformation of the protein by the peptide backbone, that give rise to many vibrations (skeletal bending, C-C and C-N stretching), and the disulphide bonds (the S-S and the C-S stretching).

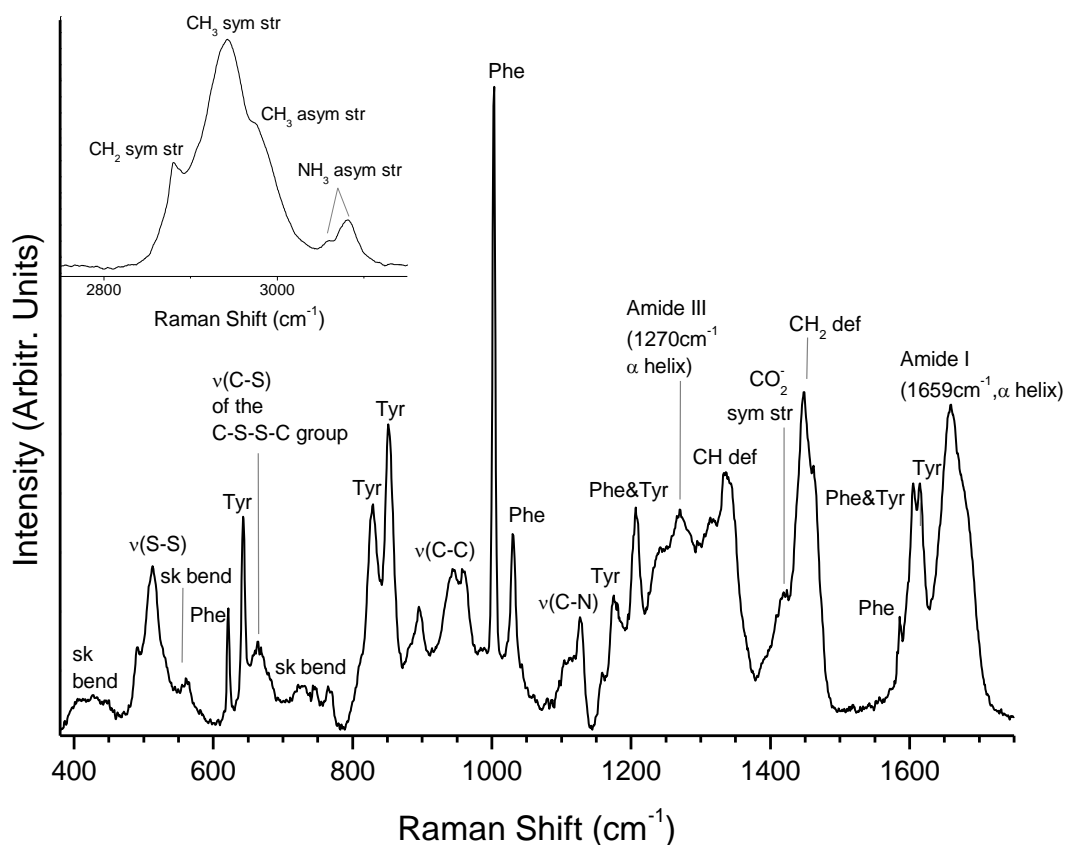


**Figure 3.6** – Raman spectrum of Bovine Pancreatic Insulin at ambient conditions. The spectrum over the high wavenumber range 2750-3150  $\text{cm}^{-1}$  is shown in the inset. [str = stretching, sym = symmetrical, asym = antisymmetrical, def = deformation, sk = skeleton, bend = bending, v() = stretching]

By comparing the spectrum collected in this thesis and shown in Figure 3.6 with those shown in Figure 3.1, it is possible to verify that no one of the signs of protein denaturation is observed in the spectrum we have collected from the native powder. To better realize the power of the Raman

spectroscopy in studying the status of a protein, it is important to compare the spectrum of native BPI with that of the protein in the fibrillar conformation.

Fibrillation of BPI was obtained following the procedure described in section 2.6. Raman spectra of insulin fibrils were obtained using a drop coating deposition Raman (DCDR) method (see section 2.3), in which the solution is deposited onto a suitable substrate (in this case a quartz slide), followed by solvent evaporation through dried vacuum.<sup>12</sup>

The Raman spectra of the insulin fibrils samples (fibrillar-4h and fibrillar-22h, see section 2.6) are shown in Figure 3.7 together with that of the native powder.

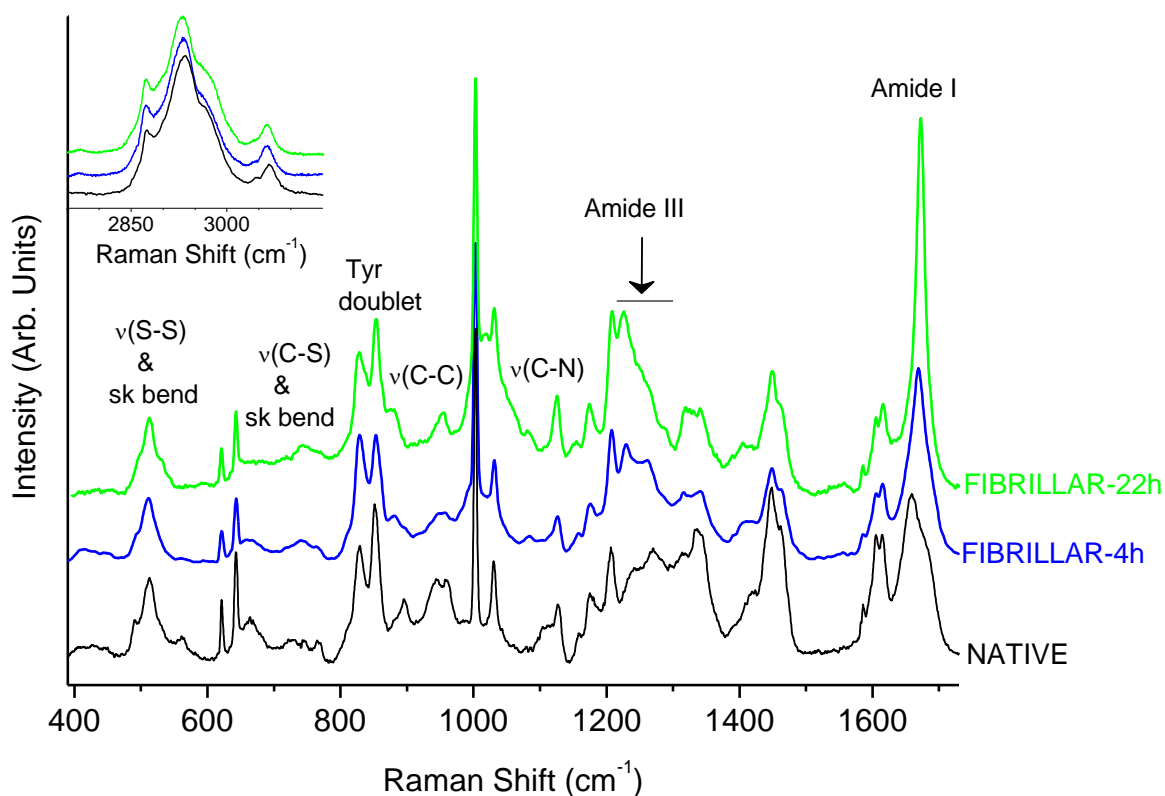


**Figure 3.7** – Raman spectra of BPI at ambient conditions: native powder (black), fibrillar-4h (blue) and fibrillar-22h (green) BPI. The Raman spectra of the three samples in the region of the CH stretching modes are shown in the inset. The vibrations related to the tertiary and secondary structures are labeled, see text for details. [sk = skeleton, bend = bending, v() = stretching]

All the spectra were normalized in the frequency region of the Phe peak, between 990 and 1015  $\text{cm}^{-1}$ . The spectral regions of Amide bands and those labeled in Figure 3.7 were the regions where differences (in frequency and/or in spectral shape) among the spectra were more evident. Following the behavior of some specific peaks in the Raman spectra it is possible to investigate the effects of the thermo-chemical process over the tertiary structure.

### S-S bonds

The correlation between the band frequencies and the conformers of the disulfide bond has been well established through normal coordinate analysis and extensive experimental investigation.<sup>13,14,15</sup>

The disulphide bridges are still present in the Raman spectra of the two fibrillar samples and their spectral shapes were rather similar whereas both apparently differ from the native sample (see Figure 3.7).

Sugeta et al. (ref. 13) performed the detailed normal mode analysis of disulfide bond model compounds and concluded that the frequency of the S–S stretching mode depends on the conformation of CCSSCC moiety (see Figure 3.8).

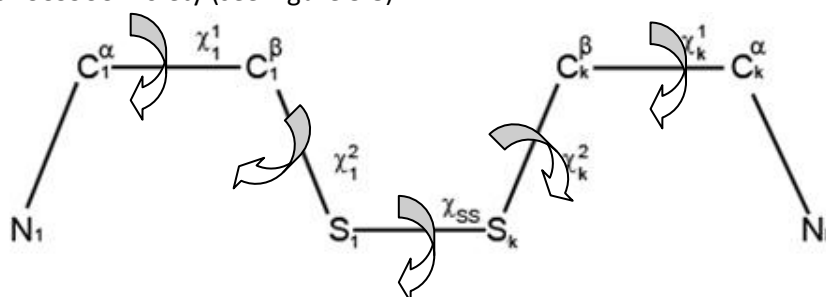


**Figure 3.8** – Definition of dihedral (torsional) angle for a cysteine disulfide bridges.

In principle, torsional flexibility about the  $C_1^\alpha - C_1^\beta$  ( $\chi_1^1$ ),  $C_1^\beta - S_1$  ( $\chi_1^2$ ),  $S_1 - S_k$  ( $\chi_{SS}$ ),  $S_k - C_k^\beta$  ( $\chi_k^2$ ) and  $C_k^\beta - C_k^\alpha$  ( $\chi_k^1$ ) bonds can give rise to a variety of conformations about the cysteine bridge (see Figure 3.8). The dihedral angle about the disulfide bond ( $\chi_{SS}$ ) is generally restricted to values of  $\pm 90^\circ - \pm 20^\circ$ .<sup>16</sup> The GGG (gauche-gauche-gauche) conformer of the disulfide bond in the CCSSCC moiety exhibits a S–S stretching band at  $508 \text{ cm}^{-1}$  and the GGT (gauche-gauche-trans) conformer has a peak at  $527 \text{ cm}^{-1}$  while the TGT (trans-gauche-trans) conformer produces a band at  $544 \text{ cm}^{-1}$ , respectively.<sup>17</sup> The fit analysis of the S-S stretching region of the Raman spectra shows only small variations of the peak frequencies. The observed differences must be indeed ascribed to peaks broadening and to an overall decrease of the intensities of these structures. The modification induced on the native protein by thermo-chemical treatments can be thus related to small variations of the average values of the dihedral angles but mainly to a larger dispersion of these values, i.e. disorder in the orientations of the CCSSCC moiety. Data thus confirm that, beside a certain level of angular disorder, thermo-chemical induced fibrillation process doesn't break the disulfide bridges<sup>18</sup> of insulin that are still present in the spectra of the fibrillar BPI.

### Skeletal modes

Within the spectral regions of skeletal bending the line at  $560 \text{ cm}^{-1}$  in the native BPI shifts to lower wavenumber in all the treated BPI samples, down to about  $555 \text{ cm}^{-1}$  in the fibrillar-4h and down to a still lower value about  $545 \text{ cm}^{-1}$  in the fibrillar-22h BPI. The three peaks at  $728$ ,  $746$ ,  $769 \text{ cm}^{-1}$  observed separately in the native BPI coalesce into a single peak at  $742 \text{ cm}^{-1}$  with a weak shoulder around  $765 \text{ cm}^{-1}$  in the treated samples. All these differences have been previously observed by the comparison between the Raman spectra of native and denatured insulin in ref. 1. The strong indication that both the treated samples have suffered of a structural reorganization of the internal polypeptide chain orientation is confirmed looking at the remarkable modifications observed in the frequency regions of the C-C and C-N stretching modes ( $890-990 \text{ cm}^{-1}$  and  $1110-1160 \text{ cm}^{-1}$ , respectively). Since these vibrational modes are considered a spectroscopic markers of the secondary structure,<sup>19</sup> their remarkable rearrangement under thermo-chemical treatment indicate an extensive unfolding of the protein backbone.

Looking at Figure 3.7 it is well clear that all the above mentioned denaturation markers strengthen on going from fibrillar-4h to fibrillar-22h.

### Tyrosine Fermi Doublet

The Tyrosine Fermi doublet (around  $830$  and  $850 \text{ cm}^{-1}$ ) is an important marker of the hydrogen bond.<sup>14</sup> Siamwiza et al.<sup>20</sup> demonstrated that the Tyr doublet arises from an energy level coupling

between the normal mode  $\nu_1$  (ring breathing fundamental) and the second harmonic  $2\nu_{16a}$  (ring deformation overtone) of the para-substituted phenolic side chain. They also pointed out that the peaks intensity ratio  $I_{850}/I_{830}$  is strongly dependent upon the hydrogen-bonding state of the phenoxyl group. In particular, a donor character of the phenoxyl group is indicated by a value of  $I_{850}/I_{830}$  around 0.30, while a value around 1.3 indicates a hydrogen bond character which is both donor and acceptor typical of a solvent exposed residue. The value found in this work for the  $I_{850}/I_{830}$  ratio is close to 1.4 in the native, to 1.1 in the fibrillar-22h and to 0.8 in the fibrillar-4h BPI. The lowering of this ratio suggests a possible decrease in solvent exposure of the Tyr residues going from native towards the misfolded states. In order to discuss these results it is worth to recall that insulin primary structure has four Tyr residues.<sup>21</sup> In the B chain Tyr26 is involved in the formation of H-bonds that build up the insulin dimer and is located in a hydrophobic part of the protein, Tyr16 is part of the long segment composing the helix located in the core of the protein. Tyr14 and Tyr19 in the A chain are both positioned in one of the two  $\alpha$  helices and are exposed to the surface of the protein. The lowest  $I_{850}/I_{830}$  value (0.8) found for fibrillar-4h BPI is in agreement with ref. 20 and suggests that the Tyr residue associated with the  $\alpha$  helix in the A chain were buried inside the protein core, revealing that the reorganization induced by the starting process of fibrillation involve the  $\alpha$  helix structure.<sup>22</sup> The intermediate value between the native and the fibrillar-4h found for the fibrillar-22h may suggest that at the end of the misfolding pathway the Tyr residues is involved in the strong hydrogen bonds that build up the fibrils.

### Amide I band

Since it is well known that different secondary structures origin different components in the Raman Amide bands (see section 2.1.2),<sup>23</sup> a standard analysis was carried out to obtain quantitative information on the secondary structures of BPI. A second derivative method together with the LMA fitting procedure was used, as described in section 2.4. In the native conformation the insulin results to have a predominantly percentage of  $\alpha$  helix (around 60%) and a minor percentage of  $\beta$  sheets (around 30%).<sup>24</sup> The result of the fitting analysis on the Amide I band is reported in Table 3.2.

	Native	Fibrillar-4h	Fibrillar-22h	
<b>Random</b>	1640	1642	1631	Frequency (cm <sup>-1</sup> )
	12	15	14	Area (%)
<b><math>\alpha</math> helix</b>	1658	1655	1657	Frequency (cm <sup>-1</sup> )
	50	10	11	Area (%)
<b><math>\beta</math> sheet inter-chain</b>	-	1669	1672	Frequency (cm <sup>-1</sup> )
	0	38	49	Area (%)
<b><math>\beta</math> sheets intra-chain</b>	1682	1683	1677	Frequency (cm <sup>-1</sup> )
	38	37	26	Area (%)

**Table 3.2** – Results of the fitting procedure on the Amide I band in native and fibrillar conformations. The frequency and the percentage of each components were reported.

Looking at the values reported in Table 3.2 for the native and the two fibrillar samples, we can clearly see that the conversion of  $\alpha$  helix into  $\beta$  structures (either intra- or inter-molecular) occurs within a rather short time interval, whereas the fibril growth, i.e. the progressive alignment of beta-sheets,<sup>25</sup> requires much longer time intervals. As a matter of fact, going from the native to the fibrillar-4h sample, the alpha helix goes from 50% to 10% and the beta structures (inter- plus intra-molecular) from 38% to 75%.<sup>26</sup> Going from the fibrillar-4h to the fibrillar-22h i.e. increasing the fibril maturation time (see section 2.6), the random coil, the  $\alpha$  helix, and the overall  $\beta$  structures

percentages keep constant within 1% (random 15%  $\rightarrow$  14%,  $\alpha$  10%  $\rightarrow$  11%,  $\beta$  75%  $\rightarrow$  75%), whereas a large conversion from  $\beta$  intra-molecular to  $\beta$  inter-molecular occurs, the former decreasing from 37% to 26%, the latter growing from 38% to 49%. The percentage of  $\beta$  inter-molecular remarkably grows in the two fibrillar samples, thus providing the spectroscopic signature of the onset of protein aggregation. As above mentioned, the simultaneous remarkable band narrowing here observed indicates that highly ordered  $\beta$ -structures are formed. The increase of intensity of the  $\beta$  inter-molecular spectral contribution and its simultaneous narrowing can indeed be considered as a clear Raman indicator for the presence of protein fibrils.

### 3.1.3 Insulin Solution: Infrared Characterization

The IR spectrum of a 2mM solution of BPI in D<sub>2</sub>O at ambient condition is shown in Figure 3.9. The components of the spectrum are labeled.

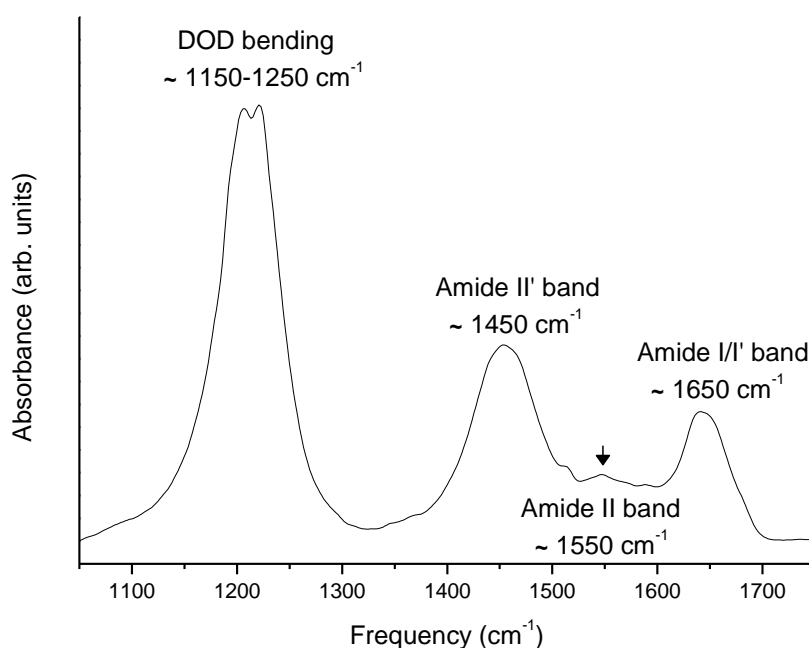


**Figure 3.9** – IR spectra of Bovine Pancreatic Insulin at 1bar and ambient temperature. The major features are labeled.

In the IR spectra the analysis of the protein conformation is mainly devoted to the fitting procedure of the Amide I band to determine the secondary structure of proteins. By applying the LMA fitting procedure together with the second derivative method and the FSD resolution enhancement technique (see section 2.4) it has been possible to determine the frequencies and the percentages of the secondary structure of the protein (see Figure 3.10). The results of the fitting procedure are reported in Table 3.3.

The amide II band is also a feature of great importance in the study in which D<sub>2</sub>O is involved. In fact the D-H exchange involves the external hydrogen of the protein in a short time and the internal one in a very long time (around a couple of hours and some weeks respectively).<sup>27</sup> This will mean that if the Amide II band loses intensity while a possibly denaturant experiment is taking place, then the D-H exchange is ongoing, the internal residues of the protein are exposed to the solvent, and the denaturation is happening.<sup>5</sup>

	BPI 2mM ambient condition	
Random	1641	Frequency (cm <sup>-1</sup> )
	13	Area (%)
$\alpha$ helix	1655	Frequency (cm <sup>-1</sup> )
	45	Area (%)
$\beta$ sheet intra-chain	1634, 1669, 1681	Frequency (cm <sup>-1</sup> )
	42	Area (%)

**Table 3.3** – Result of the fitting procedure on the Amide I region of the HEWL sample in both native and fibrillar status. The unordered structure comprise the random structure (low frequency) and the turns structure (high frequency).

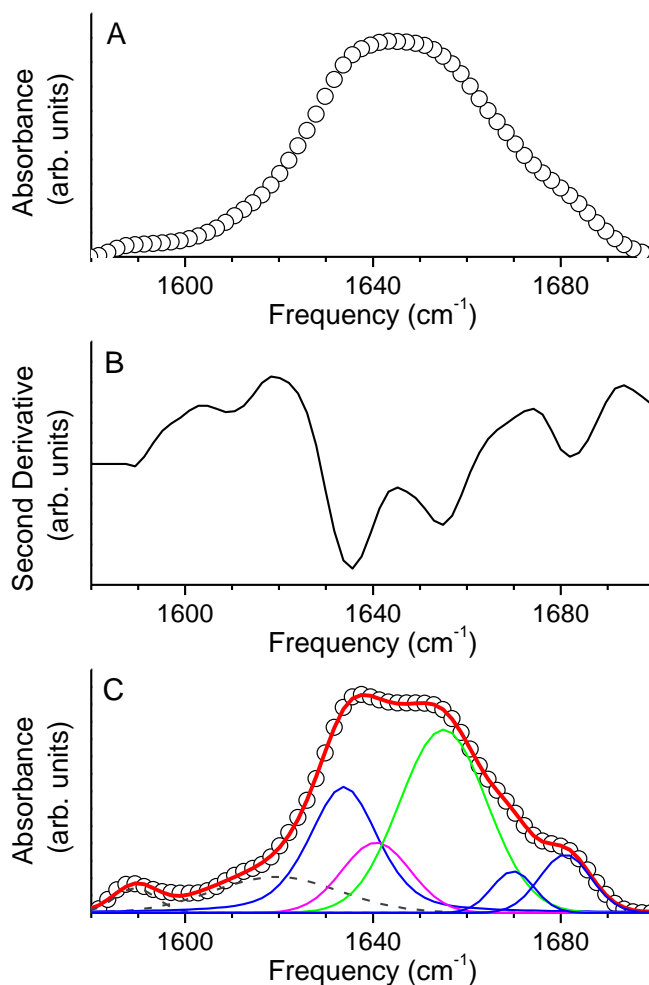


**Figure 3.10** – A: original IR spectrum of the 2 mM solution at ambient condition. B: second derivative curve. C: Fourier-self deconvolution of the original spectrum (circles, parameters: FWHM 10 cm<sup>-1</sup> and NR 0.5); fitting curve (red lines); components outside the amide I band (dashed lines); components of the Amide I band ( $\alpha$  helix, green line;  $\beta$  sheets, blue lines, and random coils, magenta line).

## 3.2 Hen Egg White Lysozyme

The Hen Egg White Lysozyme (HEWL) is one of the most studied proteins in the literature. As for the BPI measurements, the Raman spectra of this protein were performed using the apparatus in Figure 2.12. The Raman measurements of the native and of the fibrillar HEWL were collected to characterize the Raman spectra of the protein in these two conformations and also to have reference spectra for renaturation experiments (see Chapter 6).

### 3.2.1 Lysozyme: State of the Art

The first Raman spectrum of native lysozyme in solution was published by Garfinkel and Edsall in 1958 using mercury-arc excitation and photographic recording.<sup>28</sup> Since the development of high-power cw gas-lasers and the use of photoelectric recording highly improved Raman spectra have become available: Tobin<sup>29</sup> investigated crystalline lysozyme and Lord and Yu<sup>30</sup> found a spectrum of native lysozyme in aqueous solution. In 1972-1973 two papers presented an even more detailed Raman spectrum of lysozyme dissolved in water in its native state and after thermal induced denaturation (see Figure 3.11 and 3.12).<sup>31,32</sup>

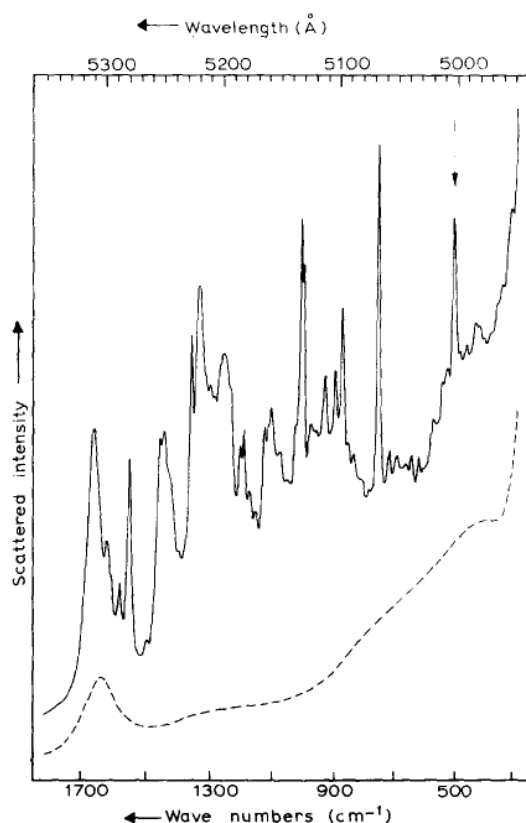


**Figure 3.11** – Raman spectrum of 21 mM lysozyme (solid line) in water, pH 5.0, temperature 25°C. From ref. 31.

Chen et al. (ref 32) concluded that heating of a 7% wt sample at 100°C for 2h produces permanent changes in those Raman frequencies that are sensitive to conformation of the peptide backbone, mainly in the Amide I, Amide III and disulfide regions. In particular, the center of the Amide III triplet at 1230-1270 cm<sup>-1</sup> was shifted to 1247 cm<sup>-1</sup> and its peak intensity was increased. The shoulders at 1238 and 1273 cm<sup>-1</sup> in the native enzyme were overlapped still further as a result of denaturation but clear-cut traces of these shoulders were still present, suggesting residual ordered structure ( $\beta$

sheet and  $\alpha$  helix, respectively). The Amide I band, as expected, shifted upward from 1660 to 1670  $\text{cm}^{-1}$  revealing more clearly the previously overlapped tryptophan line at 1622  $\text{cm}^{-1}$ . The amide I band of the irreversibly denatured enzyme had a half-width of about 60  $\text{cm}^{-1}$ , compared to about 75  $\text{cm}^{-1}$  in the native protein solution. Moreover, thermal denaturation at 100°C appears to eliminate at most one disulfide bond, but a conclusion equally compatible with observation is that the number of disulfide bonds is not altered, but their geometry is substantially changed.

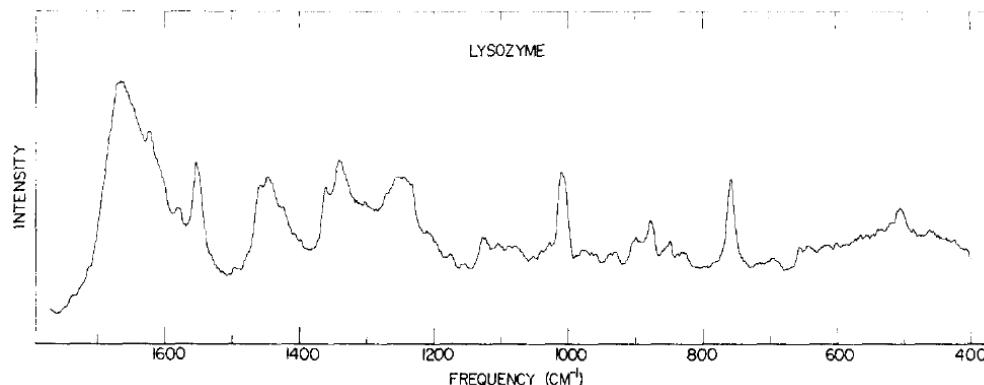


**Figure 3.12** –Raman spectrum of denatured lysozyme solution 7% w/w in water, pH 5 (0.1 NaCl). The spectrum was recorded at 32°C. The irreversibly denatured sample is obtained by heating the solution at 100°C for 2h. Figure is taken from ref. 32.

The frequencies of native and thermally denatured lysozyme from ref. 32 were reported in Table 3.4.

Frequency ( $\text{cm}^{-1}$ )	Relative intensity at $t^\circ\text{C}$			Origin of line	Frequency ( $\text{cm}^{-1}$ )	Relative intensity at $t^\circ\text{C}$			Origin of line
	32°	76°	32° (den)			32°	76°	32° (den)	
429	1	1	1	v(S-S)	1078	1	1	2	v(C-N)
509	4	4	3		1105			2	
518			1	Trp	1110	3	3	3	Tyr
527	1	1			1128	3	3	3	
540			1	Phe	1178	1	1	1	Tyr and Phe
577	1	1	1		1199	2	2	1sh	
624	1	1	1	v(C-S) disulfide	1206	2	2		1sh 3sh
645	1	1	2		1210				
661			2	v(C-S) methionine	1232				2sh 2sh
698	1	1	1		1238				
718			1	Trp	1247			8	Amide III
724	1	1			1260	5	5		
761	10	10	10	Tyr	1273	3sh	3sh	3sh	Trp and C-H deformation N-H bending vibration of the indole rings C-H <sub>2</sub> deformation
833			2		1300	1	1		
836	1	1		Trp	1304			1	Trp and C-H deformation N-H bending vibration of the indole rings C-H <sub>2</sub> deformation
854			3		1338	10	10	10	
858	1	1		v(C-C)	1363	4	4	3	Trp
879	5	5	5		1428	4sh	4sh	4sh	
900	4	4	3	Phe	1448	9	9	9	Trp
933	4	4	2		1459	5sh	5sh	5sh	
960			1	Trp	1553	9	9	9	Trp
980	1	1	1		1582	2	2	2	
1005	5sh	5sh	6sh	Phe	1622	2	2	2	Trp, Tyr and Phe
1012	8	8	10		1660	19	19		
1030	1sh	1sh	1sh		1670			25	Amide I and H <sub>2</sub> O

**Table 3.4** – The Raman frequencies and intensities of aqueous lysozyme, solution 7% by wt, pH 5, 0.1 NaCl. (den)-denaturation: the irreversibly denatured sample is obtained by heating the solution at 100°C for 2h. (sh)-shoulder. Intensity scale relative to line at 761  $\text{cm}^{-1}$  taken as (10). v( ) = stretching. From ref. 32.



Since 1958 many papers have been published in literature about the spectroscopic characterization of lysozyme in its native<sup>33</sup> and aggregated state<sup>34</sup>, its fibrillation process<sup>35,36</sup> and on the influence on lysozyme structure and function of denaturants (like ethanol<sup>37,38</sup>, urea and guanidine hydrochloride<sup>39</sup>) and other stresses (like pulsed electric field<sup>40</sup>).

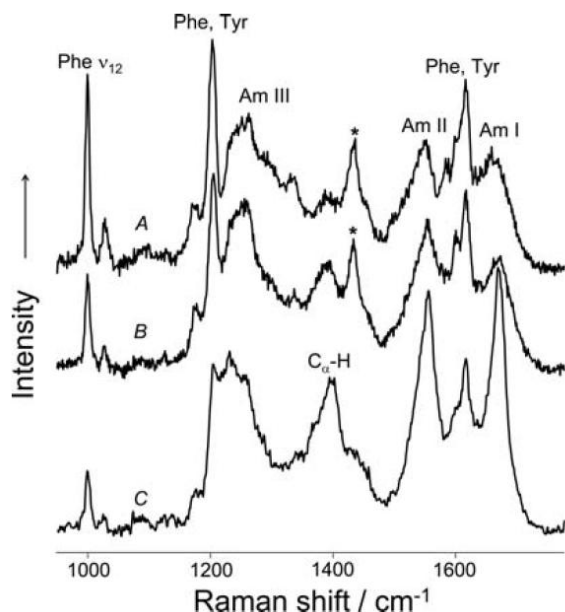


**Figure 3.13** – DUVV Raman spectrum of fibrillar lysozyme (C). The major features are highlighted by proper labels.. A and B are non incubated lysozyme. Figure from ref. 46.

As it was already observed in section 1.3, human lysozyme is related to hereditary amyloid nephropathy, a form of amyloidosis primarily presenting in the kidney associated with fibrinogen alpha chain,<sup>41</sup> apolipoprotein A1,<sup>42</sup> and lysozyme.<sup>43,44</sup> Also lysozyme from chicken (HEWL) is able to form amyloid fibrils. Moreover HEWL is readily available and represents an excellent experimental system through which to study the determinants of protein aggregation, being highly homologous to human lysozyme in structure, although only 40% identical in its sequence.<sup>45</sup>

As examples of the HEWL capability of forming amyloid fibrils the deep-UV resonance Raman (DUVRR) spectrum of fibrillar lysozyme<sup>46</sup> is shown in Figure 3.13, and, finally, the AFM height images of fibrils from ref. 35 formed from HEWL solution at pH 2.0 heated at 57°C, 60°C and 80°C are shown in Figure 3.14. In the latter, behind the fibrils, at 80°C a considerable amount of spherical aggregates were formed.

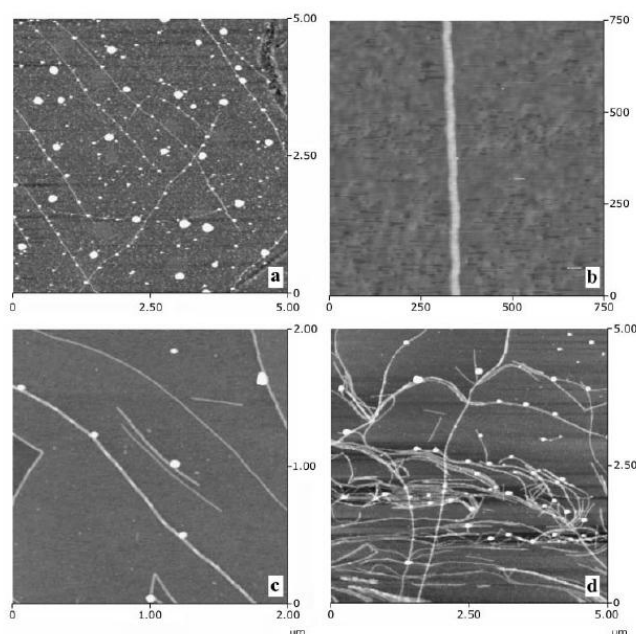


**Figure 3.14** – Figure from ref. 35. Tapping mode AFM height images of fibrils formed from lysozyme solutions at pH 2.0: (a) 1.0 wt %, 4 days at 80°C; (b) 1.0 wt %, 6 days at 60°C; (c) 2.0 wt %, 69 h at 57°C; (d) 3.4 wt %, 69 h at 57°C.

### 3.2.2 The Raman Spectra of Lysozyme in Native and Fibrillar Conformations

As for BPI, preliminary measurements on powder sample were carried out to find the best experimental conditions and verify the sample homogeneity.

HEWL fibrils were made as described in section 2.6. Raman spectra of lysozyme fibrils were obtained using a drop coating deposition Raman (DCDR) method, as previously described (see section 2.3).<sup>47</sup>

The Raman spectra of HEWL are shown in Figure 3.15 (native conformation: magenta, and fibrillar conformation: blue). By comparing the HEWL with the BPI spectra it is possible to see some common features like the disulphide bridges, the side chains Phe and Trp and the polypeptide chain vibrations. In the HEWL primary structure there is also the tryptophan side chain (Trp in the following) that has a strong Raman signal, as it can be seen from Figure 3.15. All the spectral features that will be discussed in the following are highlighted by labels in Figure 3.15.

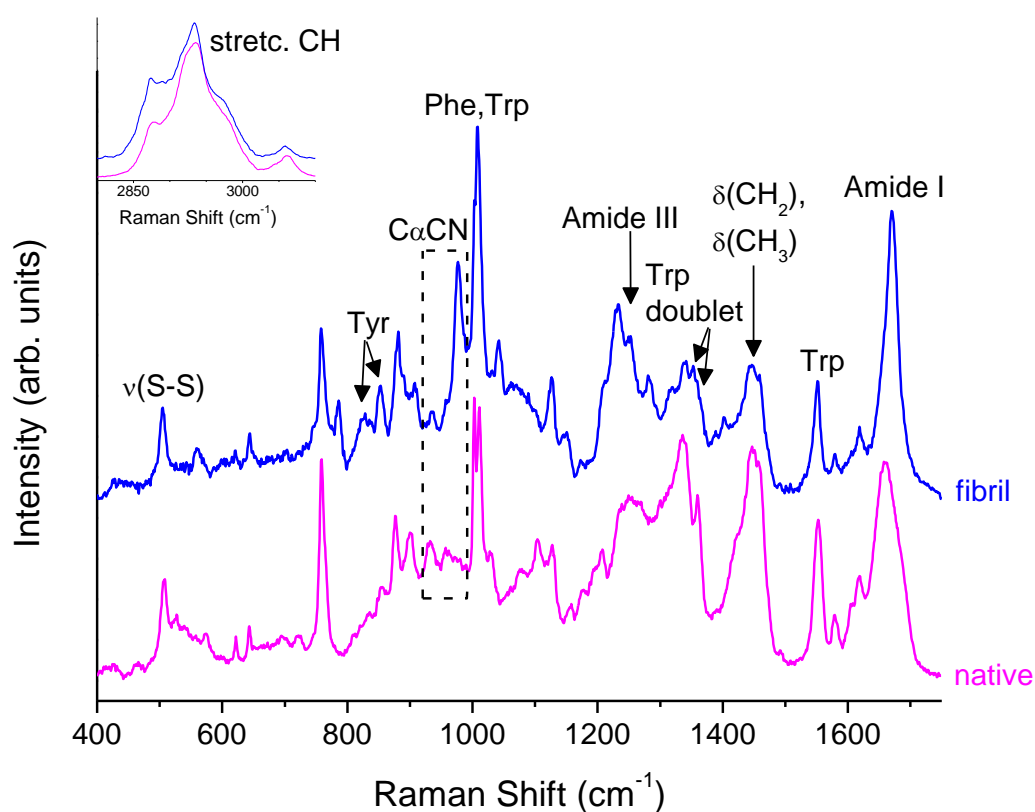


**Figure 3.15** – Raman spectra of the HEWL in native (magenta) and fibrillar conditions (blue). In the inset the region of CH stretching mode is shown. Some of the peaks that will be discussed in the text are labeled.

#### S-S bonds

The peaks ascribable to the S-S stretching vibrations are between 500-550  $\text{cm}^{-1}$  and are still present after the thermo-chemical process, even if their shapes are clearly modified. As shown in Figure 3.15, the four S-S bridges in native lysozyme (magenta curve) give rise to three Raman bands near 507, 526 and 540  $\text{cm}^{-1}$ , indicating that the intra-molecular S-S bonds in native lysozyme are in GGG, GGT and TGT conformations (see Figure 3.8 and related text),<sup>48</sup> which is in agreement with the results of van Wart et al.<sup>14</sup> With the fibril formation, the intensity of the S-S vibrations near 530 and

540 cm<sup>-1</sup> progressively decreased and disappeared, indicating a partial distortion of the dihedral angles respect to the native structure.

### C-C stretching modes

The tertiary structure can be studied mainly by the C-C stretching peaks around 930 and 960 cm<sup>-1</sup> ascribed to the  $\alpha$  and the  $\beta$  structures, respectively.<sup>49</sup> The relative intensities of the two peaks are unbalanced towards the  $\beta$  structure on going from native to fibrillar structure.

### Tyrosine and Tryptophan Fermi Doublet

The Raman spectra of HEWL both in the native and in the fibrillar conformations is characterized by the presence of two distinct Fermi doublets made by the Tyr residues (around 830-850 cm<sup>-1</sup>) and the Trp residues (around 1340-1360 cm<sup>-1</sup>). From the analysis of the relative intensities of the peaks that constitutes each Fermi doublet it is possible to learn something more about the environment of the residues and consequently about the structure of the protein.

The Tyr behavior as a function of an external perturbation<sup>50</sup> was already discussed in the analysis of the BPI Raman spectra (see section 3.1.2). In HEWL two Tyr residues are situated in the more interior loops and turns of the  $\alpha$  domain (Tyr20 and Tyr23) and a third in the loop of the  $\beta$  domain (Tyr53).<sup>22</sup> The intensities ratio  $I_{850}/I_{830}$  is around 1.3 in the Raman spectrum of the native sample in accordance with a solvent exposed Tyr residues. After thermo-chemical treatment it exceeds 2.5, suggesting that all the three Tyr residues in lysozyme were exposed to the solvent after the thermal stress and that they are acceptor of a strong hydrogen bond.<sup>51,52</sup> Moreover the motion of Tyr side chains in lysozyme during the unfolding of the tertiary structure under external stresses (like temperature) is related to the activity change. Indeed, Tyr53 is hydrogen bonded with the amino acid group of Asp66 and is adjacent to the catalytic residue Asp52 and can influence the enzymatic active site of lysozyme.<sup>53</sup>

About the Trp Fermi doublet, it has been suggested that the relative intensity of the Fermi doublet of Trp  $I_{1360}/I_{1340}$  is a good indicator of the hydrophobic/hydrophilic environment of the tryptophan indole ring.<sup>54</sup> The tryptophan doublet arises from a Fermi resonance between a fundamental mode at 1340 cm<sup>-1</sup> and a combination of two out-of-plane modes involving the benzene and pyrrole rings comprising the Trp side chain.<sup>55</sup> If the relative intensities ratio of the Fermi doublet  $I_{1360}/I_{1340}$  is smaller than 1.0, the tryptophan indole ring is considered to be in a hydrophilic environment or exposed to aqueous medium, on the other hand, if it is greater than 1.0, it is considered to be in a hydrophobic environment or in contact with aliphatic side chains. The relative intensities of the Fermi doublet of Trp in HEWL assume a value around 0.4 in the native sample and around 2.7 in the fibrillar one. From the previous consideration it is possible to say that the Trp side chains pass from a hydrophilic to a hydrophobic (or in contact with aliphatic side chains) environment. Moreover the Trp band frequency around 1550 cm<sup>-1</sup> has been correlated to the dihedral angle between the indole ring and the peptide bond plane.<sup>56</sup> The frequency of this vibration is different in the two Raman spectra: 1553 cm<sup>-1</sup> for the native sample and 1550 cm<sup>-1</sup> for the fibrillar one. Owing to the different frequency it is possible to infer that the torsional angle is around 106° in the native sample and around 36° in the fibrillar HEWL,<sup>57</sup> confirming that a structural reorganization has occurred in the fibrillation process. The shift of the Trp frequency that is around 1011 cm<sup>-1</sup> in the native sample towards a lower frequency (around 1009 cm<sup>-1</sup>) in the fibrillar HEWL can be used as a marker of the fibrillation process. Indeed this shift is accompanied by a change in the relative intensity respect to the Phe peaks around 1003 cm<sup>-1</sup> both in the native and in the fibrillar samples.<sup>46</sup> It has been previously reported that this remarkable variation is mainly due to the dramatic decrease of the Phe

peak intensity under the thermal treatment owing to the exposure of Phe to water rather than to an increase of the Trp peak .

The HEWL is a globular protein that has a structure with approximately 40-45% of  $\alpha$  helix and around 20% of  $\beta$  sheets structure in its native conformation. The results of the LM fitting procedure (see section 2.4) of the Amide I band for the native structure are in good agreement with the literature values and were reported together with the results of the fitting procedure on the fibrillar sample in Table 3.5. The process of fibrillation decreases the  $\alpha$  helix and increases the  $\beta$  components (inter-chain + intra-chain). The random components of the secondary structure plays a relevant role in the fibrillation process, as in the first stage of the fibrillation process the native structure falls in a disordered structure and then re-arrange itself in the  $\beta$  inter-chain structure (see section 1.3).<sup>38</sup> It is important to recall once again that around  $1670\text{ cm}^{-1}$  is typical frequency of the  $\beta$  sheets that are extremely well organized in the aggregated sample, and that this feature together with the narrowing of the Amide I band is the marker of the fibrils conformation of the protein in the Raman spectrum.<sup>58</sup>

	<b>Native HEWL</b>	<b>Fibrillar HEWL</b>	
<b>Unordered (Random + Turns)</b>	1644, 1693 31	1649, 1692 17	Frequency ( $\text{cm}^{-1}$ ) Area (%)
<b><math>\alpha</math> helix</b>	1660 45	1656 6	Frequency ( $\text{cm}^{-1}$ ) Area (%)
<b><math>\beta</math> sheet inter-chain</b>	- 0	1670 56	Frequency ( $\text{cm}^{-1}$ ) Area (%)
<b><math>\beta</math> sheet intra-chain</b>	1679 23	1680 20	Frequency ( $\text{cm}^{-1}$ ) Area (%)

**Table 3.5** – Results of the fitting procedures of the Amide I band of the HEWL sample in native and fibrillar states. The unordered structures comprise the random structure (low frequency) and the turns structure (high frequency).

## *Bibliography of Chapter 3*

- <sup>1</sup> N.T. Yu et al., *J. Mol. Biol.*, 1972, 70, 117-132.
- <sup>2</sup> E.J. Ambrose and A. Elliott, *Proc. Roy. Soc. London. A, Math. Phys. Sci.*, 1951, 208, 1092.
- <sup>3</sup> L. Nielsen et. al., *J. Pharmaceut. Sci.*, 2001, 90(1), 29-37.
- <sup>4</sup> W. Dzwolak et. al., *Protein Sci.*, 2004, 13, 1927-1932.
- <sup>5</sup> W. Dzwolak et al., *Biochemistry*, 2005, 44, 8948-8958.
- <sup>6</sup> R. Jansen, W. Dzwolak, and R. Winter, *Biophys. J.*, 2005, 88, 1344–1353.
- <sup>7</sup> C. Dirix et. al., *High Pressure Res.*, 2003, 23, 63-66.
- <sup>8</sup> W. Dzwolak et. al., *Advances in High Pressure Bioscience and Biotechnology 2*, R. Winter Ed., 2003, SPRINGER.
- <sup>9</sup> Y. Taniguchi, N. Takeda, K. Ado and R. Maeda, *High Pressure Res.*, 2009, 29, 676-679.
- <sup>10</sup> S. Grudzielanek, V. Smirnovas and R. Winter, *J. Mol. Biol.*, 2006, 356, 497–509.
- <sup>11</sup> S. Gruzielanek, Y. Zhai, and R. Winter, *Chem. Phys. Chem.*, 2010, 11, 2016 – 2020.
- <sup>12</sup> C. Ortiz, D. Zhang, Y. Xie, A.E. Ribbe, D. Ben-Amotz, *Anal. Biochem.*, 2006, 353, 157–166.
- <sup>13</sup> H. Sugeta, *Spectrochim. Acta*, 1975, 31A, 1729–1737.
- <sup>14</sup> H.E. Van Wart, A. Lewis, A. Scheraga, F.D. Saeva, *Proc. Natl. Acad. Sci. USA*, 1973, 70, 2617–2623.
- <sup>15</sup> W. Qian, W. Zhao and S. Krimm, *J. Mol. Struct.*, 1991, 250, 89-102.
- <sup>16</sup> R. Kishore, H. Ishizaki, A.T. Tu, A. Ravi and P. Balaram, *Int. J. Peptide Res.*, 1987, 30, 474-480.
- <sup>17</sup> Zai-Quing Wen, *J. Pharm. Sci.*, 2007, 96, 2861-2878.
- <sup>18</sup> C. Jiang, J.-Y. Chang, *FEBS Lett.*, 2005, 579, 3927–3931.
- <sup>19</sup> R. Zheng, X. Zheng, J. Dong, and P.R. Carey, *Protein Sci.*, 2004, 13, 1288-1294.
- <sup>20</sup> M.N. Siamwiza, R.C. Lord, M.C. Chen, T. Takamatsu, I. Harada, H. Matsuura, and T. Shimanouchi, *Biochemistry*, 1975, 14, 4870.
- <sup>21</sup> M. Aoyama, K. Kurihara and K. Shibata, *Biochim. Biophys. Acta*, 1965, 107, 257-265.
- <sup>22</sup> L. Ashton, J. Dusting, E. Imomoh, S. Balabani, and E.W. Blanch, *Biophys. J.*, 2010, 98, 707–714.
- <sup>23</sup> R.W. Williams RW, *Methods Enzymol.* 1986, 130, 311-31.
- <sup>24</sup> <http://www.rcsb.org/pdb/home/home.do>
- <sup>25</sup> F. Librizzi and C. Rischel, *Protein Sci.*, 2005, 14, 3139-3134.
- <sup>26</sup> K. Huang, N.C. Maiti, N.B. Philips, P.R. Carey, and M.A. Weiss, *Biochemistry*, 2006, 45, 10278-10293.
- <sup>27</sup> K. Kunihiro, P. Kim, and R.L. Baldwin, *Biopolymers*, 1984, 22, 59-67.
- <sup>28</sup> D. Garfinkel and J. T. Edsall, *J. Am. Chem. Soc.*, 1958, 80, 3818.
- <sup>29</sup> M. C. Tobin, *Science*, 1968, 161, 68.
- <sup>30</sup> R. C. Lord and N.-T. Yu, *J. Mol. Biol.*, 1970, 50, 509.
- <sup>31</sup> H. Brunner and H. Sussner, *Biochim. Biophys. Acta*, 1972, 271, 16-22.
- <sup>32</sup> M.C. Chen, R.C. Lord and R. Mendelsohn, *Biochim. Biophys. Acta*, 1973, 328, 252-260.
- <sup>33</sup> E.W. Blanch, I.H. McColl, L. Hecht, K. Nielsen, L.D. Barron, *Vibrational Spectrosc.*, 2004, 35, 87–92.
- <sup>34</sup> P. Sassi, A. Giugliarelli, M. Paolantoni, A. Morresi, G. Onori, *Biophys. Chem.*, 2011, 158, 46–53.
- <sup>35</sup> L. N. Arnaudov and R. de Vries, *Biophys. J.*, 2005, 88, 515–526.
- <sup>36</sup> M. Xu, V.V. Ermolenkov, W. He, V.N. Uversky, L. Fredriksen, I.K. Lednev, *Biopolymers*, 2005, 79, 58–61.

- 
- <sup>37</sup> S. Goda, K. Takano, Y. Yamangata, R. Nagata, H. Akutsu, S. Maki, K. Namba, and K. Yutani, *Protein Sci.*, 2000, 9, 369–375.
- <sup>38</sup> M. Xu, V.A. Shashilov, V.V. Ermolenkov, L. Fredriksen, D. Zagorevski and I.K. Lednev, *Protein Sci.*, 2007, 16, 815–832.
- <sup>39</sup> A. Hedoux, S. Krenzlin, L. Paccou, Y. Guinet, M.P. Flament and J. Siepmann, *Phys. Chem. Chem. Phys.*, 2010, 12, 13189–13196.
- <sup>40</sup> W. Zhao and R. Yang, *J. Phys. Chem. B*, 2010, 114, 503–510.
- <sup>41</sup> T. Uemichi, J.J. Liepnieks, M.A. Gertz, M.D. Benson, *Amyloid*, 1998, 5(3), 188–92.
- <sup>42</sup> A.K. Soutar, P.N. Hawkins, D.M. Vigushin, et al., *Proc. Natl. Acad. Sci. U.S.A.*, 1992, 89(16), 7389–93.
- <sup>43</sup> B. Granel, J. Serratrice, P. Disdier, et al., *Am. J. Med.*, 2005, 118(3), 321–2.
- <sup>44</sup> B. Granel, S. Valleix, J. Serratrice, et al., *Medicine (Baltimore)*, 2006, 85(1), 66–73.
- <sup>45</sup> E. Frare, P. Polverino de Laureto, J. Zurdo, C.M. Dobson and A. Fontana, *J. Mol. Biol.*, 2004, 340, 1153–1165.
- <sup>46</sup> M. Xu, V.V. Ermolenkov, V.N. Uversky, and I.K. Lednev, *J. Biophoton.* 2008, 1, 215–229.
- <sup>47</sup> C. Ortiz, D. Zhang, Y. Xie, A. E. Ribbe, D. Ben-Amotz, *Anal. Biochem.*, 2006, 353, 157–166.
- <sup>48</sup> A. T. Tu, *Spectroscopy of Biological System*; Clark, R.J. H.; Hester, R. E., Eds.; John Wiley and Sons: New York, 1986, 47.
- <sup>49</sup> A. Hedoux, Y. Guinet, and L. Paccou, *J. Phys. Chem. B*, 2011, 115, 6740–6748.
- <sup>50</sup> J.L. McHale, *J. Raman Spectrosc.* 1982, 13, 21.
- <sup>51</sup> A. Torreggiani, M.D. Foggia, I. Manco, A.D. Maio, S.A. Markarian, S. Bonora, *J. Mol. Struct.* 2008, 891, 115.
- <sup>52</sup> R. Ionov, A. Hedoux, Y. Guinet, P. Bordat, A. Lerbret, F. Affouard, D. Prevost, M. Descamps, *J. Non-Cryst. Solids.*, 2006, 352, 4430.
- <sup>53</sup> C.C.F. Blake, G.A. Mair, A.C.T. North, D.C. Phillips, V.R.P. Sarma, *R. Soc. London B*, 1967, 167, 365.
- <sup>54</sup> I. Harada, T. Miura, H. Takeuchi, *Spectrochim. Acta A*, 1986, 42, 307–312.
- <sup>55</sup> H. Takeuchi, and I. Harada, *Spectrochim. Acta* 1986, 42A, 1069-1078.
- <sup>56</sup> T. Miura, H. Takeuchi, I. Harada, *J Raman Spectrosc*, 1989, 20, 667–671.
- <sup>57</sup> L.J. Juszczak and R.Z. B. Desamero, *Biochemistry*, 2009, 48(12), 2777–2787.
- <sup>58</sup> W.S. Gosal, A.H. Clark, and S.B. Ross-Murphy, *Biomacromolecules*, 2004, 5, 2408-2419.

# *Chapter 4*

## *Raman and Infrared Measurements on Insulin Solutions Under Pressure*

The present Chapter is devoted to the investigation of the effects of pressure on insulin in water solution. Two neutral solutions of insulin in water at two different concentrations (2mM and 20mM) have been studied as a function of pressure by means of optical spectroscopy using a diamond anvil cell. The maximum pressure achieved was limited to a rather low pressure range (below 2 GPa) owing to the pressure-induced ice-forming which can affect the structural properties of the protein and thus the results of the spectroscopic measurements. In particular the low concentration solution has been investigated by both Raman and Infrared spectroscopy whereas only the Raman spectroscopy has been used for the high concentration solution owing to the high absorption of insulin within the infrared frequency range.

The result of our present measurements demonstrated the possibility of using pressure for converting the pristine hexameric aggregation into oligomers predominantly into dimeric/monomeric form and confirmed the anomalous resistance of insulin to applied pressure.

## 4.1 High Pressure Behavior of Insulin 2 mM Solution at Neutral pH

Two neutral solutions of BPI in water at two different concentrations (2mM and 20mM) have been object of study in this thesis. Since Raman is very sensitive to fluorescence, the use of buffers has been avoided and all the solutions were made in purified, distilled water (H<sub>2</sub>O in Raman and D<sub>2</sub>O in IR measurements).

### 4.1.1 Raman Measurements

To obtain a 2mM solution 11.6 mg of BPI powder have been dissolved in 1 ml of purified, distilled water. At this low concentration insulin retains its hexameric structure at ambient condition.

To study the behavior of the solution under pressure a small drop of the sample was loaded into a 150  $\mu\text{m}$  hole of a Copper gasket 200  $\mu\text{m}$  thick and it was pressurized, step by step, up to 2 GPa in a DAC by means of a screw mechanism. At each working pressure Raman spectra have been collected after waiting for at least 20 minutes from the attainment of the chosen pressure in order to allow the stabilization of the protein structure. The Raman spectra collected on increasing/decreasing pressures are shown in Figure 4.1 over a spectral range which includes the contribution from the Amide I band (centered at around 1650  $\text{cm}^{-1}$ ). Bearing in mind that the latter is the most sensitive spectral feature for the analysis of the secondary structure of proteins, insulin shows a remarkable stability<sup>1</sup> in this structure: actually nothing happens during the pressurizing-depressurizing cycle. This qualitative conclusion can be made quantitative using a fitting procedure for the spectral analysis of the Amide contribution.

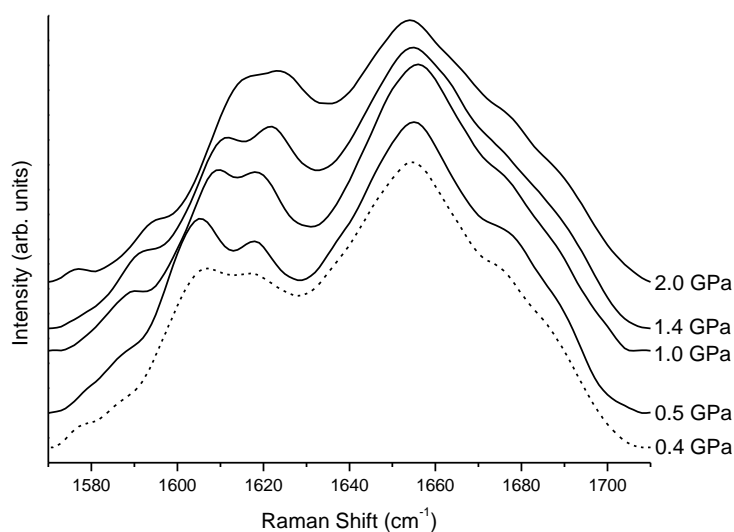


**Figure 4.1** – Raman spectra in the Amide I region. Solid lines represent the spectra collected on increasing the pressure, dashed line is the spectrum collected on decreasing the pressure.

Curve fitting of the Amide I band of 2mM solution was performed by means of the LMA together with the second derivative method (as described in section 2.4). The second derivative method selected three peaks in the Amide I region (respectively assigned to random coil,  $\alpha$  helix and  $\beta$  sheet) with about 25  $\text{cm}^{-1}$  full width at half maximum (FWHM). As an example, the spectrum collected at 1 GPa, the best fit curve obtained, and the single fit components are shown in Figure 4.2. It must be noticed that the dashed curves in Figure 4.2 represent the contributions due to the ring modes from aromatic side chains of Phe and Tyr residues and were included in the fitting curve



since they can be hardly disentangled from the Amide I band contributions. A linear baseline was assumed over the frequency range considered in the fitting procedure.

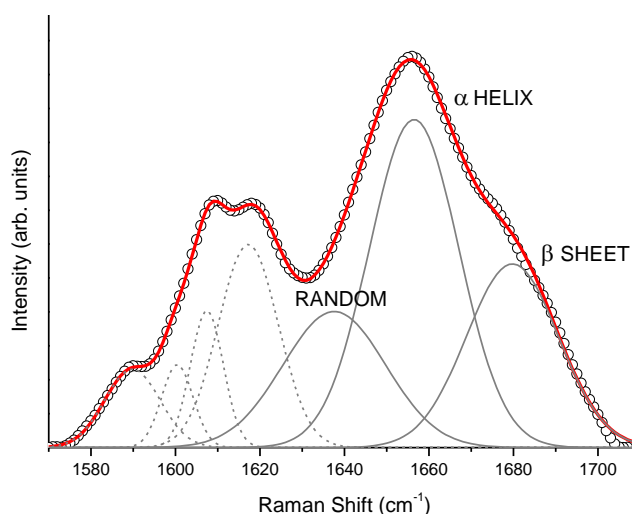


**Figure 4.2** – Raman spectrum of the 2 mM BPI solution at 1 GPa (circles). The red curve is the best fit curve, the solid grey lines represent the Amide I components and the grey dashed lines the spectral contributions from the Phe and Tyr residues.

The percentages of the different structural components of the BPI secondary structure obtained by the fitting procedure are reported in Table 4.1.

	0.5 GPa	1.0 GPa	1.4 GPa	2.0 GPa	0.4 GPa	
Random	1637	1639	1636	1636	1636	Frequency (cm <sup>-1</sup> )
	27	28	24	22	25	Area (%)
α helix	1657	1657	1656	1655	1657	Frequency (cm <sup>-1</sup> )
	47	48	49	47	48	Area (%)
β sheet	1684	1684	1684	1685	1684	Frequency (cm <sup>-1</sup> )
	26	25	27	31	27	Area (%)

**Table 4.1** – Result of the fit analysis of the Raman spectra of the 2mM solution of BPI under pressure. For each component (random, α helix or β sheet) the central frequency (cm<sup>-1</sup>) and the percentage of occurrence (%) are reported.

The pressure is actually ineffective on the alpha helices and has only a little effect, apparently reversible, on the beta-sheets and the random-coils favoring the occurrence of the former (an increase of about 5% of β sheets is observed at the maximum pressure  $P_{\max} = 2$  GPa). To this respect it is worth to notice that the larger increase of β sheets occurs on increasing the pressure at those pressure when ice formation is expected. This can affect the structure of the protein introducing an additional uncertainty factor to the study of the insulin pressure behavior.

## 4.1.2 Infrared Measurements

A 2mM solution in D<sub>2</sub>O of BPI at neutral pD has been analyzed by IR spectroscopy in the same range of pressure than Raman experiment, (0-2 GPa). The solution was loaded in the DAC inside the 150 μm hole of a 70 μm thick copper gasket. The solution was made in D<sub>2</sub>O instead of H<sub>2</sub>O to avoid that the intense absorption spectrum of water could mask the Amide I band (the frequencies of the molecular vibrational modes in which H is involved are shifted by a factor basically proportional to the square root of the mass ratio H/D) .

The collected IR spectra are shown in Figure 4.3 over the spectral range 1350 - 1750 cm<sup>-1</sup>. The Amide II' band at 1450 cm<sup>-1</sup> is attributed to deuterated BPI, while the Amide II band at 1550 cm<sup>-1</sup> to hydrogenated BPI. These two bands can be very useful when investigating the protein denaturing process, because a protein that is denaturing would expose its internal structure to the solvent, favoring the H-D exchange. In the IR spectrum this exchange should be revealed by the spectral weight transfer from the Amide II (H containing) to the Amide II' (D containing) band. Looking at Figure 4.3 we can notice that at ambient pressure the Amide II' is the most prominent spectral feature indicating that most of the protein deuteration is already occurred but also that applying pressure does not affect the intensity ratio Amide II/Amide II' suggesting that the protein structure is not modified by the pressure cycle.

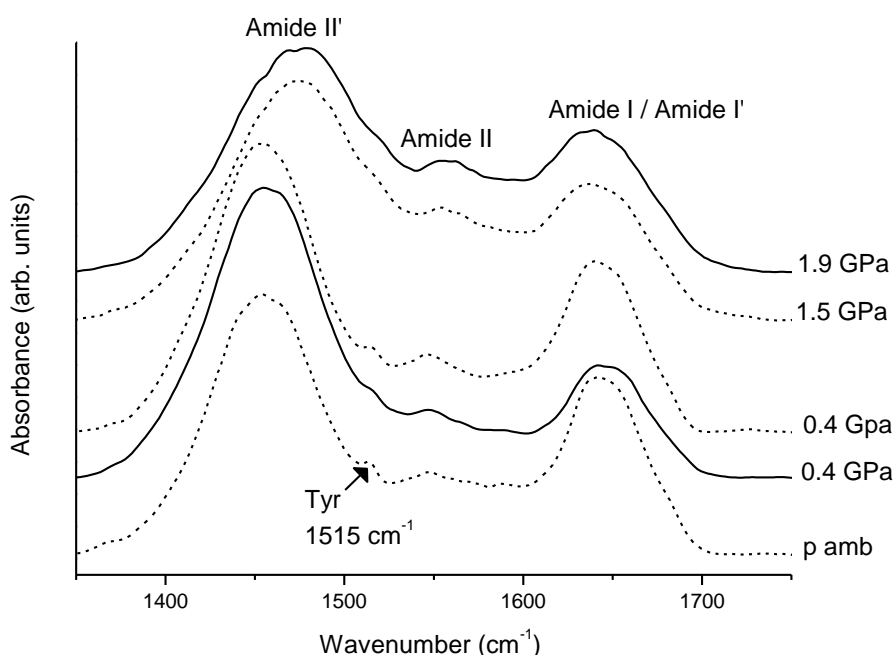


**Figure 4.3** – IR spectra in 1350-1750 cm<sup>-1</sup> range. Solid lines are the spectra acquired on increasing the pressure, dashed curves those collected on decreasing the pressure.

The Fourier Self Deconvolution (FSD) technique was applied to the Amide I-I' band before the fitting procedure (see section 2.4). The parameter used to deconvolve the spectra were: 13 cm<sup>-1</sup> of FWHM and a Noise Reduction (NS) of 0.4. The goodness of the procedure is demonstrated by the comparison of the original spectrum, the deconvolved one and the second derivative curve, all shown in Figure 4.4. The peaks obtained from the deconvolved spectra (4.4 b) are the same displayed from the second derivative curve (4.4 c), this means that the two analysis agree both on the number and the frequencies of the secondary structure components. Moreover, by comparing the original spectra (4.4 a) with the FSD spectra (4.4 b) it is possible to see that no artificial peaks arise from the deconvolution procedure.

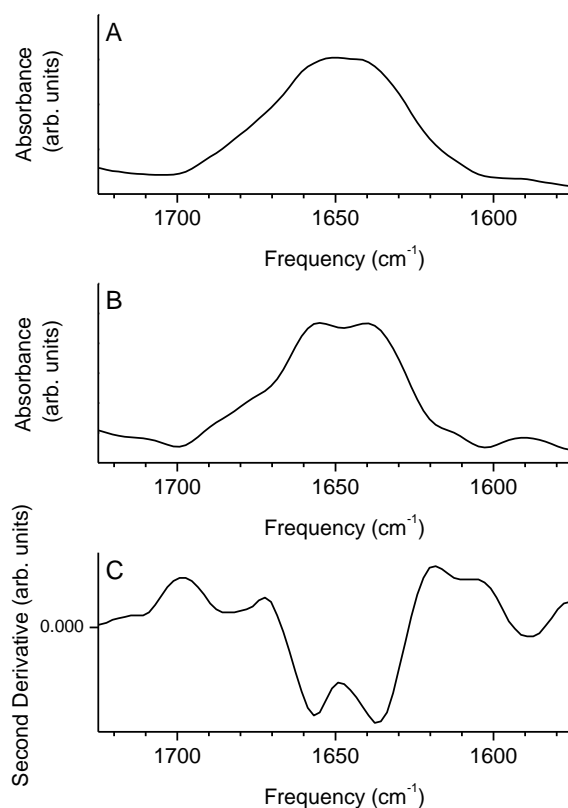


**Figure 4.4** – (A) IR spectra of 2 mM solution at 0.4 GPa; (B) Fourier Self-Deconvolved Spectra, parameters:  $13\text{ cm}^{-1}$  and 0.4 NR; (C) Second Derivative.

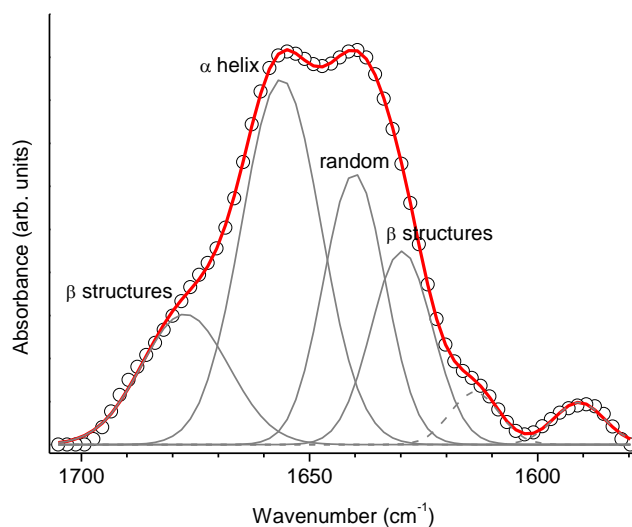


**Figure 4.5** – Fit of the IR spectrum of 2 mM solution of BPI at 0.4 GPa (circles). The red curve is the line of best fit, the solid grey line represents the components of the Amide I band. The dashed lines are the side chains contributes, while the solid lines are the secondary structure components.

The deconvoluted spectra were then fitted by means of the LMA the fitting results are reported in Table 4.3. The goodness of the fitting procedure applied to the FSD spectra of the 2 mM solution of BPI at the pressure of 0.4 GPa (in phase of compression) is shown in Figure 4.5.

The result obtained by applying the fitting procedure to the IR spectra is in good agreement with that obtained by the Raman fit (compared Table 4.3 with Table 4.1).

	0.4 GPa	1.9 GPa	1.6 GPa	0.4 GPa	P amb	
<b>Random</b>	24	22	22	24	24	Area (%)
<b><math>\alpha</math> helix</b>	42	38	36	37	39	Area (%)
<b><math>\beta</math> sheet</b>	34	40	42	38	37	Area (%)

**Table 4.3** – Estimated percentage of the components of the secondary structures obtained by means of a fitting procedure of the Amide I-I' band of the IR spectra of the 2 mM solution of BPI under pressure (0-1.9 GPa).

The most relevant point which emerges from both Raman and IR measurements is that applying pressure up to 2 GPa on a 2 mM solution in neutral pH does not induce remarkable conformational changes in the protein, neither on increasing nor on decreasing pressure.

## 4.2 High Pressure Behavior of Insulin 20 mM Solution at Neutral pH

The 20 mM solution in neutral condition was obtained dissolving 100 mg of BPI powder in 1 ml of purified, distilled water. We notice that this is the same concentration that was studied by Yu and coworkers.<sup>2</sup> Following the same procedure as for 2 mM solution, a drop of 20 mM solution was loaded into a 150  $\mu$ m hole of a Copper gasket and it was pressurized up to 2 GPa in a DAC by means of a screw mechanism.

Before analyzing the results obtained by pressurizing the most concentrated solution, it is worth to notice that insulin is actually not a soluble protein under neutral condition. The concentration of the previously investigated solution, namely 2 mM can be considered as the limiting concentration value, so that the word “solution” for concentration higher than that is used here improperly. Nevertheless this point is not a problem since the focus of our present research is to investigate any possible changes in the secondary structure ascribable to the occurrence of different aggregation states.

In Figure 4.6 the Raman spectra of 20 mM solution up to 2 GPa and back down to ambient pressure are shown. Labels are also reported to mark the main features of the Raman spectra of BPI that will be discussed in the text.

Following the pressure behavior of some specific peaks in the Raman spectra it is possible to investigate the effects of the applied pressure over the tertiary structure. The correlation between the frequency of the S-S stretching mode and the conformation of CCSSCC moiety has been already pointed out in section 3.1.2 (see Figure 3.8).<sup>3,4,5,6</sup>

On pressurizing the frequencies ascribed to the S-S vibration shift linearly towards highest frequencies in a reversible manner (see Figure 4.8 A). Moreover the shape of the disulphide peaks remain the same over all the P cycle except at the highest pressure reached (2 GPa and 1.5 GPa) where its spectroscopic structure broadens (see Figure 4.6). The reversibility in shape suggests that the above mentioned broadening at the highest pressure may be a consequence of the ice formation.

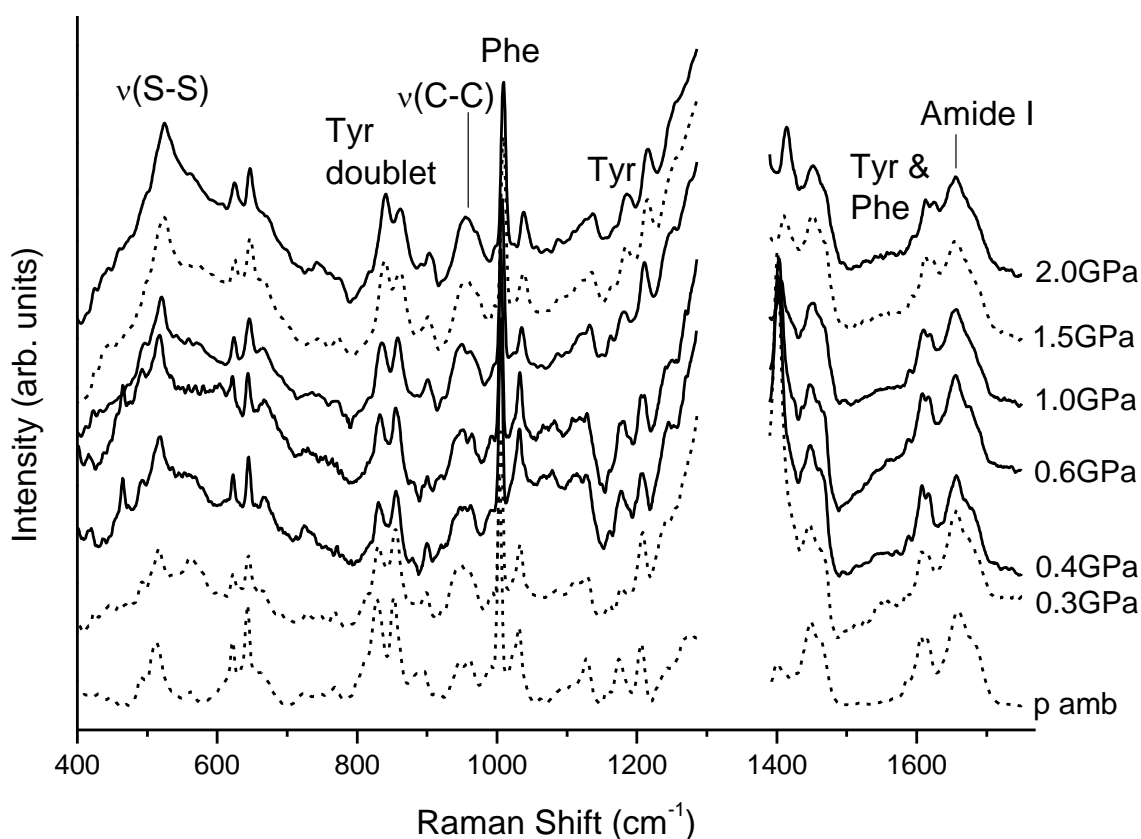


**Figure 4.6** –Raman spectra of 20 mM solution of BPI in the pressure range between 0 and 2 GPa. Solid lines represent the spectra collected on increasing the pressure, dashed lines those collected on decreasing the pressure. The spectral region between 1290 and 1390  $\text{cm}^{-1}$  is not shown owing to the presence of the strong Raman signal of the diamond anvils.

The tertiary structure can be also monitored in the Raman spectrum through the skeletal ( $\dots\text{C}^\alpha\text{C}^\beta\text{NC}^\alpha\dots$ ) bending (around 380-490  $\text{cm}^{-1}$ , 550  $\text{cm}^{-1}$  and 730-770  $\text{cm}^{-1}$  of the Raman spectrum) and stretching ( $\nu(\text{C-C})$  is around 880-990  $\text{cm}^{-1}$ , while  $\nu(\text{C-N})$  is around 1110-1160  $\text{cm}^{-1}$ ). The pressure behavior of the frequencies of some of these peaks (A and C), together with the pressure behavior of the frequencies of the Tyrosine Fermi doublet (B) and that of the central frequency of the Amide I band (D) are shown in Figure 4.7. Some of these frequency trends show a linear behavior in pressure (see for example S-S bonds or Tyr doublet), while others show discontinuities (see the bending and stretching of the protein skeletal). It is clear from the pressure behavior that all the frequency shifts (linear and non-linear) are completely reversible.

It has already pointed out (see section 3.1.2) that the Tyrosine Fermi doublet is an important marker of the hydrogen bond.<sup>4,7</sup> The intensity ratio  $I_{850}/I_{830}$  is around 1.3 for the ambient pressure suggesting that the Tyr residues are exposed to the solvent in native condition.<sup>8</sup> Up to 0.6 GPa the value of the ratio is still around this value. Above 0.6 GPa the ratio starts clearly to diminishing. The reduction of the Fermi doublet ratio suggests a possible decrease in solvent exposure of the Tyr14 and Tyr19 residues in one of the helices in the A chain (that at ambient conditions are exposed to the surface) on going from ambient pressure to 2 GPa.<sup>9</sup>

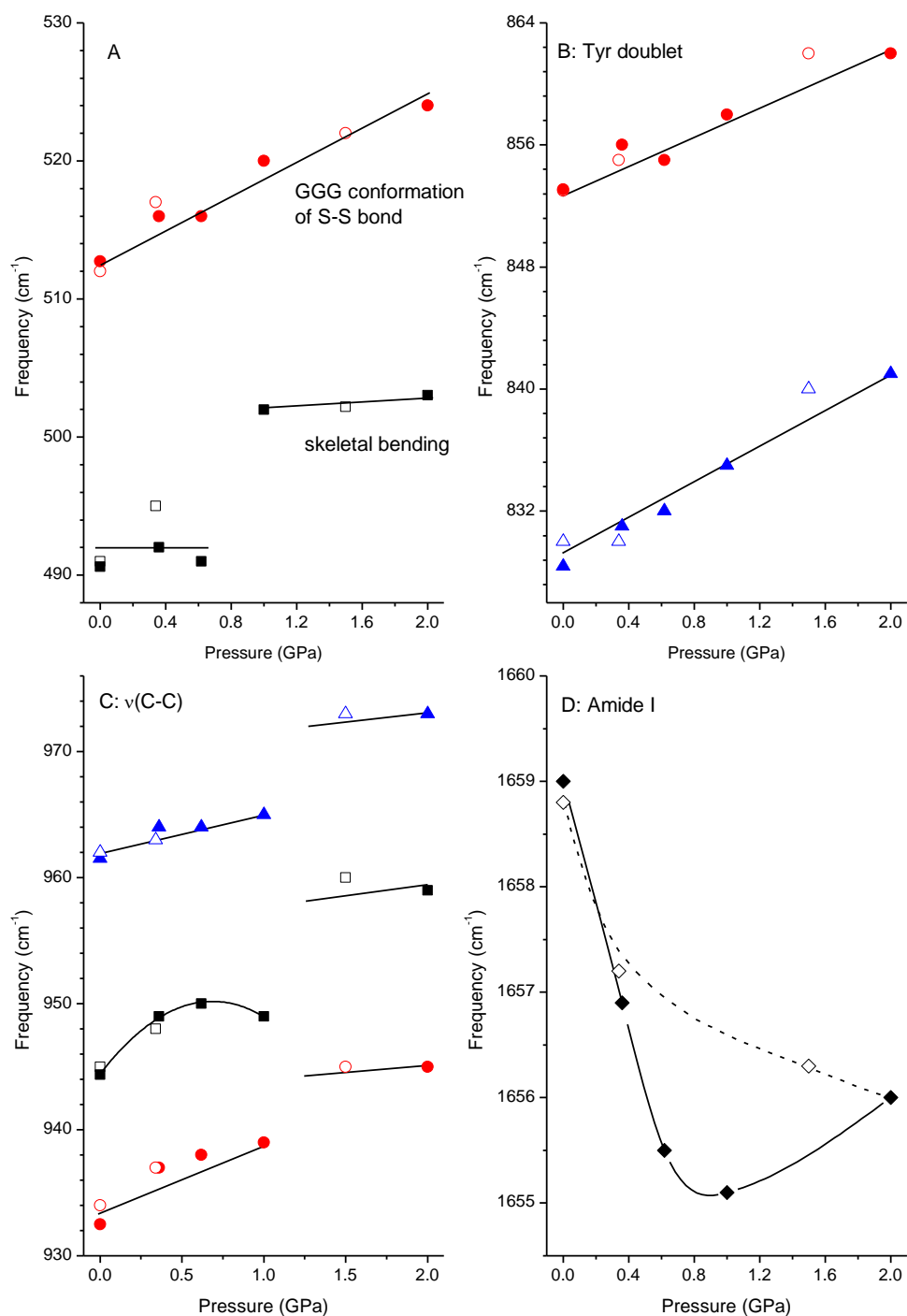


**Figure 4.7** – Frequency pressure behavior of: the S-S bond and the skeletal bending (A), Tyr Fermi doublet (B), stretching of C-C bond (C), and the central frequency of the Amide I band (D). Increasing pressure: closed symbols, decreasing pressure: open symbols. The lines are guide to the eyes. The points at ambient pressure before the pressure cycle are from literature (ref. 2).

The low  $I_{850}/I_{830}$  value (0.8) found for the 20 mM solution BPI at 2 GPa suggests<sup>8</sup> that the Tyr residue associated with the  $\alpha$  helix in the A chain are buried inside the protein core, revealing that the reorganization induced by pressure involves the  $\alpha$  helix structure.<sup>10</sup> On decreasing the pressure up to ambient conditions the ratio, even if following a different path, returns to its original value around 1.3. On these bases we can conclude that pressure clearly affect the insulin tertiary structure within the 20 mM solution but, at least up to a maximum pressure of about 2 GPa, the pressure induced modifications appear to be completely reversible.

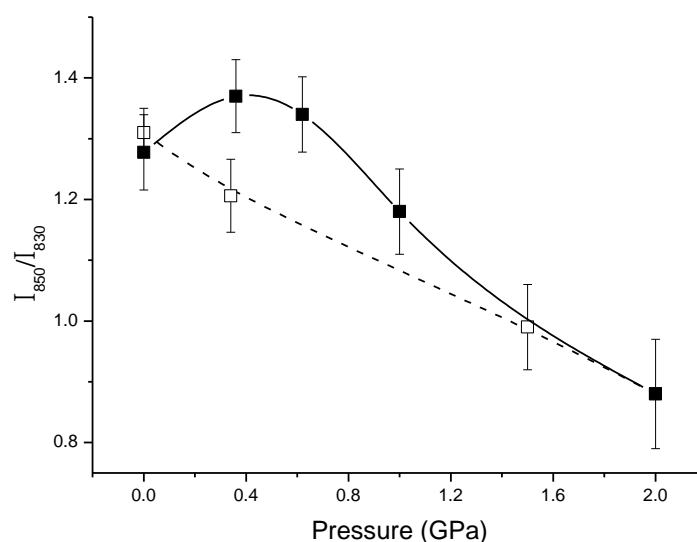


**Figure 4.8** – Pressure behavior of the intensity ratio of the two peaks of the Tyr Fermi doublet. Closed symbols are on increasing pressure and open symbols are on decreasing pressure. The lines are guides to the eyes. The value at ambient pressure has been obtained from ref. 2. The error bars have been calculated by varying the fit parameters around the best values.

The decreasing trend of the Amide I central frequency from ambient pressure up to 1 GPa is in agreement with the literature,<sup>11</sup> the stronger is the H-bond the lower is the stretching frequency vibration in the Amide I band and the higher is the bending frequency in the Amide III band.<sup>2</sup> At pressure higher than 1 GPa the trend is inverted and the central frequency of the Amide I band experienced a blue shift.

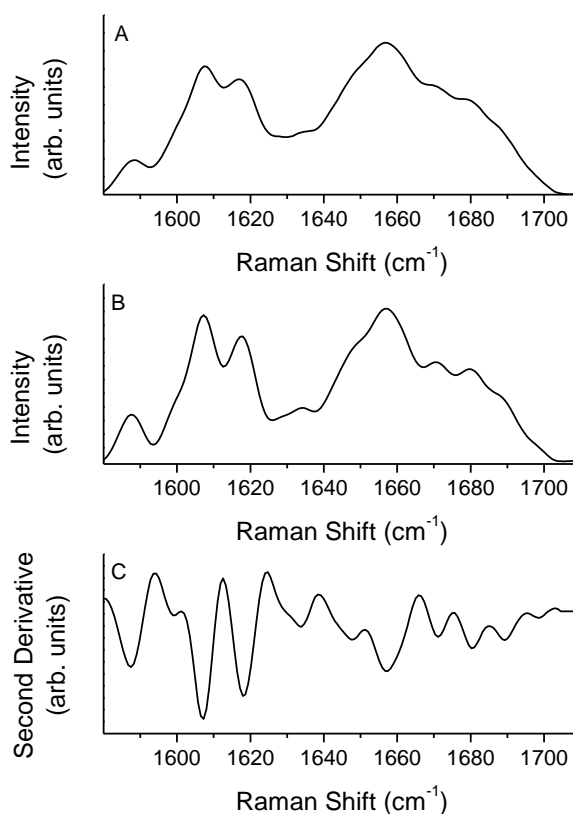


**Figure 4.9** – (A) Raman spectra of 20 mM solution at 0.4 GPa; (B) Fourier Self-Deconvolved Spectra, parameters:  $15 \text{ cm}^{-1}$  and 0.3 NR; (C) Second Derivative.

The quantitative analysis of the Amide I band was carried out following the same fitting procedure applied for the 2 mM solution. In the case of 20 mM solution the second derivative analysis results in more than the usual three components. The shape of the Amide I band is different from that of the solution 10 fold less concentrated. That was not completely unexpected: at this high concentration insulin results in an aggregate state characterized by new Amide vibration typical of inter-chain hydrogen bonds. This two components are around 1625 and 1670  $\text{cm}^{-1}$ .

As the complexity of the Amide I vibrations vertically increases the FSD technique has become a very useful tool (see section 2.4). All the spectra were deconvolved using 15  $\text{cm}^{-1}$  as FWHM and NR factor of 0.3. An example of the application of the FSD is given in Figure 4.9. From the comparison between the Fourier Self-Deconvolved spectrum (Fig. 4.10 (B)) and the second derivative one (Fig. 4.10 (C)) it is possible to appreciate the goodness of the deconvolution as the peaks present in the FSD spectrum are exactly the same that comes out from the analysis of the second derivative.

The spectra deconvolved were then fitted by the LMA and the results are reported in Table 4.5.

	P_amb*	0.4 GPa	0.6 GPa	1 GPa	2 GPa	1.5 GPa	0.3 GPa	P amb	
<b>Random</b>	11	25	26	40	36	28	21	20	Area (%)
<b><math>\alpha</math> Helix</b>	43	30	43	28	27	36	33	40	Area (%)
<b><math>\beta</math> intra-chain</b>	28	25	23	18	26	28	18	29	Area (%)
<b><math>\beta</math> inter-chain</b>	17	21	8	14	11	9	28	11	Area (%)

**Table 4.5** – Percentage of the different components of the secondary structure determined by the Amide I fitting procedure. The three colors deal with the three set defined in the text and in the contour plot analysis. \* Ambient pressure is taken from literature (ref. 2).

The analysis of the Amide I vibrations clearly shows that up to 0.6 GPa the main effect of applying of pressure is to dissociate the oligomers that are present in the BPI solution.<sup>12</sup> On further applying pressure up to 2 GPa the 20 mM solution of BPI leads to a consistent increase in the random components. On depressurizing the percentage of the structure that is in a  $\beta$  structure appears similar to that at the starting pressure. The random structure and the inter-chain components decrease. It is important to see that on decreasing the pressure the protein has a renaturation, as it is evidenced by the growing percentage of the  $\alpha$  helix on going from the maximum pressure reached to the ambient pressure; but no re-aggregation processes happened, in fact the final  $\beta$  inter-chain percentage at ambient pressure is lower than the initial one.

To better understand the effect of pressure on the Amide I vibrations a two-dimensional Raman correlation study has been performed (see the Appendix at the end of this Chapter for mathematical details). The following Figures show the synchronous and asynchronous correlation plot between Raman spectra as a function of the applied pressure. Raman spectra have been divided in three sets: one covering the pressure range from 0.4 to 0.6 GPa, a second one from 0.6 GPa to the maximum pressure applied (2 GPa) and a third one on decreasing pressure from 2 GPa to ambient pressure. These sets were studied for a better comprehension of the Amide I vibrations under pressure. Analyzing the synchronous plot (see Figure 4.10 A, 4.11 A and 4.12 A) for the three sets previously defined it is possible to see that there are one prominent peak in the first plot in the region of the  $\alpha$  frequency (around 1660  $\text{cm}^{-1}$ ), while in the second and third plots the lines become smoothed and the differences between the three components of the secondary structure that changes simultaneously when applying pressure becomes less evident.



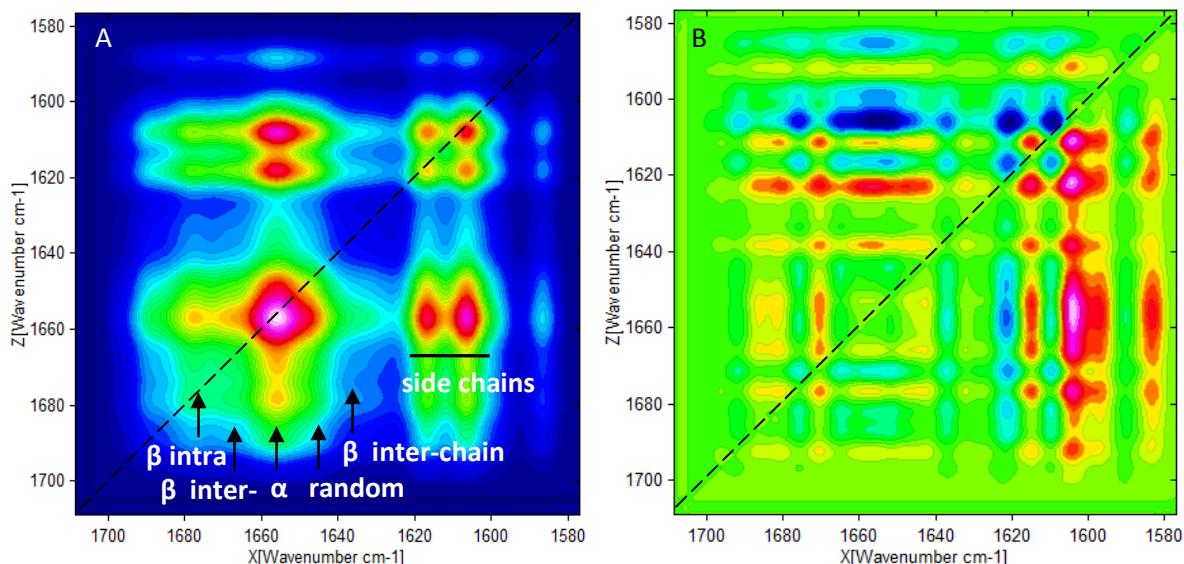


**Figure 4.10** –Correlation plot between 0.4 and 0.6 GPa: (A) Synchronous and (B) Asynchronous.

The asynchronous correlation between the 0.4 and 0.6 GPa (Figure 4.10 B) shows that the  $\beta$  inter-chain components (around 1625 and 1670 cm<sup>-1</sup>) were the first to experience the pressure effect. This is a first interesting result that confirm the pressure capability to dissociate oligomers. As it was already observed the 20 mM solution is beyond the limit of insulin solubility at neutral pH, and the sample results to be aggregate. Moreover that 0.6 GPa was an important pressure for the insulin structure can be already observed from the pressure behavior of the skeletal bending, one of the tertiary structure Raman marker analyzed before (see Figure 4.7 A).

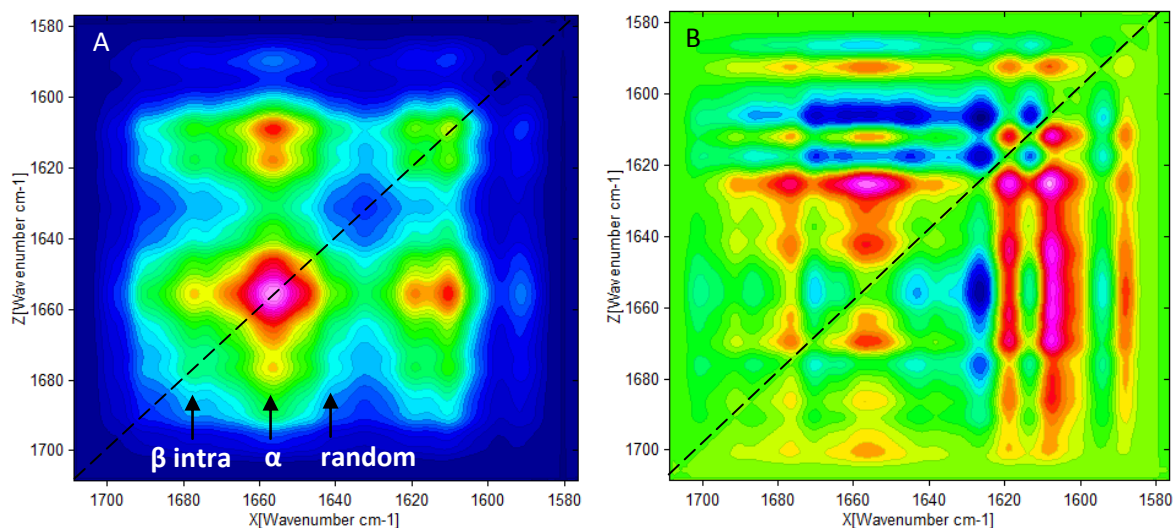


**Figure 4.11** –Correlation plot between 0.6 and 2.0 GPa: (A) Synchronous and (B) Asynchronous.

The asynchronous correlation of the series of spectra between 0.6 and 2.0 GPa (Figure 4.11 B) shows that the system is randomizing. The positive peaks that characterize the  $\alpha$  helix structure (see the sign convention in the appendix at the end of this chapter) testify that is this one the first structure to be involved in the structural changes. Pressure up to 2.0 GPa partially disrupts the  $\alpha$  chains in favor of the  $\beta$  and random structures. Also the  $\beta$  structures collaborate to the randomization process, as it is showed by the negative peaks corresponding to the frequencies around 1678 and 1690 cm<sup>-1</sup> and those of the random vibrations around 1630-1640 cm<sup>-1</sup>.

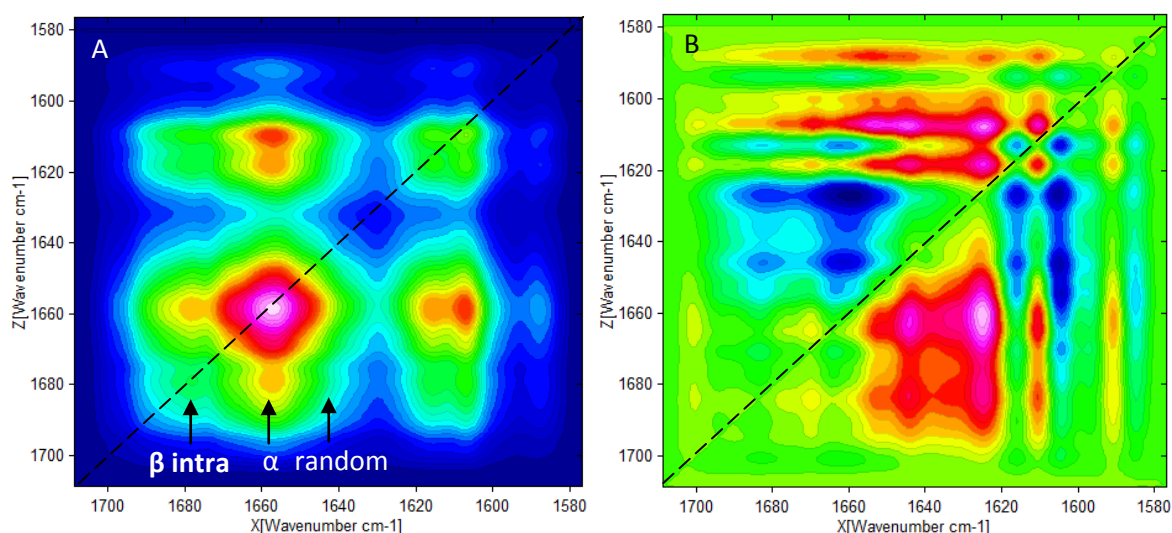


**Figure 4.12** –Correlation plot between 2.0 GPa and ambient pressure: (A) Synchronous and (B) Asynchronous.

On decreasing the pressure down to ambient conditions the following conclusions can be inferred directly from the asynchronous 2D Raman plot in Figure 4.12 (B): the positive correlation of both the random components (between 1630 and 1650  $\text{cm}^{-1}$ ) and the  $\beta$  inter-chain (around 1625 and 1670  $\text{cm}^{-1}$ ) with the  $\beta$  intra-chain structures (around 1680  $\text{cm}^{-1}$ ) and the  $\alpha$  helix (around 1660  $\text{cm}^{-1}$ ) identifies the latter as the later events. This can be read as a renaturation process.

On concluding the band fitting of the Amide I band and the contour plot gives the same results that are summarize in the following.

In the low regime of pressure (up to 0.6 GPa) the main effect of pressure is to dissociate the oligomeric structure present in this high concentrated solution. The decrease in the  $\beta$  inter-chain percentage in Table 4.5 clearly shows that and the analysis of the contour plot in Figure 4.11 B reinforce this thesis.

At higher pressure the protein starts to randomize, losing part of its  $\beta$  and  $\alpha$  structures (see Table 4.5). The negative correlation peak between the vibrations associated to the random components of the Amide I band and that of the  $\alpha$  and  $\beta$  structures in the contour plot presented in Figure 4.12 B suggest that the random components are the last to change under pressure on increasing pressure up to the maximum pressure applied (2 GPa).

On decreasing the pressure down to ambient conditions the BPI solution experienced a partial renaturation that increases the percentage of  $\alpha$  helix up to 40%.

### 4.3 Appendix: 2D Correlation Plot

2D correlation methodology for the analysis of spectra was developed by Noda<sup>13</sup> and then advanced in multiple step to a more generalized mathematical application. Actually it is a very useful technique to obtain information on the protein unfolding process.<sup>14,15</sup> The 2D correlation approach is used here to exploit deviations of spectral intensities from an expected value when Raman spectra are collected sequentially as a function of a perturbing parameter (pressure in the present case). This comparison is achieved by Fourier transforming the pressure variable as shown in equation 4.1:

$$Y(\nu, \omega) = \int_{-\infty}^{+\infty} y(\nu, p) e^{-i\omega p} dP \quad (4.1)$$

This transformation is followed by calculating the correlation between  $Y(\nu_1, \omega)$  and  $Y^*(\nu_2, \omega)$  as shown in equation 4.2, where  $\nu$  and  $\omega$  are the spectral and the Fourier frequencies, respectively,  $P$  the pressure and  $y(\nu, \omega)$  the dynamic intensity fluctuations:

$$\Phi(\nu_1, \nu_2) + i\Psi(\nu_1, \nu_2) = (\pi P)^{-1} \int_0^{\infty} Y(\nu_1, \omega) \cdot Y^*(\nu_2, \omega) d\omega \quad (4.2)$$

The real part  $\Phi(\nu_1, \nu_2)$  is the synchronous part of the correlation intensity and the imaginary part  $\Psi(\nu_1, \nu_2)$  is the asynchronous part of the correlation intensity. Each of the two parts of the correlation intensity can be plotted as a contour plot over the  $\nu_1, \nu_2$  plane.

The synchronous 2D Raman correlation plot highlight the similarities between the variations of spectral intensity to a perturbation, whereas the asynchronous 2D Raman correlation plot detects the differences. Although the synchronous plot is always required for interpreting data, it's the asynchronous plot that is of particular interest, because it permits the distinction of the spectral intensity changes that occurs out of phase (i.e. delayed or accelerated) as a function of the applied perturbation (in the present case the pressure).

The sign convention and a brief explanation to read easily the contour plot is given in Figure 4.13.

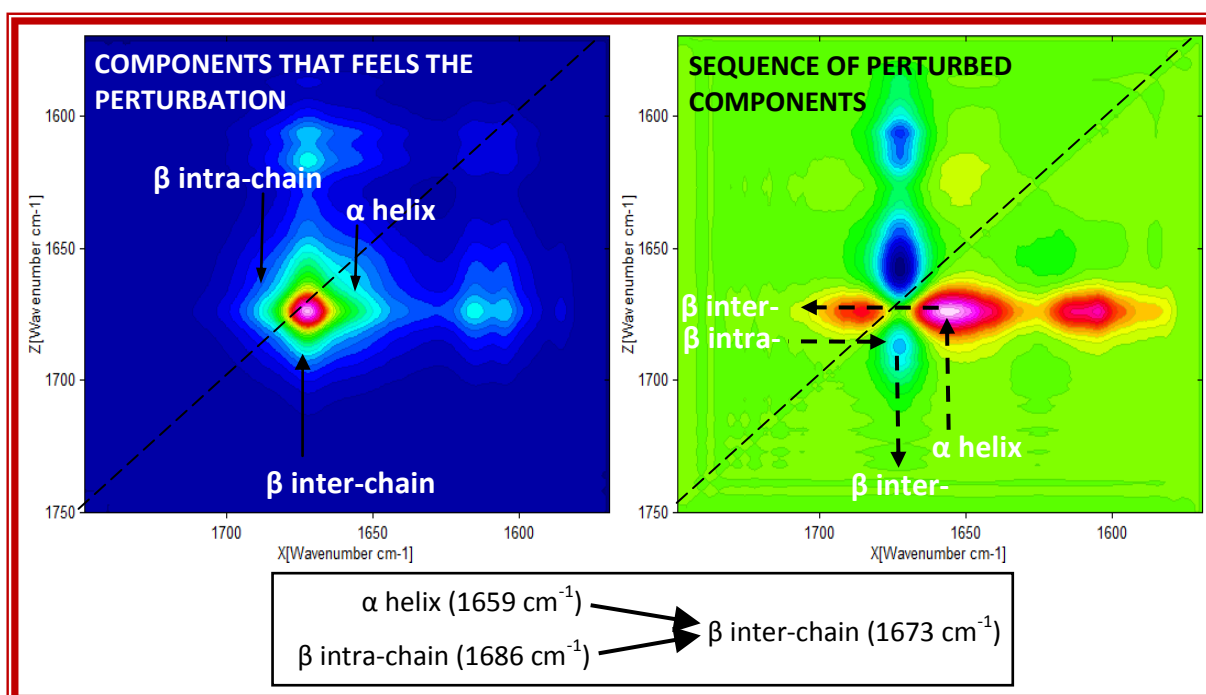


Figure 4.13 – Sign convention of the contour plot adopted in this work of thesis.

## *Bibliography of Chapter 4*

---

- <sup>1</sup> C. Dirix, F. Meersman, & K. Heremans, *High Pressure Res.*, 2003, 23, 63–66.
- <sup>2</sup> N.T. Yu et al., *J. Mol. Biol.*, 1972, 70, 117-132.
- <sup>3</sup> H. Sugeta, *Spectrochim. Acta*, 1975, 31A, 1729–1737.
- <sup>4</sup> H.E. Van Wart, A. Lewis, A. Scheraga, F.D. Saeva, *Proc Natl Acad Sci USA*, 1973, 70, 2617–2623.
- <sup>5</sup> H.E. Van Wart, H.A. Scheraga, *Proc Natl Acad Sci USA*, 1986, 83, 3064–3067.
- <sup>6</sup> W. Qian, W. Zhao and S. Krimm, *J. Mol. Struct.*, 1991, 250, 89-102.
- <sup>7</sup> M.N. Siamwiza, R.C. Lord, M.C. Chen, T. Takamatsu, I. Harada, H. Matsuura, and T. Shimanouchi, *Biochemistry*, , 1975, 14, 4870.
- <sup>8</sup> Zai-Qing Wen, *J. Pharm. Sci.*, 2007, 96, 2861.
- <sup>9</sup> M. Aoyama, K. Kurihara and K. Shibata, *Biochim. Biophys. Acta*, 1965, 107, 257-265.
- <sup>10</sup> L. Ashton, J. Disting, E. Imomoh, S. Balabani, and E.W. Blanch, *Biophys. J.*, 2010, 98, 707–714.
- <sup>11</sup> L. Smeller, K. Goossens, K. Heremans, *Vibrat. Spectr.*, 1995, 8, 199-203.
- <sup>12</sup> J.L. Silva, and G. Weber, *Annu. Rev. Phys. Chem.*, 1993, 44, 89–113.
- <sup>13</sup> I. Noda, *Appl. Spectrosc.*, 1993, 47, 1329-1336.
- <sup>14</sup> H. Fabian, H. H. Mantsch, and C. P. Schultz, *Proc. Natl. Acad. Sci. USA*, 1999, 96, 13153–13158.
- <sup>15</sup> V. Shashilov, M. Xu, V.V. Ermolenkov, L. Fredriksen, and I. K. Lednev, *J. Am. Chem. Soc.* 2007, 129, 6972-6973.

# *Chapter 5*

## *Raman Measurements on Insulin Powder Under Pressure*

This chapter is devoted to the high pressure Raman measurements on protein powder. The aim of this study is to extend the range of pressure applied to BPI and to look for stable conformational changes in the protein secondary structure. The use of hydrated powder allows to overcome the problems related to the pressure induced ice-forming and can shed light on the anomalous pressure stability shown by insulin. Pressurization/depressurization cycles as well as careful investigation of the pressure dependence of the Raman spectrum showed a remarkable stability of the protein conformation up to about 4 GPa, whereas a plastic irreversible structural transition occurs at  $P=4.2$  GPa.

## 5.1 Determination of the Maximum Pressure for the Elastic Response: Pressurizing/Depressurizing Cycles

BPI powder was loaded without any further purification into the 150  $\mu\text{m}$  hole of a 50  $\mu\text{m}$  Molybdenum gasket together with a ruby nanosphere as internal pressure calibrant. To apply pressure to the sample a membrane diamond anvil cell was used (see paragraph 2.2 for more details).

BPI powder was slowly pressurized up to 1 GPa, kept under constant pressure for about 1 hour and then the pressure was slowly released down to ambient pressure. The same procedure was followed allowing for a maximum pressure of 2 GPa, 3 GPa, and 4 GPa. Raman spectra collected after the pressurizing/depressurizing cycles are shown in Figure 5.1 together with the spectrum of the pristine (non-pressurized) BPI powder.

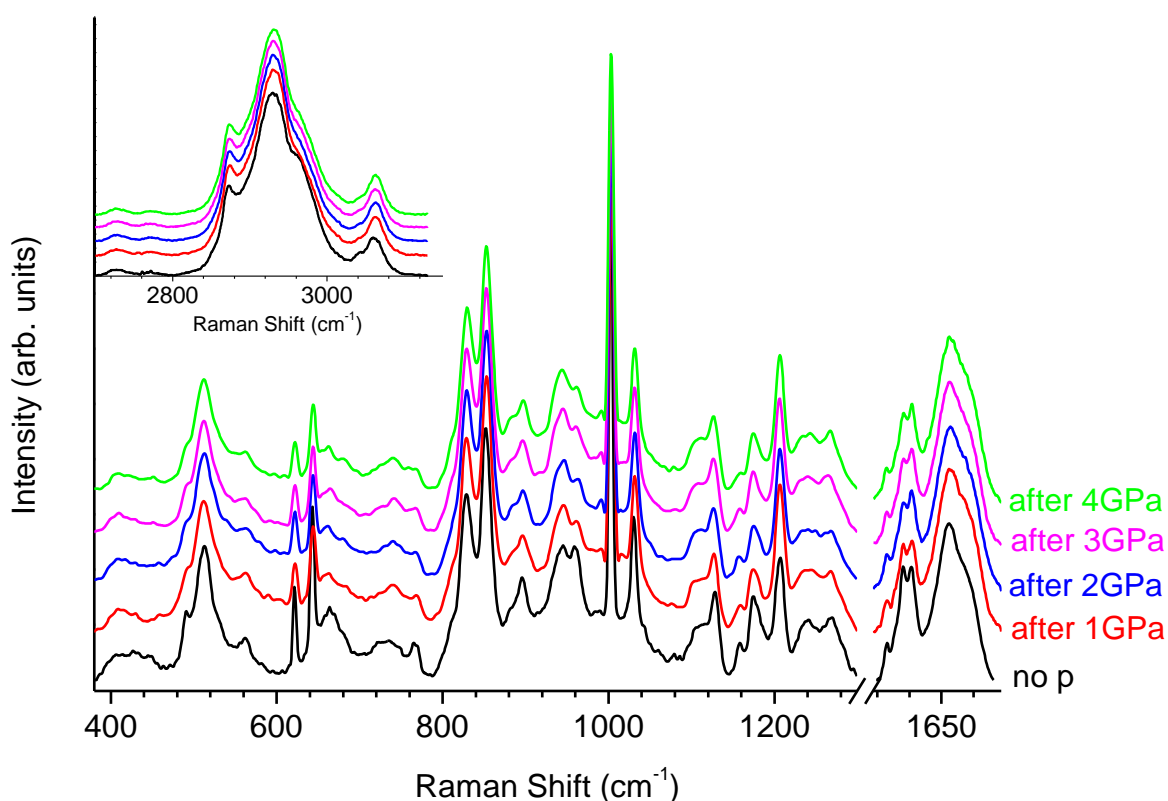


**Figure 5.1** – Raman spectra of BPI at ambient pressure after pressurizing/depressurizing cycles up to 0 GPa (black), 1 GPa (red), 2 GPa (blue), 3 GPa (magenta), and 4 GPa (green).

Looking at the Raman markers of the tertiary conformation no striking changes can be seen among the five spectra shown in Figure 5.1, the main effect of pressure is a generalized decrease of the Raman intensity. Spectroscopic markers of the disulphide bridges around 500  $\text{cm}^{-1}$  do not show pressure-induced frequency shift or shape modifications suggesting that the bridges are still intact and that the dihedral angles of the CCSSCC moiety are still the same than in the pristine structure. The same conclusion can be drawn for the skeletal bending (around 380-490  $\text{cm}^{-1}$ , 550  $\text{cm}^{-1}$  and 730-770  $\text{cm}^{-1}$ ) and C-N stretching (around 1110-1160  $\text{cm}^{-1}$ ). The only marker of the tertiary structure that seems to be slightly different between the pressurized and the un-pressurized BPI is the skeletal stretching around 900-980  $\text{cm}^{-1}$  (C-C stretching). In literature the Raman bands located at 930 and 960  $\text{cm}^{-1}$  were assigned to  $\text{C}\alpha$ -C-N stretching vibration in  $\alpha$  helix and  $\beta$  sheet structures in the secondary structure.<sup>1</sup> After being pressurized up to 1 GPa (but the same discussion is true for

the other pressure cycle) the relative intensity of the  $\alpha$ -C-N stretching vibration ascribed to the  $\beta$  sheets decreased respect to the one ascribed to the  $\alpha$  helix. It is possible to conclude that the high pressure treatment for pressure cycle from 1 to 4 GPa slightly changed the peptide linkages towards a configuration that could favor the  $\alpha$  helix conformation.

One of the results of this thesis is the identification of the relative intensity of the side chains at  $1605\text{ cm}^{-1}$  (Tyr and Phe) and  $1615\text{ cm}^{-1}$  (Tyr) as a sensible marker of the quaternary structure of BPI. The Raman spectrum of the hexameric structure of BPI shows the two side chains peaks with the same intensity (see black curves in Figure 5.2 where  $I_{1615}=I_{1605}$ ). A change in the relative intensities ( $I_{1615}>I_{1605}$ ) can already be seen in the sample pressurized up to 1 GPa and is even more evident in the spectra of the BPI pressurized at pressures  $\geq 2$  GPa. In all the spectra treated by pressure the change of relative intensities is well clear, underlying the transition from a predominantly hexameric structure to a dimeric/monomeric one. It is worth to mention that the same pressure induced dissociation of the oligomeric structure has been already reported for the insulin solutions under pressure discussed in section 4.1 and 4.2.

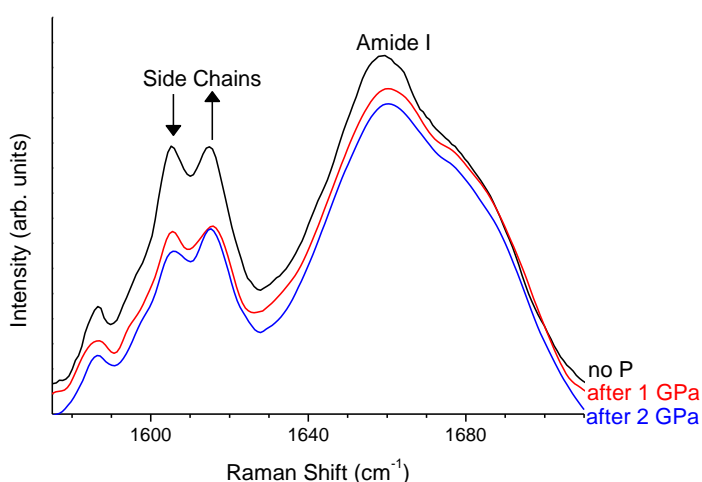


**Figure 5.2** – Raman spectra of BPI in the Amide I region. Black curve: spectrum of the un-pressurized sample, red and blue curves: spectra of the sample pressurized up to 1 and 2 GPa respectively.

Some weak differences can be found also in the shape of the Amide I band (see Figure 5.2) and its qualitative analysis can lead to the same conclusion. In fact it was already observed by Dong et al. that insulin in the monomeric forms possess a more rounded shape than hexameric one.<sup>2</sup>

	No P applied	After 1 GPa	After 2 GPa	After 3 GPa	After 4 GPa	
<b>Random</b>	1638	1638	1640	1640	1639	Frequency ( $\text{cm}^{-1}$ )
	32	33	33	33	37	FWHM ( $\text{cm}^{-1}$ )
	20	18	18	17	18	Area (%)
<b><math>\alpha</math> helix</b>	1659	1660	1660	1659	1660	Frequency ( $\text{cm}^{-1}$ )
	26	28	28	28	28	FWHM ( $\text{cm}^{-1}$ )
	48	49	50	50	49	Area (%)
<b><math>\beta</math> intra-chain</b>	1683	1684	1684	1684	1684	Frequency ( $\text{cm}^{-1}$ )
	26	26	27	27	27	FWHM ( $\text{cm}^{-1}$ )
	32	32	33	33	32	Area (%)

**Table 5.1** – Results of the fitting procedure (frequency, FWHM and area) on the BPI powders collected at ambient pressure after different P cycle: no P applied, 1 GPa, 2 GPa, 3 GPa and 4 GPa.

Indeed despite the slightly different shapes of the Amide I band, the fitting procedure underlying the resistance of the insulin to pressurization, even applying pressure up to 4 GPa (see Table 5.1).

The above presented results confirm the well known stability of insulin under volume compression but extend the pressure range of the elastic response to unexpected values and indeed a clear indication of plastic conformation changes was found only above 4 GPa.

## 5.2 The Pressure Dependence of the Raman Spectrum: the Plastic Transition at 4.2 GPa

The above discussed pressurizing/depressurizing cycles were carried out only up to 4 GPa since high pressure test experiments carried out at higher pressures on native BPI in powder showed the occurrence of a remarkable structural instabilities just above 4 GPa. To investigate the nature of this phenomenon, a high pressure experiment was carried out over a much larger pressure range. The Raman spectra of the native BPI powder collected at different pressures along a pressurizing-depressurizing cycle with  $P_{\max} = 8.1$  GPa are shown in Figure 5.3. The waiting time to stabilize the system at each working pressure was of about 30 minutes and the acquisition time for each Raman spectrum was of about 30 minutes for each of the spectral ranges exploited.

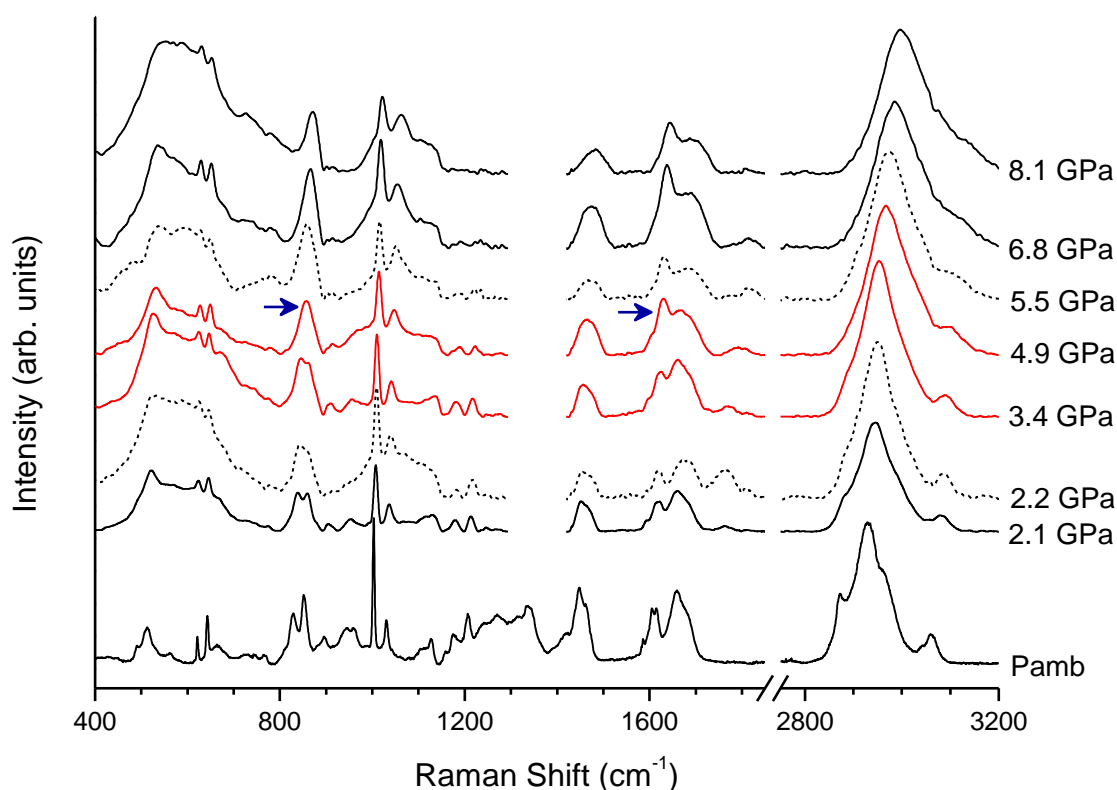


**Figure 5.3** – Raman spectra of BPI in the two spectral ranges  $400\text{-}1830\text{ cm}^{-1}$  and  $2750\text{-}3200\text{ cm}^{-1}$  on increasing pressure (solid lines) up to 8.1 GPa and on decreasing pressure (dashed lines). The spectral region between  $1290\text{ cm}^{-1}$  and  $1410\text{ cm}^{-1}$  is not shown owing to the strong Raman signal of the diamond anvils. All the spectra were normalized to the area of the peaks in the high wavenumbers region  $2800\text{-}3200\text{ cm}^{-1}$ . The two red curves highlight the discontinuity between 3.4 and 4.9 GPa, the arrows indicate the spectral features in which major changes occur.

Looking at Figure 5.3, besides the expected overall hardening of the peak frequencies with increasing pressure, a discontinuity in the pressure dependence of the Raman response can be observed by comparing the spectra collected at 3.4 GPa and at 4.9 GPa (red curves in Figure 5.3). As a matter of fact, abrupt spectral shape modifications occur over different spectral ranges (see for



example the Tyr doublet around 830-850  $\text{cm}^{-1}$  and the Amide I band around 1650  $\text{cm}^{-1}$ , both marked with blue arrows in Figure 5.3). To obtain quantitative information on the pressure effects on BPI, all the spectra were fitted as reported in section 2.4.

The pressure dependence of the central frequency of several peaks is shown in Figure 5.4. A discontinuity in the pressure behavior is clearly observed, at least in some cases, and thus the threshold pressure value was set at  $P_t = 4.2$  GPa (intermediate between 3.4 and 4.9 GPa). A clear discontinuity around  $P_t$  is apparent in the case of the Tyr doublet (up and down triangles in Figure 5.4A), which merge in a single band above  $P_t$ . Other discontinuities are evident in the peaks related to the C-C stretching mode (squares in Figure 5.4A), to the Tyr mode (down triangles in Figure 5.4B), and to the  $\text{CH}_2$  asymmetrical stretching mode (squares in Figure 5.4C). On the contrary, the Phe mode (diamonds in Figure 5.4B) and the peak related to  $\text{CH}_2$  deformation (circles in Figure 5.4C) show a continuous pressure dependence of their frequencies.

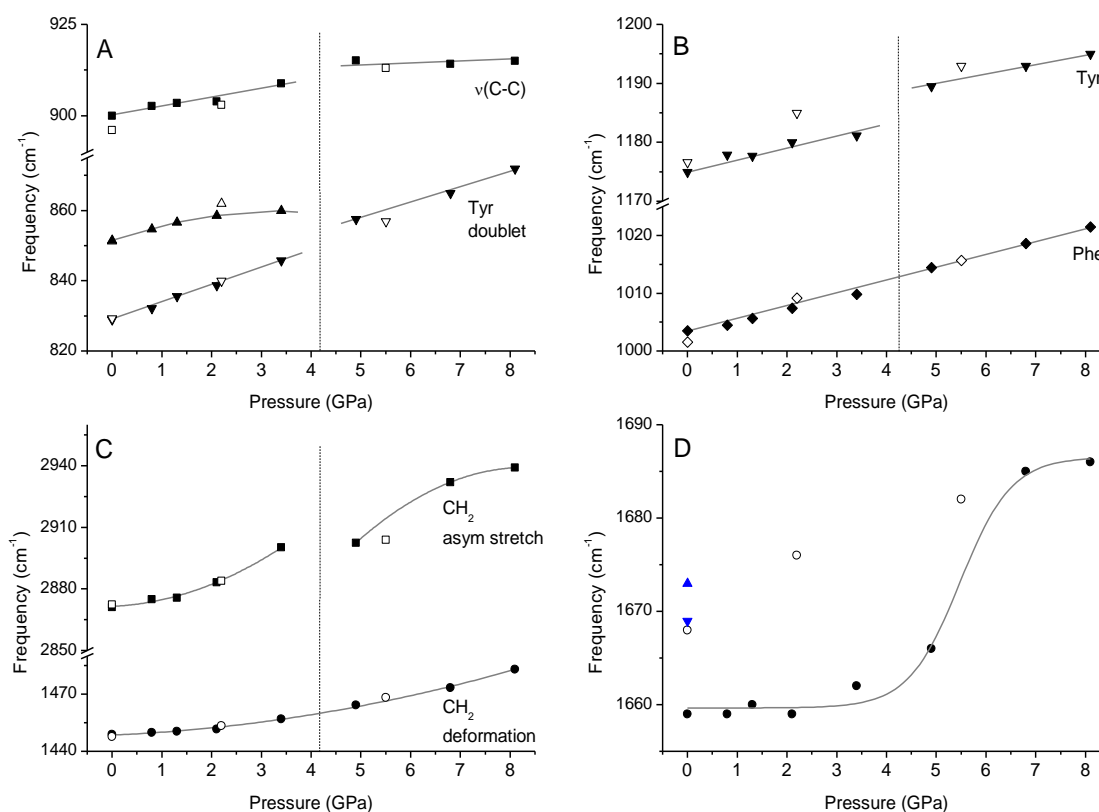


**Figure 5.4** – Pressure dependence of the central frequency of selected Raman peaks of native BPI (closed symbols on increasing pressure, open symbols on decreasing pressure). Vertical dashed lines mark the threshold pressure ( $P_t = 4.2$  GPa, see text). Continuous lines are guide to the eyes. In panel D the central frequency of the Amide I band is fitted by a sigmoidal curve (Boltzmann function), the up and down blue triangles are the central frequency of the Amide I band for fibrillar-22h and fibrillar-4h, respectively (see the text on the next paragraph).

Figure 5.4D shows how the frequency of the maximum of Amide I band shifts toward high frequency on increasing pressure. This behavior, in agreement with literature results, is recognized as a signature of the unfolding process of the secondary structure.<sup>3,4</sup> On decreasing pressure, it can be clearly observed a downshift of the Amide I central frequency, which reflects a partial refolding process. As shown in Figure 5.4D, the non reversibility of pressure-induced transformation of BPI is clear. On the basis of the above results, we remark that a stable new pressure-induced state of BPI can be achieved only by applying a pressure above  $P_t$ .

### Tyrosine Fermi Doublet

To gain a deeper understanding of the pressure effects, the pressure dependence of the intensity ratio of the Fermi doublet of Tyrosine  $I_{850}/I_{830}$  was analyzed, as it can provide information on strength and character of the hydrogen bond.<sup>5</sup> The pressure dependence of the  $I_{850}/I_{830}$  ratio is shown in Figure 5.5 for pressures up to  $P_t$  since for  $P > P_t$  the doublet merge into a single peak (see Figure 5.4A). On increasing pressure, the  $I_{850}/I_{830}$  ratio shows a decreasing trend. This effect is probably due to a loss of stability of the helical structures in the A-chain that leads to a partial unfolding of the protein and to the displacement of the two Tyr residue that in the native conformation are positioned in one of the two  $\alpha$  helices and are exposed to the surface of the protein (Tyr14A and Tyr19A) towards a less hydrophilic environment, i.e. towards the protein core. Alternatively, the effect that is observed for Tyr residues could be explained by the reduction of the polarity in the environment of the protein, due to a displacement of water molecules caused by pressure,<sup>6</sup> with a subsequent destabilization and unfolding of the helices in A chain. The general pressure trend is consistent with the results obtained in the evaluation of the secondary structure content. Indeed the unfolding of the helices of the A chain would lead to a decrease of the percentage of helices in the protein of about 27%, close to the value found through the Amide I analysis (see later on in the text). As to the single peak structure observed for  $P > P_t$ , it is worth to recall that a single peak structure for Tyr was found in Raman measurements at ambient pressure on the bacteriophage Ff, and attributed to the extremely hydrophobic environment in which Tyr residues are located inside the virus.<sup>7</sup> Following the same idea the data collected for this thesis suggest that Tyr residues are in a highly hydrophobic ambient above  $P_t$ .<sup>8</sup>

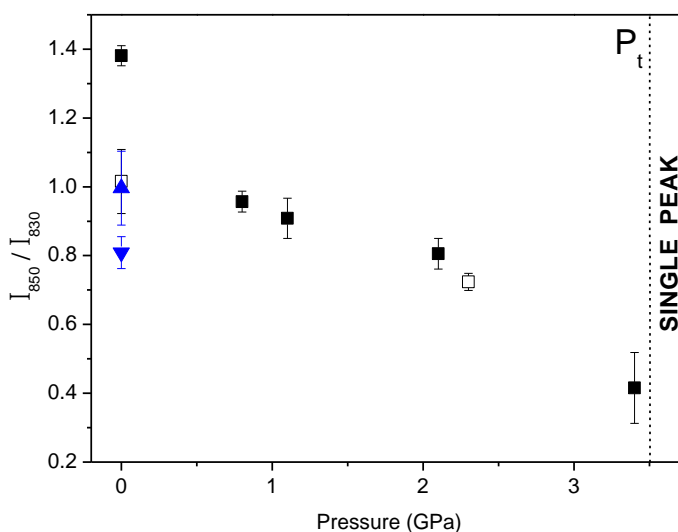


**Figure 5.5** – Pressure behavior of the intensity ratio,  $I_{850}/I_{830}$ , between the Tyr peaks around 850 and 830  $\text{cm}^{-1}$  (closed and open symbols on increasing and decreasing pressure, respectively). The dashed line marks the threshold pressure  $P_t = 4.2$  GPa. The error bars were evaluated by varying fitting parameters around the best-fit value. The up and down blue triangles show the intensity ratios at ambient conditions for fibrillar-22h and fibrillar-4h samples respectively (see next paragraph).

### Tyrosine around 1177 $\text{cm}^{-1}$ and Phenylalanine around 1003 $\text{cm}^{-1}$

Other important information can be obtained considering the Tyr (1177  $\text{cm}^{-1}$ ) and the Phe (1003  $\text{cm}^{-1}$ ) peaks. As shown in Figure 5.4B, the central frequency of the Phe peak shows a linear and reversible pressure dependence, while that of Tyr shows a sharp discontinuity at  $P_t$ , where the structural transition occurs. The different behavior of the two peaks can be explained bearing in

mind that the Phe peak is basically conformational independent<sup>9</sup> whereas Tyr is sensitive to changes in its surrounding ambient especially to the strength and character of the hydrogen bond. Indeed it has been suggested that the  $I_{\text{Tyr}}/I_{\text{Phe}}$  intensity ratio is related to the extent of the protein hydration.<sup>10</sup> Analyzing the present data (see Figure 5.6) it has been found a value of 0.32 for the ambient pressure powder which is consistent with that one reported in ref. 10 for a crystals of BPI under ambient conditions (1<sup>st</sup> range). On increasing the pressure the ratio decreases and its value stabilizes around 0.25 (2<sup>nd</sup> range). On crossing  $P_t$  it abruptly decreases (around 0.13, 3<sup>rd</sup> range) and keeps constant up to the maximum applied pressure. On releasing the pressure its value remains constant. Since hydration and internal water are known to be structurally relevant,<sup>11</sup> the analysis of the powder samples may suggest that the pressure treatment changes the water distribution around the protein.

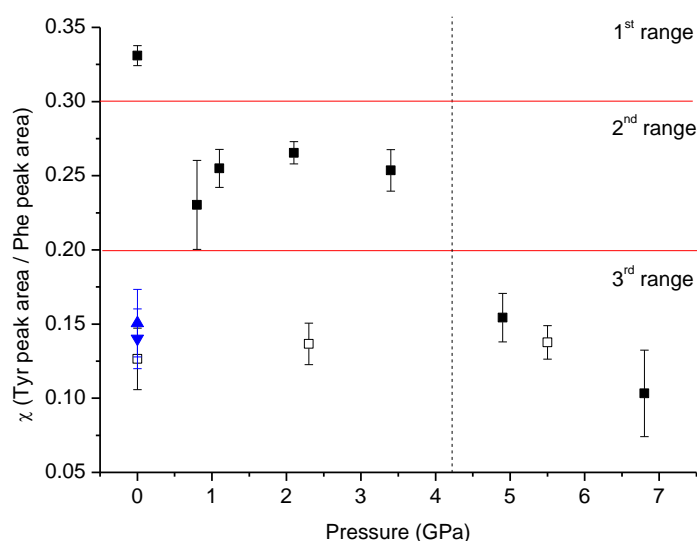


**Figure 5.6** – Pressure behavior of the intensity ratio,  $I_{\text{Tyr}}/I_{\text{Phe}}$ , between the Tyr peak centered around  $1177\text{ cm}^{-1}$  and the Phe peak centered around  $1003\text{ cm}^{-1}$  (closed and open symbols on increasing and decreasing pressure, respectively). The dashed line marks the threshold pressure  $P_t = 4.2\text{ GPa}$ . The error bars were evaluated by varying fitting parameters around the best-fit value. The up and down triangles show the intensity ratios at ambient conditions for the fibrillar-22h and fibrillar-4h samples respectively (see next paragraph in the text).

All the analysis above presented will gain even more importance by the comparison among the pressure treated sample ( $P_{\text{max}}=8.1\text{ GPa}$ ) and two thermo chemical treated BPI. See next paragraph for more details.

### 5.2.1 Pressure Treated Insulin Vs Thermo-Chemical Treated Insulin

Raman measurements were performed on different BPI powders: native BPI, the pressure treated BPI above discussed (P-treated in the following), and two thermo-chemical fibrillated BPI. Fibrillation of BPI was obtained as described in section 2.6. Raman spectra of insulin fibrils were obtained using a drop coating deposition Raman (DCDR) method (for more details see section 2.3).<sup>12</sup> All the spectra were analyzed by applying the LM-fit procedure. The best-fit values of all the clearly detectable peak frequencies resulting from the LM-fit procedure are reported in Table 5.2 together with their assignment obtained following the pioneering work of Yu.<sup>13</sup> All the experimental frequencies of native powder are in good agreement with literature data.<sup>13,14</sup>

Native BPI (cm <sup>-1</sup> )	P-treated BPI (cm <sup>-1</sup> )	Fibrillar-4h BPI (cm <sup>-1</sup> )	Fibrillar-22h BPI (cm <sup>-1</sup> )	Assignment
367 406 430 w , br 450 490	413 441 vw , br 490	411 430 vw , br 451 491	411 430 vw , br 451 491	skeletal bending
513 s 536 sh	509 s 527 sh	510 s 526 sh	513 s 531 sh	v(S-S)
560 m	555 w , br	555 vw , br	545 vw , br	skeletal bending
622 s 643 s	621 s 643 s	621 s 643 s	621 s 643 s	Phe Tyr
664 m , br 681 sh	664 vw , br	662 vw , br		v(C-S) of the C-S-S-C group
728 w , br 746 vw , br 769 vw , br	742 br 765 vw , br	742 br 764 vw , br	741 br 769 vw , br	skeletal bending
829 s 853	828 s 852	830 s 854	828 s 854	Tyr
895 943 m 962 1003 vs 1011 1032 s 1112 1129 m , br 1158	890 948 w , br 990 1002 vs 1031 s 1110 1126 m , br 1158	883 954 vw 993 1003 vs 1032 s 1116 1127 m , br 1157	882 953 vw 994 1003 vs 1031 s 1117 1126 m , br 1155	v(C-C) Phe Phe v(C-N)
1173 m 1182 1207 s	1174 w 1188 1207 s	1174 w 1190 1207 s	1174 w 1202 s	Tyr Phe
1200-1300	1200-1300	1200-1300	1200-1300	AMIDE III
1314 1339 m 1354	1314 1339 w 1368	1315 w 1342	1312 w 1338	CH deformation
1418 sh	-	1406 w , br 1419	1406 w , br 1419	symm CO <sub>2</sub> <sup>-</sup> stretching
1448 s 1462	1448 s 1463	1448 s 1464	1449 s 1464	CH <sub>2</sub> deformation
1585 sh 1600 s 1606 s 1616 s	1585 sh 1601 s 1604 s 1616 s	1585 sh 1599 s 1605 s 1615 s	1585 sh 1599 s 1605 s 1616 s	Phe Phe&Tyr Tyr
1600-1700	1600-1700	1600-1700	1600-1700	AMIDE I

**Table 5.2** – Frequencies of Raman spectra of native, P-treated and fibrillar BPI.[vs=very strong, s=strong, m=medium, w=weak, vw=very weak , sh=shoulder , br=broad , v(=)stretching]

As it has been observed in section 3.1.2, Raman spectroscopy is a powerful method to analyze the state of a protein as shown by the comparison among the four samples in Figure 5.7. The spectra of

fibrillar (4h and 22h) and P-treated BPI were normalized to the spectrum of native BPI in the frequency region of the Phe peak, between 990 and 1015  $\text{cm}^{-1}$ . The spectral regions of Amide bands and those framed by dashed squares in Figure 5.7 are the regions where differences (in frequency and/or spectral shape) among the spectra are more evident.

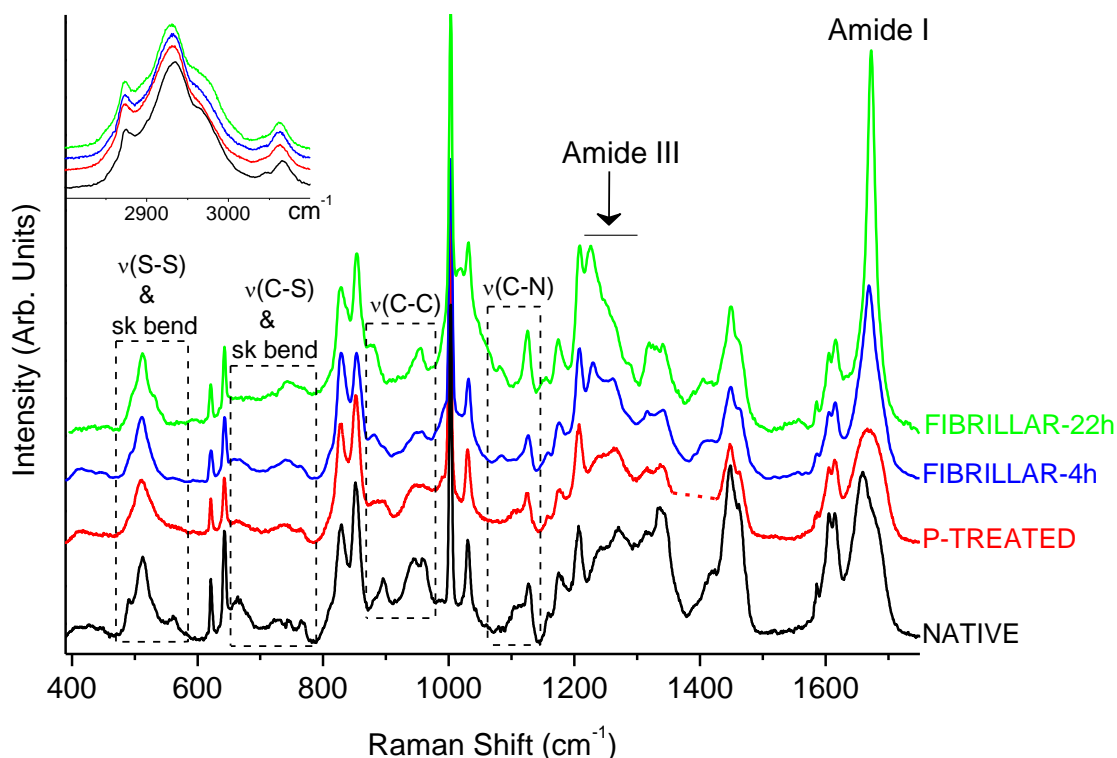


**Figure 5.7** – Raman spectra of BPI at ambient conditions: native (black), P-treated (red), fibrillar-4h (blue) and fibrillar-22h (green) BPI. The Raman spectra of the four samples in the region of the CH stretching modes are shown in the inset. The regions framed by dashed squares are those where remarkable spectral differences occur. [sk = skeleton, bend = bending,  $\nu$ ( ) = stretching]

### S-S bonds

To better investigate the effect of the applied pressure on the tertiary structure it has been conducted a detailed analysis of the spectral features ascribed to this structure. The three disulfide bridges of insulin (within the 510-540  $\text{cm}^{-1}$  range and at about 670  $\text{cm}^{-1}$ ) are still present in both fibrillar samples and P-treated BPI. These samples show spectral shapes rather similar but significantly different from those in the native sample. The analysis of the frequencies related to the disulfide bridges, that are directly affected by the possible conformations of the CCSSCC moiety (see Figure 3.8 and the relative text)<sup>15,16</sup>, shows only small variations of the peak frequencies in the four Raman spectra. The observed differences must be indeed ascribed to a peak broadening and an overall decrease of the intensities of these structures. The modification induced on the native protein by thermo-chemical and pressure treatments can be thus related to small variations of the average values of the dihedral angles but mainly to a larger dispersion of these values, i.e. disorder in the orientations of the C-S-S-C moiety. Data thus confirm that, beside a certain level of angular disorder, thermo-chemical induced fibrillation process doesn't break the disulfide bridges<sup>17</sup> of insulin that are still present in the spectra of the fibrillar BPI and show, surprisingly, that S-S bonds survive also to the huge volume compression applied.

### Skeletal modes

As far as the secondary structure is concerned, the comparison shown in Figure 5.7 and the careful data analysis lead to different results. Within the spectral regions of skeletal bending the line at  $560\text{ cm}^{-1}$  in the native BPI shifts to lower wavenumber in all the treated BPI samples, down to about  $555\text{ cm}^{-1}$  in the fibrillar-4h and P-treated BPI and to a still lower value about  $545\text{ cm}^{-1}$  in the fibrillar-22h BPI. The three peaks at  $728, 746, 769\text{ cm}^{-1}$  observed separately in the native BPI coalesce into a single peak at  $742\text{ cm}^{-1}$  with a weak shoulder around  $765\text{ cm}^{-1}$  in the treated samples. These differences have been previously observed by the comparison between the Raman spectra of native and denatured insulin in ref. 13. The strong indication that all the treated samples have suffered of a structural reorganization of the internal polypeptide chain orientation is confirmed looking at the remarkable modifications observed in the wavenumber regions of the C-C and C-N stretching modes ( $890\text{-}990\text{ cm}^{-1}$  and  $1110\text{-}1160\text{ cm}^{-1}$ , respectively). Since these vibrational modes are considered a spectroscopic markers of the secondary structure,<sup>18</sup> their rearrangement under pressure and thermo-chemical treatment indicate an extensive unfolding of the protein backbone.

All the above mentioned signs of denaturation progressively strengths going from bottom to up in Figure 5.7, i.e. going from native to P-treated to fibrillar-4h and finally to fibrillar-22h BPI. This consideration proves once again that Raman Spectroscopy is a powerful method to appreciate the degree of denaturation/fibrillation and it also indicates that the P-treated sample is quite similar to the BPI spectra all over the above discussed regions, even if the two spectra are not identical. Apart from the Amide bands to be discussed in the following, well detectable differences can be found in specific frequency regions of the Raman spectrum.

### Tyrosine Fermi Doublet

As already noticed, for its implication in the hydrogen character (see previous paragraph and section 3.1.2), it is of particular interest the analysis of the relative intensity of the peaks in the Tyr Fermi doublet ( $830\text{-}850\text{ cm}^{-1}$ ). The value found in this work for the  $I_{850}/I_{830}$  ratio is close to 1.4 in the native, to 1.1 in both the P-treated and the fibrillar-22h and to 0.8 in the fibrillar-4h BPI. The lowering of this ratio suggests a possible decrease in solvent exposure of the Tyr residues going from native to misfolded state.<sup>19</sup> The low  $I_{850}/I_{830}$  value (0.8) found for fibrillar-4h BPI in agreement with ref. 19 suggests that the Tyr residue associated with the  $\alpha$  helix in the A chain (Tyr14 and Tyr19) are buried inside the protein core, revealing that the reorganization induced by the starting process of fibrillation involve the  $\alpha$  helix structure.<sup>20</sup> The intensity ratio for fibrillar-22h and fibrillar-4h samples are shown in Figure 5.6 as up and down blue triangles respectively. The intermediate value found for the P-treated sample and the fibrillar-22h may have two different explanations. In the case of the P-treated sample the 1.1 value for the Tyr ratio may suggests that high pressure could change at least partially the protein structure, even if no exposure of the main  $\alpha$  helix segment occurs. While as it was already pointed out in section 3.1.2, for the fibrillar-22h BPI it is possible that at the end of the misfolding pathway the Tyr residues are involved in the strong hydrogen bonds that build up the fibrils.

### Tyrosine around $1177\text{ cm}^{-1}$ and Phenylalanine around $1003\text{ cm}^{-1}$

Another similarity, between P-treated and fibrillar samples, is the low level of hydration of the protein (see Figure 5.6). Indeed it has been shown in the previous paragraph that the intensity ratio between the vibration of the Tyr residue around  $1177\text{ cm}^{-1}$  and that of the Phe around  $1003\text{ cm}^{-1}$  decrease on increasing pressure up to 4.2 GPa. After that value it jumps to a still lower value that is maintained on decreasing pressure down to ambient condition. It has been found that the value of

this ratio for the P-treated sample is similar to that of the two fibrillar sample (up and down blue triangles in Figure 5.6). The analysis of the pressure treated BPI powder does not simply suggest that the pressure treatment changes the water distribution around the protein, but it also shows that this new water configuration resembles the one that is in the fibrillar state.

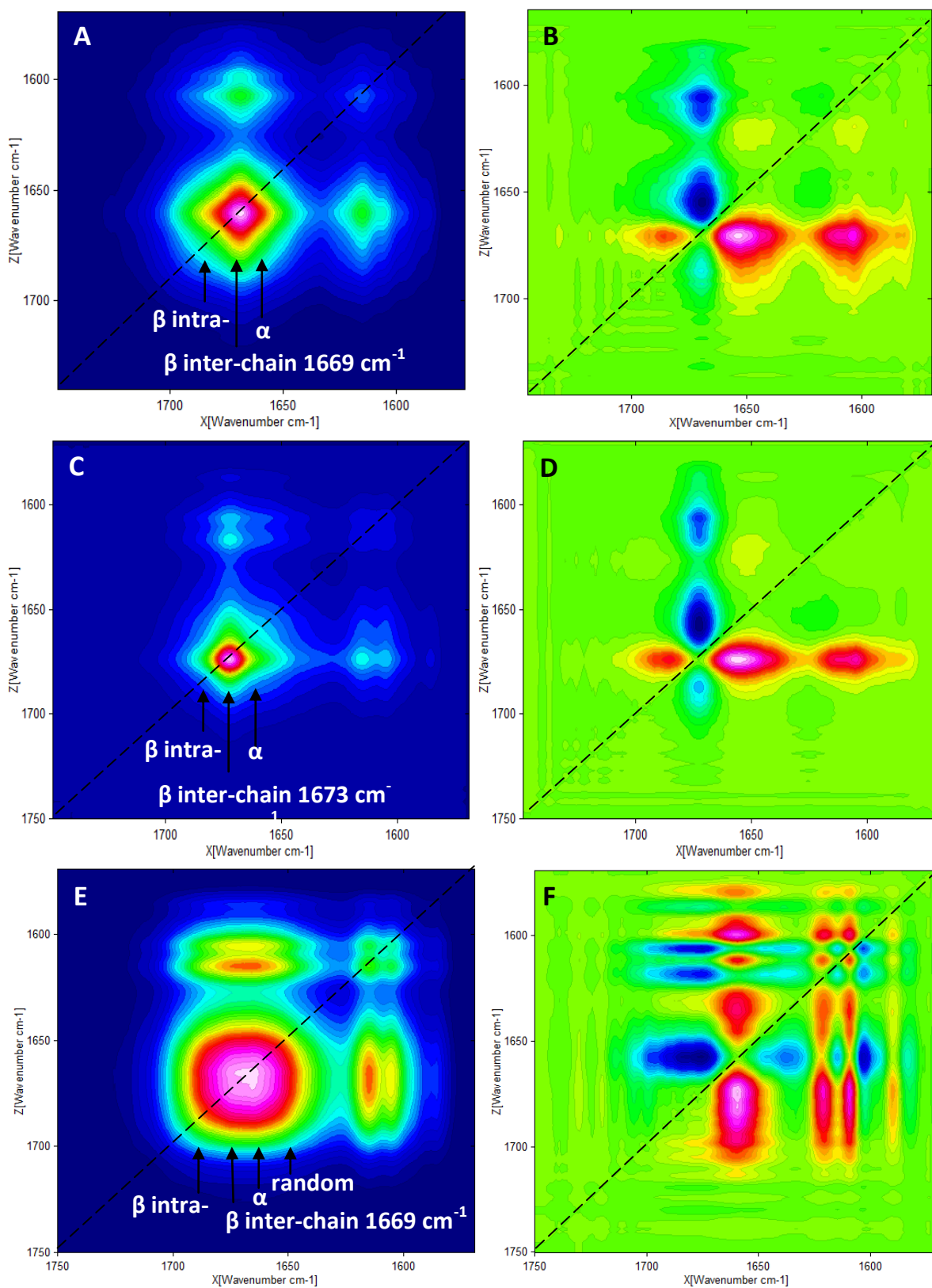


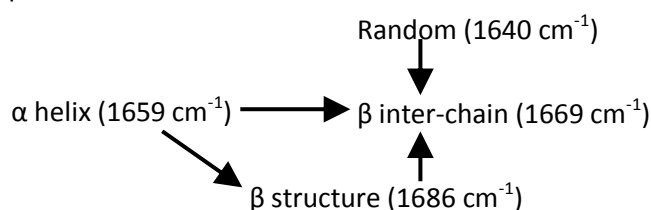
**Figure 5.8** – A: Synchronous and B: Asynchronous plots of native and fibrillar-4h BPI, C: Synchronous and D: Asynchronous plots of native and fibrillar-22h BPI, E: Synchronous and F: Asynchronous plots of native and P-treated BPI.

The above discussed similarities and differences among the spectra of native, fibrillar and P-treated BPI point out a remarkable denaturing effect of high pressure albeit the P-treated sample seems to be in a partially denatured state different from the one shown by the fibrillar samples.

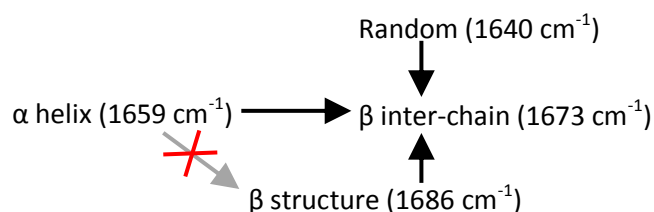
In Figure 5.8 are shown the contour plots (synchronous and asynchronous) in the Amide I region of all the ambient pressure Raman spectra shown in Figure 5.7 (see the appendix in Chapter 4 for mathematical details and for the sign convention).

The synchronous plots evidence that the number of components involved in spectral intensities variation is different depending on the type of the perturbation applied (temperature in A and C, pressure in E) but also from the degree of the “reaction”, i.e. at the beginning or at the end of the fibrillation process (see the synchronous plots A and C). It is clearly possible to distinguish the  $\alpha$  helix component, the random coil one and two different  $\beta$  sheet structure.  $\beta$  sheets around  $1680\text{ cm}^{-1}$  are due to peptide residues that are in Ramachandran  $\beta$ -space but that are not forming inter-strand hydrogen bonds<sup>21</sup> and are typical of the native structure, while the  $\beta$  sheets that constitute the fibrils are at a lower frequency, around  $1670\text{ cm}^{-1}$  and show inter-chain bonding.<sup>22</sup>

The asynchronous plot of the fibrillar-4h spectrum against the native powder makes possible to follow the fibrillation process:

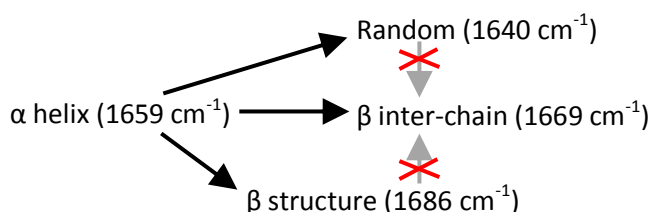


After 24h at  $80^\circ\text{C}$  at pH2 the solution of BPI is known to be in a complete fibrillar state. So for the fibrillar-22h the process is almost complete and it is not possible to follow the intermediate passages of the fibrillation process. The asynchronous plot reveals only the initial and final step:



In this case there is no direct nor indirect correlation between the  $\alpha$  helix and the  $\beta$  intra-chain structure. Moreover the different frequency for the  $\beta$  inter-chain may be correlated to different strength in the hydrogen bonding between the fresh (4h) and the mature (22h) fibrils. The higher frequency of the mature fibrils means that the  $\beta$  inter-chain has gained a higher degree of order.<sup>23</sup>

Finally comparing the synchronous plot of the P-treated and native BPI with that of fibrillar-4h and native BPI it is possible to see that the number of components to the contour plot are the same. But the asynchronous plot reveals that using high pressure on BPI powder leads to a different denaturation sequence:





Different denaturation sequences are compatible with different mechanism of denaturation: in a parallel process mechanism, random coil and  $\beta$  sheet are produced directly from the native protein, while in a step-by-step mechanism,  $\beta$  sheet develops from the partially unfolded intermediate.<sup>24</sup> The latter mechanism is typical for BPI fibrillation (see section 1.3.1), while the former resembles more the mechanism of denaturation found in this high pressure experiment. The four spectra clearly differ (see Figure 5.7 and the analysis of the contour plot) in the spectroscopic regions ascribed to the Amide bands.

### Amide I and Amide III bands

The four spectra over the frequency range of the Amide I band are shown in Figure 5.8. In agreement with previous results,<sup>18</sup> in native BPI the band appears to be peaked around  $1660\text{ cm}^{-1}$  with a large shoulder at around  $1680\text{ cm}^{-1}$ , with a FWHM (full width half maximum) close to  $50\text{ cm}^{-1}$ , in the fibrillar-4h BPI the band is sharper (FWHM close to  $35\text{ cm}^{-1}$ ) and peaked at  $1669\text{ cm}^{-1}$  and in the fibrillar-22h BPI the band becomes even sharper (FWHM close to  $25\text{ cm}^{-1}$ ) and the central frequency shifts to higher wavenumber at  $1673\text{ cm}^{-1}$  indicating a more compact structure. In the case of the P-treated BPI, the Amide I band is broad and completely unstructured, with a FWHM close to that of the native one, while the frequency of its maximum is comparable to that of the fibrillar-4h BPI.

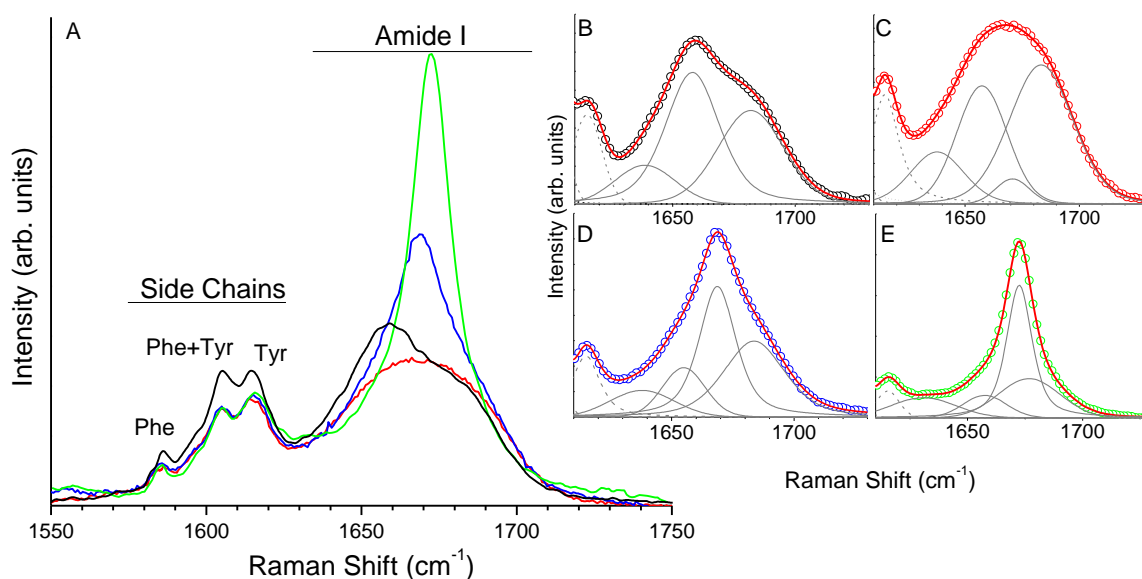


**Figure 5.8** – Panel A: Raman spectra of BPI at ambient conditions over the  $1550\text{-}1750\text{ cm}^{-1}$  spectral range: native hexameric BPI (black), P-treated BPI (red), fibrillar-4h BPI (blue) and fibrillar-22h BPI (green). Raman spectra and fitting components of Amide I band of native hexameric BPI (panel B), P-treated BPI (panel C), fibrillar-4h BPI (panel D) and fibrillar-22h BPI (panel E). In each of the A-E panels: experimental data (open circles), best fit curves (red lines), tails of low frequency components (dashed grey lines), and components of the secondary structure (grey solid lines).

Starting from two different conformations, the native and the fibrillar one, it is possible to check the accuracy of the spectroscopic marker that has been identified in this work. In particular in that case Figure 5.8 allows a direct comparison between the relative intensities of the side chains of the P-treated sample, the native one and the two fibrillar ones. It is well known that the active structure of the BPI (and the one that fibrillates) is the monomer,<sup>25</sup> and moreover this change in the relative intensities ( $I_{1615} > I_{1605}$ ) can be seen in the spectra published by Zheng et al. in ref. 18 on going from

the native to fibrillar BPI. These observations validate the choice of the relative intensity of these two side chains (Phe and Tyr) as a marker of the more external structure of the BPI. Following the fitting procedure described in section 2.4 an estimate of the secondary structure of the BPI after the pressure cycle was performed. In table 5.3 is reported a comparison among the percentage found by the fitting analysis of the Amide I band for all the insulin conformations studied in this chapter (native, P-treated and fibrillar). Best fit curves related to the different components of the Amide I band are shown in Figure 5.8B, 5.8C, 5.8D and 5.8E. In table 5.4 are reported the results obtained by the same analysis performed on the Amide III band. Best fit curves related to the different components of the Amide III band are shown in Figure 5.9A, 5.9B, 5.9C and 5.9D.

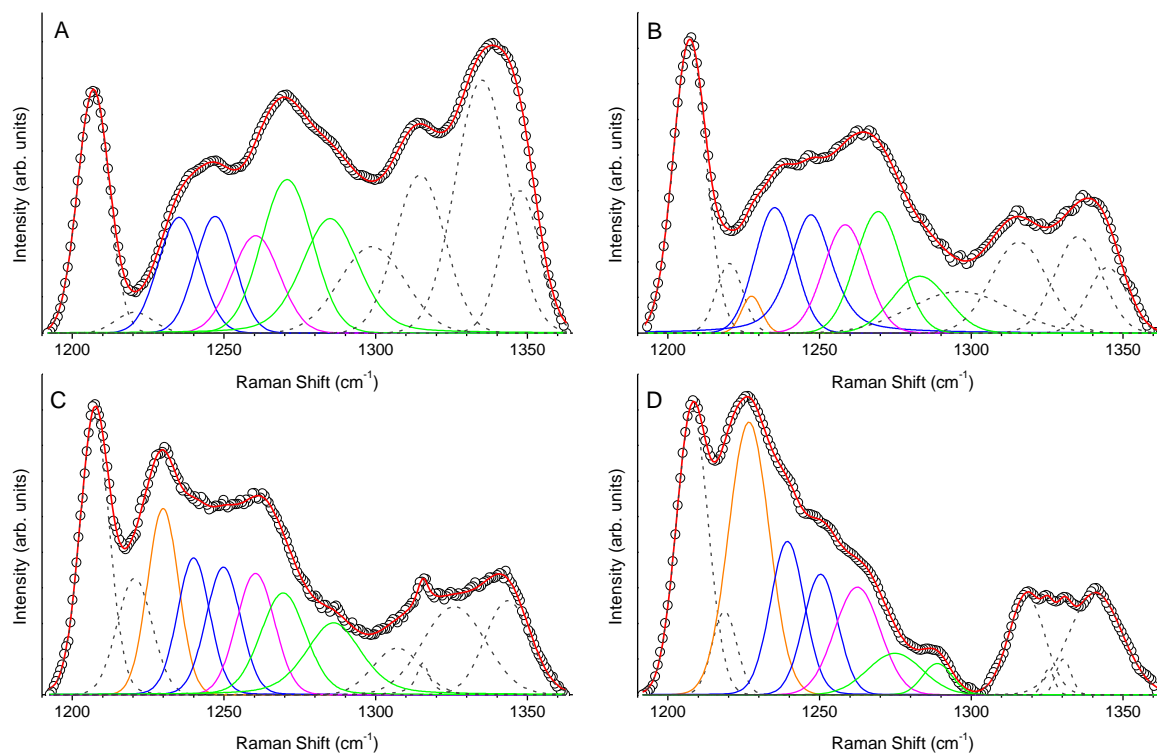


**Figure 5.9** –Fit of the Amide III band of the Raman spectra of BPI at ambient condition: in native conformation (A), after the pressure cycle (B), and in fibrillar conformation 4h (C) and 22h (D). Circles are the experimental data, dashed lines are the components of the fit outside the Amide III band, while solid lines are the components ascribed to the secondary structure that constitute the Amide III band ( $\alpha$  helix: green lines; random coil: magenta lines;  $\beta$  sheet intra-chain: blue lines; and  $\beta$  sheet inter-chain: orange lines).

First we observe that the analysis of the two amide bands provides the same results, thus supporting the reliability and the consistency of the present approach. Then, to simplify the discussion, we focus on the Amide I results also because, due to a measured intensity larger than the Amide III, they have a higher statistical reliability. The results for the P-treated sample show that the main effect of applying pressure is a partial unfolding of insulin, with a conversion from  $\alpha$  helix (decreasing from 50% to 33%) to intra- and inter-chain  $\beta$  structures (increasing from 38 to 53%). The small, although detectable, percentage of  $\beta$  inter-chain (around 6%) indicates the occurrence of some kind of protein aggregation in the P-treated sample. The percentage of  $\beta$  inter-chain remarkably grows in the two fibrillar samples, thus providing the spectroscopic signature of the onset of protein aggregation. The simultaneous remarkable band narrowing here observed (see

Figure 5.9) indicates that highly ordered  $\beta$ -structures are formed. The increase of intensity of the  $\beta$  inter-chain spectral contribution and its simultaneous narrowing can indeed be considered as a clear Raman indicator for the presence of protein fibrils (see section 3.1.2).

Amide I	Native	P-treated	Fibrillar-4h	Fibrillar-22h	
<b>Random</b>	1640	1638	1642	1631	Frequency (cm <sup>-1</sup> )
	12	14	15	14	Area (%)
<b><math>\alpha</math> helix</b>	1658	1656	1655	1657	Frequency (cm <sup>-1</sup> )
	50	33	10	11	Area (%)
<b><math>\beta</math> sheet inter-chain</b>	-	1669	1669	1672	Frequency (cm <sup>-1</sup> )
	0	6	38	49	Area (%)
<b><math>\beta</math> sheet intra-chain</b>	1682	1683	1683	1677	Frequency (cm <sup>-1</sup> )
	38	47	37	26	Area (%)

**Table 5.3** – Amide I: assignments, frequencies and estimated conformations.

Amide III	Native	P-treated	Fibrillar-4h	Fibrillar-22h	
<b>Random</b>	1257	1258	1263	1262	Frequency (cm <sup>-1</sup> )
	13	19	15	10	Area (%)
<b><math>\alpha</math> helix</b>	1270, 1284	1269, 1283	1274, 1287	1269, 1289	Frequency (cm <sup>-1</sup> )
	48	34	12	14	Area (%)
<b><math>\beta</math> sheet inter-chain</b>	-	1228	1227	1225	Frequency (cm <sup>-1</sup> )
	0	3	36	50	Area (%)
<b><math>\beta</math> sheet intra-chain</b>	1236, 1250	1235, 1247	1230, 1247	1240, 1250	Frequency (cm <sup>-1</sup> )
	40	44	37	24	Area (%)

**Table 5.4** – Amide III: assignments, frequencies and estimated conformations.

In summary, the effect of pressure on BPI is to partially unfold the protein, driving its structure from a mostly  $\alpha$  helix structure towards a mostly  $\beta$ -structure, although the latter percentage appears to be still much smaller than that observed in fibrils (i.e. 53% vs. 75%). Moreover, although pressure apparently promotes protein aggregation, it does not occur in an ordered phase as suggested by the results in the fibril samples. An inhibiting factor for the onset of ordered states can reasonably be the lower mobility of BPI powder under pressure with respect to that of a protein solution.

## *Bibliography of Chapter 5*

---

- <sup>1</sup> A.B. Kudryavtsev et al., *Acta Crystallogr. D*, 1998, 54, 1216.
- <sup>2</sup> J. Dong, Z. Wan, M. Popov, P. R. Carey and M. A. Weiss, *J. Mol. Biol.*, 2003, 330, 431–442.
- <sup>3</sup> K. Heremans and P.T.T. Wong, *Chem. Phys Lett.*, 1985, 118, 101.
- <sup>4</sup> L. Smeller, F. Meersman, K. Heremans, *Eur. Biophys. J.*, 2008, 37, 1127-1132.
- <sup>5</sup> Zai-Qing Wen, *J. Pharm. Sci.*, 2007, 96, 2861.
- <sup>6</sup> Ruan K, Lange R, Bec N, Balny C. *Biochem. Biophys. Res Commun.*, 1997, 239, 150.
- <sup>7</sup> Overman SA, Thomas GJ Jr., *J. Raman. Spectrosc.*, 1998, 29, 23–29.
- <sup>8</sup> Z. Arp, D. Autrey, J. Laane, S. A. Overman and G.J. Thomas Jr, *Biochemistry*, 2001, 40, 2522–2529.
- <sup>9</sup> Toensmeier, L. G.; Shields, J. E. *Proc. SPIE–Int. Soc. Opt. Eng.* 1990, 1336, 222–234.
- <sup>10</sup> G. Zeng, K.-K. Li, Y.-H. Zhang, *AIP Conf. Proc.*, 2010, 1267, 642.
- <sup>11</sup> A.R. Bizzarri and S. Cannistraro, *J. Phys. Chem. B*, 2002, 106, 6617-6633.
- <sup>12</sup> C. Ortiz, D. Zhang, Y. Xie, A.E. Ribbe, D. Ben-Amotz, *Anal. Biochem.*, 2006, 353, 157–166.
- <sup>13</sup> N.T. Yu et al., *J. Mol. Biol.*, 1972, 70, 117-132.
- <sup>14</sup> C. Ortiz, D. Zhang, Y. Xie, V.J. Davisson, D. Ben-Amotz, *Anal. Biochem.*, 2004, 332, 245–252.
- <sup>15</sup> W. Qian, W. Zhao and S. Krimm, *J. Mol. Struct.*, 1991, 250, 89-102.
- <sup>16</sup> H.E. Van Wart, A. Lewis, H.A. Scheraga, and F.D. Saevat, *Proc. Nat. Acad. Sci. USA*, 1973, 70, 2619-2623.
- <sup>17</sup> C. Jiang, J.-Y. Chang, *FEBS Lett.*, 2005, 579, 3927–3931.
- <sup>18</sup> R. Zheng, X. Zheng, J. Dong, and P.R. Carey, *Protein Sci.*, 2004, 13, 1288-1294.
- <sup>19</sup> M.N. Siamwiza, R.C. Lord, M.C. Chen, T. Takamatsu, I. Harada, H. Matsuura, and T. Shimanouchi, *Biochemistry* 1975, 14, 4870.
- <sup>20</sup> L. Ashton, J. Dusting, E. Imomoh, S. Balabani, and E.W. Blanch, *Biophys. J.*, 2010, 98, 707–714.
- <sup>21</sup> P.R. Carey, *Annu. Rev. Phys. Chem.*, 2006, 57, 527–54.
- <sup>22</sup> L. Nielsen, S. Frokjaer, J.F. Carpenter, J. Brange, *J. Pharm. Sci.*, 2001, 90, 29-37.
- <sup>23</sup> K. Huang, J. Dong, N.B. Phillips, P.R. Carey, and M.A. Weiss, *J. Biol. Chem.*, 2005, 280, 42345.
- <sup>24</sup> V. Shashilov, M. Xu, V.V. Ermolenkov, L. Fredriksen, and I.K. Lednev, *J. Am. Chem. Soc.* 2007, 129, 6972-6973.
- <sup>25</sup> A. Ahmad, V.N. Uversky, D. Hong and A.L. Fink, *J. Biol. Chem.*, 2005, 280, 42669–42675.

# *Chapter 6*

## *Proteins Renaturation by Ionic Liquids*

In this Chapter the property of Ionic Liquids of dissolving protein fibrils and of, at least partially reconstructing the native conformation and functionality, will be tested on the two proteins object of this thesis.

A brief introduction to Ionic Liquids and a review of the most recent and relevant works about the effects of these fluids on the protein conformation are reported. Raman spectra of Ionic Liquids and of the BPI and HEWL fibrils before and after the treatment with these particular solvents are shown. This part of the PhD work is still actively under investigation and several experiments will be performed soon but, unfortunately, will not be part of this thesis.

## 6.1 Ionic Liquids

The typical ionic liquid (IL) is composed by an organic cation and an inorganic anion. ILs have low melting points ( $<100^{\circ}\text{C}$ ) and remain in the liquid phase up to rather high temperature ( $<400^{\circ}\text{C}$ ).<sup>1</sup> The physical and chemical properties of ILs mainly depend on the cation structure (the symmetry and the length of alkyl chains, the presence of hydrophobic groups, etc.) as well as on the degree of anion charge delocalization.<sup>2</sup> ILs thus represent a large class of solvents that can be designed to have specific physical and chemical properties. Many of the ILs properties can be tuned over a range so large that they can hardly be classified into few general categories. A rather comprehensive database of the physical properties of ILs such as melting point, density and viscosity has been presented by Zhang and co-workers.<sup>3</sup> Other solvent properties as to polarity, hydrophobicity and solvent miscibility behavior of ILs, have been reported in the literature for specific applications.<sup>4,5,6</sup> Based on the solvation standpoint, ILs are generally considered to be highly polar solvents. A number of different methods have been used to provide information about their polarity, including solvatochromic dyes,<sup>7</sup> partition<sup>8</sup> and fluorescence probe methods.<sup>9</sup> However, for a given anionic group, the polarity of ILs generally decreases with increasing the alkyl chain length appended on the imidazolium ring in the cation.<sup>10</sup> This is an important consideration as the polarity of ILs can affect enzyme stability and selectivity.<sup>11</sup>

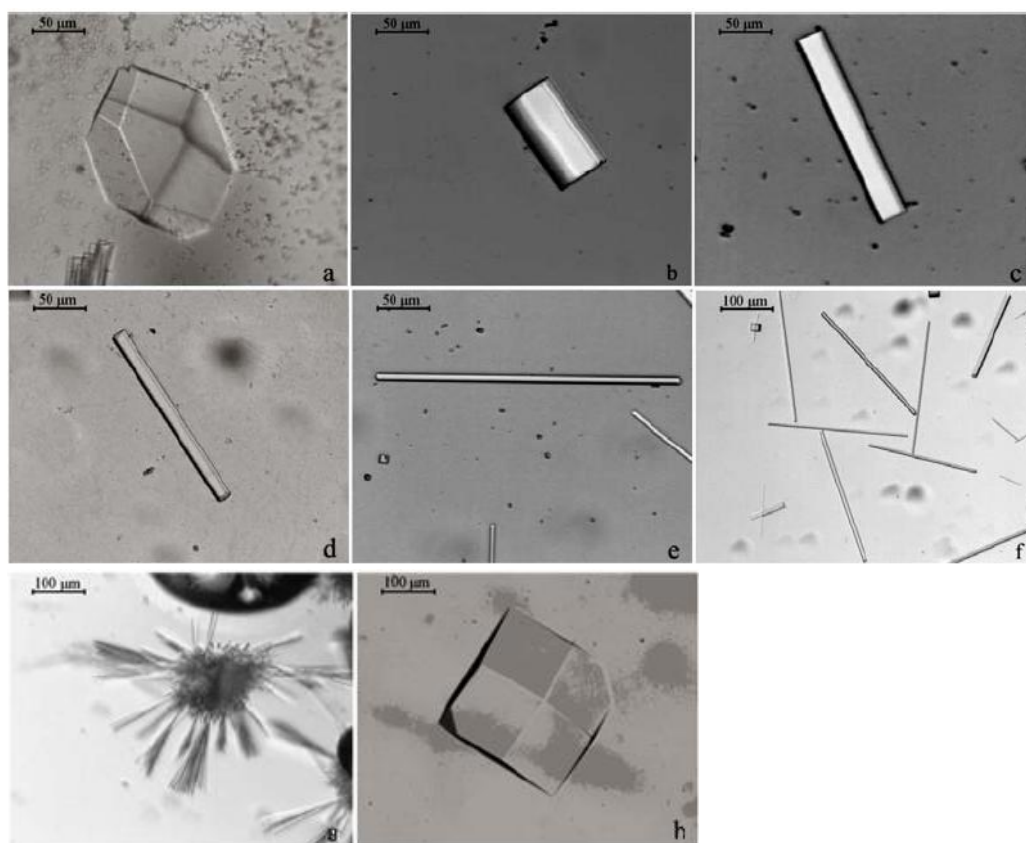


**Figure 6.1** – Micrographs of lysozyme crystals grown in different proportion of the IL 1-butyl-3-methylimidazolium. a, b, c, d, e, f, were the crystals under condition (pH=4.6) 14:0 (Buffer: IL), 13:1, 12:2, 11:3, 10:4 and 9:5, respectively; while g, h were grown under the conditions (pH=4.5 and with a concentration of NaCl=4% in the solution) of 14:0 and 13:1. From ref.21 .

Interestingly, ILs having coordinating anions which are strong hydrogen bond acceptors (e.g.,  $\text{Cl}^-$ ,  $\text{NO}_3^-$ ,  $\text{CH}_3\text{COO}^-$  and  $(\text{MeO})_2\text{PO}_2^-$ ) can dissolve many compounds which are insoluble or sparingly

soluble in water and in most of the organic solvents. Examples include cellulose<sup>12</sup> and some compounds having pharmacological activity.<sup>13</sup> The ability of ILs to dissolve such compounds generally depends on the hydrogen bonding ability of anions.<sup>8,14</sup>

More recently ILs have been shown to dissolve and stabilize proteins<sup>15,16,17,18</sup> and they have been used also as solvents for protein crystallization.<sup>19,20</sup>

The wide tunability of the ILs properties enables researchers to modify the protein properties in solution, such as their character, solubility, and stability. This provides additional chances to design ideal conditions (pH, ionic strength, etc.) for protein crystallization and enhances the controllability of crystallization process (examples of are shown in Figure 6.1<sup>21</sup> and Figure 6.2<sup>22</sup>).

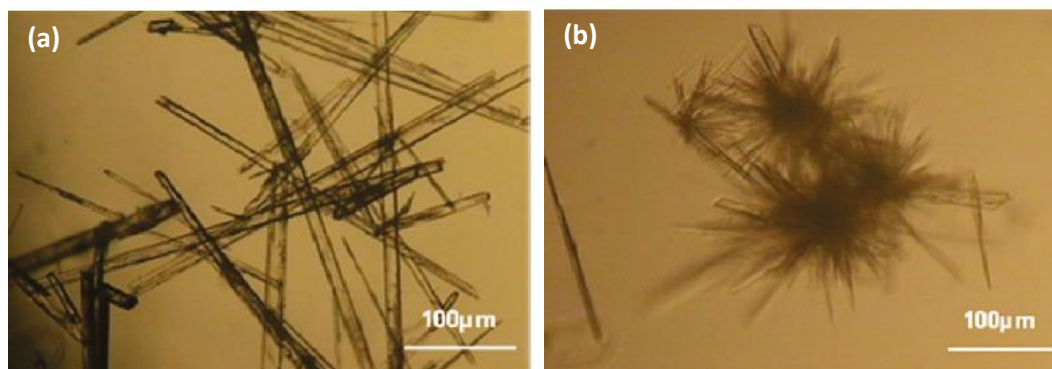


**Figure 6.2** – Typical shapes of adefovir dipivoxil (AD) polymorphs obtained at a crystallization temperature of (a) 80°C and (b) 90°C. The composition of the 1-allyl-3-ethylimidazolium tetrafluoroborate (AEImBF<sub>4</sub>) water mixture was fixed at 50:50 (vol %). From ref.22.

Sample and treatment <sup>a</sup>	Activity ± 5%
HWL in EAN, dissolved in neat pIL (denat.)	80%
HWL in TEATf, dissolved in neat (denat.)	73%
HWL in TEAMS, dissolved neat pIL with denat.	53%
Fibrils from Method 1, redissolved in EAN	46%
Fibrils from Method 2, redissolved in EAN	72%
Fibrils from Method 3, redissolved in EAN	22%
Fibrils from Method 1, redissolved in TEATf	20%
Fibrils from Method 2, redissolved in TEATf	60%
Fibrils from Method 3, redissolved in TEATf	5%
Fibrils from Method 1, redissolved in TEAMS	0
Fibrils from Method 2, redissolved in TEAMS	10%
Fibrils from Method 2, redissolved in TEAMS	0

<sup>a</sup> All samples diluted to normal aqueous solution state for assay. Results are averages of three independent assays.

**Table 6.1** - Enzymatic activities of lysozyme. Values are activities relative to that of native lysozyme in pH 7 phosphate buffer. ILs are Ethyl Ammonium Nitrate (EAN), triethylammonium mesylate (TEAMS), triethylammonium triflate (TEATf). Method 1: temperature and EAN as a solvent; Method 2: ethanol solution; Method 3: temperature and solution at pH2 (HCl). Table from ref. 23.

More recently N. Byrne and C.A. Angell<sup>23</sup> found that some protic ILs (PILs) have the property of recovering lysozyme functionality even after fibrils formation. The percentage of the restoration of enzymatic activity depends on both the type of ionic liquid used and the experimental method by which the fibrils were obtained. The latter dependence is a consequence of the different strength of

the hydrogen bonding obtained on varying the fibrillation conditions (see Table 6.1) whereas the former can be mostly ascribed to the “effective acidity” of the PIL.<sup>18</sup> We recall that a PIL is formed by the transfer of a proton from Brønsted acid to a Brønsted base and that its proton activity (PA) can be adjusted by varying the nature of the acid and base from which the PILs is formed. In the absence of the solvent, the PA plays the role of pH in ordinary solutions. It has been demonstrated that the denaturing temperatures of both hen egg lysozyme and ribonuclease A are extremely sensitive to the PA of the PIL as much as they are to pH in aqueous solutions.<sup>18</sup> Moreover by the PA tuning of the PILs folding or unfolding pathway can be selected featuring the intermediate states occurring denaturation process.

### 6.1.1 The Raman Spectra of Ammonium Based Ionic Liquids

The class of PILs that have been investigated in this theses is based on the nitrate anion,  $\text{NO}_3^-$ , and it is schematically depicted in Figure 6.3.

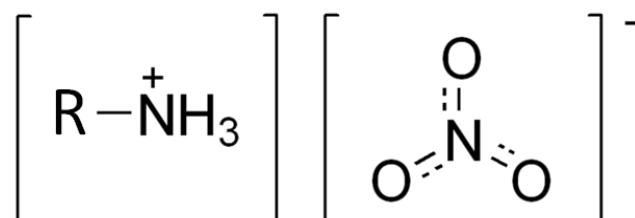


**Figure 6.3** – General formula of the PILs used in this thesis.

The R in Figure 6.3 is different in all the ionic liquid studied and their complete chemical formulas are reported in Table 6.2.

Name	Formula
2-Methyl Oxy Ethyl Ammonium Nitrate (MOEAN)	$[\text{CH}_3\text{OCH}_2\text{CH}_2\text{N}^+\text{H}_3][\text{NO}_3]^-$
Ethyl Ammonium Nitrate (EAN)	$[\text{CH}_3\text{CH}_2\text{N}^+\text{H}_3][\text{NO}_3]^-$
Propyl Ammonium Nitrate (PAN)	$[\text{CH}_3\text{CH}_2\text{CH}_2\text{N}^+\text{H}_3][\text{NO}_3]^-$
Buthyl Ammonium Nitrate (BAN)	$[\text{CH}_3\text{CH}_2\text{CH}_2\text{CH}_2\text{N}^+\text{H}_3][\text{NO}_3]^-$

**Table 6.2** –Name and complete chemical formulas of PILs used in this thesis.

This class of PILs is coordinate to the  $\text{NO}_3^-$  anion that, as it was already observed before, is a strong hydrogen bond acceptor and can dissolve many compounds which are insoluble in water (like proteins fibrils for example). Moreover alkylammonium nitrates are among the most studied PILs.<sup>24,25,26</sup> and two of them (EAN and BAN) has been already used in fibrils dissolution.<sup>23</sup>

The final aim is to test the renaturation capacity of this fluids on fibrillated proteins by means of the Raman spectroscopy. The first step was to collect the PILs Raman spectrum and to provide the assignations of their Raman modes.

In Figure 6.4 the Raman spectra of the PILs reported in Table 6.2 are shown. The PILs have been measured in a quartz cuvette with a 20x objective. The acquisition time was 60s for each spectral range (4 ranges were studied to cover the frequencies between 200 and 3800  $\text{cm}^{-1}$ ). All the data were shown as a unique spectrum for each of the PIL measured in Figure 6.4.



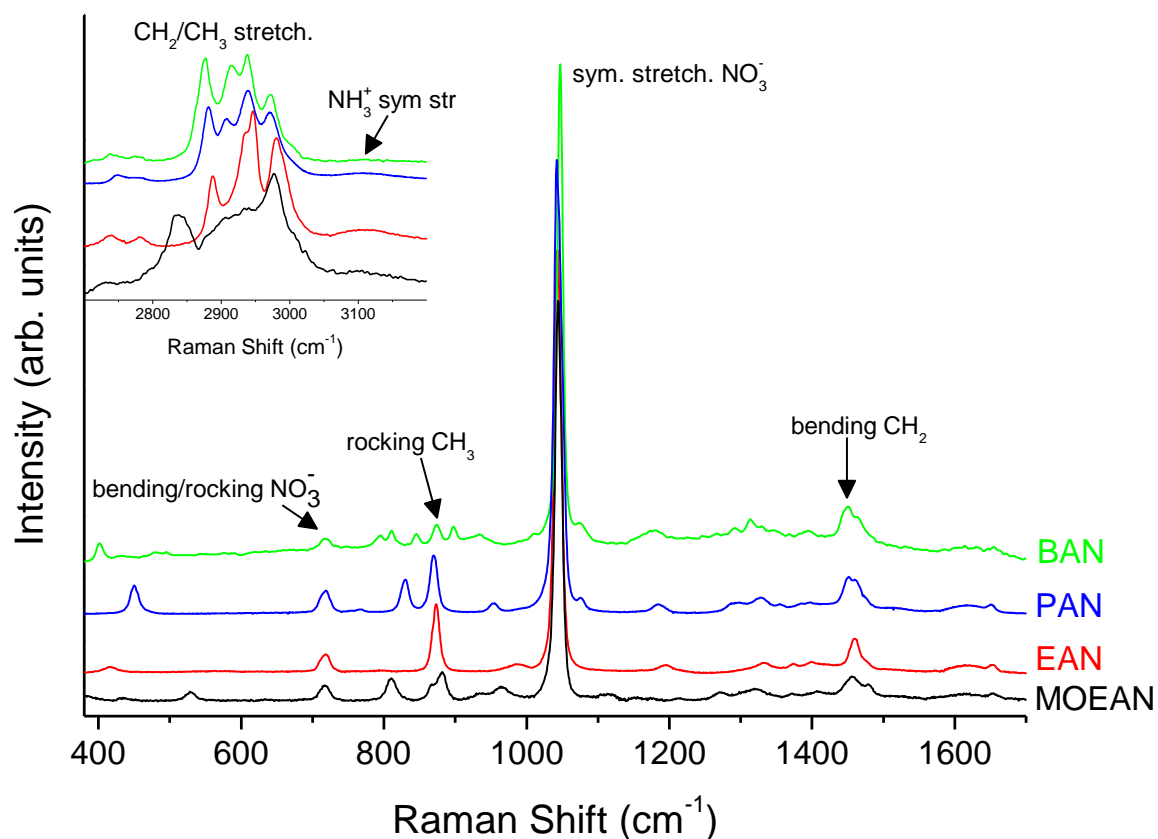


**Figure 6.4** – Raman spectra of the PILs: MOEAN (black), EAN (red), PAN (blue) and BAN (green). In the inset the high frequency region is shown. The major peaks are labeled. [stretch. = stretching, sym = symmetric]

EAN and PAN were acquired from IoLiTec (Ionic Liquids Technologies), while BAN and MOEAN was product in the laboratory of Prof. R. Caminiti (Dpt of Chemistry, Sapienza University). All the PILs were put in a cuvette (1mm of optical path) and de-hydrated standing at least 48h in controlled atmosphere (under a flux of nitrogen) before the Raman measurements.

The Raman modes reported in Figure 6.4 were assigned from literature<sup>27</sup> and from ab-initio calculations performed by Prof. Bodo (Dpt of Chemistry, Sapienza University).

I want to mention that most of the Raman spectra collected and presented in Figure 6.4 are part of a research project carried out in collaboration with the group of Prof. R. Caminiti (Dept. Chemistry Sapienza University) and devoted to the investigation of the optical properties of this class of PILs. Although this specific research has been carried out in parallel to the thesis work the optical characterization measurements have been instrumental to the present achievements. A paper on this subject has been accepted to JPC and others are in progress.

## 6.2 Insulin Fibrils in Ionic Liquids

Weighted samples (1 mg) of BPI mature fibrils (see section 2.6 for the fibrillation method and 3.1.2 for more details on the Raman spectrum of fibrillar-22h) were placed in vials and an aliquot (1 ml) of PILs were added. After 20 minutes at ambient conditions the solutions were centrifuged for 3 minutes, decanted and washed for 3 times. Then they were dried to be measured by Raman microspectrometer (see Figure 6.7).

To a first visual inspection the EAN was the only PIL in which the BPI fibrils seem to be dissolved, while when the BPI fibrils was immersed into the MOEAN and BAN one big aggregate was formed in both the PILs.

The two aggregates formed by the sample inside the MOEAN and the BAN appeared to be different. In particular in the MOEAN treated sample there were also spherical part “spherulites” (see Figure 6.5 A and B). The images were collected by Raman microscopy with the 20x objective.

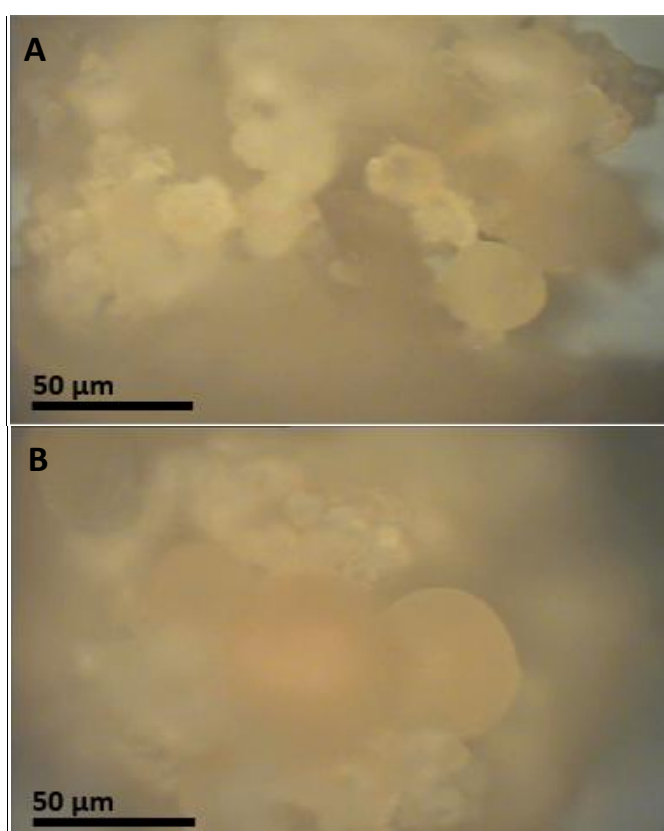


**Figure 6.5** – Photos (A and B) of the BPI sample after have been immersed in MOEAN for 20 minutes. Photo has been collected by Raman microscopy (20x objective).

Spherulites are most commonly associated with synthetic polymers,<sup>28,29</sup> but many other systems have been found to form spherulitic structures, such as synthetic cellulose,<sup>30</sup> proteins such as lysozyme<sup>31,32</sup> and carboxypeptidase<sup>33</sup> under crystallization conditions, etc.. Surprisingly, spherulitic deposits have also been observed in vivo associated with amyloid tumors<sup>34</sup> and, albeit occasionally, with other amyloid diseases.<sup>35,36</sup> Like their disease-associated counterparts, several amyloid fibril-forming polypeptide sequences have been observed to form spherulites in vitro.<sup>37,38,39</sup>

The ability of bovine insulin to form fibrillar structures and spherulites is known from more than 60 years.<sup>40</sup> In an article of 2004 Krebs et al.<sup>41</sup> suggested that the spherulites are composed of amyloid

fibrils that grow outwards from a core (see Figure 6.6), which may be a protein aggregate with a random structure rather than an amyloid structure.

Spherulites do not assemble from the dispersed fibrils, but more likely from a small precursor species—either insulin monomers or small oligomers in solution. Therefore, assembly of proteins into spherulites may proceed along a separate (though not necessarily dissimilar) pathway to assembly of proteins into dispersed fibrils.<sup>41</sup>

The observation of spherulites formation starting from fibrils dispersed in MOEAN is original and still lack of an explanation (usually the formation of fibrils and spherulites goes onto parallel path).

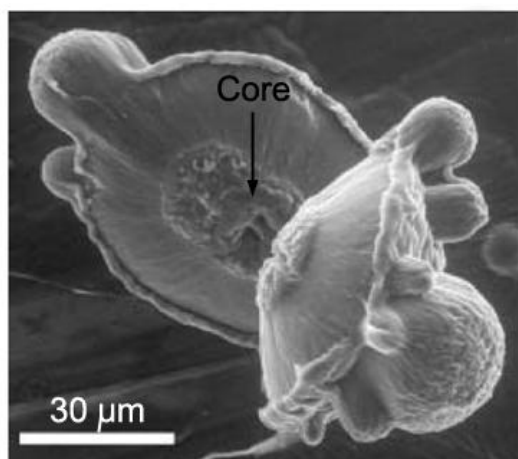


**Figure 6.6** – Scanning electron microscopy (SEM) images of insulin spherulites. Insulin spherulite formed by incubating 1 mM insulin at pH 2 and 65°C for 24 h. After rapid dehydration in the SEM chamber, the spherulite shown has cracked and opened up, showing radial lines from the periphery to the center. The latter is not apparently regularly organized (figure from ref. 41).

Beside the above phenomenological analysis of the effects of PILs on insulin we have also carried out a careful spectroscopic analysis. The Raman spectrum of the fibrillar BPI together with those of the PIL and that of the fibrillar BPI sample after PIL-treatment are shown in Figure 6.7. All the spectra of the PIL-treated fibrils were normalized to the spectrum of the pristine fibrils using the intensity of the Phe peak (around 1003  $\text{cm}^{-1}$ ). The spectra of the PILs were normalized to the spectra of the BPI fibrils after the PILs treatment using the intensity of the peak of  $\nu(\text{NO}_3^-)$  to render the peaks ascribable to PILs directly comparable with those in the spectra of the BPI fibril after the PIL treatment. The three comparisons clearly show that the washing procedure adopted for fibrils after ILs treatment (three cycles of centrifugation/dilution) wasn't completely effective and traces of IL can be still detected. Nevertheless, since the most intense Raman peaks shown by PILs do not superimpose to the protein relevant spectral features, an analysis of the protein conformation can be safely carried out on the samples.

As a matter of fact, it is rather clear that the whole Raman spectrum of the insulin fibrils is not affected by the treatments with BAN and EAN suggesting a weak, if any, PIL-protein interaction. Moreover, looking at the spectroscopic markers of the secondary structure (mostly within the frequency region of the Amide I band) the comparisons between the spectra of pristine and PILs-treated fibrils do not show any evidence of conformational modification of the fibril induced by none of the three PILs used.

The most interesting results between the treated samples is shown by the comparison reported in Figure 6.8 between the MOEAN treated sample and the fibrillar one. It has been already observed that the interaction of the BPI fibrils with the MOEAN drives the system towards a new structure that, on a phenomenological base, is witnessed by the appearance of spherulites as shown in Figure 6.5. Moreover the spectral modifications observed upon MOEAN-treatment can also be indeed ascribed to both a different spatial aggregation and a change in the tertiary structure.

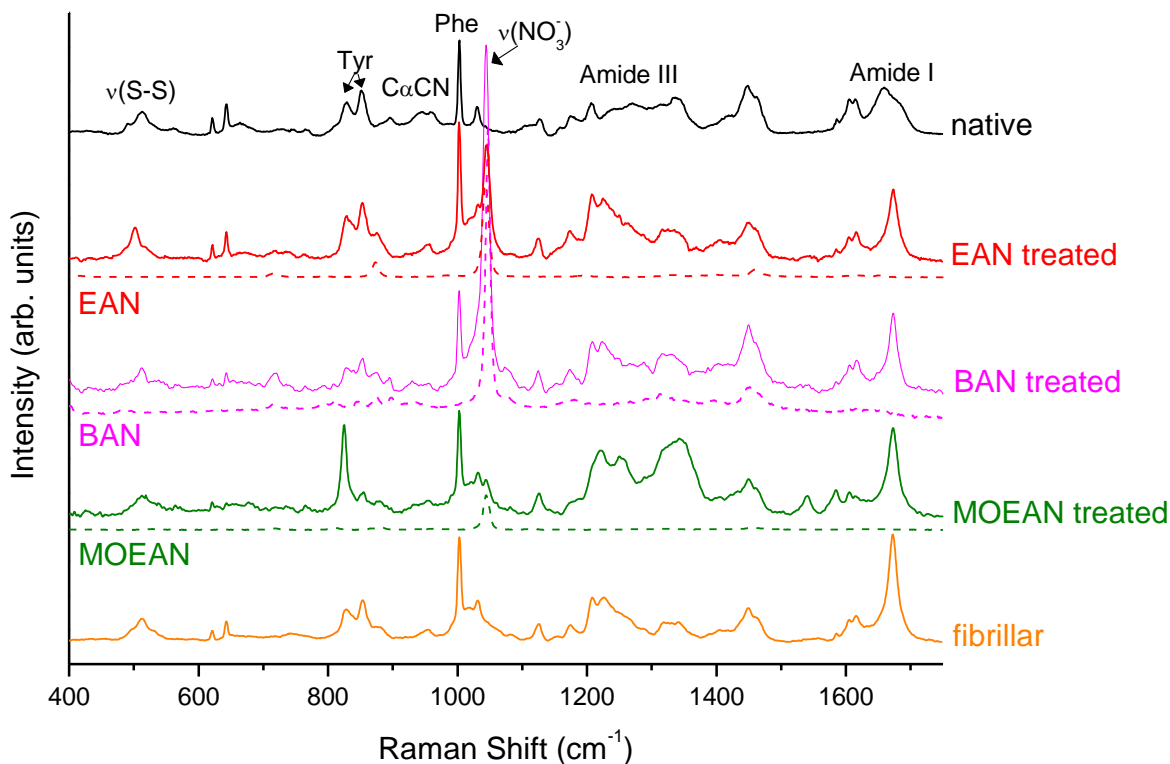


**Figure 6.7** – Raman spectra of insulin on native and fibrillar conditions (black and orange curves, respectively), and treated with ILs (see text for details): EAN (red), BAN (magenta) and MOEAN (green). The dashed lines are the Raman spectra of the pure ILs normalized to the peak of the  $\nu(\text{NO}_3^-)$  shown in the Raman spectra of the treated samples.

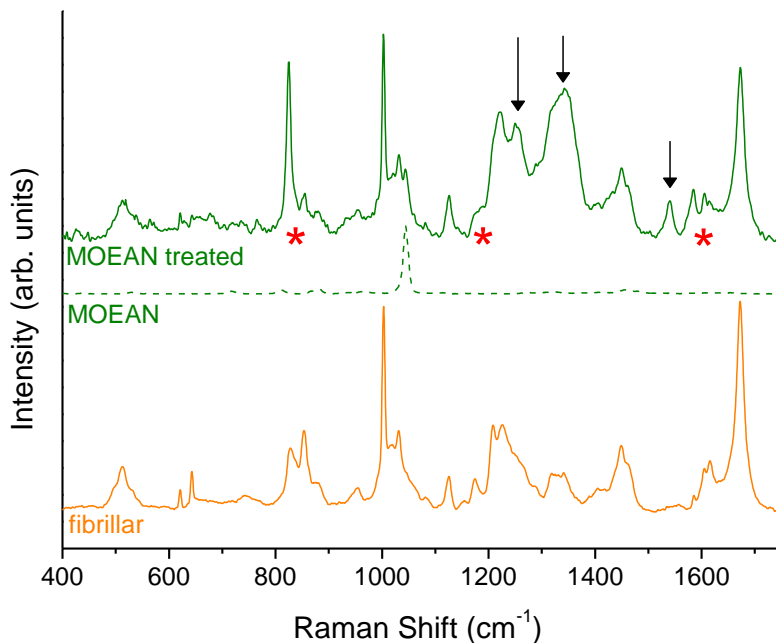


**Figure 6.8** – Comparison of the Raman spectra of insulin on fibrillar conditions (orange curve) and after being treated with MOEAN (green curve). The dashed line is the Raman spectra of the pure MOEAN normalized to the peak of the  $\nu(\text{NO}_3^-)$  shown in the Raman spectrum of the treated samples. The stars and the arrows highlight the regions where the major changes in the Raman spectra occurred. The former are ascribable to the Tyrosine vibrations, while the latter are mainly due to modes related with the NH bond (see text for details).

The stars in Figure 6.8 highlight changes in intensities of the peaks ascribable to the Tyr residues.<sup>42</sup> In particular the most impressive difference between the spectra of fibrillar and fibrillar treated with MOEAN concerns the intensity ratio of the Tyr Fermi doublet. The  $I_{850}/I_{830}$  value goes from 2.4 in the Raman spectra of fibrils to 0.3 in that of the treated sample. Till now it is not still clear what is the main force driving these changes. The most promising explanation (that yet needs to be proven) is a cation- $\pi$  interaction between the  $\text{NH}_3^+$  cation of the MOEAN and the delocalized negative charges along the aromatic ring of the Tyr residues. This electrostatic interactions between a positive charge and the electrons of the aromatic ring have been already observed in proteins and are interactions that involve proteins both from a structural point of view and from a functional one.<sup>43,44</sup> These thesis is also supported from other the changes in the Raman spectrum of the sample treated with MOEAN, indicated by arrows in Figure 6.8. They are all peaks connected to the structure of the protein:  $1255\text{ cm}^{-1}$  is part of the Amide III band (CN stretching and NH bending out of plane), around  $1340\text{ cm}^{-1}$  reflects CH deformation and around  $1540\text{ cm}^{-1}$  is the frequency of vibration of NH bending in plane and CN stretching (usually very low in the Raman spectra excited by visible light). What is the most surprising is that the Amide III band and the frequency around  $1540\text{ cm}^{-1}$  are both connected to the NH bending vibration, that may be enhanced by the particular conformation assumed by the protein in interaction with MOEAN, confirming the hypothesis on the cation- $\pi$  interactions.

To better understand the capacity of dissolving the BPI fibrils of this particular class of PILs it will be really interesting to repeat the same measurements on BPI fibrils that display different degree of maturity, and further information will also be also gained by varying the ambient condition (temperature and/or pressure) in which the dissolution should occur. These studies will be conducted by means of Raman spectroscopy in the next months.

### **6.3 Lysozyme Fibrils in Ionic Liquids**

Weighted samples (1 mg) of lysozyme fibrils (obtained as described before) were placed in vials and an aliquot (1 ml) of PILs were added.<sup>23</sup>

After 20 minutes at ambient conditions the solutions were centrifuged for 3 minutes, decanted and washed for 3 times. Then they were dried to be measured by Raman micro-spectrometer (see Figure 6.9).

After a first inspections of the Raman spectra presented in Figure 6.9 it is possible to see that the peak of the C $\alpha$ CN stretching modes related to  $\beta$  secondary structure of the protein is clearly diminished in all the treated samples (see Figure 6.11) and is completely absent in the EAN treated sample. This feature is a clear sign of a change in the tertiary structure induced by all the PILs used in this work.

Moreover taking a closer look on the Amide I band of all the spectra shown in Figure 6.9 it is possible to see that something changed in the shape of this band, mainly in the sample treated with EAN. The first qualitative observation is about the FWHM of the Amide I band that is broader in the EAN treated sample respect to the fibrillar one ( $30\text{cm}^{-1}$  VS  $25\text{ cm}^{-1}$  respectively). In Figure 6.10 are shown a superimposition of the data and the fitting results for the fibrillar HEWL and the sample treated with EAN (Figure 6.10 A and B, respectively).

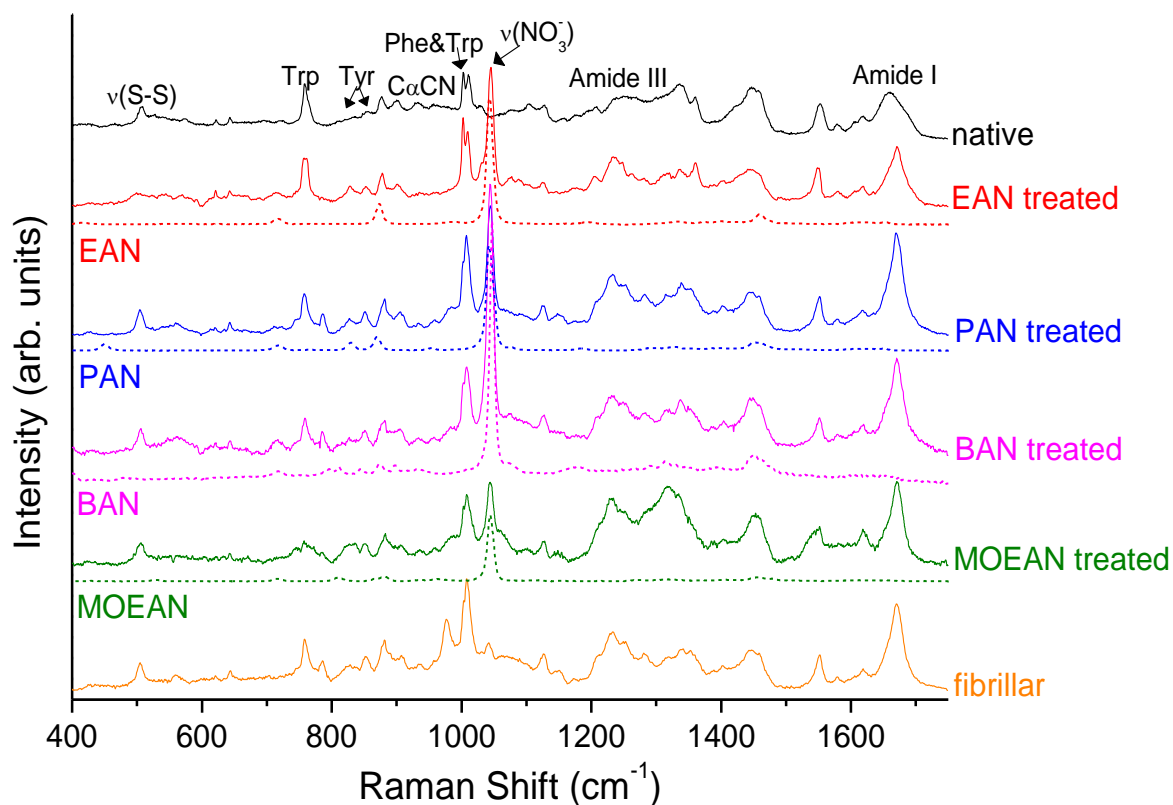


**Figure 6.9** – Raman spectra of the HEWL in native (black) and fibrillar conditions (orange), and of the HEWL samples after being in contact with different PILs: EAN (red), PAN (blue), BAN (magenta) and MOEAN (green). The dashed curves are the Raman spectra of the pure PILs.

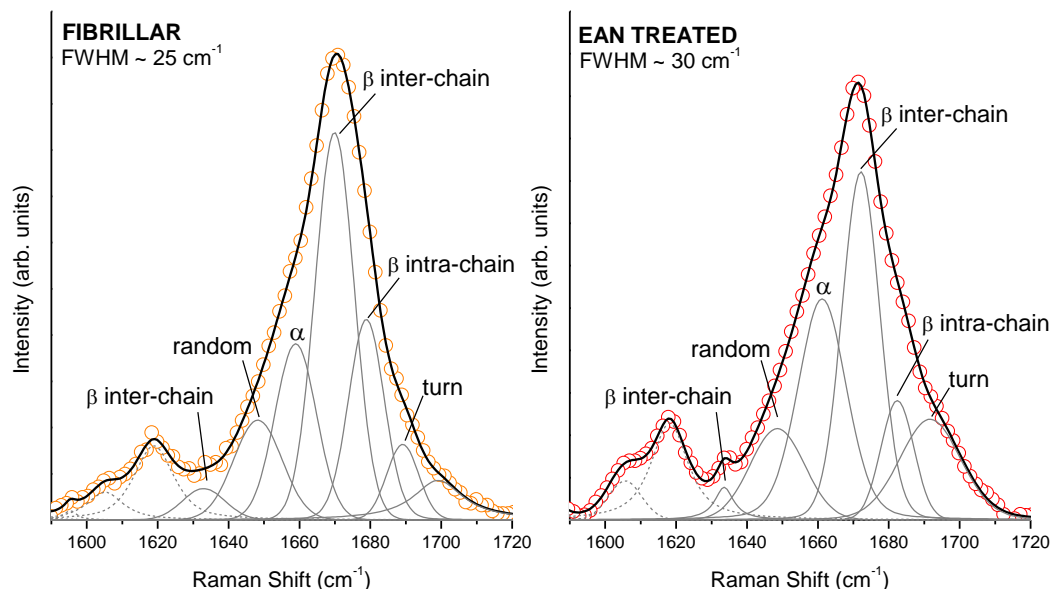


**Figure 6.10** – Raman spectra of the fibril HEWL (orange circles) and the fibril HEWL treated with EAN (red circles) fitted through the LMA (black line in both panels). In solid grey are shown the components of the Amide I band and in dashed grey are shown the residue.

The fitting were realized by LMA (see section 2.4) and the results are reported in Table 6.3 for all the sample examined. The HEWL redissolved in EAN is the only one to experienced a renaturation process, its fibrils content diminishing from 40% to 30% (see the  $\beta$  sheet inter-chain in Table 6.3).

The secondary structure that mostly increases is the random (included in the unordered structure in Table 6.3, but clearly distinguishable in Figure 6.10).

	Native HEWL	Fibrillar HEWL in EAN	Fibrillar HEWL in PAN	Fibrillar HEWL in BAN	Fibrillar HEWL in MOEAN	Fibrillar HEWL
Unordered (random + turns)	31	27	20	15	11	19
$\alpha$ helix	45	31	14	16	16	19
$\beta$ sheet inter-chain	0	30	35	37	39	39
$\beta$ sheet intra-chain	23	12	31	33	34	23

**Table 6.3** – Result of the fitting procedure on the Amide I region of the native HEWL, fibrillar HEWL untreated and treated with PILs. The unordered components are random and turns structures.

From the comparison between the Raman spectra of the fibrillar and the EAN treated samples it is possible to find other markers of the ongoing renaturation. The peak around  $786\text{ cm}^{-1}$  (see Figure 6.11) is absent in the native HEWL and is present in the Raman spectra of all the fibrillar HEWL (treated and untreated) except that diluted with EAN. This peak actually is not clearly assigned. The Phe and Tyr peaks in the Raman spectrum of the HEWL treated with EAN are at the frequency close to those of the native sample ( $1003\text{ cm}^{-1}$  and  $1011\text{ cm}^{-1}$ ) and their relative intensities in the EAN treated samples are similar to those in the native one, and opposite to those of all the fibrillar samples treated with the others PILs (see Figure 6.11). It has been observed in literature that during denaturation the Phe peak (around  $1003\text{ cm}^{-1}$ ) diminishes for the exposure of Phe to water during the incubation time.<sup>45</sup>

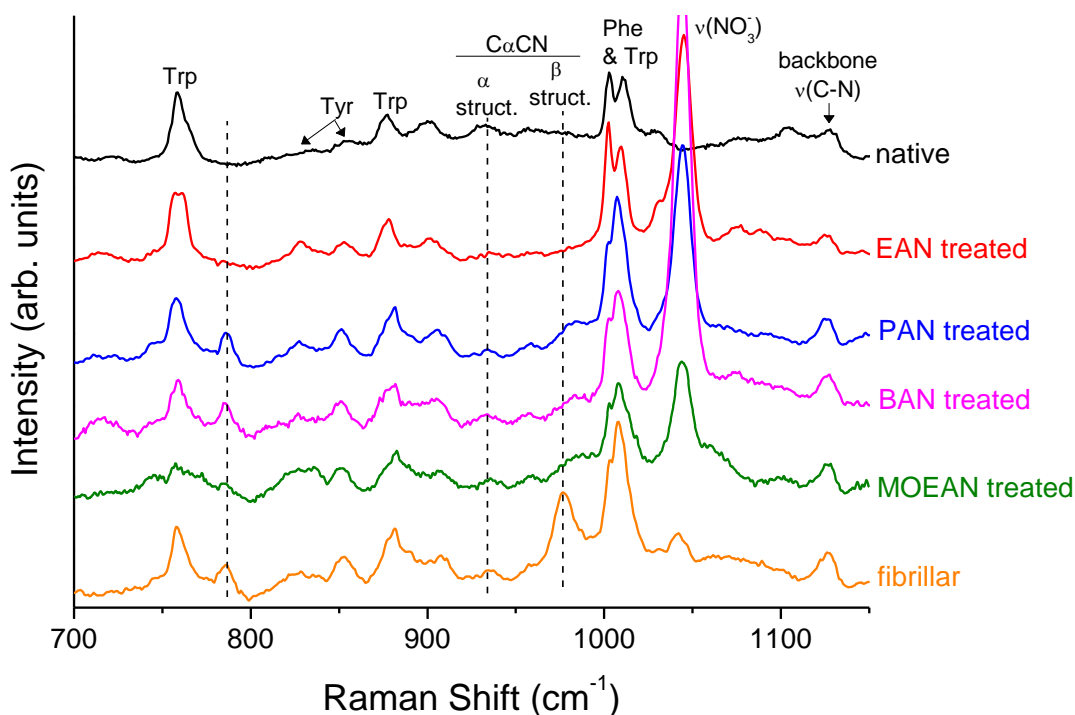


**Figure 6.11** – Raman spectra of the native HEWL (magenta), fibrillar HEWL (black) and treated samples (red). The major features in this range of frequencies are labeled.

Moreover, as it was already observed before in this thesis, the Trp residue is a good indicator of the hydrophobic/hydrophilic environment of the tryptophan indole ring, by the relative intensity of the Fermi doublet around 1360 and 1340  $\text{cm}^{-1}$ . The ratio  $I_{1360}/I_{1340}$  for the native sample is around 0.4 and it is representative of a hydrophilic environment, while for the fibrillar sample it is around 2.7, reflecting a hydrophobic environment. The value of the ratio remains around that value for the fibrillar sample treated with all the PILs but the EAN. The latter shows a diminished value around 1, that is an intermediate value between that of the native sample and the fibrillar one (but  $\ll 2.7!$ ). Finally we would like to mention that MOEAN acts on the lysozyme tertiary structure mainly on the aromatic residues (Phe, Tyr and Trp) by means of a cation- $\pi$  interactions.<sup>46</sup> This behavior is well evidenced in the Raman spectra by the changing in the frequencies and/or intensities of the Trp (around 757, 1339, and 1553  $\text{cm}^{-1}$ ) and Tyr (around 830, 850 and 1610  $\text{cm}^{-1}$ ) peaks. In particular the frequency around 1553  $\text{cm}^{-1}$  ascribed to the Trp residues is around that value in all the Raman spectra but the one treated with MOEAN. As it was already observed in literature<sup>47</sup> a downshift of that Raman peak is typical in the case of a cation- $\pi$  interactions. Moreover the Raman spectrum of the treated MOEAN shows changes respect to the fibrillar one also in peaks involved in the NH modes (see around 1317 and 1540  $\text{cm}^{-1}$ ) reinforcing the hypothesis of a cation- $\pi$  interactions between the  $\text{NH}_3^+$  cation of the MOEAN and the electrostatic negative charges on the aromatic ring of residues. To have a deeper understanding about this hypothesis other measurements will be made in our laboratory in the next months.

The results just presented from the analysis of the Raman spectrum of HEWL fibrils redissolved in EAN are in good agreement with what was found by N. Byrne and C.A. Angell in ref. 23. They prepared HEWL fibrils following a thermo-chemical protocol, pH was adjusted to 2 by adding HCl, temperature and time of fibrillation were unreported. By re-dissolving the pellet in EAN they obtained a recover of the HEWL activity of only 22%, even if the widely used ThT fluorescence intensity<sup>48</sup> wasn't able to detect fibril signal inside the re-dissolved solution. It is known that the EAN capacity of dissolving HEWL fibrils depends on the method used to obtain the fibrils,<sup>23</sup> and from the Raman measurements it is not possible to determine the enzyme activity, but obviously enzyme activity is related to the structure of the enzyme, and Raman measurements are a well established method to study the secondary structure of proteins.



## Bibliography of Chapter 6

- <sup>1</sup> M. Moniruzzamana, K. Nakashimab, N. Kamiyaa, M. Goto, *Biochem. Eng. J.*, 2010, 48, 295-314.
- <sup>2</sup> K.R. Seddon, *J. Chem. Technol. Biotechnol.* 1997, 68, 351–356.
- <sup>3</sup> S. Zhang, N. Sun, X. He, X. Lu, X. Zhang, *J. Phys. Chem. Ref. Data*, 2006, 35, 1475–1517.
- <sup>4</sup> H. Tokuda, K. Ishii, M.A.B.H. Susan, S. Tsuzuki, K. Hayamizu, M. Watanabe, *J. Phys. Chem. B*, 2006, 110, 2833–2839.
- <sup>5</sup> J.G. Huddleston, A.E. Visser, W.M. Reichert, H.D. Willauer, G.A. Broker, R.D. Rogers, *Green Chem.*, 2001, 3, 156–164.
- <sup>6</sup> P. Bonhôte, A.P. Dias, N. Papageorgiou, K. Kalyanasundaram, M. Grätzel, *Inorg. Chem.*, 1996, 35, 1168–1178.
- <sup>7</sup> A.J. Carmichael, K.R. Seddon, *J. Phys. Org. Chem.*, 2000, 13, 591–595.
- <sup>8</sup> J.L. Anderson, J. Ding, T. Welton, D.W. Armstrong, *J. Am. Chem. Soc.*, 2002, 124, 14247–14254.
- <sup>9</sup> S.N.V.K. Aki, J.F. Brennecke, M.A. Stadtherr, *Chem. Commun.*, 2001, 413–414.
- <sup>10</sup> J.G. Huddleston, A.E. Visser, W.M. Reichert, H.D. Willauer, G.A. Broker, R.D. Rogers, *Green Chem.*, 2001, 3, 156–164.
- <sup>11</sup> S.H. Schofer, N. Kaftzik, P. Wasserscheid, U. Kragl, *Chem. Commun.*, 2001, 425–426.
- <sup>12</sup> R.P. Swatloski, S.K. Spear, J.D. Holbrey, R.D. Rogers, *J. Am. Chem. Soc.*, 2002, 124, 4974–4975.
- <sup>13</sup> D.M. Anderson, Patent WO000057-A1, 2003.
- <sup>14</sup> Y. Fukaya, K. Hayashi, M. Wada, H. Ohno, *Green Chem.*, 2008, 10, 44–46.
- <sup>15</sup> N. Byrne, L.-M. Wang, et al., *Chem. Commun.*, 2007, 2714–2716.
- <sup>16</sup> S.N. Baker, T.M. McCleskey et al., *Chem. Commun.*, 2004, 940–942.
- <sup>17</sup> K. Fujita, D.R. MacFarlane, and M. Forsyth, *Chem. Commun.*, 2005, 4804–4806.
- <sup>18</sup> N. Byrne and C.A. Angell, *J. Mol. Biol.*, 2008, 378, 707–714.
- <sup>19</sup> M.L. Pusey, M.S. Paley, M.B. Turner and R.D. Rogers, *Cryst. Growth Des.*, 2007, 7(4), 787–793.
- <sup>20</sup> D. Hekmat, D. Hebel, J. Sebatstian, M. Schmidt and D. Weuster-Botz, *Biotechnol. Lett.*, 2007, 29(11), 1703–1711.
- <sup>21</sup> X. Li, X. Xu, Y. Dan, J. Feng, L. Ge, and M. Zhang, *Cryst. Res. Technol.*, 2010, 43, 10.
- <sup>22</sup> J.-H. An, J.-M. Kim, S.-M. Chang, and W.-S. Kim, *Crystal Growth & Design*, 2010, 10,(7).
- <sup>23</sup> N. Byrne and C.A. Angell, *Chem. Commun.* 2009, 1046–1048.
- <sup>24</sup> Atkin, R.; Warr, G. G., *J. Phys. Chem. B*, 2008, 112, 4164–4166.
- <sup>25</sup> Greaves, T. L.; Weerawardena, A.; Krodkiewska, I.; Drummond, C. J., *J. Phys. Chem. B*, 2008, 112, 896–905.
- <sup>26</sup> Mamontov, E.; Luo, H.; Dai, S., *J. Phys. Chem. B*, 2009, 113, 159–169.
- <sup>27</sup> T.J. O’Leary and I.W. Levin, *J. Phys. Chem.* 1984, 88, 4074–4078.
- <sup>28</sup> Bassett, D. C., *J. Macromol. Sci. Phys.*, 2003, 42, 227–256.
- <sup>29</sup> Magill, J. H., *J. Mater. Sci.*, 2001, 36, 3143–3164.
- <sup>30</sup> Kobayashi, S., L. J. Hobson, J. Sakamoto, S. Kimura, J. Sugiyama, T. Imai, and T. Itoh, *Biomacromolecules*. 2000, 1, 168–173.
- <sup>31</sup> Chow, P. S., J. Zhang, X. Y. Liu, and R. B. H. Tan., *Int. J. Mod. Phys. B.*, 2002, 16, 354–358.
- <sup>32</sup> Tanaka, S., M. Yamamoto, K. Ito, R. Hayakawa, and M. Ataka., *Phys. Rev. E.*, 1997, 56, R67–R69.
- <sup>33</sup> Coleman, J. E., B. J. Allan, and B. L. Vallee., *Science*, 1960, 131, 350–352.
- <sup>34</sup> Acebo, E., M. Mayorga, and J. F. Val-Bernal., *Pathol.*, 1999, 31, 8–11.

- 
- <sup>35</sup> Manuelidis, L., W. Fritch, and Y.-G. Xi., *Science*, 1997, 277, 94–98.
- <sup>36</sup> Jin, L.-W., K. A. Claborn, M. Kurimoto, M. A. Geday, I. Maezawa, F. Sohraby, M. Estrada, W. Kaminsky, and B. Kahr., *Proc. Natl. Acad. Sci. USA.*, 2003, 100, 15294–15298.
- <sup>37</sup> Aggeli, A., M. Bell, L. M. Carrick, C. W. G. Fishwick, R. Harding, P. J. Mawer, S. E. Radford, A. E. Strong, and N. Boden., *J. Am. Chem. Soc.*, 2003, 125, 9619–9628.
- <sup>38</sup> Fezoui, Y., D. M. Hartley, D. M. Walsh, D. J. Selkoe, J. J. Osterhout, and D. B. Teplow. *Nat. Struct. Biol.*, 2000, 7, 1095–1099.
- <sup>39</sup> Westlind-Danielsson, A., and G. Arnerup, *Biochemistry*, 2001, 40, 14736–14743.
- <sup>40</sup> Waugh, D. F., *J. Am. Chem. Soc.*, 1946, 68, 247–250.
- <sup>41</sup> M.R.H. Krebs, C.E. MacPhee, A.F. Miller, I.E. Dunlop, C.M. Dobson, and A.M. Donald, *Proc. Natl. Acad. Sci.* 2004, 101, 40, 14420–14424.
- <sup>42</sup> M. Tsuboi, Y. Ezaki, M. Aida, M. Suzuke, A. Yimit, K. Ushizawa, T. Ueda, *Biospectroscopy*, 1998, 4, 61–71.
- <sup>43</sup> R.M. Johnson, K. Hecht, and C.M. Deber, *Biochemistry*, 2007, 46, 32.
- <sup>44</sup> C. Ruan and M.T. Rodgers, *J. AM. CHEM. SOC.* 2004, 126, 14600-14610.
- <sup>45</sup> M. Xu, V.V. Ermolenkov, W. He, V.N. Uversky, L. Fredriksen, I.K. Lednev, *Biopolymers*, 2005, 79, 58–61.
- <sup>46</sup> D.A. Dougherty, *Science*, 1996, 271, 163-168.
- <sup>47</sup> Z.-Q. Wen, X. Cao, A. Vance, *J. Pharmaceut. Sci.*, 2008, 97, 6, 2228.
- <sup>48</sup> H. Naiki, K. Higuchi, M. Hosokawa and T. Takeda, *Anal. Biochem.*, 1989, 177, 244-249.

# *Conclusion and Outlook*

In this final Chapter we report and discuss the main results obtained on insulin (mainly) and lysozyme in the present thesis work. This will allow us to get a deeper insight into the sequences of different protein conformations we obtained using different denaturation/renaturation protocols either well-established (thermo-chemical) or more exotic (pressure and ionic liquids) procedures. Results will be further discussed and some general conclusions will be drawn.

The modulation of the insulin structure by pressure and other factors, the study of the pathway from folded to unfolded states, the extent of aggregation and the stability of fibrillar configurations have been the main themes of the present work. In particular the combined use of optical spectroscopy and high pressure technique has revealed a novel structural phase of insulin stable at ambient pressure. The denaturation process has been carefully followed using Raman spectroscopy on increasing the pressure from ambient to  $P_{\text{max}}=8.1$  GPa. We decided to carry out this sort of crash test since, according to literature and to our preliminary measurements in water solution, insulin shows an anomalous resistance to volume compression.

High pressure Raman and Infrared spectra collected as function of pressure on two neutral insulin water solutions (one compatible with physiological conditions, 2mM, and the other one ten folds concentrated, 20mM) were indeed compatible with the previous literature in not revealing irreversible conformational modifications. The high quality of the optical data allowed for a careful quantitative analysis of the Amide I band. The whole of the results obtained up to  $P_{\text{Max}} = 2$  GPa (i.e. slightly above the freezing point of water) revealed indeed only completely reversible changes of secondary structure while pressurizing/depressurizing insulin solutions. The high-concentration solution shows an aggregated state at ambient pressure and the partial dissociation of these aggregates is the only irreversible effect obtained by the pressure cycle. This analysis has been carried out by studying the intensities of the Raman peaks ascribed to inter-molecular bonded  $\beta$  sheet which we have demonstrated to be highly sensible markers of the extent of protein aggregation. In this respect our present results confirm the capability of high pressure in dissociating aggregates in proteins solution already reported in the literature for several proteins.

The quest for a plastic structural deformation of insulin drives our investigation from insulin solutions towards insulin powder, since the ice formation induced by high pressure at pressure slightly above 1 GPa can strongly bias the protein response.

Samples of insulin powder was thus used in several pressurizing/depressurizing cycles carried out from 0 to a maximum applied pressure  $P_{\text{Max}} = 1, 2, 3, 4$  GPa. After each single pressure cycle we collected a spectrum pretty identical to the one collected before the pressurization. These first results lead to well defined conclusions:

- the range of the elastic pressure behavior of insulin is extended up to 4 GPa, well beyond the previous limit of 1.2 GPa;
- using the spectroscopic markers of the  $\beta$  inter-molecular peaks we confirm that applying pressure has an effect of aggregate dissociation;
- we identify a Raman marker of the outer structure of insulin (hexameric, dimeric and monomeric) in the side chains of the Tyr and Phe peaks ( $1600\text{-}1620\text{ cm}^{-1}$ );
- similarly to the dissociation effect of pressure in solution we find that volume compression drives the protein powder from a predominantly hexameric to a predominantly dimeric/monomeric structure (Figure C1).

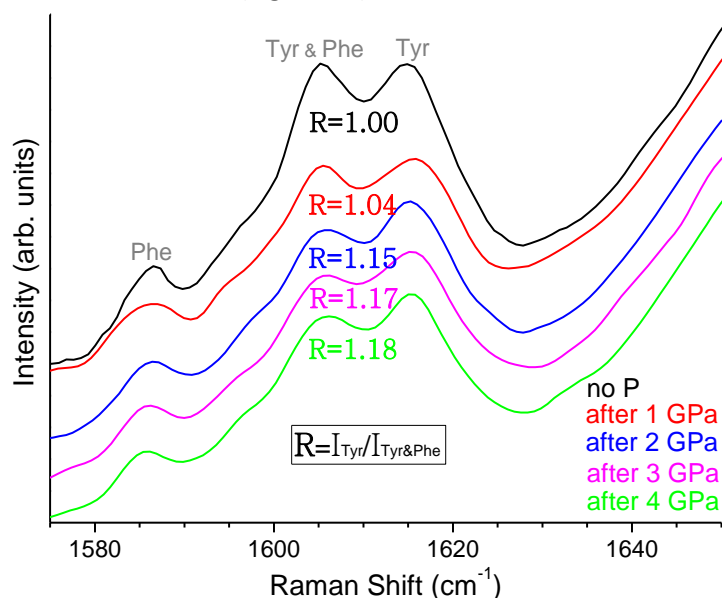


**Figure C1** – Raman spectra of the insulin powder at ambient pressure when no pressure was applied (black line) and after being pressurized up to 1, 2, 3 and 4 GPa (see the color code in figure). The ratio  $R$  is the markers of the dissociation of the outer structure of insulin identified in this thesis. Tyr: tyrosine, Phe: phenylalanine.

The plastic transition was finally reached pressurizing insulin powder beyond 4 GPa. Above the threshold pressure of about  $P_t = 4.2$  GPa an abrupt and irreversible change is shown by the Raman spectra (see Figure C2). In particular the Amide I band shows a remarkable and mostly permanent modifications in shape and frequency on crossing  $P_t$ .

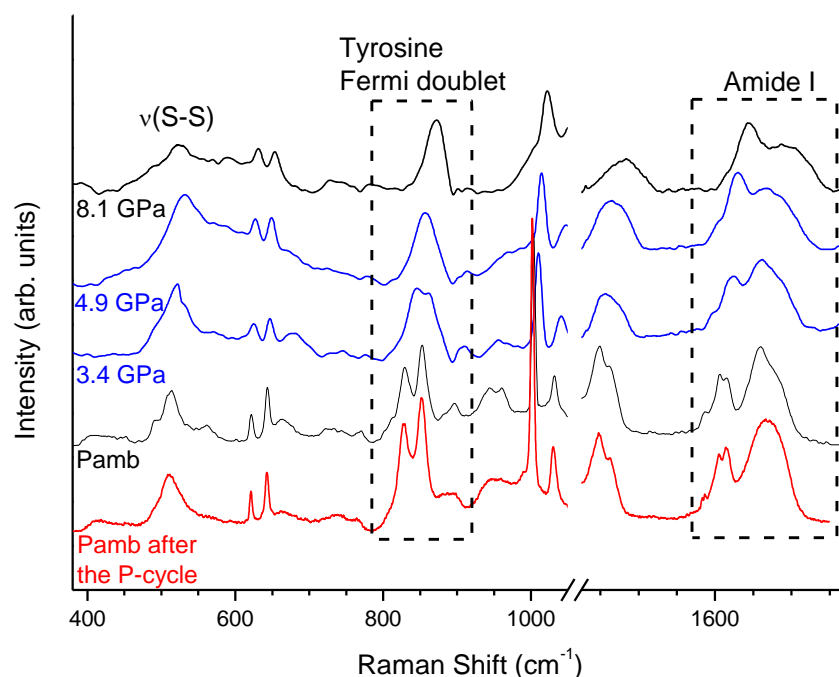


**Figure C2** – Raman spectra of insulin in powder on increasing pressure up to 8.1 GPa. The two blue curves highlight the discontinuity between 3.4 and 4.9 GPa, while the red spectrum is the one collected at ambient pressure after the P-cycle. The dashed squares are the region where changes under pressure were more evident.

As the pressure is increased the central frequency of the Amide I band showed a sigmoidal behavior (see Figure C3) as the one typically observed in proteins undergoing a denaturation process. The slightly decreasing behavior observed on releasing the pressure indicates a partial renaturation process, which, in any case, is not sufficient to recover the pristine frequency value (follow the dashed lines in Figure C3).

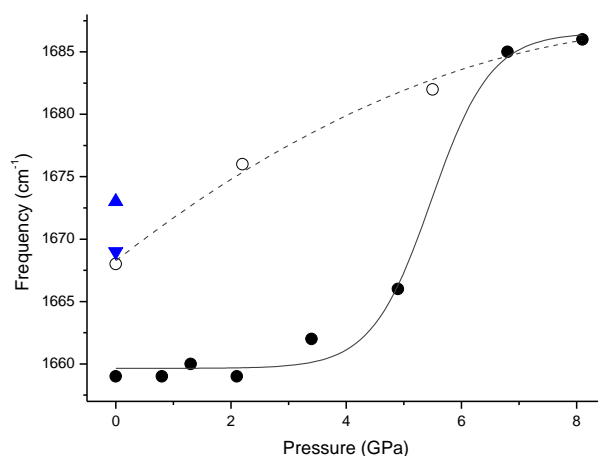


**Figure C3** – Pressure behavior of the frequencies of the Amide I band on increasing (closed symbols) and decreasing (open symbols) pressure. The up and down triangle in B are the central frequencies of the fibrillar samples (22 and 4 hours respectively).

It is important to notice the sudden discontinuity in the pressure behavior of the Tyrosine Fermi doublet ( $830\text{-}850\text{ cm}^{-1}$ ), which on increasing the pressure becomes a singlet (see Figure C4). This abrupt modification of the spectral response strongly suggest that, above  $P_t$  Tyr residues experience an extremely hydrophobic ambient. This finding is also supported by the decrease of the Tyr

intensity ratio observed on increasing the pressure up to 4.2 GPa (see Figure C4 C). This is caused by a structural rearrangement of the Tyr residues, while the pressure induced doublet-to-singlet spectral transition above 4.2 GPa is probably driven by the rearrangement of the water molecules that penetrate inside the protein cavities. The latter mechanism is also supported by the analysis of the intensity ratio of the Tyr around 1177  $\text{cm}^{-1}$  and the Phe around 1003  $\text{cm}^{-1}$  (see Figure 5.6 and related text). We would like to stress that the water penetration process is basically coherent with the microscopic mechanisms underlying the pressure driven denaturation process.

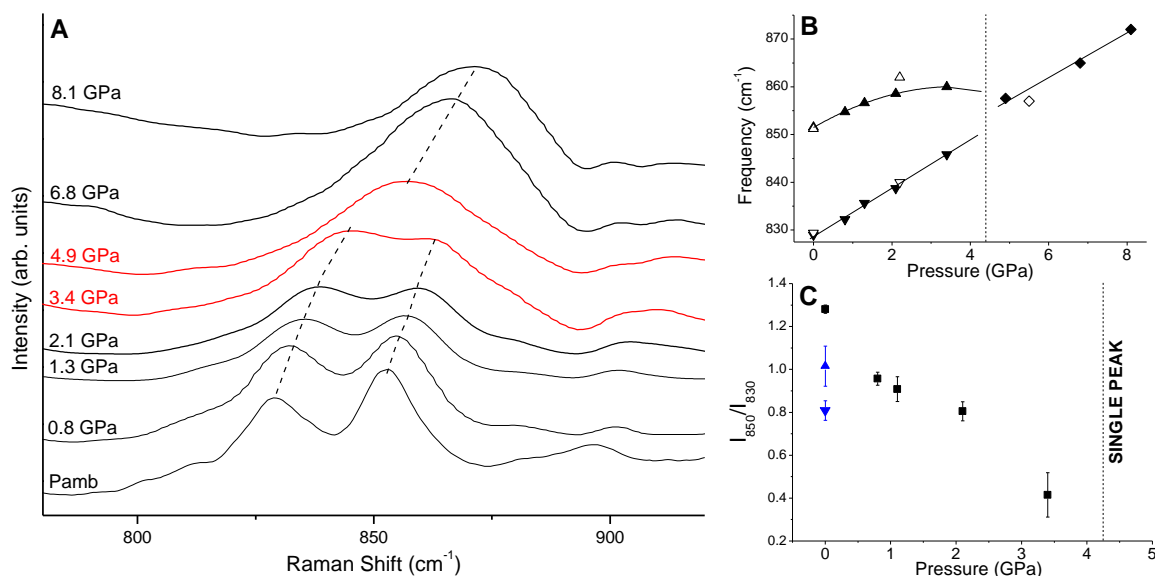


**Figure C4** –A: Raman spectra of the Tyrosine Fermi doublet on increasing pressure up to 8.1 GPa. The two red curves highlight the discontinuity between 3.4 and 4.9 GPa; B: Pressure behavior of the frequencies of the Tyr doublet; C: Intensity ratio on pressurize the protein up to 3.9 GPa. The up and down blue triangles are the value of the intensity ratio for the fibrillar-22h and fibrillar-4h.

The direct comparison (see Figure C5) among the pressure-treated spectrum ( $P_{\text{Max}} = 8$  GPa) with those obtained for the native and the two fibrillar samples provides a further insight into the structural modifications induced by compression. The comparison shown in Figure C5 clearly demonstrates the high potentiality of the Raman spectroscopy for studying secondary and tertiary structures of a protein. In particular it provides a measure of the extent of the pressure-induced denaturation and a clear indication about the *nature* of the structural rearrangement occurred in the P-treated sample. The latter indeed shows the spectral signature of a remarkable denaturation process testified by the modification of back-bone chain vibrational peaks ( $\nu(\text{C-S})$ ,  $\text{CaCN}$ , and  $\nu(\text{C-N})$ ). Moreover a careful spectral analysis of the Amide I band shows the onset of protein aggregation (the increase of the  $\beta$ -inter-molecular component) although the aggregates remain in disordered phase as shown by the comparison with the Amide I band in the Raman spectra of the two differently fibrillar samples. Applying very high pressure drives insulin from the native to a new misfolded state characterized by a predominantly  $\beta$  structure in a disordered configuration. As a matter of fact insulin in the native state is a predominantly  $\alpha$  helix protein (50%) whereas the pressurization above 4.2 GPa converts the protein into a predominantly  $\beta$  sheet one (53%). It is important to note that nevertheless a remarkable percentage of  $\alpha$  helix structure (33%) was maintained after the pressure cycle.

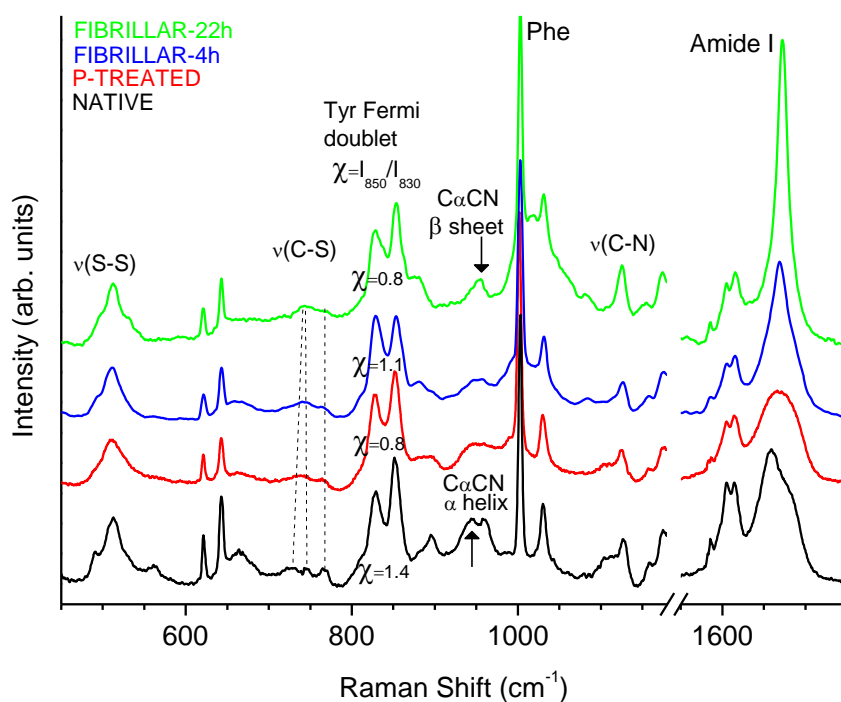


**Figure C5** – Raman spectra of insulin at ambient conditions: native (black), P-treated (red), fibrillar-4h (blue) and fibrillar-22h (green) insulin. The labeled peaks are those better analyzed in this thesis.

These second series of measurements thus lead to the following conclusions:

- the detection of the plastic transition of insulin under pressure at 4.2 GPa;
- the identification of a new stable structural phase at ambient pressure obtained after the P-cycle and characterized by a high percentage (53%) of mostly disordered  $\beta$  structures;
- an explanation of the pressure behavior of the Tyr doublet/singlet above  $P_t$  provided by the rearrangement of water molecules, in agreement with the current opinion on the microscopic mechanisms underlying the pressure driven denaturation process.

A different way of exploring protein configuration plane has been also exploited by mixing protic ionic liquids (EAN, PAN, BAN and MOEAN see Chapter 6 for the specific denomination) with the insulin fibrillar sample. In this case lysozyme was also investigated as a sort of reference sample. Hen egg white lysozyme (HEWL) was indeed chosen because of the preliminary studies performed by Byrne et al. on the renaturation effects of ionic liquids. Present measurements confirm and extend the previous knowledge on this particular renaturation process. The results obtained by Byrne et al. were indeed achieved mainly using a qualitative technique (the ThT fluorescence) and by analyzing the enzymatic activity, whereas in the present work, Raman spectroscopy allows for a direct quantitative conformational analysis. It is worth to notice that our conformational estimate for lysozyme is in good agreement with the enzymatic activity previously reported. Raman spectra of the investigated lysozyme samples under the effect of the ethyl-ammonium nitrate (EAN) are shown in Figure C6.

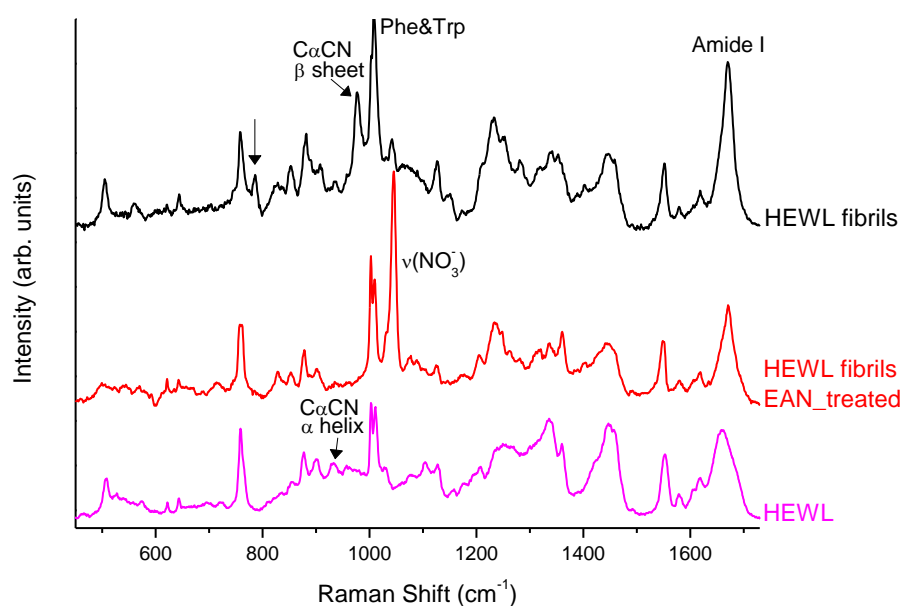


**Figure C6** – Raman spectra of the hen lysozyme (HEWL) in different conformation: native (magenta), fibrillar (black), and after being treated with EAN (red). The region where major changes among the three spectra occurred are labeled. The  $\nu(\text{NO}_3^-)$  is a peak due to residues of the ionic liquid (ethyl ammonium nitrate, EAN).

As to the insulin fibrillar sample (fibrillar-22h) the ionic liquids that induce the greatest changes in the Raman spectrum was the 2-methyl-oxy-ethyl-ammonium nitrate (MOEAN). Those changes were probably due to a re-crystallization of the protein, testified, from a macroscopic point of view, by the spherulites formation (see the inset in Figure C7) and by the relative intensities variation of the Tyrosine residues in the Raman spectra (see Figure C7). It is still unclear the pattern that starting from the fibrils leads to the spherulites formation, as in literature their formation is shown to be concurrent.

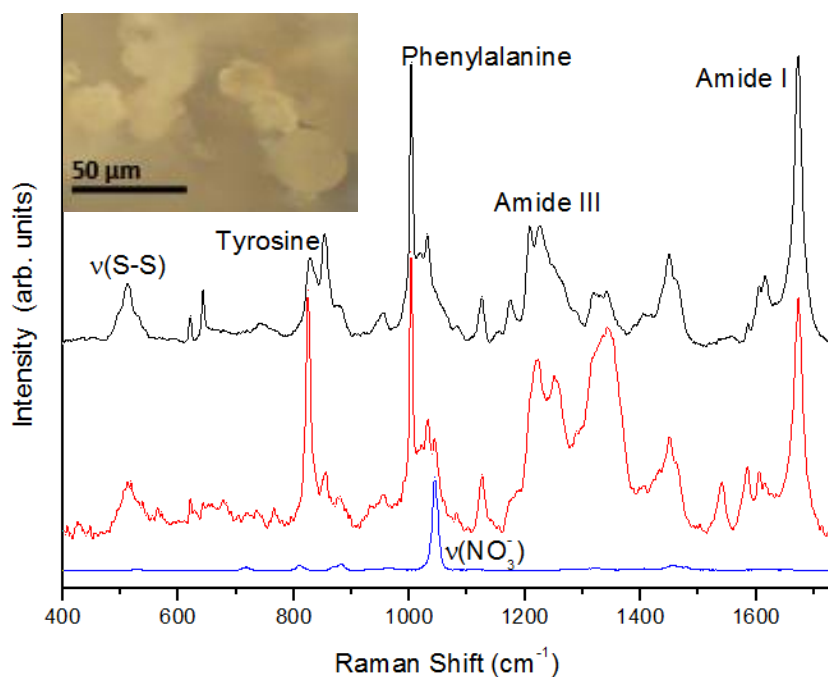


**Figure C7** – Raman spectra of the BPI in different conformation: fibrillar (black) and after being treated with 2-methyl-oxy-ethyl-ammonium nitrate (MOEAN) (red). In blue is reported the Raman spectra of the pure MOEAN. In the inset there is a photo of the sphere induced by the re-dissolution of BPI fibrils in MOEAN.



This part of the thesis is still under active investigation although present results are absolutely encouraging. Quite schematically these can be summarized as follow:

- the only ionic liquids stimulating a renaturing effect appear to be the EAN for lysozyme and (perhaps) MOEAN for insulin;
- Raman spectroscopy allows for a careful quantitative analysis of the renaturation process induced by ionic liquids;
- insulin re-crystallization under the effect of MEOAN is conjectured on the basis of the macroscopic observation of spherulites (see Figure C7).

## **Outlook**

The results reported in the present thesis open to a novel approach to the investigation of the high pressure structure of proteins. Raman spectroscopy has indeed demonstrated to be a very powerful tool to study the high pressure behavior of proteins and it will surely be interesting and important to extend this kind of measurements to other proteins. A comparative analysis could reveal general aspects of the proteins response to volume compression and provide a deeper knowledge of the pressure induced unfolding pathway.

Nevertheless parallel proper structural studies must be carried out and, in particular, x-ray crystallography under pressure. Given the intrinsic difficulties and the need of very high photon flux (samples for high pressure measurements are very small) we plan to ask for beam-time on the ID09A high-pressure x-ray diffraction beam-line at ESRF. Insulin and lysozyme are obviously the first candidates to be investigated. If these experiments will be successful, we could extend this combined Raman-X-ray diffraction investigations to other proteins of interest.

A second research line will be devoted to the study of fibrils renaturation by means of the ionic liquids. In this case Raman experiments will be continued in the following months in our laboratory. In particular a careful and systematic study on varying the maturity degree of the fibrils treated with ionic liquids will be undertaken. Other series of measurements with different anion (i.e. different proton activity) will be undertaken in our laboratory in the next months. Moreover it will be very interesting to study the effects of the combined action of ionic liquids and high pressure on the insulin conformational states.



# *Appendix*

## *Application of Raman Spectroscopy on Samples of Biological Interest*

In these Appendix two spectroscopic investigations carried out with Raman and Infrared spectroscopy on two materials of biological interest are presented and discussed. The first one reports on a careful spectroscopic study of natural calcification (bio-apatite) found in heart valves (App. A), and the second one describes the results of an extended experimental investigation of eumelanin films carried out with several techniques (including Raman and IR spectroscopy) (App. B).

## **App. A – Biological Apatites from Cardiac Valves**

In this appendix pathological bio-apatite from patients undergoing valvular replacement due to severe aortic and mitral stenoses were studied by Raman and Infrared spectroscopies. Three different types of mineralized human cardiac valves were analyzed with the aim of infer the presence of carbonate group and evaluate the carbonate substitution in bio-apatite structure.

### **Introduction**

The growth of pathological mineral deposits in human heart valves, better known as calcification, can lead to loss of functionality of the cardiac valves, causing aortic and mitral stenosis. Calcification represents the first reason for valve replacement in Europe and North America and the third leading cause of cardiovascular diseases.<sup>1</sup> Little is known about these pathological mineral formations even if they are quite common. Bio-apatite are calcium phosphate bio-mineralization, like the normal mineralization (enamel, dentin, bone),<sup>2,3</sup> but they shown different characteristics.<sup>4,5</sup> Mineral deposits are constituted mainly by calcium phosphate crystals and are characterized by multiple ionic substitutions both inside and at the surface of the crystals at all crystallographic sites which allow to accommodate a large number of elements and molecules such as  $\text{Sr}^{2+}$ ,  $\text{Na}^+$ ,  $\text{K}^+$ ,  $\text{Mg}^{2+}$ ,  $\text{F}^-$ ,  $\text{HPO}_4^{2-}$ ,  $\text{CO}_3^{2-}$ ,  $\text{P}_2\text{O}_7^{4-}$ ,  $\text{Pb}^{2+}$ ,  $\text{Ba}^{2+}$ ,  $\text{Zn}^{2+}$  etc..<sup>6,7,8</sup>

The  $\text{CO}_3^{2-}$  group is an important component of bio-apatite due to its ability to take place in the apatite structure and because it seems to control formation, evolution, morphology, and physical properties of biological apatite and synthetic nano-carbonated hydroxylapatite.<sup>9,10</sup> Carbonate group can take the place of  $\text{OH}^-$  group (A-type substitution),  $\text{PO}_4^{3-}$  group (B-type substitution) or either (AB-type substitution).<sup>11</sup> In biological apatite, mainly normal mineralized tissue, the dominant substitution appears to be  $\text{CO}_3^{2-}$  groups for  $\text{PO}_4^{3-}$  groups although the  $\text{OH}^-$  ions replacement also occurs.<sup>12</sup> For pathological deposits it is still uncertain if it appears in A-type or B-type structural location or also as a separate phase.

### **Materials and Methods**

The analyzed samples are calcified human cardiac valves: two tricuspid aortic valves (TV14a, TV12a), two bicuspid aortic valves (TV18ab, TV9ab), and two mitral valves (TV3m, TV16m) (see Table A1). They were collected as surgical waste from patients undergoing valvular replacement because of severe aortic and mitral stenosis. The surgical interventions were performed in the Dept. of Cardiac Surgery, Regional Hospital in Treviso (Italy). Ages of patients ranged from 43 to 83 years old. Patients have a male to female ratio of 4 : 2. The samples were preserved and dehydrated in absolute alcohol, then sterilized through the exposition to UV radiations for 72-180 hours. Each sample was fractured and cut in pieces. Some of these pieces were ground in an agate mortar into a fine powder. In order to remove the organic matrix, mainly collagen, the powders were subjected to an enzymatic attack, with trypsin in basic pH conditions. After the enzymatic attack the powders were exposed to UV radiations for 32-96 hours and then sifted using sieves smaller than 50  $\mu\text{m}$ . The intact part of the samples (= untreated), constituted of mineral deposits and collagen, and the powders treated with trypsin (mainly mineral deposits) were investigated using Raman spectroscopy.

Sample Name	Sex/Age	Sample Description	State of the Sample
TV12a	M/70	Tricuspid Aortic Valve	Powder
TV14a	M/71	Tricuspid Aortic Valve	Powder and Untreated
TV9ab	M/73	Bicuspid Aortic Valve	Powder
TV18ab	M/43	Bicuspid Aortic Valve	Powder and Untreated
TV3m	F/83	Tricuspid Mitral Valve	Powder and Untreated
TV16m	F/61	Tricuspid Mitral Valve	Powder

**Table A1** – Analyzed samples by Raman and IR spectroscopy. *a* = tricuspid aortic valve, *ab* = bicuspid aortic valve, *m* = mitral valve.

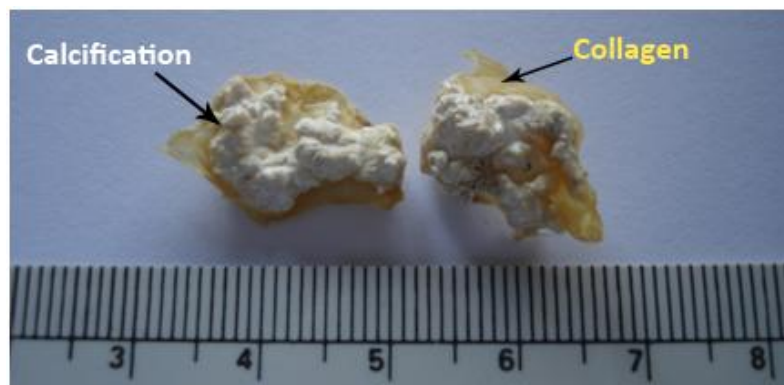


**Figure A1** – Photo of two pieces of an aortic valve.

Raman measurements were carried out using the same apparatus shown in Figure 2.12. Spectra were collected between 200 and 4000  $\text{cm}^{-1}$  using the 1800 lines  $\text{mm}^{-1}$  grating, which allows a resolution of about 3  $\text{cm}^{-1}$  from at least 20 minutes to 1 hour for each frequency range. The 50x objective used in a confocal configuration (150  $\mu\text{m}$  diaphragm) gives a micrometer spot size and a small scattering volume, i.e. on average smaller than sample grain dimension. A remarkable fluorescence was observed for all samples investigated, including the treated powders. The fluorescence signal showed a remarkable time dependence strongly decreasing under the laser radiation. In order to collect a good quality Raman spectra, the laser was focused on a specific point of the sample, and the Raman signal was collected only after a time interval longer enough to get a remarkable fluorescence decay. The absolute frequencies of Raman spectra were calibrated using neon lines and the intensities normalized respect to the  $\nu_1(\text{PO}_4^{3-})$  peak. Data analysis were carried out with OPUS software using Gaussian-Lorentzian (Pseudo-Voigt) profiles in the non linear peak fitting routine that employs the Levenberg-Marquardt algorithm (LMA) to minimize the chi-squared value (see section 2.5).<sup>13,14</sup>

Infrared analyses were performed using a Perkin Elmer System 2000 FTIR with a resolution of 4 $\text{cm}^{-1}$ . For IR measurements the KBr method was used. 2 mg of powdered sample were diluted in 200 mg of KBr and pressed into a pellet under vacuum at 9 ton. FTIR spectra were collected in the 4000-400  $\text{cm}^{-1}$  spectral range. In order to minimize spectral components due to atmospheric  $\text{CO}_2$  and  $\text{H}_2\text{O}$  the detector was flushed with dry nitrogen during measurements. IR spectra were analyzed with OPUS software and by Levenberg-Marquardt algorithm, as in the case of Raman spectra (see section 2.5).

Raman and Infrared spectra of pathological mineralized deposits were then compared with Raman and Infrared spectrum of synthetic hydroxylapatite  $\text{Ca}_5(\text{PO}_4)_3\text{OH}$ , a commercial calcium phosphate tribasic, 34 – 40% Ca, from Johnson and Matthey Alfa Aesar.

## Measurements

The Raman spectrum obtained for the pathological mineralized deposits grown within human heart valves is shown in Figure A2. All samples show similar Raman spectra and no relevant differences among the three different types of calcified cardiac valves have been observed. In Figure A3 the Raman spectra of all the samples investigated are compared with the Raman spectrum of the synthetic hydroxylapatite (CaOH).

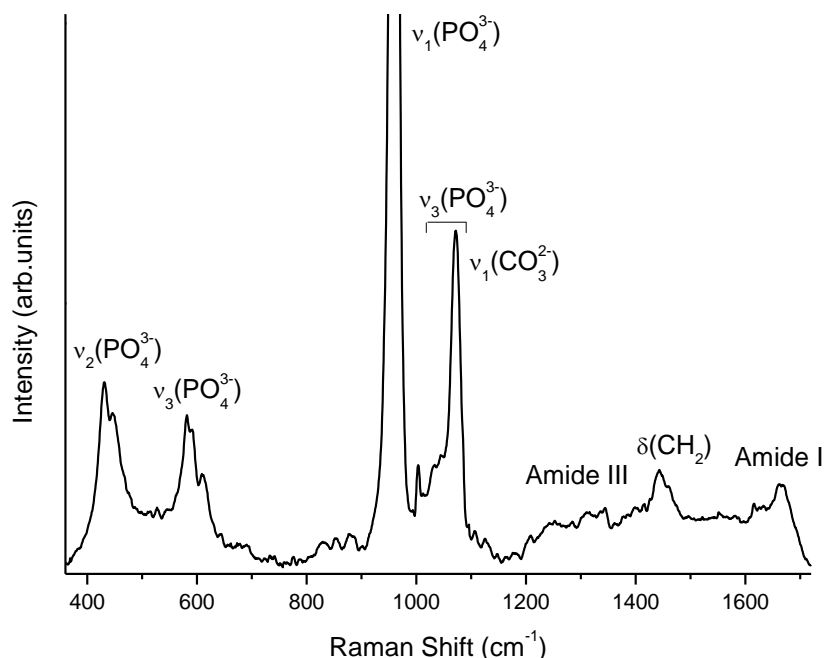


**Figure A2** – Background-subtracted Raman spectrum of heart valve bio-mineralization in the 360-1720  $\text{cm}^{-1}$  range after normalization to  $\nu_1\text{-PO}_4$  mode. The major features are highlighted by specific labels. The  $\nu_1\text{-PO}_4$  peak is not completely shown because it is 4.5 times more intense than  $\nu_2\text{-PO}_4$  peak. ( $\nu$  = stretching,  $\delta$  = deformation).

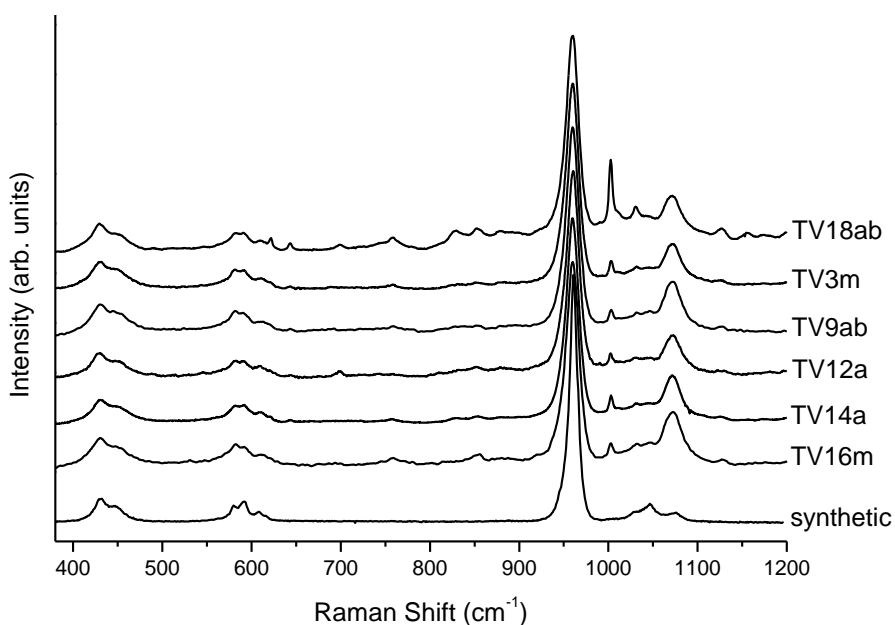


**Figure A3** – Background subtracted Raman spectra of heart valve bio-mineralization in the 380-1200  $\text{cm}^{-1}$  after normalization to  $\nu_1\text{-PO}_4$  mode (935-985  $\text{cm}^{-1}$ ). Spectra were collected from treated powder and compared with Raman spectrum of a synthetic hydroxylapatite (CaOH).

The Raman spectra collected from mineralized part and collagen part of the intact sample TV14a are shown in Figure A4. In the inset a comparison among the  $\text{HPO}_4^{2-}$  peak of all sample and the spectrum of the collagen is shown. The greater intensity of the  $\text{HPO}_4^{2-}$  peak for the TV18ab sample is ascribable to the higher presence of collagen in the powder of this sample.

The Raman band positions (mean values) and relative assignments are listed in Table A2 (left).

Raman Assignment <sup>19,20,21</sup>	Heart Valve		IR Assignment <sup>15,16,17</sup>	Heart Valve	
	CaOH [cm <sup>-1</sup> ]	Biom mineralization [cm <sup>-1</sup> ]		CaOH [cm <sup>-1</sup> ]	Biom mineralization [cm <sup>-1</sup> ]
$\nu_2(\text{PO}_4^{3-})$ out of plane bend	430	430	$\nu_2(\text{PO}_4^{3-})$ bend	473	469
	448	449			
$\nu_4(\text{PO}_4^{3-})$ in plane bend	580	581	$\nu_4(\text{PO}_4^{3-})$ bend	564	562
	591	592		574	579
	608	608		604	605
	617	616			
$\nu_2(\text{CO}_3^{2-})$ out of plane bend <sup>22</sup>		826	(OH) librational	632	
		836			
		854			
(P-OH) stretch		878	$\nu_2(\text{CO}_3^{2-})$ out of plane bend		867
		888			873
$\nu_1(\text{PO}_4^{3-})$ sym stretch	958	953	$\nu_1(\text{PO}_4^{3-})$ sym stretch		880
	961	961			958
(HPO <sub>4</sub> <sup>2-</sup> )		1004	$\nu_3(\text{PO}_4^{3-})$ asym stretch		993
		1084 <sup>16</sup>		1033	1023
$\nu_3(\text{PO}_4^{3-})$ asym stretch	1042	1042		1050	1057
	1047			1070	1101
	1075			1094	
$\nu_3(\text{PO}_4^{3-})$ asym str. & $\nu_1(\text{CO}_3^{2-})$ sym str.		1071		1110	
		1237	HPO <sub>4</sub> <sup>2-</sup> bend(P-OH)		1153
Amide III		1276		1230	1393
		1315	$\nu_3(\text{CO}_3^{2-})$ asym stretch		1419
	1342			1449	
	1441			1473	
	1462			1500	
$\delta(\text{CH})$ <sup>[35]</sup>		1666		1540	
$\delta(\text{CH}_2)$ <sup>[35]</sup>			amide I / bend(OH)		1662
					2850-2950 <sup>18</sup>
Amide I			$\nu_1(\text{HPO}_4^{2-})$ stretch(OH)		3000-3600

**Table A2** – Raman (left) and IR (right) band positions and assignments of calcified human heart valves and synthetic hydroxylapatite (CaOH). (stretch=stretching, bend=bending,  $\delta$ =deformation, sym=symmetric, asym=antisymmetric)

The comparison between the Raman spectrum of the untreated sample and that of the powder subjected to the enzymatic attack of TV14a (Figure A5) shows that there are not remarkably differences between the two Raman spectra. The different intensities in the two spectra of the  $\text{CH}_2$  deformation around 1440 cm<sup>-1</sup> and  $\text{HPO}_4^{2-}$  at ~1004 cm<sup>-1</sup>, both associated to the organic component

of the sample, are due to the natural non homogeneity in the intact samples and the degree of efficacy of the enzymatic attack for powders.

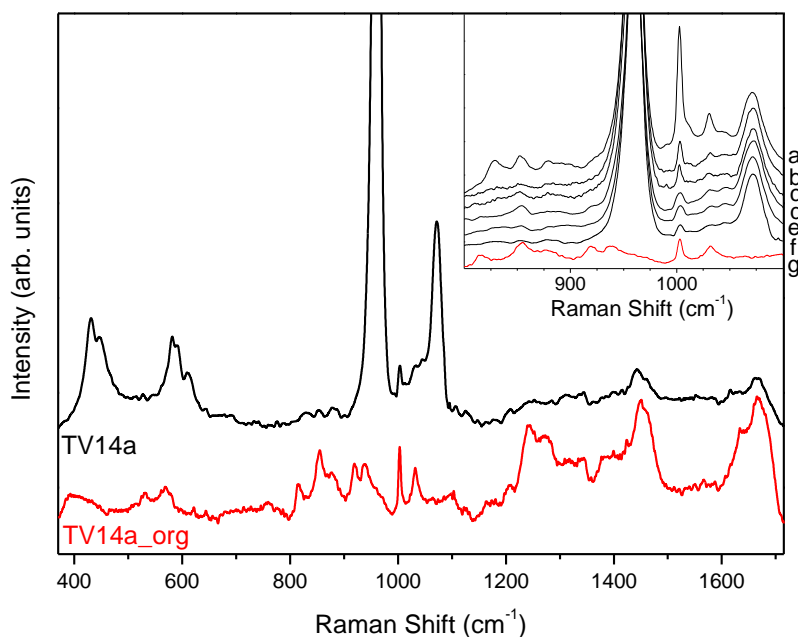


**Figure A4** – Raman spectra of the inorganic component (mineralization, black curve) and organic component (collagen, red curve) of the TV14a sample. The bands observed in the frequency region 1100-1700  $\text{cm}^{-1}$  can be ascribed to organic component of the sample. In the inset the Raman spectra of the pathological bio-mineralization collected from powdered samples (a: TV18ab, b: TV3m, c: TV12a, d: TV16m, e: TV9ab, f: TV14a) are compared with the Raman spectrum of collagen (g).

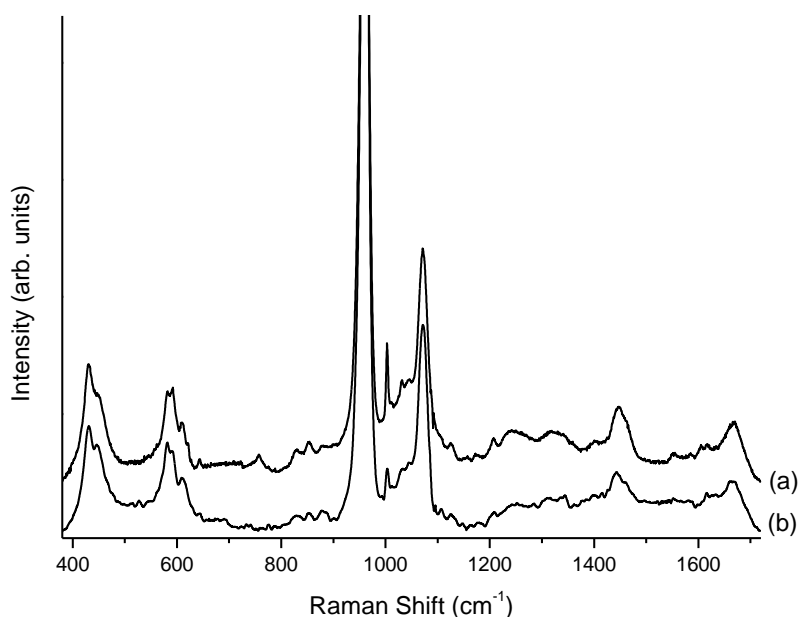


**Figure A5** – Raman spectra of TV14a collected from the powder subjected to the enzymatic attack (a) and from the untreated sample (b). The spectra were normalized respect to  $\nu_1\text{-PO}_4$  peak (935-985  $\text{cm}^{-1}$ ).

The infrared spectrum of calcified human heart valve is shown in Figure A6. All samples show similar IR spectra and a low resolution of the absorption bands due to low degree of crystallinity (see Figure A7).



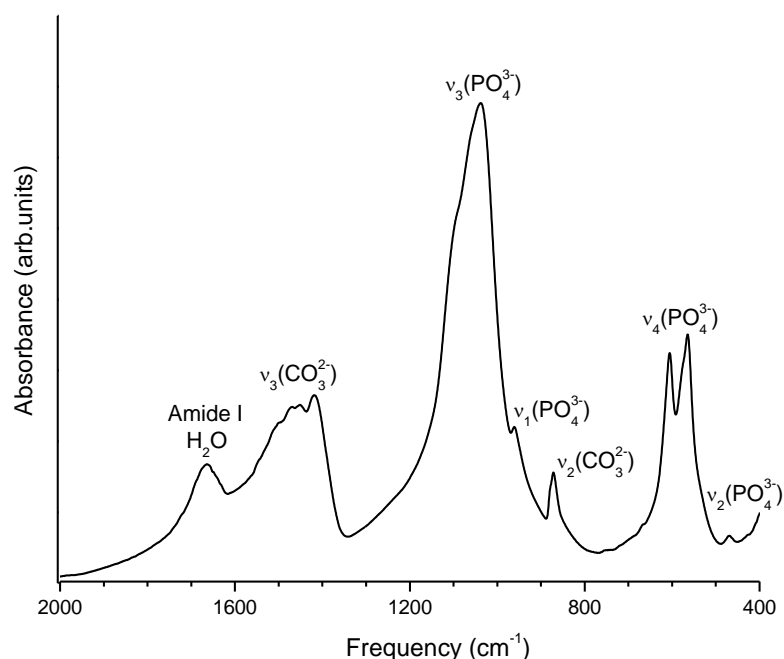


**Figure A6** – IR spectrum of TV9ab in the 2000-400  $\text{cm}^{-1}$  spectral range. Major features are labeled.

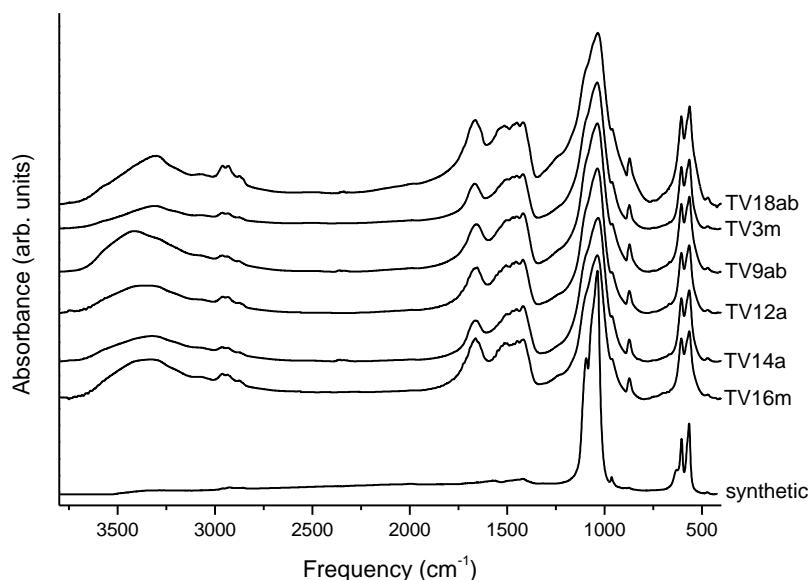


**Figure A7** – IR spectra of calcified human heart valves and of a synthetic hydroxylapatite collected in the 3800-400  $\text{cm}^{-1}$  spectral range. Spectra have been normalized respect to  $\nu_3$  phosphate band (900-1200  $\text{cm}^{-1}$ ) and are arbitrary shifted for sake of clarity.

The IR band positions (mean values) and relative assignments are listed in Table A2 (right) and are compared with the IR spectrum of a synthetic hydroxylapatite.

## Results

The spectroscopic calibration method described by Awonusi et al.<sup>23</sup> to determine the carbonate content in bone and synthetic samples was used to estimate the percentage of carbonate in the calcified heart valves. In particular, using the Raman data, the 1050-1100  $\text{cm}^{-1}$  spectral range ascribable to the  $\nu_3$ - $\text{PO}_4$  and  $\nu_1$ - $\text{CO}_3$  peaks was studied as one peak because when the percentage of carbonate is major than 3% there are no possibilities to de-convolve this region in two peaks.<sup>23</sup> From

the fitting procedure the area and the FWHM were estimated and combined with the regression lines found in ref 23 (see Figure A8). The curves were normalized to the  $\nu_1(\text{PO}_4^{3-})$  peak and then the LMA was applied in the 900-1100  $\text{cm}^{-1}$  range of the Raman spectra. The error in Figure A7 were inferred through a Bayesian analyses.<sup>24,25</sup> The percentage of the carbonate was estimated to be around 5-10% both from the intensity ratio 1071/961  $\text{cm}^{-1}$  (Figure A8 a) and from the Full Width Half Maximum (FWHM) of the peak at 1071  $\text{cm}^{-1}$  due to convolution of  $\nu_3\text{-PO}_4$  and  $\nu_1\text{-CO}_3$  (Figure A8 b).

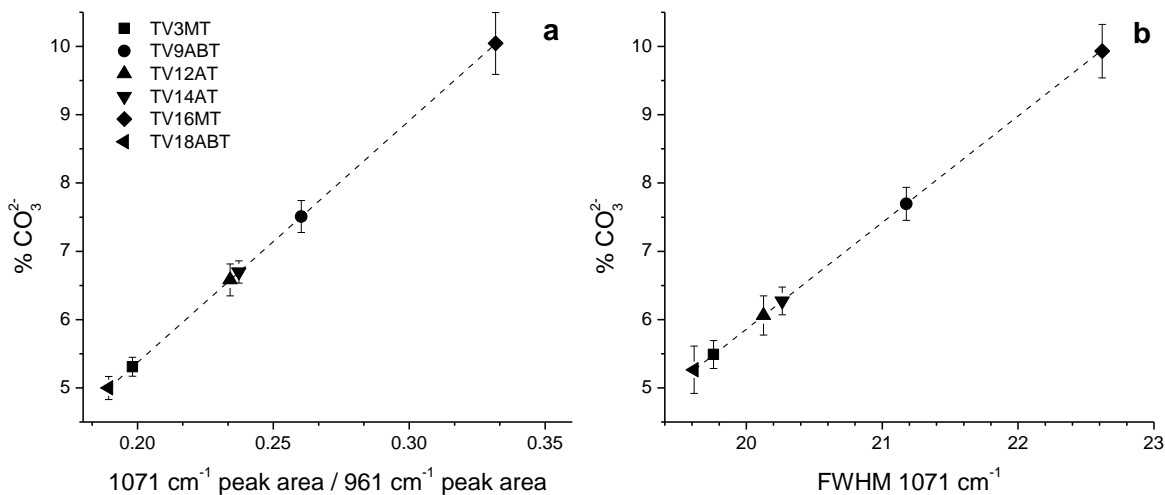


**Figure A8** – Carbonate content of calcified human heart valves estimated from the Raman data. **a:** Peak area at 1071  $\text{cm}^{-1}$  divided by peak area at 961  $\text{cm}^{-1}$  as a function of carbonate content.; **b:** FWHM of the peak at 1071  $\text{cm}^{-1}$  as a function of carbonate content. Both the regression equation used are from ref 23.

The same type of analysis was conducted on the IR spectra. On the base of the linear relationship observed by Ou-Yang et al. (ref. 20) between the IR intensity ratio of the  $\nu_3\text{-CO}_3$  (around 1419  $\text{cm}^{-1}$ ) /  $\nu_3\text{-PO}_4$  (around 1023  $\text{cm}^{-1}$ ) and the carbonate levels, the percentage of  $\text{CO}_3^{2-}$  in heart valve bio-mineralization was determined by the intensity ratio  $I_{1419}/I_{1023}$  (Figure A9).

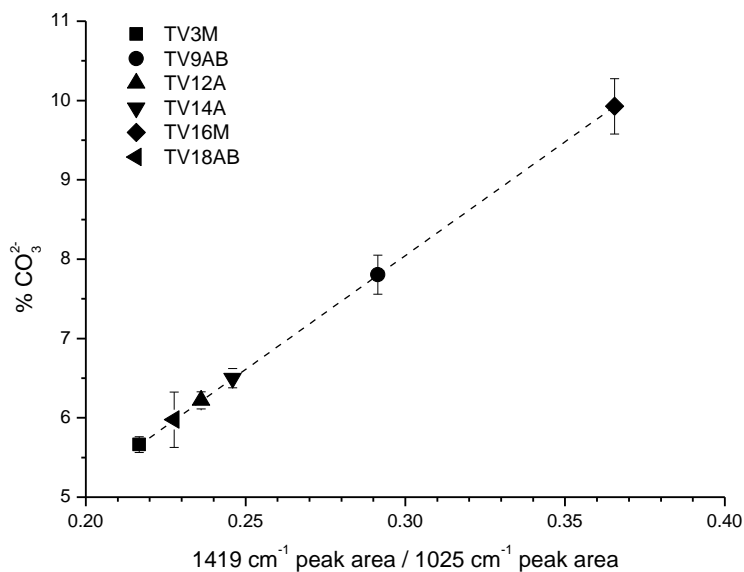


**Figure A9** – Carbonate content in calcified heart valves plotted as a function of the peak area at 1419  $\text{cm}^{-1}$  divided by peak area at 1023  $\text{cm}^{-1}$  of the IR spectra. The regression curve is from ref. 20.

The  $\text{CO}_3^{2-}$  content determined using IR data are in agreement with the  $\text{CO}_3^{2-}$  percentages estimated using the fitting procedure of the Raman data within an error around 0.2% for all samples except for TV18ab. For this sample the difference between the calculated  $\text{CO}_3^{2-}$  percentage by Raman and Infrared data is around 0.7%. The latter find its explanation in the a higher content of collagen in the sample (already detected by the Raman spectrum) that overlap the region of the  $\nu_3\text{-CO}_3$ .

By analyzing the Raman and IR data it is possible to give an estimation of the degree of crystallinity of each sample.

The broadening of the FWHM of  $\nu_1\text{-PO}_4$  peak observed in the Raman spectra of bio-mineralization respect to that of the synthetic hydroxylapatite is a symptom of the crystallinity degree of the heart valves apatite ascribable to the high  $\text{CO}_3^{2-}$  percentage in the lattice (see Figure A10).

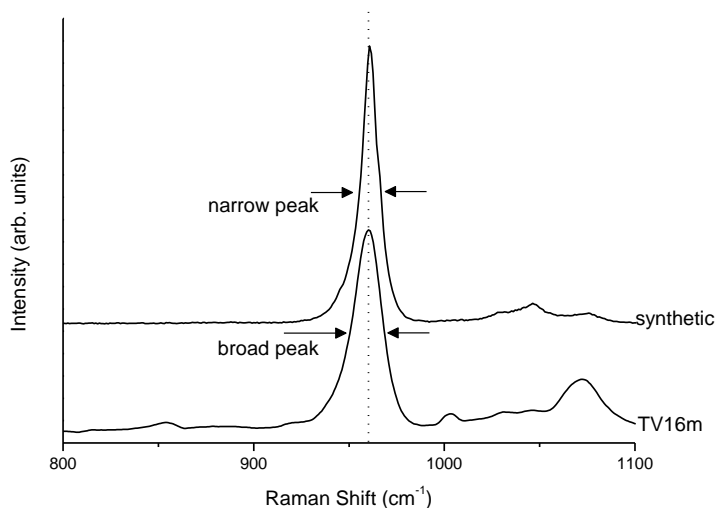


**Figure A10** –Comparison of the Raman FWHM of  $\nu_1(\text{PO}_4^{3-})$  peak between the synthetic apatite and one of the heart valves bio-mineralization (TV16m). The wider peaks of the bio-mineralization indicate a shorter-range disorder than in the synthetic hydroxylapatite. The dotted line indicates the  $\nu_1(\text{PO}_4^{3-})$  peak for the TV16m spectrum.

From the empirical correlation found by Pleshko et al.<sup>26</sup> between the crystal size calculated by X-ray diffraction line and the area of the peak near  $1060\text{ cm}^{-1}$  in the IR spectra that arises from the disordered phosphate phase the degree of crystallinity in the biological samples and in the synthetic one were estimated.

For each sample the  $1200\text{-}900\text{ cm}^{-1}$  spectral region was resolved by curve fitting analysis (LMA). Six components were necessary to obtain a very good fit (see Figure A11), in agreement with Pleshko. The percentage area of component at  $1059\text{ cm}^{-1}$  indicated as B component in Figure A11 was used to estimate the crystal size of the pathological phase investigated and for comparison also of the synthetic one. The crystal size estimated is in the range of  $14.5\text{-}15.0\text{ nm}$  for the bio-mineralization, and is  $19.3\text{ nm}$  in the synthetic hydroxylapatite. The comparison between the two values found allows to assess that the heart valve bio-mineralization has a very low degree of crystallinity.

## Conclusion

Micro-Raman and IR spectroscopy analyses performed on calcified human cardiac valves showed that the pathological mineral phase grown in human heart valves is constituted by a carbonated apatite and pointed out that there are no remarkably differences between the calcified deposits

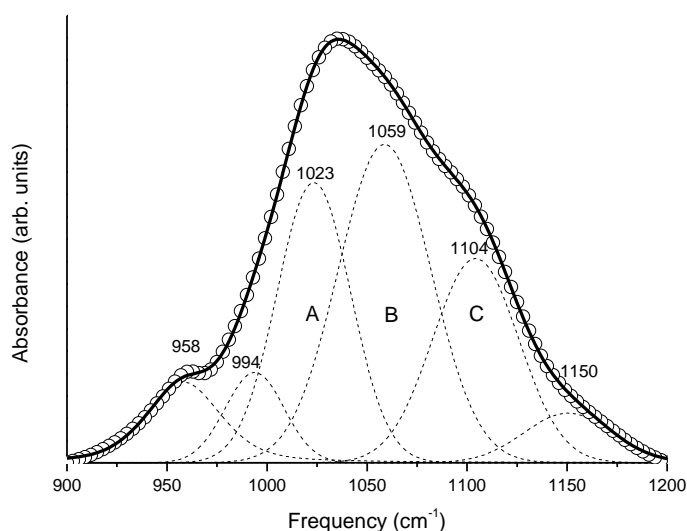


**Figure A11** – LMA fit of TV16m. IR data (o), fit (thick line) and components (dash line). The component B of the fit is ascribable to the disordered phosphate phase and it is the one used to estimate the degree of crystallinity of the various samples.

grown in the three different types of cardiac valves analyzed. The Raman band at  $\sim 1067 \text{ cm}^{-1}$  observed in all the Raman spectra and due to  $\nu_1\text{-CO}_3$  is specific of B-type carbonate apatite.<sup>15,16</sup>

However a precise frequency was impossible to assign to  $\nu_1\text{-CO}_3$  mode due to the strong overlap with  $\nu_3\text{-PO}_4$  mode. The band at  $\sim 1107 \text{ cm}^{-1}$  due to  $\nu_1\text{-CO}_3$  mode and used to identify A-type substitution ( $\text{CO}_3\text{-for-OH}$ ) wasn't detected in the Raman spectra. As indicated in Table A2 (left) the  $\nu_1\text{-PO}_4$  mode splits in two bands at  $\sim 953 \text{ cm}^{-1}$  and at  $\sim 961 \text{ cm}^{-1}$ . The latter component corresponds to a crystalline stage as it was reported by Karanci et al. in Raman studies on bones,<sup>27,28</sup> on the contrary the  $\nu_1\text{-PO}_4$  mode detected at  $\sim 953 \text{ cm}^{-1}$  indicates the presence of amorphous calcium phosphates such as ACP and OCP. Considering the band at  $961 \text{ cm}^{-1}$  as an indicator of the degree of crystallinity of the bio-mineralization it is possible to assess that the pathological mineral phase investigated seem to be in its maturity stage<sup>27,28</sup>.

FT-IR spectra confirmed the B-type carbonate substitution ( $\text{CO}_3\text{-for-PO}_4$ ) and showed evidences for a very poor replacement of  $[\text{OH}]$  by  $[\text{CO}_3]$ , i.e. A-type substitution (the highest percentage of A substitution found was 12% for TV18ab sample). The individual peak components due to  $\nu_3\text{-CO}_3$  IR-mode (Table A3), obtained from FTIR spectral analysis of carbonate bands in the  $1600\text{-}1400 \text{ cm}^{-1}$  spectral range indicates the presence of  $[\text{CO}_3]$  at both A- and B-sites according to the literature.<sup>21,22,29,30</sup>

The carbonate content estimated for the bio-mineralized samples using Raman and IR data are in agreement with the range of values indicated for biological apatite, mainly natural bone even if one sample (TV16MT) seems to have a carbonate content greater than the other samples and greater than the values reported for biological apatite in literature.<sup>15,31,32</sup> The possibility that the amorphous components could play an important role on the area and on the FWHM of the peaks which were used to estimate the carbonate content cannot be completely rejected.

All samples show a low degree of crystallinity and the crystal size estimated using IR data is in the nanometer range of biologic apatite crystals and appears to be lower than typical crystal size of bones (25-50 nm).<sup>32,33</sup>

## App. B – Eumelanin Films

This work has been included in a series of studies with different techniques (Raman spectroscopy, scanning microscopy, XPS, Fourier Transform infrared spectroscopy and optical absorption) that aim to investigate the modified property of electro spray deposited (ESD) melanin films.<sup>34</sup> Raman spectroscopy in particular played an important role for the control of the local structure and chemistry. All the techniques used for the characterization showed large discrepancies between the physical properties of the films after ESD depositing providing sizeable information on the melanin functionality and its polymorphic structure. In the following is reported only an extended Raman section of the paper.

### Introduction

Melanins, as pigments, are important bio-macromolecules which can be found in living organisms such as human skin, hair, eye, inner ear and even brain. Depending on the composition and structural differences, they can be mainly classified into black or brown nitrogenous eumelanin, yellow or reddish brown sulfur containing pheomelanin and intermediate type neuromelanin.<sup>35</sup> This class of pigments has been attracting much attention of biophysicists due to their biological functions and their interesting physical properties.<sup>36,37</sup> Melanins showed relatively high electrical conductivity compared to amorphous organic semiconductors,<sup>38</sup> a threshold switching behavior which is crucial for electronic device,<sup>39</sup> a strong broad band UV-Visible optical absorption and photoconductivity (PC)<sup>40</sup> and a great efficiency in converting energy into heat.<sup>41</sup> The above ones and other interesting physical properties of melanin pigment suggest a number of applications to a variety of organic bio-electronic devices.<sup>42</sup>

Synthetic melanin can be synthesized from tyrosine by means of the tyrosinase enzyme. After the hydroxylation and oxydation to DOPA and subsequent oxidation to dopaquinone and dopachrome, decarboxylation leads to 5,6-Dihydroxyindole (DHI or HQ) and 5,6-Dihydroxyindole-2-carboxylic acid (DHICA) with final polymerization to melanin.<sup>43</sup>

Currently, there is no general agreement on the secondary structure model because of the indetermination on the possible presence of oxidized forms like indolequinone (IQ), hydroxyquinone (HQ) and semiquinone (SQ), increasing the numbers of possible configurations that the melanin monomers might adopt (see Figure B1).<sup>44</sup>

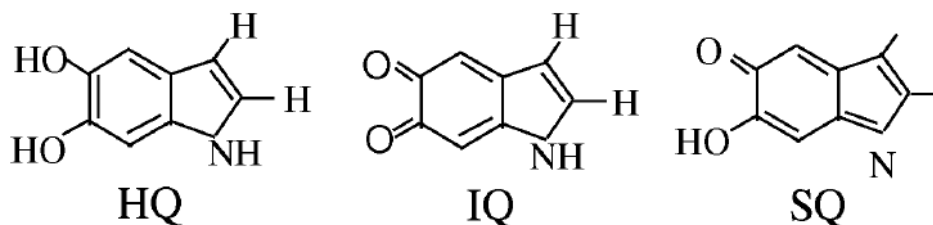


**Figure B1** – Schematic representation of melanin monomers: hydroquinone (HQ), indolequinone (IQ), and semiquinone (SQ). From ref. 44.

The models that have been considered for the secondary structure are mainly two: a) heteropolymeric model: the polymer is formed by means of random bonds between monomers, this model is able to explain the optical and electric properties of the eumelanin, in particular the wide absorption band, the chemical stability and the little solubility;<sup>45</sup> b) oligomeric model:

according to this model the oligomeric macromolecule is made by 3 or 4 layers of a protomolecule with 5-6 DHI/DHICA monomers 15-20 Å large and 10-15 Å high, this model is supported by the atomic force microscopy (AFM) images.<sup>46</sup>

Structure and functional relations have not been established yet, due to the complexity of the system. Recent advances in isolation, purification, synthesis methods, imaging techniques<sup>47</sup> as well as various characterization methods<sup>36</sup> again boosted the research activities on this interesting system. However, a number of questions remain unaddressed: how can the experimental conditions such as source, purification, synthesis, solubilization conditions, thin film process and substrate eventually affect the entire functionality of the melanin films? Some discrepancies remain unresolved. The effective mechanism of organic conjugation in melanin films and the influence in the electric and optical properties are also under intense debate.<sup>48,49,50</sup>

From the technological point of view, melanin thin films deposition on suitable substrate, is particularly relevant. Actually, the deposition of continuous layers of melanin is difficult to achieve and consequently the studies on the condensed phase physical properties are rather challenging as directly depending on the structure. Once in solution state, organic thin films are rather easy to be processed without the need for high vacuum as other inorganic thin films. However, the properties of the melanin films are difficult to be controlled because of their significant dependence on the solvent, its extremely low solubility, but also the preparation techniques and substrates employed. Casting or spin coating are among the most commonly used techniques,<sup>51,52</sup> but are not able to guarantee an overall homogeneity of the films. Electrochemical deposition has also been used with the limitation on the film thickness and substrate preference.<sup>48,53</sup>

For all these reasons, it is important to consider the electro-spray technique that could efficiently reduce the solvent effects on the monomers aggregation. Electrospray is commonly used in mass spectrometry, where the macromolecules were efficiently separated from the solvents through electro-ionization. It has also been used to prepare various type of thin films in ambient condition<sup>54</sup> as well as in ultra high vacuum on clean substrates.<sup>55,56</sup> In this way a modified assembly and aggregation with respect to the observed disordered forms studied so far could be achieved. Two-dimensional growth of such biopolymer films will be obtained as the results of the isolation of a single monomer and its direct interaction with the substrate and/or the film; such an interaction is based on the soft landing on the surface and on the reduced effects of the ambient contaminants. Furthermore for some applications like multicomponent films and/or superlattices films the present electrospray method might be very versatile.

## ***Measurements and Results***

Raman measurements have been taken by using the same apparatus described in Chapter 3. A 50x objective allowed the visual inspection of the samples and the determination of the localized portion of the sample giving rise to the Raman spectrum. All the spectra have been taken by using a confocal diaphragm (100 μm) to limit the beam dispersion. The power has been taken under control between 0.15-15 mW to avoid sample degradation during the typical times of the measurements (between 100 and 150 s). The spectral resolution is 2-3 cm<sup>-1</sup> for the holographic gratings with sinusoidal modulation with 1800 lines/mm.

A fluorescence background contribution<sup>57,58,59</sup> have been subtracted to all the spectra collected. This procedure didn't affect the analysis of the Raman responses since we have obtained basically the same results using quite different subtraction strategies, i.e. using a polynomial best fit curve over a

large spectra range ( $\sim 500\text{-}3250\text{ cm}^{-1}$ ) or a simple linear fit over the small relevant frequency range ( $950\text{-}1800\text{ cm}^{-1}$ ).

The samples investigated appear to be rather homogeneous either by visual inspection with microscope or by the Raman spectroscopic analysis which allows a spatial resolution on the sample surface of less than  $1\text{ }\mu\text{m}$ . Raman spectra have been collected from different eumelanin samples in powder, spray deposited (SD) or ESD on different substrates (ITO and ZnSe).

In Figure B2 are the 50x optical images of the inhomogeneous samples and the position of the micro probe for the spray deposited (SD) sample (a) and the ESD one (on ZnSe) (b). Spectra were collected from various regions of the samples. In both the samples every point collected gave the same Raman spectrum (see Figure B3). The conclusion was that in both the samples different visible colours mean different amount of sample (darker zone = thicker film).

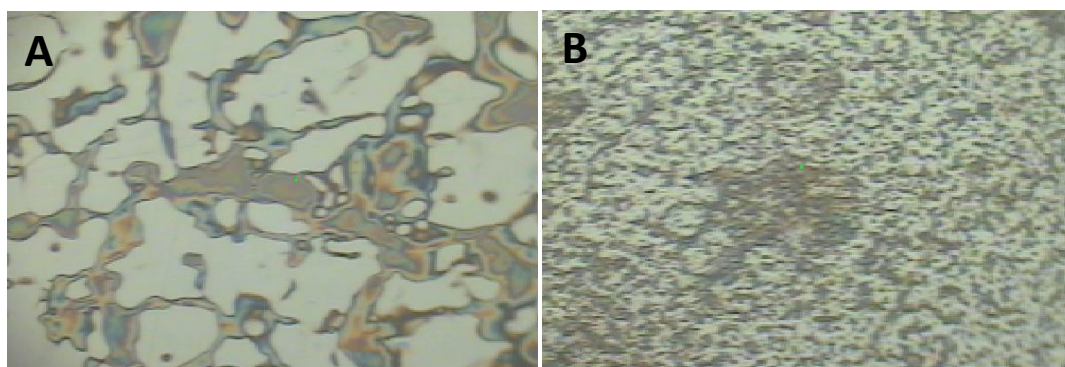


**Figure B2** – Photo obtained by the microscope of the Raman apparatus, objective 50x. A: spray deposited sample; B: electro-spray deposited sample.

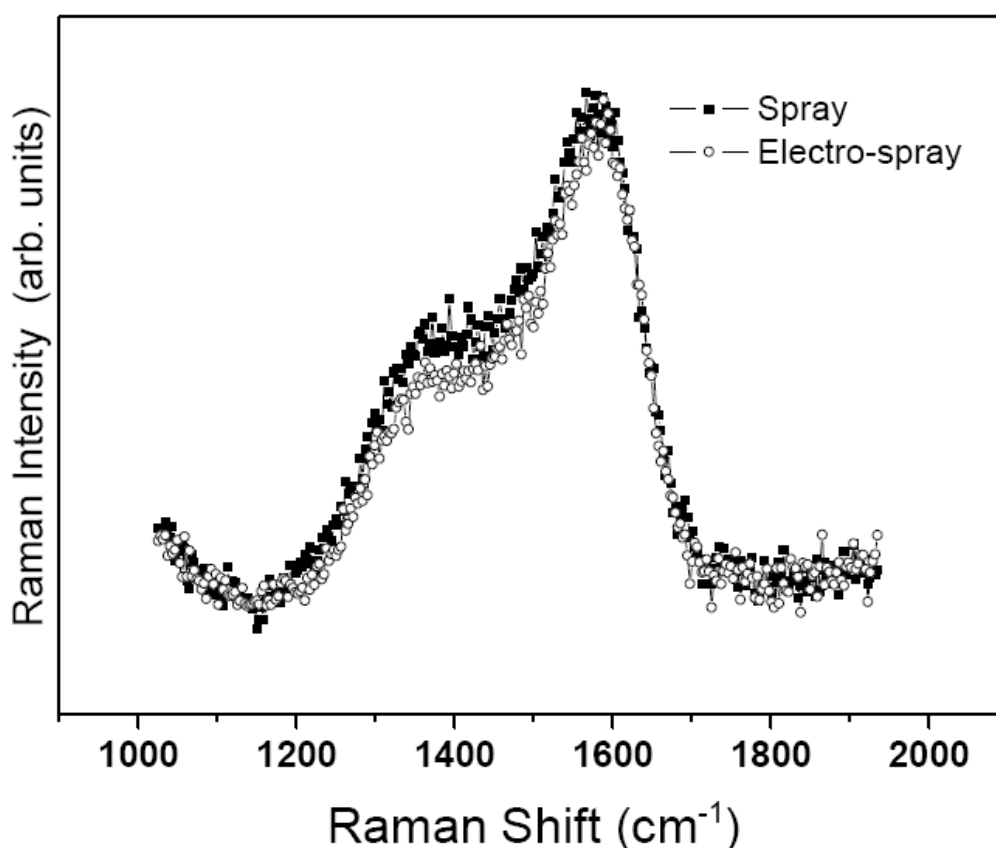


**Figure B2** – Raman spectra of the SD and ESD (on ZnSe) sample. The spectra were background subtracted (see text).

The Raman spectra of the ESD samples were collected on two different substrates: ZnSe and ITO, and were compared with that of the eumelanin powder and all the spectra are shown in Figure B3.

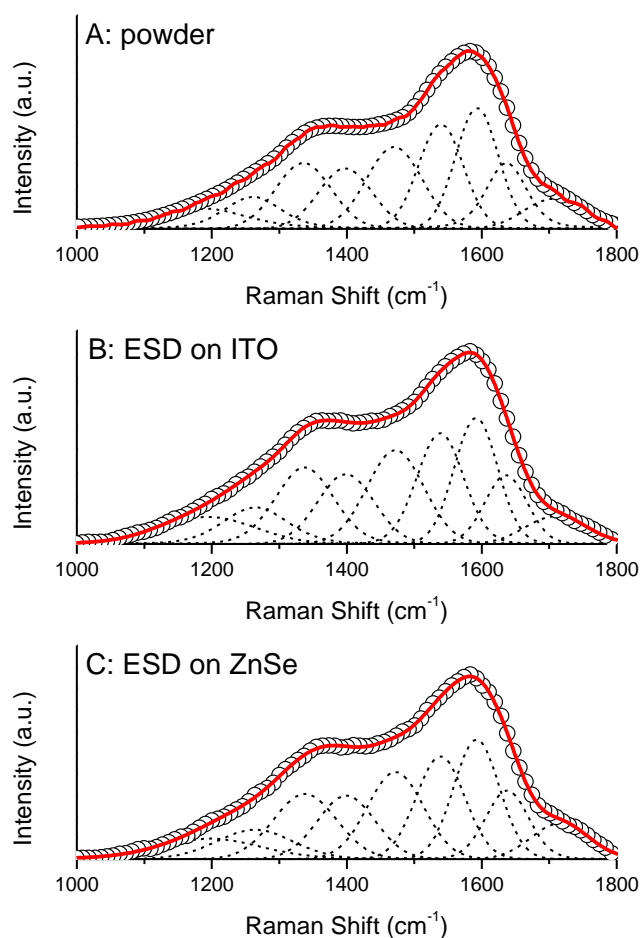


**Figure B3** – Raman spectra (circles) of the eumelanin in powder (A) and ESD deposited onto ITO (B) and ZnSe (C) substrates. The spectra were background subtracted (see text) and fitted by LMA (red curves: best fit lines, black dashed curves: components to the fit).

It is clear at a glance that the three spectra shown in Figure B3 are very similar. The Raman signals have been analysed using the Levenberg–Marquardt algorithm (LMA)<sup>13,14</sup> with nine Gaussian components over the 950-1800 cm<sup>-1</sup>. The number of components and the frequency of each component have been determined through a second derivative analysis.<sup>60</sup> The best fitting curves are also shown in Figure B3 together their respective nine Gaussian components. Also in this case the very strong similarity among the three results is qualitatively well clear. A quantitative comparison among the best fitting parameter values for the central frequencies obtained for the three samples are reported in Table B1 together with the assignment of all the peaks. The values reported for the ESD melanin samples have been obtained as an average over different samples and that the reported uncertainties have been obtained by the observed maximum data dispersion. Finally in Figure B4 the histograms of the intensities of the observed peaks for each sample are shown for sake of comparison. The whole of the Raman results thus shows a very good agreement between the spectral response of the melanin powder and those of the ESD samples.



Assignment	Powder (cm <sup>-1</sup> )	ESD on ITO (cm <sup>-1</sup> )	ESD on ZnSe (cm <sup>-1</sup> )
s(C-C) ring breathing	1191 ± 2	1196 ± 7	1199 ± 6
δ(C-H in plane)	1261 ± 2	1266 ± 3	1263 ± 2
Indole ring vibration/s(CN)	1336 ± 2	1338 ± 2	1338 ± 2
s(Pyrrole ring)	1398 ± 2	1399 ± 2	1399 ± 2
C=C aromatic ring vibration/s sym(COO <sup>-</sup> )	1470 ± 2	1472 ± 2	1471 ± 2
C=C aromatic/pyrrole ring stretching vibration	1539 ± 2	1539 ± 2	1539 ± 2
s(C=C aromatic)/s(Pyrrole ring)/indole ring vibration	1593 ± 2	1592 ± 2	1592 ± 2
C=C aromatic ring vibration/s antisymmetric (COO <sup>-</sup> )	1637 ± 2	1635 ± 2	1638 ± 2
s(C=O in COO <sup>-</sup> , quinone or ketone)	1706 ± 2	1712 ± 4	1715 ± 7

**Table B1** – Raman band positions and assignments of eumelanin powder and eumelanin ESD onto ITO and ZnSe substrates. (*s*=stretching, *δ*=deformation, *sym*=symmetric, *asym*=antisymmetric)

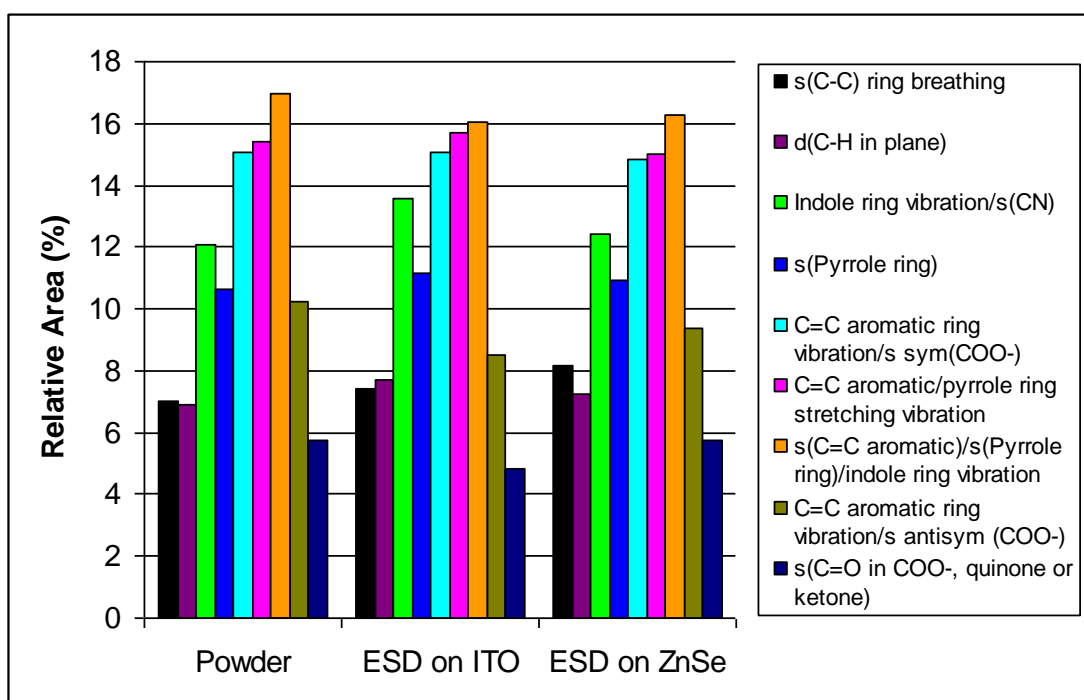


**Figure B4** – Plot of relative area obtained from LM fit for eumelanin powder, eumelanin ESD on ITO substrate and eumelanin ESD on ZnSe substrate (*s* = stretching, *d* = deformation).

## Conclusion

The Raman spectra were able to check the right conformation of the eumelanin that has been electro spray deposited onto ZnSe and ITO substrates and the results obtained from the fitting procedure were in agreement with the IR measurements made onto the same samples. Moreover on the basis of the calculation of individual contributions to Raman scattering from each monomers<sup>44</sup> (with the exclusion of the DHICA) by means of a non linear root mean square minimization it was identified that 66% of the contribution is from the HQ monomer for both types

(SD and ESD (both substrates)) of melanin in agreement with what found by Sangaletti et al. (ref 44). It is important to note that, in doing this estimate, two strong assumptions on the integrity of the monomers and the conservation of their Raman scattering at the macromolecules level were made.

## *Bibliography of Appendix*

- 
- <sup>1</sup> Akat K., Borggreffe M., Kaden J.J., Heart, 2009, 95, 616-623.
- <sup>2</sup> Elliot J.C., Rev. Mineral. Geochem., 2002, 48, 427-453.
- <sup>3</sup> Maras. A., Cottignoli V., Cavarretta E., Salvador L., Valfrè C., Acta Mineral Petrograph., 2010, 6, 374.
- <sup>4</sup> LeGeros R.Z., Z Kardiol, 2001, 90: III116-III124.
- <sup>5</sup> LeGeros R.Z., LeGeros J.P., Phosphate Minerals in Human Tissue, Eds Nriagu Jo and Moore, PB, Springer-Verlag, Berlin Heidelberg, 1986, 351-385.
- <sup>6</sup> Hughes J. M. , Rakovan J., Rev. Mineral. Geochem., 2002, 48, 1-11.
- <sup>7</sup> Pan Y., Fleet M. E., Rev. Mineral. Geochem., 2002, 48, 13-49.
- <sup>8</sup> Wopenka B. & Pasteris J. D., Material Science and Engineering C, 2005, 25, 131-143.
- <sup>9</sup> Liao S., Watari F., Xu G., Ngiam M., Ramakrishna S., Chan C.K., Materials Lett., 2007, 61, 3624-3628.
- <sup>10</sup> Leventouri T., In Biomaterials Research Advances, Chapter 6, Editor: J.B Kendall, 2007, 145-182.
- <sup>11</sup> Elliot J.C., Wilson R.M., Dowker S.E.P., JCPDS - International Centre for Diffraction Data, Advances in X-ray Analysis, 2002, 45.
- <sup>12</sup> Skinner H.C.W., In: Selinus O, Alloway BJ. Academic Press, New York, 2005, 667-693.
- <sup>13</sup> D.W. Marquardt., SIAM J. Appl. Math., 1963, 11(2), 431-441.
- <sup>14</sup> K. Levenberg, Quarterly of Applied Mathematics, 1944, 2(2), 164-168.
- <sup>15</sup> Antonakos A., Liarokapis E., Leventouri T., Biomaterials, 2007, 28, 3043-3054.
- <sup>16</sup> Fleet M.E., Liu X., Biomaterials, 2007, 28, 916-926.
- <sup>17</sup> Fleet M.E., Biomaterials, 2009, 30, 1473-1481.
- <sup>18</sup> Prabakaran K., Rajeswari S., Trends Biomater. Artif. Organs, 2006, 20(1), 20-23.
- <sup>19</sup> Penel G., Leroy G., Rey C., Bres E., Calcif. Tissue Int., 1998, 63, 475-481.
- <sup>20</sup> Ou-Yang H., Paschalis E.P., Mayo W.E., Boskey A.L., Mendelsohn R., J. Bone Miner Res., 2001, 16, 5.
- <sup>21</sup> Shi J., Klocke A., Zhang M., Bismayer U., American Mineralogist, 2003, 88, 1866-1871.
- <sup>22</sup> Delogne C., Lawford P.V., Habesch S.M., Carolan V.A., J. Microsc., 2007, 228, 62-77.
- <sup>23</sup> Awonusi A., Morris M.D., Tecklenburg M.M.J., Calcif. Tissue Int., 2007, 81, 46-52.
- <sup>24</sup> R. E. Kass et al., J. Am. Stat. Ass., 1995, 90, 773.
- <sup>25</sup> Caldwell et al., arXiv0808.2552v1.
- <sup>26</sup> Pleshko N., Boskey A., Mendelsohn R., Biophys. J., 1991, 60, 786-793.
- <sup>27</sup> Karanci M., Fratzl P., Klaushofer K., Paschalis E.P., Calcif. Tissue Int., 2006, 79, 354-359.
- <sup>28</sup> Bazin D., Chappard C., Combes C., Carpentier X., Rouziere S., André G., Matzen G., Allix M., Thiaudière D., Reguer S., Jungers P., Daudon M., Osteoporosis Int., 2009, 20, 1065-1075.
- <sup>29</sup> Shimoda S., Aoba T., Moreno E.C., Miake Y., J. of Dent. Res., 1990, 69, 1713-1740.
- <sup>30</sup> Michel V., Ildefonse P., Morin G., Appl. Geochem., 1995, 10, 145-159.
- <sup>31</sup> Olszta J.M., Cheng X., Jee S.S., Kumar R., Kim Y., Kaufman M. J., Douglas E.P., Gower L. B., Mater. Sci. Eng., 2007, R58, 77-116.
- <sup>32</sup> Vallet-Regi M., Gonzàlet- Calbet J.M., Prog. Solid State Chem., 2004, 32, 1-31.
- <sup>33</sup> Pekounov Y., Petrov O.E., J. Mater. Sci.: Mater. Med., 2008, 19, 753-759.
- <sup>34</sup> M. Abbas, M. Ali, S. K. Shah, F. D'Amico, P. Postorino, S. Mangialardo, M. Cestelli Guidi, A. Cricenti, and R. Gunnella , J. Phys. Chem. B, 2011, 115(38), 11199-11207.

- 
- <sup>35</sup> G. Prota, *J. Invest. Derm.*, 1980, 75, 122.
- <sup>36</sup> P. Meredith, B.J. Powell, J. Riesz, S.P. Nighswander-Rempel, M.R. Pederson and E.G. Moore, *Soft Matt.*, 2006, 2, 37 and references therein.
- <sup>37</sup> P. Meredith, T. Sarna, *Pigment Cell Res.*, 2006, 19, 572.
- <sup>38</sup> J.E. McGinness, *Science*, 1972, 177, 896.
- <sup>39</sup> J.E. McGinness, P. Corry, and P. Proctor, *Science*, 1974, 183, 853.
- <sup>40</sup> R.P. Crippa, V. Cristofolletti, N. Romeo, *Biochim. Biophys. Acta*, 1978, 538, 164.
- <sup>41</sup> H. Seppa, *IEEE Trans. Appl. Supercod.*, 2001, 11, 759.
- <sup>42</sup> M. Berggren, A. Richter-Dahlfors, *Adv. Mater.*, 2007, 19, 3201.
- <sup>43</sup> C. C. Felix, J. S. Hyde, T. Sarna, R. C. Sealy, *J. Am. Chem. Soc.*, 1978, 100 (3922).
- <sup>44</sup> L. Sangaletti, S. Pagliara, P. Vilmercati, C. Castellarin-Cudia, P. Borghetti, P. Galinetto, R. Gebauer, and A. Goldoni, *J. Phys. Chem. B*, 2007, 111, 5372-5376.
- <sup>45</sup> A. Pullman and B. Pullman, *Biochim. Biophys. Acta*, 1961, 54, 384.
- <sup>46</sup> G. W. Zajac, J. M. Gallas, and A. E. Alvarado-Swaigood, *J. Vac. Sci. Technol. B*, 1994, 12, 1512.
- <sup>47</sup> Y. Liu and J.D. Simon, *Pigm. Cell. Res.*, 2003, 16, 606 and references therein.
- <sup>48</sup> M. Jastrzebskaa, A. Kocotb and L. Tajbera, *J. Photochem. Photobiol. B: Biology* 2002, 66, 201.
- <sup>49</sup> V. Capozzi, G. Perna, P. Carmone, A. Gallone, M. Lastella, E. Mezzenga, G. Quartucci, M. Ambrico, V. Augelli, P.F. Biagi, T. Ligonzo, A. Minafra, L. Schiavulli, M. Pallara, and R. Cicero, *Thin. Solid. Films.*, 2006, 511512, 362.
- <sup>50</sup> S. Subianto, G. Will and P. Meredith, *Polymer*, 2005, 46, 11505.
- <sup>51</sup> S.N. Deziderio C.A. Brunello M.I.N. da Silva M.A. Cotta and C.F.O. Graeff, *J. Non-Cryst. Solids*, 2004, 338340, 634.
- <sup>52</sup> G.S. Lorite, V.R. Coluci, M.I.N. da Silva, S.N. Dezidrio, C.F.O. Graeff, D.S.Galvao and M.A.Cotta, *J. Appl. Physics*, 2006, 99, 113511.
- <sup>53</sup> P. Diaz, Y. Gimeno, P. Carro, S. Gonzalez, P. L. Schilardi, G. Benitez, R. C. Salvarezza, and A. H. Creus, *Langmuir*, 2005, 21, 5924.
- <sup>54</sup> A. Jaworek *J. Mater. Sci.*, 2007, 42, 266.
- <sup>55</sup> J. C. Swarbrick, J. B. Taylor, J. N. OShea, *Appl. Surf. Sci.*, 2006, 252, 5622.
- <sup>56</sup> N. Dam, M. M. Beerbom, J. C. Braunagel and R. Schlafa, *J. Appl. Phys.*, 2005, 97, 024909.
- <sup>57</sup> V. Capozzi et al., *J. Mol. Struct.*, 2005, 744–747, 717–721.
- <sup>58</sup> P. Meredith, J. Riesz, *Photochem. Photobiol.*, 2004, 79, Issue 2, 211–216.
- <sup>59</sup> G. Perna et al., *J. Luminescence*, 2009, 129, 44 – 49.
- <sup>60</sup> Byler, D. M., and Susi, H., *Biopolymers*, 1986, 25, 469-487.

# *Acknowledgments*

Vorrei ringraziare innanzitutto i miei genitori che hanno sempre accompagnato e supportato le mie scelte. Grazie anche a mia sorella per tutto il bene che mi vuole! Un pensiero sincero anche ai miei nonni, avrei tanto voluto averli tutti qui con me, ma sono sicura che mi stanno ancora sorridendo.

Grazie alle mie amiche, che hanno sempre creduto in me, anche quando a me qualche dubbio è venuto! Grazie al mio ragazzo che caparbiamente cerca sempre di spiegarmi il mondo ... anche se, nonostante gli anni di studi siano ormai molti, io continuo sempre a vederlo a modo mio ...

Grazie al Prof. Postorino per la pazienza ed i preziosi consigli, e al Prof. Dore per l'altrettanta pazienza nel rispondere alle mie domande e per i bei momenti leggerezza!

Grazie ai compagni di viaggio che per poco o molto tempo sono stati con me in laboratorio: Carlo, Daniele, Ilaria, Matteo, Michele, Sara, Federica e Leonetta (queste ultime mi hanno dovuto sopportare pure in trasferta, grazie!).

Grazie a tutte le belle persone che ho incontrato per le stanze del 4° piano del nuovo edificio di Fisica, professori, post-doc, dottorandi e laureandi.

Grazie al Prof. Caminiti per i campioni e soprattutto per il suo contagioso entusiasmo! E grazie anche a Francesca e Francesca per avermi risposto con un sorriso tutte le volte che sono entrata nel laboratorio del vecchio edificio di chimica per qualche campione da misurare e rimisurare ...

Grazie alla Prof.ssa Congiu e al Sig. Belardinelli per l'immensa disponibilità nelle ore passate davanti alla centrifuga ...

Grazie al Prof. Bordi per i suoi insegnamenti sia nel corso che ho seguito che nelle successive discussioni ...

Sono certa che sto dimenticando qualcuno, ma se quel qualcuno mi conosce sa anche che sono un pochino smemorata (eufemismo!) e quindi sono certa che non se la prenderà a male!



# *List of Publications*

List of publications inherent with the present PhD thesis:

- S. Mangialardo, F. Piccirilli, A. Perucchi, P. Dore, P. Postorino, “Raman analysis of Insulin Denaturation induced by High-Pressure and Thermal Treatments”, accepted to J. Raman Spectrosc. 2011.
- M. Abbas, M. Ali, S. K. Shah, F. D’Amico, P. Postorino, S. Mangialardo, M. Cestelli Guidi, A. Cricenti, and R. Gunnella, “Control of Structural, Electronic, and Optical Properties of Eumelanin Films by Electrospray Deposition”, J. Phys. Chem. B, 2011, 115(38), 11199–11207.
- E. Bodo, P. Postorino, S. Mangialardo, G. Piacente, F. Ramondo, F. Bosi, P. Ballirano, and R. Caminiti, “The structure of the molten salt methyl ammonium nitrate explored experiments and theory”, accepted to J. Phys. Chem. B.
- S. Mangialardo, V. Cottignoli, P. Postorino, M. Marras, “Raman and Infrared Study on Bioapatite from Cardiac Valves”, to be submitted to Applied Spectroscopy.
- S. Mangialardo et al., “Raman Study on Lysozyme Different Conformations: Native, Fibrillar and Ionic-Liquids Treated”, to be submitted.